UNIVERSITÀ
DEGLI STUDI
DI PADOVA

UNIVERSITÀ DEGLI STUDI DI PADOVA

DIPARTIMENTO DI BIOLOGIA

SCUOLA DI DOTTORATO DI RICERCA IN: BIOSCIENZE E BIOTECNOLOGIE

INDIRIZZO: BIOLOGIA CELLULARE

XVII CICLO

Study of the tissue determinants of cardiac arrhythmias with novel biophysical approaches

Direttore della Scuola: Ch.mo Prof. Giuseppe Zanotti

Coordinatore di indirizzo: Ch.mo Prof. Paolo Bernardi

Supervisore: Dott. Marco Mongillo

Dottoranda: Giulia Borile

INDEX

ABBREVIATIONS

Ab	**A**nti**b**ody
Ad	**Ad**eno
AP	**A**ction **P**otential
ATP	**A**denosine1,4,5, **T**ris**P**hosphate
AV	**A**trio**v**entricular
β- AR	**β**-**A**dreno**r**eceptor
BrdU	5-**Br**omo-2'-**d**eoxy**U**ridine
BSA	**B**ovine **S**erum **A**lbumin
BVT	**B**idirectional **V**entricular **T**achycardia
CaM	**Ca**l**m**odulin
CaMKII	**Ca**$^{2+}$/cal**m**odulin-dependent protein **K**inase **II**
CASQ	**Ca**l**s**e**q**uestrin
CFP	**C**yan **F**luorescent **P**rotein
ChR2	**Ch**annel-**R**hodopsin **2**
CICR	**C**alcium-**I**nduced-**C**alcium **R**elease
CM	**C**ardio**M**yocyte
CMV	**C**yto**M**egalo**V**irus
CPV	**C**ircularly **P**ermuted **V**enus
CPVT	**C**atecholaminergic **P**olymorphic **V**entricular **T**achycardia
CTRL	**C**on**tr**o**l**
Cy3	**Cy**anine-**3**
DAD	**D**elayed **A**fter **D**epolarization
DAPI	4,6-**D**i**A**minidino-2-**P**henyl**I**ndole
DCR	**D**iastolic **C**a^{2+} **R**elease
DMEM	**D**ulbecco's **M**odified **E**agle **M**edium
DNA	**D**eoxyribo**n**ucleic **a**cid
DTT	**D**i**t**hio**t**hreitol
EAD	**E**arly **A**fter **D**epolarization
ECC	**E**xcitation **C**ontraction **C**oupling
ECFP	**E**nhanced **C**yan **F**luorescent **P**rotein
ECG	**E**lectro**c**ardio**g**ram
EDTA	**E**thilene**D**iamine**T**etraacetic **A**cid
EGFP	**E**nhanced **G**reen **F**luorescent **P**rotein
EMRE	**E**ssential **M**CU **Re**gulator
ER	**E**ndoplasmic **R**eticulum
FBS	**F**etal **B**ovine **S**erum
FDM	**F**irst **D**ay **M**edium
FPS	**F**rames **P**er **S**econd
FRET	**F**örster **R**esonance **E**nergy **T**ransfer
FWHM	**F**ull **W**idth at **H**alf **M**aximum
GC	**G**enome **C**opies

GECI	**G**enetically **E**ncoded **C**a^{2+} **I**ndicator
GFP	**G**reen **F**luorescent **P**rotein
HE	**H**aematoxylin/**E**osin
HR	**H**eart **R**ate
HRP	**H**orse **R**adish **P**eroxidase
HS	**H**orse **S**erum
ICD	**I**mplantable **C**ardioverter **D**efibrillator
IF	**I**mmuno**F**luorescence
IMM	**I**nner **M**itochondrial **M**embrane
IMS	**I**nter **M**embrane **S**pace
ITS	**I**nsulin **T**ransferrin **S**elenium
IVS	**I**nter **V**entricular **S**eptum
KO	**K**nock-**O**ut
LA	**L**eft **A**trium
LED	**L**ight **E**mitting **D**iode
LTCC	**L**-**T**ype **C**alcium **C**hannel
LV	**L**eft **V**entricle
MCS	**M**ultiple **C**loning **S**ite
MCU	**M**itochondrial **C**a^{2+} **U**niporter
MCUb	**M**itochondrial **C**a^{2+} **U**niporter **b**
MCUR1	**M**itochondrial **C**a^{2+} **U**niporter **R**egulator **1**
MEM	**M**inimal **E**ssential **M**edium
MHC	**M**yosin **H**eavy **C**hain
MICU1	**Mi**tochondrial **C**a^{2+} **U**ptake **1**
MICU2	**Mi**tochondrial **C**a^{2+} **U**ptake **2**
MMM	**M**ultispot **M**ultiphoton **M**icroscopy
MOI	**M**ultiplicity **O**f **I**nfection
MOPS	4-**Mo**rpholine**p**ropane**s**ulfonic acid
NA	**N**umerical **A**perture
NCX	**N**a^{+}/**C**a^{2+} e**x**changer
NE	**N**or**e**pinephrine
NEAA	**N**on **E**ssential **A**mino**A**cids
O/N	**O**ver**N**ight
OMM	**O**uter **M**itochondrial **M**embrane
PBS	**P**hosphate **B**uffered **S**aline
PCR	**P**olymerase **C**hain **R**eaction
Pen/Strep	**Pen**icillin-**Str**eptomycin
PF	**P**urkinje **F**iber
PFA	**P**ara-**F**orm**a**ldehyde
PKA	**P**rotein **K**inase **A**
PLB	**P**hospho**l**am**b**an
PMCA	**P**lasma **m**embrane **C**a^{2+} **A**TPase
PMT	**P**hoto**M**ultiplier **T**ube

PSF	**P**oint **S**pread **F**unction
PVDF	**P**oly**V**inyli**D**ene **F**luoride
PVC	**P**remature **V**entricular **C**omplex
RFP	**R**ed **F**luorescent **P**rotein
RNA	**R**ibo**n**ucleic **a**cid
ROS	**R**eactive **O**xygen **S**pecies
RT	**R**oom **T**emperature
RT-qPCR	**R**eal **T**ime **q**uantitative **PCR**
RV	**R**ight **V**entricle
RyR2	**Ry**anodine **R**eceptor **2**
SAN	**S**ino **A**trial **N**ode
SCD	**S**udden **C**ardiac **D**eath
SCR	**S**pontaneous **C**a^{2+} **R**elease
SDS	**S**odium **D**odecyl **S**ulphate
SEM	**S**tandard **E**rror of the **M**ean
SERCA	**S**arco-**E**ndoplasmic **R**eticulum **C**a^{2+} **A**TPase
SOICR	**S**tore **O**verload-**i**nduced **C**a^{2+} **R**elease
SR	**S**arcoplasmic **R**eticulum
STED	**St**imulated **E**mission **D**epletion
TBS	**T**ris **B**uffered **S**aline
TM	**T**rans**m**embrane
TN-C	cardiac **T**roponi**n** **C**
TN-I	cardiac **T**roponi**n** **I**
TN-T	cardiac **T**roponi**n** **T**
TPEM	**T**wo **P**hoton **E**xcitation **M**icroscopy
TTBS	**T**ween20-**T**ris **B**uffered **S**aline
VDAC	**V**oltage-**D**ependent **A**nion **C**hannel
VF	**V**entricular **F**ibrillation
VT	**V**entricular **T**achycardia
WB	**W**estern **B**lot
WT	**W**ild **T**ype
YFP	**Y**ellow **F**luorescent **P**rotein

SUMMARY

Background: Catecholaminergic Polymorphic Ventricular Tachycardia (CPVT) is a severe inherited disease leading to stress dependent arrhythmias and sudden cardiac death in young subjects with structurally normal heart. The CPVT-linked point mutation R2474S in the Ryanodine Receptor (RyR2) Ca^{2+} channel has been identified in affected families and has been shown to cause alterations in cardiomyocyte (CMs) Ca^{2+} handling, playing a key role in initiating and sustaining arrhythmias. At the single cell level, diastolic Ca^{2+} release events are a phenotypic manifestation of Ca^{2+} leak (in the form of Ca^{2+} sparks) from the RyR2, highly documented in isolated CMs. Whether such behavior occurs in the intact heart and how this is linked to the onset of tissue-wide arrhythmias, remains for some aspects unclear.

Aims: The first aim of my project was to study Ca^{2+} homeostasis in a multicellular cardiac tissue model of acute ventricular slices, in both WT and CPVT hearts, and determine the role of RyR2 mediated Ca^{2+} leak in triggering ventricular arrhythmias. In the development of my project, I have performed experiments with standard two-photon microscope and, in parallel, I have tested a newly developed multiphoton microscopy setup using parallel scanning to achieve faster acquisition rates in a large field of view, both properties instrumental to Ca^{2+} imaging in intact heart tissue.
The second aim of my research came back at the subcellular level in order to understand whether cardiac mitochondria play a role in sustaining cardiac arrhythmias, in relation to the increasing evidence in the literature about this topic.
The third and last aim of my research focused on the evaluation of the critical cell mass for extrasystolic beats activation. In the lab, optogenetic stimulation of cardiac muscle was set up and experimental data were fitted with 2 different biophysical models adopted to approximate light-tissue interaction. With this same optogenetic approach we triggered bidirectional ventricular tachycardia (BVT) in WT and CPVT mice in order to understand whether the genetic background was sufficient *per se* to sustain VTs and degenerate into ventricular fibrillation (VF).

Results: The use of two-photon excitation microscopy (TPEM) in cardiovascular research is increasing and the need of methodological improvement is arising. Several approaches have been implemented to increase performance of the microscopy systems

towards, e.g. higher spatial or temporal resolution, increased penetration depth in intact tissues or simultaneous detection of signals from multiple wavelengths. For the study of Ca^{2+} signals in the intact myocardium, especially during the complex and chaotic Ca^{2+} fluctuations characterizing arrhythmias, sufficient penetration depth is required together with subcellular resolution, at a sampling rate of at least $1/20^{th}$ second, in a field of view wide enough to simultaneously record fluorescence from several connected cells. We here describe the validation of a novel multispot multiphoton microscope (MMM), whose features fulfill all of these requirements. In this setup, the laser beam is split by a diffractive optic element in 16 beamlets that are deflected in parallel by galvanometric mirrors to raster scan the sample. Each beamlet is associated to a dedicated photo-multiplier tube (PMT); the PMTs array allows the parallel acquisition from the different beamlets and, at the same time, avoids cross-talk between channels, which is of particularly important to avoid signal deterioration during thick tissue imaging. We demonstrated that MMM enables the investigation of fast occurring Ca^{2+} dependent signals in the living cells within intact heart slices [1].

The heart slices model was used to compare CPVT and normal myocardium in a multicellular tissue model. Slices were field-stimulated and the kinetics of cytosolic Ca^{2+} transients, in terms of amplitude and decay time, was monitored with or without administration of norepinephrine (NE), a β-adrenergic agonist used to mimic the physiologic stress response. NE caused the expected increase in the gain of excitation-contraction coupling, resulting in larger Ca^{2+} transient amplitude and faster decays. β-adrenergic stimulation of CPVT slices caused abnormal Ca^{2+} dynamics including "*alternans*" and diastolic Ca^{2+} release events (DCRs), in line with the data acquired in single isolated cardiomyocytes. As DCRs are a well characterized arrhythmogenic mechanism, we set up a protocol to increase the probability of these events, consisting in a pace-stop protocol in which stimulation was performed at 3-5Hz for 5 seconds and subsequently interrupted, a procedure unmasking aberrant spontaneous Ca^{2+} releases (SCRs). The mean duration of such SCRs was 1 second and their occurrence was less than 0.4 DCRs/sec/cell. In our experiments, we observed that SCRs have the tendency to develop in clusters, suggesting that the propensity of a single cardiomyocyte to develop SCR can be influenced by the activity of the surrounding cells. Accordingly, the probability for neighboring cells to have "synchronized releases" resulted higher than that of random SCR events.

In a subsequent part of the project, we assessed whether mitochondria play a role in determining Ca^{2+} mediated arrhythmic triggers. To this aim, mitochondrial Ca^{2+} imaging was set up in neonatal CMs (NCMs), and these experiments exploited the molecular identification of the most important mediator of mitochondrial Ca^{2+} fluxes, i.e. the mitochondrial Ca^{2+} uniporter, MCU. To evaluate whether data obtained in NCMs could be transferred to the well developed cardiomyocytes constituting the adult heart, we evaluated the expression level of proteins belonging to the MCU complex during cardiac development. In agreement with the larger I_{mcu} recorded by Fieni et al. [2] in mitoplasts from neonatal than adult hearts, MCU levels were higher in the protein extract from neonatal than adult hearts.

Finally, we explored the electrotonic coupling of CMs in the heart that implies that the abnormal depolarization current resulting from a DCR in a single cell (source) would distribute to all the immediate neighbors (10-12 on average in the mammalian heart), thus hindering the propagation of the depolarization wave to the entire myocardium. For arrhythmic beats to occur, such protective factor must be overcome, meaning that the number of cells depolarizing synchronously must exceed the buffering capacity of the current 'sink'. However, the critical cell number needed to generate arrhythmic beats has never been determined directly in the intact heart.

To estimate such fundamental value for cardiac electrophysiology, we investigated the minimal tissue requirement for conducting a beat using cardiac optogenetics. We generated a transgenic mouse expressing Channelrhodopsin-2, a photoactivated ion channel, under control of the cardiac specific αMHC promoter. Photoactivation of the protein with 470 nm light leads to the entry of Na^{+} in ChR2 expressing cardiomyocytes causing membrane depolarization. We performed optical stimulation of αMHC-ChR2 hearts using differently sized fiber optics during ECG monitoring, to control the volume of depolarized myocardium. Moreover, by modulating the light power at the source it was possible to increase the depth reached by a sufficient amount of light to depolarize ChR2-expressing cardiomyocytes. We thus implemented an optogenetic assay to investigate tissue requirements for arrhythmic beats. As a basis for such assay, we built a geometrical model of light attenuation inside cardiac tissue to measure the number of cells activated by the light flash in each experimental condition (i.e. fiber diameter and starting power). To determine the light attenuation of the heart, we prepared tissue phantoms (both frozen

and fresh) of variable thickness and measured the transmitted light across the tissue. Experimental data were then fitted with the commonly used Beer-Lambert Law that models light attenuation with a mono-exponential decay function and we obtained the path length parameter $\delta \sim 240$ μm that is in line with data reported in the literature (290 μm for guinea-pig). Considering the low numerical aperture (NA) of the optical fibers, we approximated the light emerging from the tip to a cylinder.

The minimal tissue volume necessary to evoke an ectopic beat, as estimated by the combination of fiber diameter and light intensity, resulted of approximately 1800 cardiomyocytes.

To further confirm this estimation we applied another model of light-matter interaction, the Kubelka-Munk model. In this model the fiber's NA and the refractive index of the tissue are considered. The experimental data previously obtained for light attenuation were thus fitted with this model generating the scattering parameter S = 14-20 mm^{-1} (consider that for brain is 12 mm^{-1}). Such value was used to estimate the total tissue mass enclosed by a given light power/fiber size combination and the calculated number of cardiomyocytes necessary to trigger ectopic beats in the myocardium was around 1100 cardiomyocytes.

Moreover, with the same optogenetic approach it was possible to externally trigger extrasystolic beats originating alternatively from the right and left ventricle (bidirectional ventricular tachycardia, BVT), that were obtained in both WT and CPVT hearts. While in basal conditions no differences were observed between the two genotypes after BVT stimulation, upon NE and caffeine administration, CPVT mice showed VTs, demonstrating that the CPVT background causes increased propensity to develop ventricular arrhythmias.

Conclusions and Perspectives:

1) the multicellular model of cardiac slices was set up and successfully used as a testing platform for a novel MMM that increases imaging speed.

2) subcellular Ca^{2+} events, such as macrosparks and waves occured also in a multicellular model and were more frequent in CPVT myocardium; moreover, it was possible to observe spontaneous Ca^{2+} releases with a pattern of interdependency.

3) mitochondrial Ca^{2+} imaging has been set up in NCMs, and the evaluation of MCU complex expression highlighted once more the requirement to study $[Ca^{2+}]_{mt}$ in adult cardiomyocytes, in order to understand the role played by mitochondria in triggering and

sustaining arrhythmias. Moreover, the discordant data between mRNA and protein expression in heart postnatal development, opens to the speculation that post-transcriptional regulation of MCU is occurring.

4) optogenetics was exploited to test the tissue requirement for ectopic beats and two different models of light-tissue interaction were applied to estimate the minimal number of cells and these parameters will be compared in normal and CPVT hearts.

5) optically triggered BVTs failed to trigger sustained arrhythmias in basal conditions but were sustained upon NE and caffeine administration only in CPVT, and not in the WT hearts. Moreover, by taking advantage of a novel mouse in which ChR2 expression is confined to the cardiac conduction system, the study will continue toward understanding the role of Purkinje fibers in inherited arrhythmic diseases.

RIASSUNTO

Background: La tachicardia ventricolare polimorfa catecolaminergica (CPVT) è una grave malattia ereditaria che porta ad aritmie dipendenti da sforzo fisico e stress, e morte improvvisa per cause cardiache in soggetti giovani con un cuore strutturalmente normale. La mutazione puntiforme (R2474S) nel canale RyR2 per il Ca^{2+} è stata identificata in famiglie portatrici di CPVT ed è stato dimostrato che provoca alterazioni nell'omeostasi del Ca^{2+} dei cardiomiociti (CM), giocando un ruolo chiave nel generare e mantenere le aritmie. Al livello della singola cellula, gli eventi di rilascio diastolico di Ca^{2+} sono una manifestazione fenotipica di leakage di Ca^{2+} (in forma di Ca^{2+} sparks) dal RyR2, molto documentato in cardiomiociti isolati. Se tali manifestazioni avvengano nel cuore intero e come questi siano legati all'insorgenza di aritmie a livello del tessuto cardiaco, rimane per alcuni aspetti poco chiaro.

Obiettivi: Il primo obiettivo del mio progetto è quello di studiare l'omeostasi del Ca^{2+} in un modello di tessuto cardiaco multicellulare, che consiste in spesse fette ventricolari tagliate in acuto, sia da cuori WT sia CPVT, e determinare il ruolo del rilascio di Ca^{2+} mediato dal RyR2 nello scatenare aritmie ventricolari. Nello sviluppo del mio progetto, ho eseguito esperimenti con un microscopio a due fotoni standard e, in parallelo, ho testato un microscopio a multifotone recentemente sviluppato che sfrutta la scansione in parallelo per aumentare la velocità di acquisizione mantenendo un largo campo di vista, proprietà essenziali per l'imaging del Ca^{2+} nel tessuto cardiaco intatto.
Il secondo obiettivo della mia ricerca è tornato a livello subcellulare per capire se i mitocondri dei cardiomiociti giochino un ruolo nel sostenere le aritmie cardiache, in relazione alle crescenti evidenze presenti in letteratura su quest'argomento.
Il terzo e ultimo scopo della mia ricerca si è focalizzato sulla valutazione della massa critica di cardiomiociti necessaria per l'attivazione battiti extrasistolici. In laboratorio, è stata messa a punto la stimolazione optogenetica del cuore in un modello murino e i dati sperimentali sono stati fittati con due diversi modelli biofisici per approssimare l'interazione luce-tessuto. Con questo stesso approccio optogenetico abbiamo mimato una tachicardia ventricolare bidirezionale (BVT) in topi WT e CPVT per capire se il background genetico sia sufficiente di per sé a sostenere VT e degenerare in fibrillazione ventricolare (VF).

Risultati: L'uso di microscopia a due fotoni nella ricerca cardiovascolare sta aumentando e di conseguenza cresce la necessità di un miglioramento metodologico. Diversi approcci sono stati implementati per aumentare le prestazioni dei sistemi di microscopia attraverso, ad esempio, l'aumento di risoluzione spaziale o temporale, una maggiore profondità di penetrazione nei tessuti intatti o la rilevazione simultanea di segnali provenienti da più lunghezze d'onda. Per lo studio dei segnali Ca^{2+} nel miocardio intatto, specialmente durante le complesse e caotiche fluttuazioni di Ca^{2+} che caratterizzano le aritmie, buona profondità di penetrazione ed elevata risoluzione subcellulare sono entrambe necessarie, a una frequenza di campionamento di almeno $1/20^{mo}$ di secondo, in un campo di vista abbastanza ampio da registrare simultaneamente la fluorescenza da più cellule collegate. Qui descriviamo la convalida di un innovativo microscopio multispot a multifotone (MMM), le cui caratteristiche soddisfano tutte queste esigenze. In questo setup, il fascio laser è suddiviso da un elemento ottico diffrattivo (DOE) in 16 fascetti che sono deviati in parallelo da specchi galvanometrici per ottenere la scansione del campione. Ogni fascio è associato a un PMT dedicato; la matrice di PMT consente l'acquisizione in parallelo dei diversi fascetti e, allo stesso tempo, evita il cross-talk tra i canali, che è di particolare importanza per evitare il deterioramento dell'acquisizione durante l'imaging in un tessuto spesso. Abbiamo dimostrato che il MMM permette lo studio dei veloci segnali di Ca^{2+} nelle cellule all'interno di fette cardiache vitali [1].

Il modello di fette di cuore è stato utilizzato per confrontare il miocardio CPVT e normale in un modello di tessuto multicellulare. Le fette sono state stimolate elettricamente e la cinetica dei transienti di Ca^{2+} citosolico, in termini di ampiezza e durata, è stata monitorata con e senza somministrazione di noradrenalina (NE), un agonista β-adrenergico usato per simulare la risposta fisiologica allo stress. La NE ha causato, il previsto aumento di efficienza nell'accoppiamento eccitazione-contrazione, con conseguente aumento dell'ampiezza e riduzione della durata dei transienti di Ca^{2+}. La stimolazione β-adrenergica di fette CPVT ha causato anormali dinamiche di Ca^{2+} tra cui le "alternans" ed eventi di rilascio diastolico di Ca^{2+} (DCR), in linea con i dati acquisiti in cardiomiociti isolati. Siccome le DCRs sono un meccanismo aritmogeno ben caratterizzato, abbiamo settato un protocollo per aumentare la probabilità del verificarsi di questi eventi, che consiste in un protocollo di stimolazione e arresto, in cui la stimolazione è effettuata a 3-5Hz per 5 secondi e successivamente interrotta, una procedura per smascherare rilasci spontanei di Ca^{2+} (SCR). La durata media di tali SCR è circa di 1 secondo e la loro frequenza è inferiore a 0,4 DCR/sec/cellula. Nei nostri

esperimenti, abbiamo osservato che gli SCR hanno la tendenza a svilupparsi in clusters, suggerendo che un singolo cardiomiocita sia più propenso a svilupparne uno se influenzato dall'attività delle cellule circostanti. Di conseguenza, la probabilità per cellule vicine di avere "rilasci" sincronizzati è superiore a quello di eventi casuali con le stesse caratteristiche temporali.
In una parte successiva del progetto, abbiamo valutato se i mitocondri hanno un ruolo nei trigger aritmici dipendenti dal Ca^{2+}. A questo scopo, è stato settato l'imaging di Ca^{2+} mitocondriale in cardiomiociti neonatali in coltura (NCM), e questi esperimenti hanno sfruttato la recente identificazione molecolare del più importante mediatore dell'influsso di Ca^{2+} mitocondriale, cioè l'uniporto mitocondriale, MCU. Per valutare se i dati ottenuti in NCM possano essere trasferiti ai cardiomiociti maturi che costituiscono il cuore adulto, abbiamo valutato il livello di espressione delle proteine appartenenti al complesso MCU, durante lo sviluppo cardiaco postnatale. In accordo con la maggiore corrente (I_{mcu}) registrata da Fieni et al. [2] in mitoplasti da cuori neonati rispetto agli adulti, i livelli di MCU erano più alti nell'estratto proteico da cuori neonatali che adulti.

Infine, abbiamo esplorato l'accoppiamento elettrotonico dei cardiomiociti nel cuore che implica che la corrente di depolarizzazione anormale risultante da un DCR in una singola cellula (sorgente) è distribuita a tutti i cardiomiociti circostanti (10-12 mediamente nel cuore dei mammiferi), impedendo la propagazione dell'onda di depolarizzazione all'intero miocardio. Perché avvengano battiti aritmici, tale fattore di protezione deve essere superato, il che significa che il numero di cellule depolarizzate in sincrono deve superare la capacità di tamponamento della corrente 'sink'. Tuttavia, il numero critico di cellule necessario per generare battiti aritmici non è mai stato determinato direttamente nel cuore intatto.
Per stimare tale valore fondamentale per l'elettrofisiologia cardiaca, abbiamo studiato il requisito minimo del tessuto per condurre un battito ectopico, sfruttando l'optogenetica. Abbiamo generato un topo transgenico che esprime Channelrhodopsin-2, un canale ionico fotoattivato, sotto il controllo del promotore α-MHC cardio-specifico. La fotoattivazione della proteina con luce a 470 nm comporta l'ingresso di Na^{+} nei cardiomiociti che esprimono ChR2 causando la depolarizzazione della membrana. Abbiamo eseguito la stimolazione optogenetica dei cuori αMHC-ChR2 utilizzando fibre ottiche di dimensioni diverse durante il monitoraggio dell'ECG dell'animale, per valutare il volume di

miocardio depolarizzato. Inoltre, modulando la potenza luminosa alla fonte è stato possibile aumentare la profondità raggiunta da una quantità sufficiente di luce per depolarizzare cardiomiociti esprimenti ChR2. Abbiamo quindi implementato un test optogenetico per indagare i requisiti minimi per scatenare battiti aritmici. Come base per tali test, abbiamo costruito un modello geometrico di attenuazione della luce all'interno tessuto cardiaco per misurare il numero di cellule attivate dal flash di luce in ciascuna condizione sperimentale (ossia in funzione del diametro delle fibre e della potenza iniziale). Per determinare l'attenuazione della luce nel cuore, abbiamo preparato campioni di tessuto cardiaco (sia congelati sia freschi) di spessore variabile e misurato la luce trasmessa attraverso il tessuto. I dati sperimentali sono stati poi fittati con la legge Beer-Lambert, comunemente usata, che descrive l'attenuazione della luce con una funzione di decadimento mono-esponenziale e abbiamo ottenuto la stima della lunghezza media percorsa $\delta \sim 240$ μm che è in linea con i dati presenti in letteratura (290 μm per il guinea-pig). Considerando la bassa apertura numerica della fibra ottica abbiamo approssimato che la luce emerga dalla punta della fibra con una forma cilindrica.

Il volume di tessuto minimo necessario per evocare un battito ectopico, stimato dalla combinazione di diametro delle fibre e l'intensità della luce, è risultato di circa 1800 cardiomiociti.

Per confermare ulteriormente questa stima abbiamo applicato un diverso modello d'interazione luce-materia, il modello di Kubelka-Munk. In questo modello sono considerati l'apertura numerica della fibra e l'indice di rifrazione del tessuto. I dati sperimentali ottenuti in precedenza per l'attenuazione della luce sono stati quindi fittati con questo modello e abbiamo ricavato il parametro di scattering S = 14-20 mm^{-1} (si consideri che per il cervello è 12 mm^{-1}). Tale valore è stato utilizzato per la stima della massa di tessuto totale data da una combinazione potenza della luce/dimensione della fibra, e il numero calcolato di cardiomiociti necessario per innescare extrasistoli nel miocardio è di circa 1100 cardiomiociti.

Inoltre, con lo stesso approccio optogenetico è stato possibile attivare esternamente battiti extrasistolici provenienti alternativamente dal ventricolo destro e sinistro (tachicardia ventricolare bidirezionale, BVT), che sono stati ottenuti sia in cuori WT sia CPVT. Mentre in condizioni basali non sono state osservate differenze tra i due genotipi dopo la stimolazione di una BVT, in seguito alla somministrazione di NE e caffeina, i topi CPVT

hanno mostrato VT, dimostrando che il background CPVT causa un'aumentata suscettibilità allo sviluppo di aritmie ventricolari.

Conclusioni e prospettive:

1) il modello multicellulare di fette cardiache è stato settato applicato con successo come piattaforma di test per un innovativo MMM che aumenta la velocità di acquisizione delle immagini.

2) eventi subcellulari di Ca^{2+}, come macrosparks e onde, si verificano anche in un modello multicellulare e sono più frequenti nel miocardio CPVT; inoltre, è stato possibile osservare rilasci spontanei di Ca^{2+} con un pattern d'interdipendenza.

3) l'imaging di Ca^{2+} mitocondriale messo a punto in cardiomiociti neonatali in coltura, e la valutazione dell'espressione del complesso MCU ha evidenziato ancora una volta l'esigenza di studiare $[Ca^{2+}]_{mt}$ in cardiomiociti adulti, al fine di comprendere il ruolo svolto dai mitocondri nell'innescare e sostenere aritmie. Inoltre, i dati discordanti tra mRNA ed espressione della proteina nello sviluppo post-natale del cuore, aprono alla speculazione che possa esserci una regolazione post-trascrizionale di MCU.

4) l'optogenetica è stata sfruttata per testare i requisiti del tessuto per originare extrasistoli e sono stati applicati due diversi modelli d'interazione luce-tessuto per stimare il numero minimo di cellule nei cuori WT, e questi parametri saranno confrontati tra cuori normali e CPVT.

5) le tachicardie bidirezionali stimolate otticamente non sono riuscite a innescare aritmie sostenute in condizioni basali, ma sono state sostenute dopo somministrazione di NE e caffeina solo in CPVT, e non nei cuori WT. Inoltre, approfittando del nuovo modello murino in cui l'espressione di ChR2 è limitata al sistema di conduzione cardiaco, lo studio proseguirà verso la comprensione del ruolo delle fibre di Purkinje nelle aritmie ereditarie.

1. INTRODUCTION

1.1 The heart – Anatomy and histology

The heart is responsible for blood delivery to the entire body, thus ensuring oxygen and nutrient supply to all cells of the different tissues. The heart is divided into 4 chambers: *right atrium* (RA) and *left atrium* (LA), *right ventricle* (RV) and *left ventricle* (LV) that connect at the heart apex. Cardiac contraction and blood pumping can be physically described as originating from two pumps working in series: the right cardiac sections pump blood from the systemic veins to the pulmonary circulation while the left pump the oxygenated blood from the pulmonary arteries to the systemic circulation. The left and right ventricles are separated by the *interventricular septum* (IVS) while the *interatrial septum* separates the left from the right atria.

Each atrium is connected to the corresponding ventricle through *atrioventricular* (AV) *valves* that allow unidirectional blood flow from the atria to the ventricles.

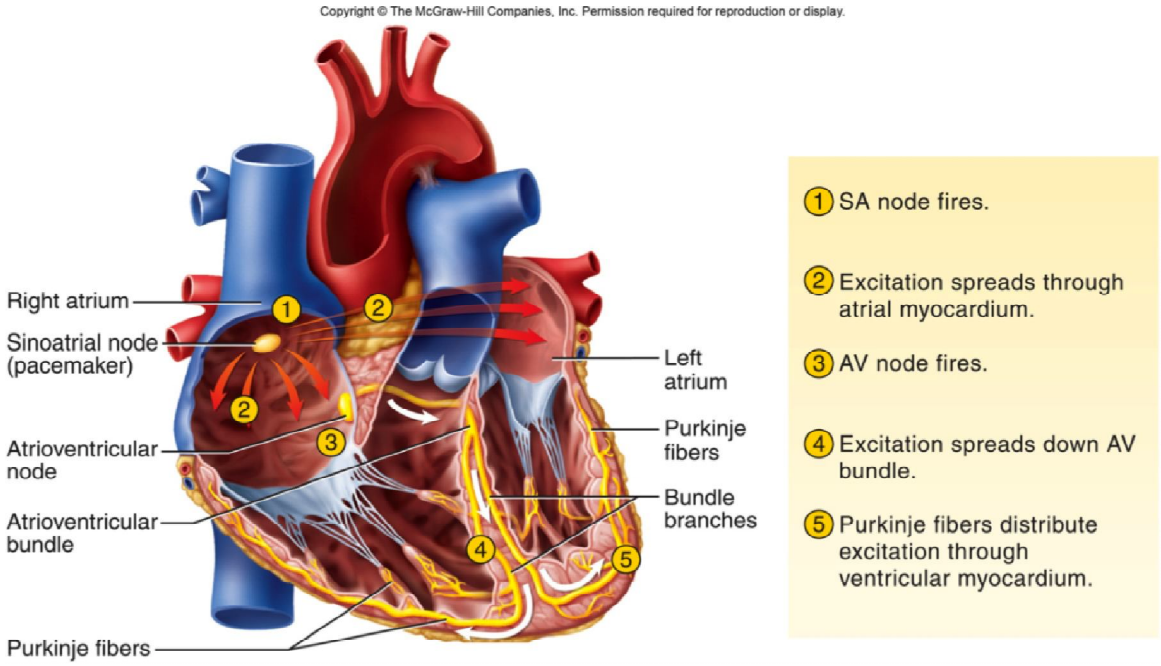

Figure 1. Heart anatomy.

A heart cycle is divided into two phases, the heart contraction and the subsequent heart relaxation, respectively called systole and diastole. Considering a normal heart rate around 80 beats per minute (bpm; source: American Heart Association, AHA), the human heart is requested to contract billions of times during life. This condition requires an

anatomical structure for efficient blood pumping and perfect synchronization of contraction and relaxation.
The architecture of cardiac walls consists into 3 portions:

1. the *epicardium* that is the external part of both ventricles;
2. the *endocardium* that faces the cardiac chambers;
3. the *myocardium* that consists in the major portion of wall thickness and is responsible for contractile activity.

The contractile cells of the heart are called *cardiomyocytes* and account for around 70% of the total cardiac volume. Cardiomyocytes can be divided in 2 subgroups:

1. *working cardiomyocytes*, that constitute the large majority and are responsible for heart contraction;
2. *cardiomyocytes of the conduction system*, including the distal part the Purkinje fibers (PFs) named after their discoverer [3, 4], that are responsible for efficient propagation of electrical signals and synchronization of ventricular activity.

Nevertheless, these are not the unique cellular components of the heart. Indeed, other cell types are present, such as cardiac fibroblasts, responsible for synthesis of collagen and other components of extra-cellular matrix, endothelial cells that constitute the highly organized vascular tree of heart muscle, with a 'fractal' distribution [5], and cardiac nerves. The heart is able to contract autonomously without nerve stimulation (if compared to skeletal muscle, as described below) but is highly innervated by the autonomic nervous system [6] that continuously tunes the force and frequency of cardiac contractions. The parasympathetic innervation is responsible for the so-called rest-and-digest activity lowering the heart rate when the body is in a relaxed state. The sympathetic innervation is responsible for the flight-or-fight response enhancing heart rate and contraction force via the release of its neurotransmitter, norepinephrine (NE).
As said previously, no nerve stimulation is essential to trigger a heartbeat. The perfect synchronization of the pumping activity is mediated by the electrical activation of the heart. Each heartbeat is, in fact, initiated by electrical impulses generated by spontaneously depolarizing cells that constitute the sinoatrial node (SAN) that serves as cardiac pacemaker. This electrical impulse is then propagated through the RA and then LA. This depolarizing wave passes through the AV node where is slowed before entering the AV bundle, constituted of PFs. This structure is highly conductive and bifurcates in

left and right branches at the top of the IVS. The entire system is called His-Purkinje system and allows rapid conduction of the electrical signals through the ventricular myocardium in order to allow coordinated contraction of all heart cells [7].

1.2 Cardiomyocytes – structure and ECC

The working cardiomyocytes (from now onward called cardiomyocytes, CMs) have a highly organized internal structure. Almost half of their volume (47%, from [8]) is occupied by contractile proteins that are organized in crystal-like arrays of striated myofibrils. The largest part of the remaining volume is occupied by mitochondria (25% at birth and 35% in the adult, [9]) as discussed in detail below. Another subcellular compartment is the sarcoplasmic reticulum (SR) that, although occupying only the 3.5% of the total volume, constitutes the main intracellular Ca^{2+} store and is crucial for cardiomyocyte contraction.

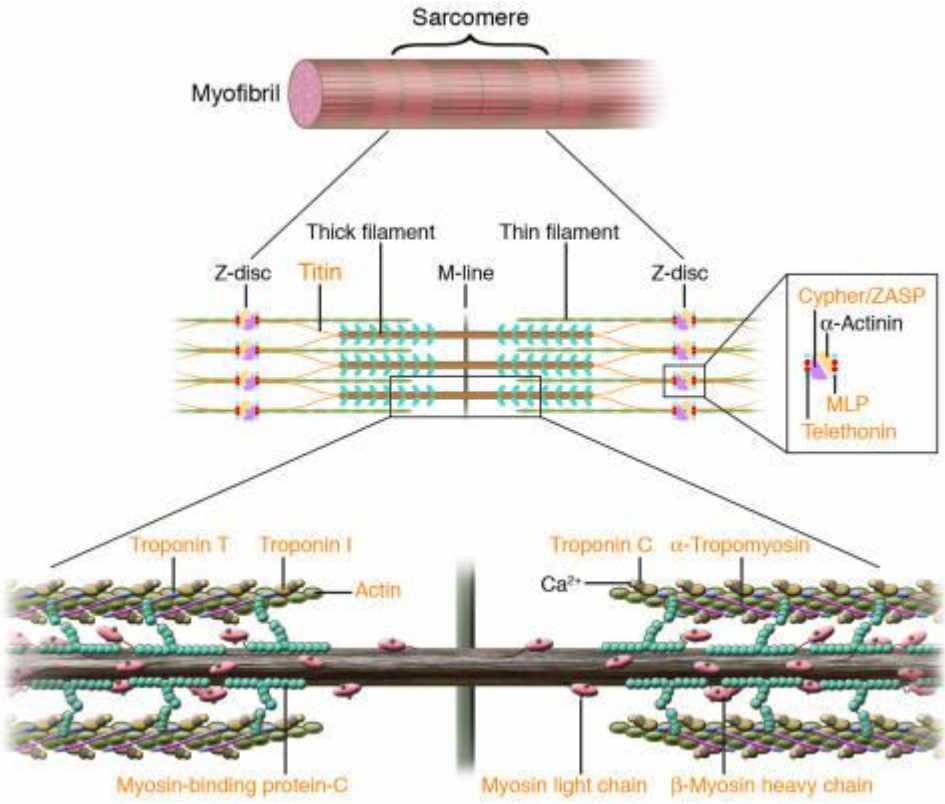

Figure 2. Sarcomere and troponin complex. From [10].

The contractile units in each cardiomyocyte, called sarcomeres, are formed by myofibrils, mainly composed by thin (actin) and thick (myosin) filaments, as shown in fig. 2. Each myosin molecule contains two heads endowed with ATPase activity. In addition to actin, the thin filaments are composed of other interacting proteins, namely tropomyosin and

troponins. Attached to tropomyosin, at regular intervals proteins of the troponin complex are found, represented by: troponin-T (TN-T), troponin-C (TN-C) and troponin-I (TN-I). Sarcomere shortening is enacted by the interaction between actin and myosin. When Ca^{2+} binds to TN-C, it induces a conformational change in the troponin complex proteins allowing the direct interaction between actin and myosin. TN-I exposes a site on the actin molecule that binds the myosin ATPase located on the myosin head. Such event results in ATP hydrolysis that supplies energy for a conformational change to occur in the actin-myosin complex: the actin and myosin filaments slide along each other, thereby shortening the sarcomere length and thus inducing cell contraction.

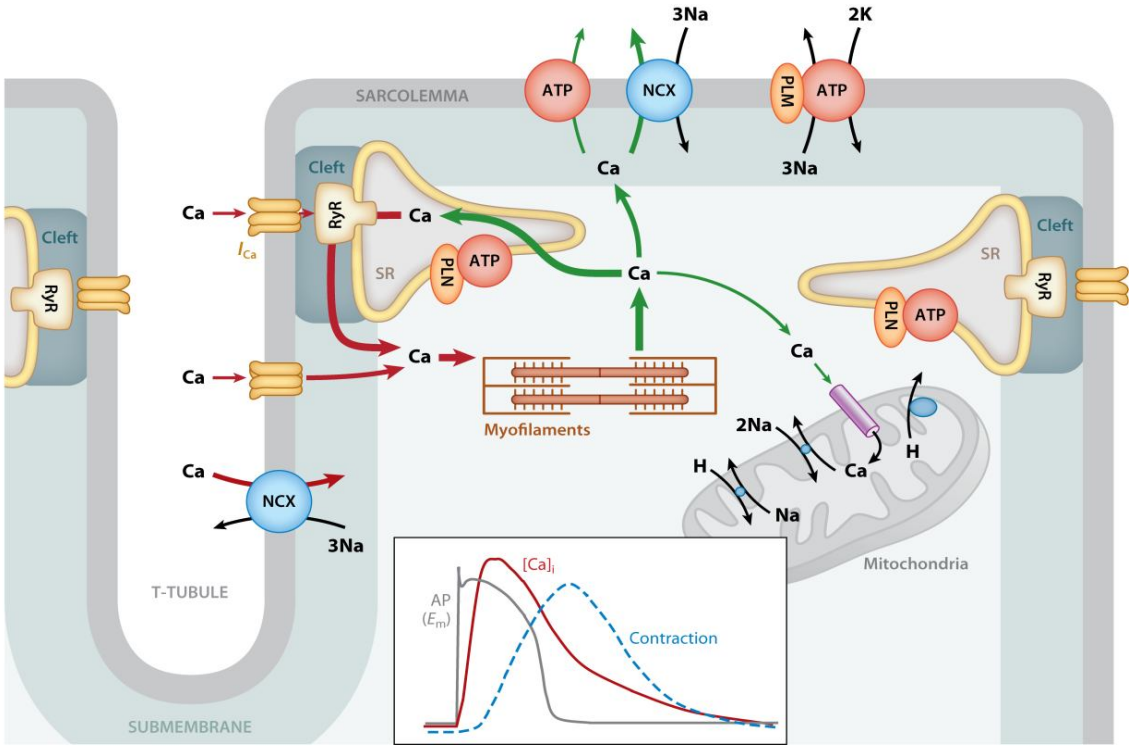

Figure 3. The role of Ca^{2+} in cardiomyocyte ECC. Ca^{2+} supply is indicated in red while Ca^{2+} removal in green. From [11].

The process whereby an action potential triggers the CM to contract is called *Excitation-Contraction Coupling* (ECC) [12] and is represented in fig. 3. CM contraction is, in fact, triggered by an action potential (AP) that opens L-type Ca^{2+} channels (LTCC) located in the T-tubule plasma membrane. The resulting Ca^{2+} influx in the cytoplasm activates a much larger release of Ca^{2+} from the sarcoplasmic reticulum (SR), the intracellular Ca^{2+} store, through activation of Ryanodine Receptor-2 (RyR2, see fig. 4). RyR2 Ca^{2+} channels are located in the sarcoplasmic reticulum membrane and, upon binding the small amount of Ca^{2+} entered through the LTCCs, increase their permeability to the ion, causing a massive release of Ca^{2+} from the SR to the cytosol. This release is a passive flux along

the concentration gradient because the $[Ca^{2+}]_{SR}$ is several order of magnitude larger than $[Ca^{2+}]_i$ in the cytosol, and is called *calcium-induce-calcium-release* (CICR) [13]. The elevated $[Ca^{2+}]_i$ in the cell is then able to trigger sarcomere shortening. Going in deeper detail, it has to be mentioned that the release of Ca^{2+} from the SR through a single RyR2 channel cluster does not cause a global increase in cytosolic Ca^{2+}, but generates individual 'elementary' Ca^{2+} release events, named *calcium sparks* [14]. The amplitude, duration and area of these Ca^{2+} sparks depend on RyRs, whose function is tightly regulated. Several proteins bind to the channels allowing its stabilization (calstabin [15, 16]) or increasing Ca^{2+} flux (such as triadin and junctin). Moreover, phosphorylation of the RyR2, either by CAMKII or PKA, increases the release of calcium, participating, to the inotropic heart response to sympathetic stimulation [17].

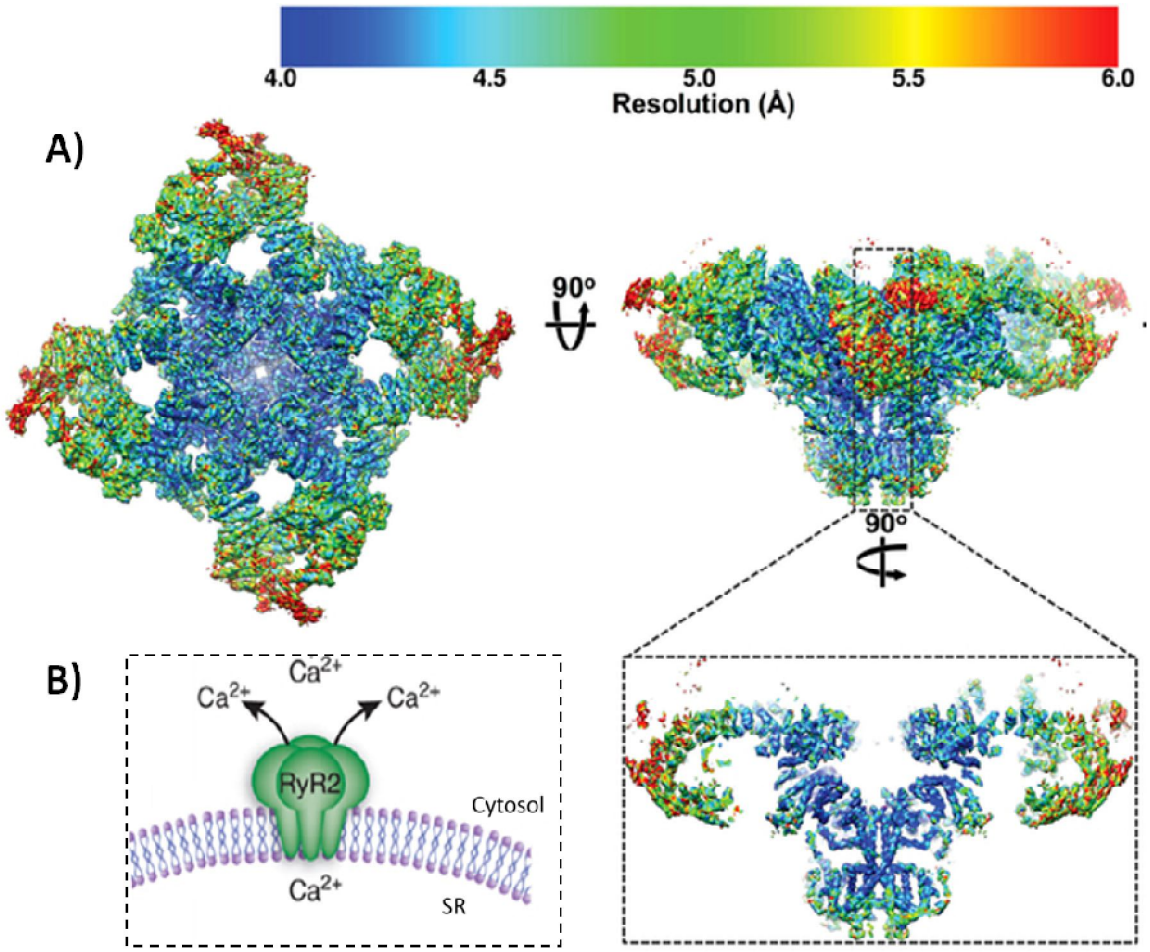

Figure 4. A) RyR1 structure. Modified from [18]. B) RyR2 intracellular localization and function. Modified from [19].

Movements between myosin and actin occur as long as cytosolic Ca^{2+} remains elevated. Ca^{2+} is then sequestered back into the SR by an ATP-dependent calcium pump

(SERCA2 ATPase), thus lowering the cytosolic Ca^{2+} concentration and removing Ca^{2+} from the TN-C. The reduction in intracellular [Ca^{2+}] induces a conformational change in the troponin complex leading, once again, to TN-I inhibition of the actin-binding site so that the initial sarcomere length is restored [20]. The effective re-uptake of Ca^{2+} from the cytosol to the SR is essential to restore the starting conditions before a new AP fires. While more than 75% of total Ca^{2+} re-enters the SR, the remaining Ca^{2+} is extruded from the cell via NCX (Sodium-Calcium Exchanger) (24%) or up-taken by the mitochondria (1%) [9].

The SERCA2 ATPase is an ion pump that uses ATP hydrolysis to transport Ca^{2+} against its concentration gradient. An essential regulator of the SERCA2 is phospholamban (PLB) that in normal condition decreases the Ca^{2+}sensitivity of the pump, thus slowing the uptake rate. Such inhibitory effect of PLB is reversed by PKA phosphorylation that causes faster relaxation and increased contractility.

The NCX is located in the plasma membrane of cardiomyocytes and is the most important mechanism of Ca^{2+} extrusion from the cytosol to the extracellular space. The NCX transports 3 Na^{+} across the membrane in exchange for a single Ca^{2+}, thus generating an inward depolarizing current consequent to Ca^{2+} efflux. This depolarizing current is usually small and impacts on the membrane potential only for few millivolts, however, as we will see, can cause dangerous arrhythmic phenomena in failing substrates [21].

Last but not least, the 1% of total contractile Ca^{2+} enters the mitochondria. The entrance is mediated by a passive uniporter (MCU) that has been molecularly identified recently [22, 23]. While in normal conditions the percentage of Ca^{2+} uptake seems not significant if compared to SERCA2 and NCX, the mitochondria have been shown to accumulate large amount of Ca^{2+} that is of particular interest in pathological Ca^{2+}-overloaded cardiomyocytes, as it will be discussed later.

1.3 Mitochondrial calcium in cardiomyocyte ECC

Mitochondrial Ca^{2+} plays several roles in heart physiology, among which the regulation of ATP production. Indeed, ATP is essential for both cardiomyocyte shortening, and for SERCA2-mediated replenishment of the SR Ca^{2+} and cardiomyocyte diastole. To give an idea, a single human heartbeat necessitates of 300 mg of ATP distributed among the cardiomyocytes; this means almost 1000 tons of ATP within human lifetime (calculated from [24]).

Almost all the cytosolic ATP is provided by mitochondria that in adult cardiomyocytes account for more than 30% of total cell volume, thus resulting in the largest mitochondrial volume fraction among mammalian cell types [8]. However, recent evidence suggests that mitochondria in heart physiology do not contribute uniquely to energy supply but are able to modulate key electrophysiological and Ca^{2+} cycling properties, either directly through the activation of mitochondrial ion channels, or indirectly, by acting on ATP levels, redox state or signaling cascades [25, 26]. While the observation that mitochondria are able to take up Ca^{2+} was performed decades ago [27], the molecular identification of the uptake machinery is still in progress, although a great momentum was given in 2011 when two independent groups [22, 23] published the molecular identification of the mitochondrial calcium uniporter, MCU. Since then, other components of the complex were identified, but the full understanding of the uptake machinery is still lacking (a schematic representation of the complex is reported in fig. 5).

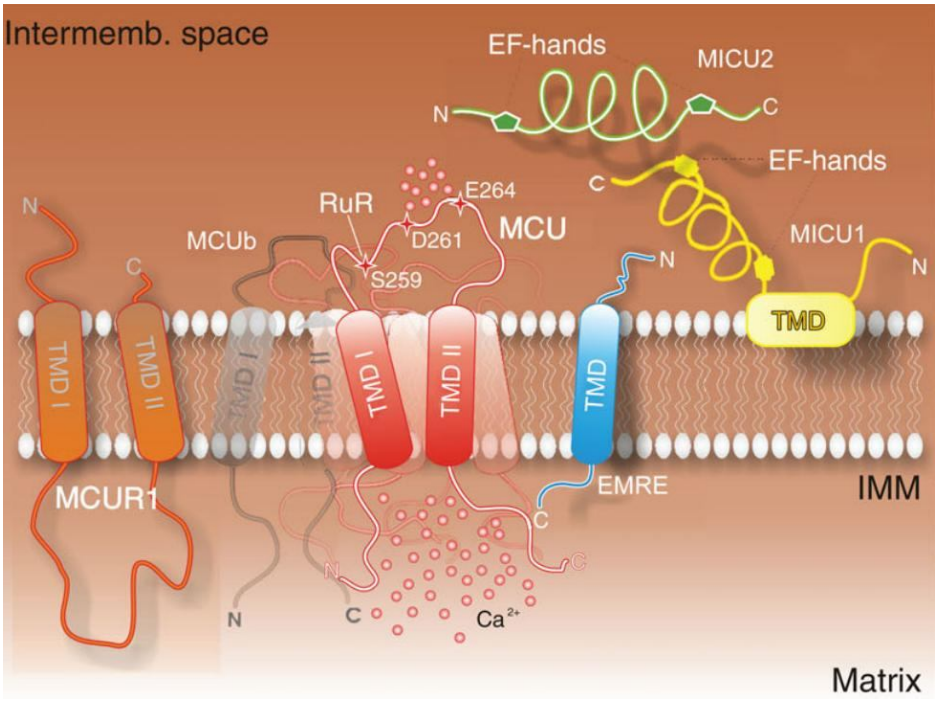

Figure 5. Mitochondrial Ca^{2+} uniporter complex. Image from [28].

In detail (see fig. 5), even though the crystallographic structure of uniporter complex is not available, it has been proposed that the protein is a hetero-tetramer of MCU and MCUb inserted in the inner mitochondrial membrane (IMM) with both the N- and C-terminals facing the matrix [29]. Both MCU and MCUb sequences show two predicted transmembrane domains with a loop in the intermembrane space (IMS) whose sequence

is crucial for Ca^{2+} binding [29]. While the outer mitochondrial membrane (OMM) is highly permeable to Ca^{2+} and other ions thanks to VDAC, a porin ion channel, the IMM can be crossed by Ca^{2+} only through the MCU. The biochemical nature of the complex was understood prior to the molecular identification. Indeed, it was clear that the Ca^{2+} flux could follow only one direction (UNI-porter) and that the channel was passive allowing Ca^{2+} entry only when the electrochemical gradient across the IMM is present. The uniporter has a low sensitivity to Ca^{2+}, meaning that it needs a large [Ca^{2+}] increase in order to open. Ca^{2+} sensitivity is likely modulated by the synergistic action of MICU1 and MICU2, which can form dimers associated to the transmembrane part of the complex [30]. The link between MICUs and MCU is ensured by the presence of EMRE [31] that binds MICUs to MCU, allowing stabilization of the channel activity [32]. The exact stoichiometry of all the components is unknown, but it has been shown, at least at the mRNA level, that the transcriptional level of the MCU gene is highly variable in different tissues, and its function, as well as its regulation are not yet understood [2, 29]. To this purpose, a knock-out (KO) mouse for MCU has been generated ($MCU^{-/-}$) and recently published [33] by Finkel and colleagues. Surprisingly, given the expectation on the fundamental role of MCU raised by its detection in all mammalian cell types, mice were alive and grossly normal even though mitochondrial Ca^{2+} uptake was completely abrogated. That said, some questions are still open considering that these mice were obtained in a mixed background (CD1-C57BL6), while $MCU^{-/-}$ mice in C57BL6 background died around E11.5-E13.5, probably for cardiac disorders [34]. This latter observation allows speculating on the key role of MCU in heart development.

1.4 Neonatal and adult CMs: from extracellular to intracellular Ca^{2+} cycle

The mechanism described above for ECC refers to adult cardiomyocytes that already completed their cellular maturation. However, the mechanism is very different in fetal/neonatal cardiomyocytes. This is of particular interest and has to be considered in relation to the fact that NCMs are a widely used cellular model for the amenability to cell culture and genetic manipulation. Fetal and neonatal cardiomyocytes have longer lasting contractions and their activation relies mostly on the influx of Ca^{2+} from the extracellular space. In such cells, Ca^{2+} cycle, including both the influx and the efflux of the ion, occurs across the plasma membrane and is accompanied by depolarizing currents. The entry of Ca^{2+} from the extracellular space is mediated, also in this case, by the L-type calcium

channels located in plasma membrane, however during diastole, Ca^{2+} is extruded from the cardiomyocytes through the NCX and the Plasma Membrane Calcium Pump ATPase (PMCA) [35, 36].

1.5 CPVT is an arrhythmogenic disease characterized by altered Ca^{2+} homeostasis

Intracellular Ca^{2+} homeostasis in cardiomyocytes requires a delicate balance of Ca^{2+} fluxes between the intracellular compartments and the extracellular space.

Alterations in Ca^{2+} signaling have been associated to a wide variety of cardiovascular pathologies, ranging from hypertrophy, to heart failure, to arrhythmias [37]. In these conditions, alterations in the mechanism of propagation of calcium waves occur, leading to either abnormalities in the strength of cardiac contraction (as in heart failure) or to abnormal generation and propagation of electrical signals (as in arrhythmias).

Catecholaminergic polymorphic ventricular tachycardia (CPVT) is an inherited disease characterized by stress induced ventricular tachyarrhythmias leading to syncope and sudden cardiac death [38-40]. The clinical presentation includes exercise- or emotion-induced syncopal events and a distinctive pattern of reproducible, stress-related, BVT. People affected by CPVT have structurally normal hearts and an unremarkable pattern on the resting electrocardiogram (ECG) [39].

The prevalence of CPVT in the population is not known, but it has been estimated around 1:10000, with clusters of much higher prevalence in some Italian regions [38]. CPVT is one of the most severe inherited arrhythmogenic disorders, and a frequent cause of sudden cardiac death (SCD) in children and young adults. Early diagnosis with clinical evaluations and genetic screening is possible. However, chronic treatment with β-adrenergic receptor blockers is the only pharmacological alternative to the use of implantable cardioverter defibrillator (ICD) devices, but despite compliance to therapy, about 30% of the patients develop life-threatening sustained VTs. Given the young age of the patients and the incomplete effectiveness of the current therapies, it is important to increase our understanding of the pathophysiology of CPVT in order to identify novel therapeutic strategies.

Molecular genetic studies have unveiled that CPVT results from inherited defects of intracellular calcium handling in cardiac myocytes [16, 40, 41]. An essential component of the delicate regulation of ECC is the RyR2 channel because it couples the AP-induced

entry of Ca^{2+} with the massive release of Ca^{2+} from the SR that is necessary to trigger cardiomyocyte contraction and the subsequent heart beat. As a consequence, the perfect correspondence of AP with SR Ca^{2+} release is essential in cardiomyocyte physiology, whereas un-triggered releases of Ca^{2+} may lead to electrical instabilities.

Since the first identification of RyR2 mutations in CPVT patients by Priori and colleagues [42], a number of different mutations in the RyR2 gene have been associated to the autosomal dominant form of CPVT. Moreover, there is another variant of CPVT that is a recessive form [43] caused by mutations in the cardiac-specific isoform of the Calsequestrin 2, *CASQ2*.

After the genetic identification of the mutations leading to CPVT, many investigations started aiming to link DNA abnormalities to functional derangement of these calcium-controlling proteins in cardiomyocytes pathophysiology. The crystal structure of the RyR2 channel is not yet available hampering some evaluation about the disease-associated amino-acids mutations. However, it is known that the channel is a tetramer with its bigger portion immersed in the cytosol and the recent report of RyR1 entire structure (reported in fig. 4) unveiled the position of the Ca^{2+} sensitive domains [18].

Several approaches have been used in the last 15 years, from in vitro expression of mutant proteins to the generation of knock-in animal models, increasing our understanding on intracellular Ca^{2+} deregulation associated to the onset of CPVT [11].

A large contribution given by the in vitro analysis consists in the characterization of RyR2 properties in lipid bilayers, showing that most mutations cause a gain-of-function and an increase in open probability upon β-adrenergic stimulation or caffeine administration. At the cell level, these mutations cause RyR2-mediated Ca^{2+} leakage from the SR during adrenergic stimulation, and this phenomenon has been reported by several groups, however, the mechanism underlying Ca^{2+} leakage is still matter of debate.

Marks and colleagues first proposed that RyR2 mutations are characterized by a defective binding to Calstabin2 (FKBP12.6) that stabilizes RyR2 closed state during diastole [16].

As an alternative hypothesis, Chen and co-workers suggested that RyR2 mutations lower the threshold for the occurrence of spontaneous releases of Ca^{2+}, and they call this phenomenon store overload-induced calcium release (SOICR) [44, 45].

A third alternative comes from George and colleagues who suggested defective interaction between the different domains of the RyR2 tetramer [46, 47].

Thanks to the generation of knock-in mouse models carrying different human mutations, it has become possible to study defective channels in a complex physiologic environment.

Different mouse models, among which the R2474S used in this thesis, showed a structurally normal heart, no arrhythmias in basal conditions, while upon caffeine and epinephrine stimulation exhibited arrhythmic events, BVT or polymorphic VT or both [41, 48].

Several studies performed in isolated CMs from different CPVT mouse models showed that disease-related mutations caused a gain-of-function of the RyR2 channels, visible in the form of increased Ca^{2+} leak from the SR, upon β-AR stimulation. This increased RyR2 open probability resulted in Ca^{2+} sparks at higher rate, with larger area and longer duration. As a consequence, it results in intracellular Ca^{2+} waves that eventually lead to triggered activity in the form of delayed after-depolarizations (DADs). Indeed, the excess of released Ca^{2+} through defective RyR2 channels during the repolarization phase, exits through the NCX causing a net depolarizing current. These DADs are cell-wide Ca^{2+} events not initiated by an external AP as during ECC, but spontaneous depolarization of the CM membrane due to elevated cytosolic Ca^{2+} concentrations. An example of DADs during triggered activity in CPVT CMs is shown in fig.6.

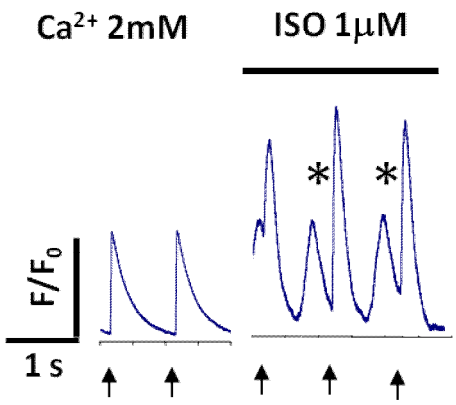

Figure 6. DADs in CPVT cardiomyocytes upon isoproterenol stimulation

As cardiomyocytes have a complex subcellular organization resulting in strict SR-mitochondria interaction, whether mitochondrial Ca^{2+} influx is able to buffer excessive levels of Ca^{2+} in diseased CMs is not clear, but evidence is raising in support of the possible role of mitochondrial Ca^{2+} influx in the genesis or sustainment of cardiac arrhythmias [49].

During the first part of this PhD thesis work, we focused our attention on DADs occurrence in terms of mutual influence between neighboring CMs. Indeed, a trademark of CPVT is the bidirectional VT (BVT) that consists in a beat-to-beat alternation of the QRS axis, that can be initiated and sustained by triggered activity [38]. Considering that

the beats of the BVT originate alternatively from left and right apical portions of the heart, two possible explanation have been proposed: 1) RV and LV have foci of activation constituted by a limited number of cells or 2) the origin consists in a kind of ping-pong between left and right branches of Purkinje fibers [50].

Whether BVTs are generated by foci of CMs or PFs aberrant alterations, the mechanisms whereby a single cell having a DAD can influence the surrounding CMs and trigger a complex arrhythmia (as shown in fig.7) remains unclear.

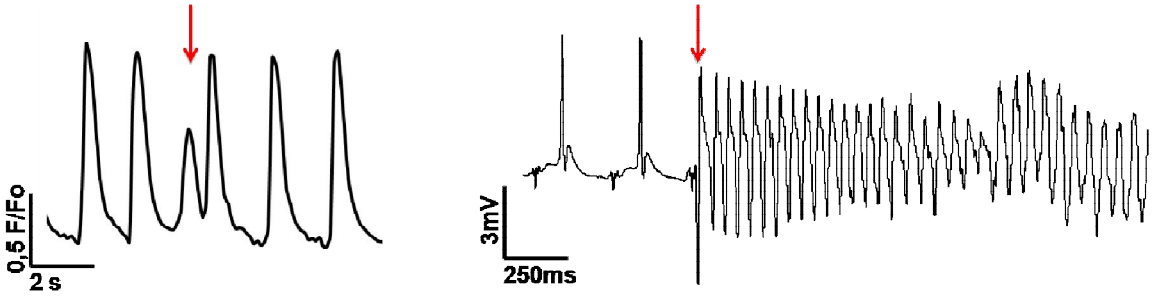

Figure 7. From the single cell to the whole heart level.

1.6 Source-sink mismatch

Propagation of focal arrhythmic beats in the heart occurs when the current density generated by the abnormally depolarizing cardiomyocytes (*current source*) is sufficient to overcome the electrotonic sink of the surrounding polarized tissue [51]. In the heart, each cardiomyocyte is coupled to around 11 other cardiomyocytes [52], that are able to buffer (*current sink*) the depolarizing wave generated by the source cardiomyocyte having a DAD. The minimal number of cardiomyocytes sufficient to generate a spreading cardiac activation wave (extrasystole) through the whole myocardium is referred as *critical mass*.

The number of cells required to bring the sink to its activation threshold has been evaluated with simulations or alternative experimental approaches leading to highly different results, from 800000 cells [52] to only 50 [53]. Thus the identification of the critical mass dimension and the mechanism by which spontaneously depolarizing cells can display synchronous activity is of particular relevance in inherited or acquired arrhythmia syndromes, in which altered electrical properties of the myocardium, caused by abnormal Ca^{2+} homeostasis, leads to electrical instability of the heartbeat, often causing sudden cardiac arrest and death.

As such, one ongoing challenge in molecular cardiology is to develop new tools with the aim to elucidate and increase general understanding of cardiomyocyte and heart function.

1.7 Technical advances in molecular cardiology

Different strategies have been adopted and developed in this thesis. Both rely on light, in terms of conversion of intracellular parameters into light signals, light activation of cellular processes and technical devices to read and interfere with cell physiology.

The first two approaches can be considered part of the optogenetic field, with its larger definition.

The term *optogenetics*, first used in 2006 by Miller [54], refers to the use of light-sensitive proteins (*opto-*) genetically targeted to cells (*-genetic*).

The Oxford English Dictionary defines optogenetics as "*the branch of biotechnology which combines genetic engineering with optics to observe and control the function of genetically targeted groups of cells with light, often in the intact animal*" [55].

Optogenetic approaches allow obtaining elevated temporal and spatial control of cell electrophysiological properties [54, 56, 57]. With such broad definition of the concept, there are two classes of optogenetic devices: sensors and actuators [55].

On the other hand, optogenetics needs to be coupled to peculiar devices in order to read the signals from sensors and to efficiently transduce light to the actuators. The first case consists in the development of microscopy techniques enabling higher spatial and temporal resolution [58, 59] as we did during this PhD thesis [1]. In the second case, the study of light-matter interaction is an essential component of the experiments as it will be described in the results section.

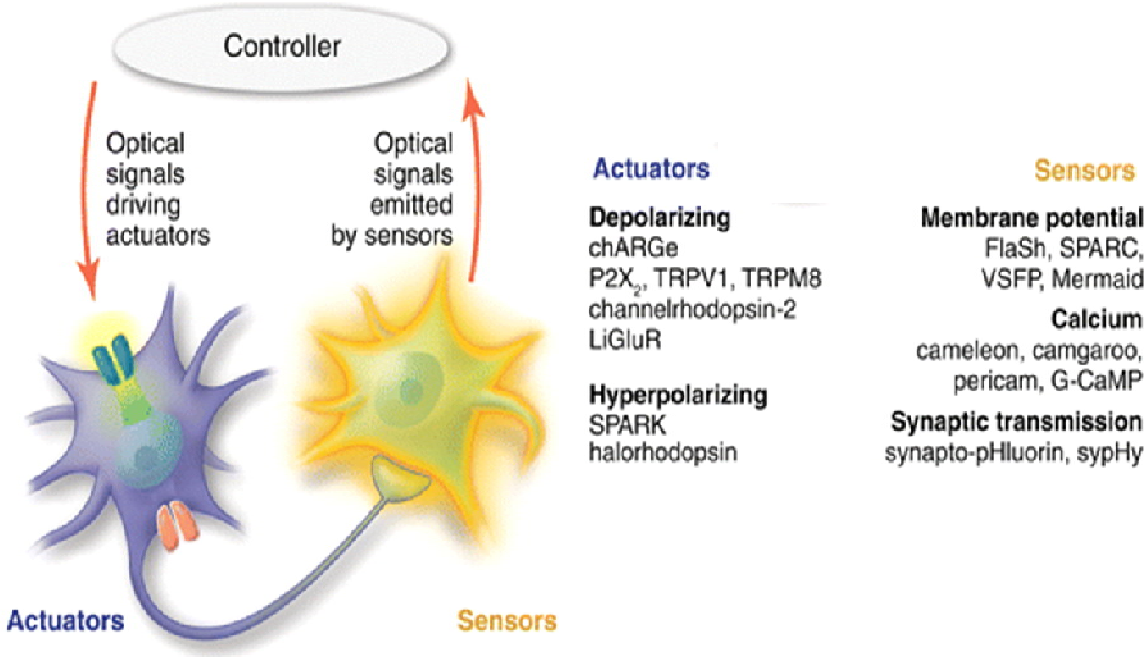

Figure 8. Actuators and sensors in optogenetics. From Miesenbock [55].

Sensors

Sensors are engineered proteins that can translate cellular signals into optical signals. Virtually, all sensors are derivative of the green fluorescent protein (GFP), a protein that emits bright green light when illuminated with UV-blue radiation and that was first isolated from the jellyfish *Aequorea Victoria* [60].

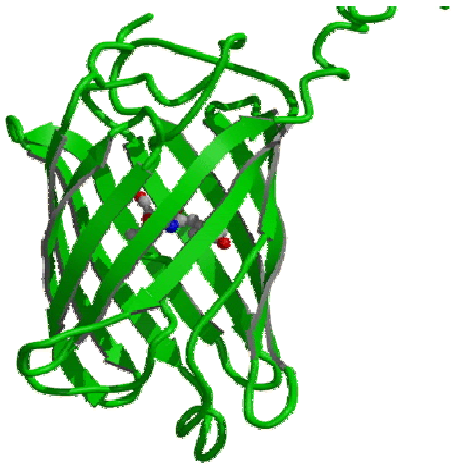

Figure 9. GFP structure. From tsienlab.ucsd.edu.

The application of GFP in cell biology has redefined the concept of fluorescence microscopy allowing initially the visualization of protein location. A further step consisted in its application to study second messengers in living cells, starting from the work of Tsien that developed the widely used Ca^{2+} sensor Cameleon [60, 61].

Since then, the use of genetically encoded Ca^{2+} indicators (GECIs) exploded and led to the development of new variants, each one with a peculiar dynamic, sensitivity or localization in order to respond to cell biology and physiology requirements [62].

Genetically Encoded Calcium Indicators (GECIs)

There are two main categories of GECIs: those based on Föster Resonance Energy Transfer (FRET) and those adopting circularly permuted GFP [63-65].

The former category takes advantage of FRET that describes the energy transfer occurring between two fluorophores with one functioning as energy donor having the emission spectrum overlapping with the second, working as energy acceptor. The resonant transfer is efficient only when the two chromophores (donor and acceptor, respectively) are close one another (the efficiency is inversely proportional to the sixth power or the distance).

The latter category consists of single wavelength sensors constituted by circularly permuted GFPs. All the sensors used in this thesis have peculiar structures and will be described in detail in the next paragraphs.

FRET measurements cytosolic and mitochondrial Calcium

To measure cytosolic and mitochondrial Ca^{2+}, genetically-encoded and targeted sensors of the Cameleon family [60, 61] have become a gold standard. The cytosolic and mitochondrial sensors used in this PhD thesis to measure Ca^{2+} have the same molecular components.

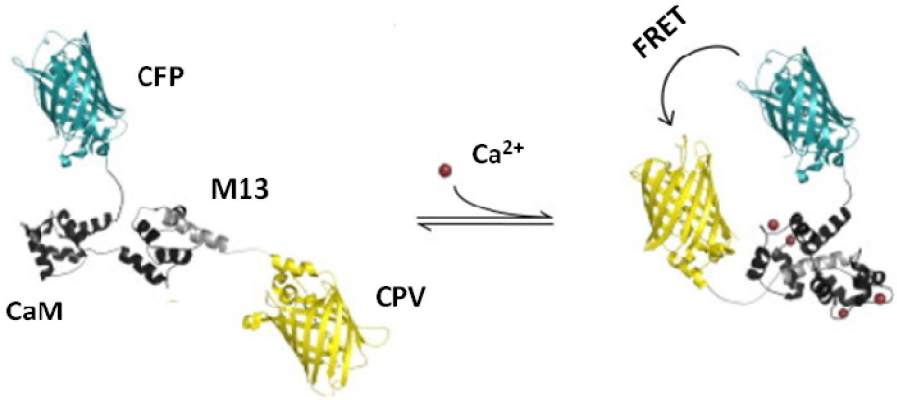

Figure 10. Schematic representation of Cameleon conformational modification upon Ca^{2+} binding. Modified from [62]

The two chromophores, a CFP (Cyan Fluorescent Protein, donor) and a CPV (Circularly Permuted Venus, acceptor), are linked through Calmodulin (CaM) and a Ca^{2+} dependent CaM-binding peptide M13, fused together (D3 component). Ca^{2+} binding to M13 enables CaM to wrap around the M13 peptide, thus shortening the distance between the chromophores and enhancing FRET efficiency. From a practical point of view the ratio between the fluorescence emitted by the acceptor and the donor (upon excitation of the latter) is proportional to the Ca^{2+} concentration [61].

GCaMP sensors

In addition to Cameleon indicators, other methods to record Ca^{2+} signals have been used. GCaMP sensors are single wavelength Ca^{2+} indicators based on circularly permuted GFP. They always maintain the CaM and M13 domains that wrap in presence of Ca^{2+}, however these two peptides are fused in such way that they can alter GFP conformation until Ca^{2+} binds, causing a large increase in fluorescence emission intensity (see fig. 11).

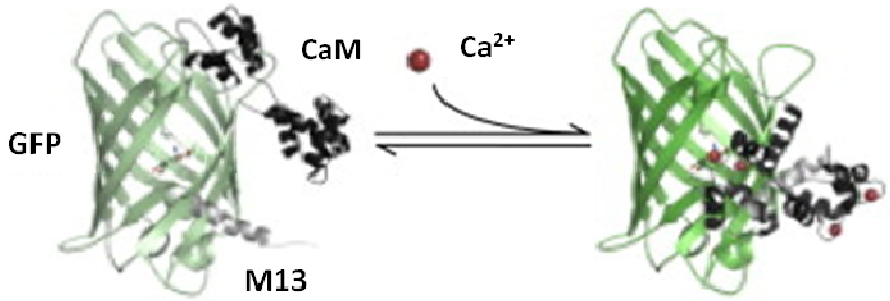

Figure 11. GCaMP schematic representation. Modified from [62].

As reported in several neuroscience experiments [64, 66], the advantage of this sensor is that it can report very rapid Ca^{2+} events, if compared to FRET-based sensors. For this reason, we tested this indicator also in NCMs that show large and rapid Ca^{2+} events.
Moreover, the insertion of specific aminoacidic sequences allows the optimal targeting in the different subcellular compartments. In particular for mitochondria, a number *n* of copies (*n*-mt) of the cytochrome C oxidase signal sequence were added to the N-terminus of the CFP: MSVLTPLLLRGLTGSARRLPVPRAKIHSLGDP [67].

Actuators

Optogenetic actuators are mainly ion channels and ion pumps that, if expressed on the plasma membrane, allow influencing trans-membrane voltage upon light absorption. The first application of this technique, to manipulate membrane potential in excitable cells, was performed by Deisseroth and colleagues in 2005 [68]. They expressed a light-sensitive channel derived from a unicellular green alga in neurons. Called channelrhodopsin-2 (ChR2), this channel opens in response to blue light allowing positive ions to enter the cell (see fig. 12). In excitable cells, such as neurons and cardiomyocytes, this causes a depolarization that optically triggers an action potential [69, 70].

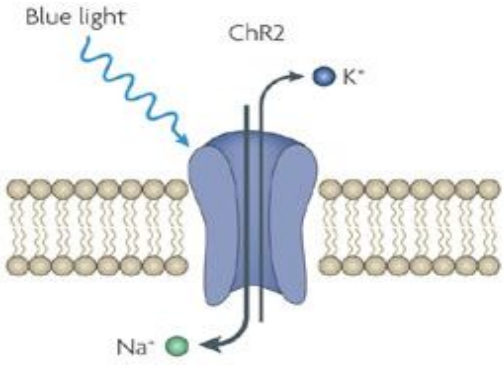

Figure 12. ChR2 channel allows Na^+ entry through the cell membrane upon blue light absorption [71].

Actuators found a large application in neuroscience while only proof-of-principle or cell culture-limited studies have been performed in cardiac electrophysiology [72-75].

Microscopy techniques

Fluorescence light microscopy is a gold standard technique used to explore signaling pathways and biochemical activity of the living cell, both *in vitro* and *in vivo*. Confocal and two-photon microscopy allow the acquisition of highly resolved fluorescent images, reducing the out-of-focus signal, thanks to their optical sectioning. However these techniques suffer of two limits. On one hand they have a spatial resolution limited to ~ 250 nm that hampers the detailed observation of many subcellular characteristics (e.g. the intricate mitochondria network or microdomains); on the other hand, they suffer of limited temporal resolution in a large field of view.

Several approaches have been developed to solve the first limitation (see [58] for an extensive review). Superresolution imaging techniques pushed the resolution limit to the nanometer scale allowing visualization of protein super-complexes (e.g. RyR2 clusters) and Ca^{2+} sparks with unprecedented detail; in parallel, with stimulated emission depletion (STED) microscopy, Lehnart and colleagues showed remodeling of the transverse-tubule network during heart failure [76].

Concerning the temporal resolution, the limitation of laser scanning microscopy is the difficulty in acquiring full frame images at a frame rate significantly higher than 1 Hz, necessary to visualize dynamic cellular events in relatively far locations within the field of view. A commonly-used approach is line-scan where a single line of the field is monitored with ms temporal resolution. However, this temporal detail is achievable at the expense of spatial resolution. Other techniques exploit mirror-less scanning, using acousto-optic deflectors to move the laser beam on the field of view, thus eliminating the

inertia of galvanometric scanners, but also with this settings the spatial definition is compromised [77, 78]. As will be shown in the results section, we tested the alternative approach based on parallelization of raster scanning and acquisition, to determine whether this technique provides a good compromise between spatial and temporal detail [1].

Light-matter interaction

In neuroscience, light stimulation of neuronal populations is a commonly used technique since the introduction of optogenetics. When applied to isolated neurons or brain slices, light delivery is usually ensured by microscope objectives in order to focus laser light sources over the sample [79]. However, in the case of in vivo studies, a much more versatile light source is required. For this reason, fiber optics coupled to fluorescent light sources allow an easier manipulation [80] and have been applied to moving animal brains. Fiber optics are generally made of flexible glass transmitting light with high efficiency, surrounded by a cladding layer that must have a refractive index lower than that of the core. This property allows the confinement of light inside the core thanks to total internal reflection. In this configuration, the light entering with the acceptance angle is transmitted along the fiber without boundary dispersion (see fig. 13). The sinus of the maximal angle of acceptance identifies the numerical aperture (NA) of the optic.

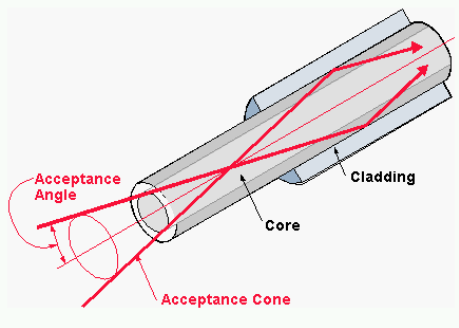

Figure 13. Optic fiber characteristics.

The light path inside the target illuminated tissue depends on the physical properties of fiber optics, the intensity and spectrum of the excitation light, and here modeling was used to determine the photoactivated tissue volume in cardiac optogenetics experiments.

2. RESULTS

The results section is divided into 5 chapters presented as research papers:

A. Multispot multiphoton microscopy in acute cardiac slices;
B. Multiphoton Ca^{2+} imaging in acute myocardial slices of CPVT hearts;
C. Mitochondrial Ca^{2+} uptake machinery in cardiac physiology;
D. Modeling blue light transmission for cardiac optogenetics;
E. Optogenetic investigation of arrhythmia triggers in CPVT.

Each chapter is then divided in introduction, methods, results and discussion. All figures are shown after each discussion section.

Multispot multiphoton Ca^{2+} imaging in acute myocardial slices

Giulia Borile,[a,d] Claudio de Mauro,[b] Andrea Urbani,[a,d] Domenico Alfieri,[b] Francesco S. Pavone [c,*] and Marco Mongillo[a,d,*]

[a] University of Padova, Department of Biomedical Science, Viale Colombo 3, Padova, Italy
[b] Light4Tech Firenze s.r.l., Via Pisana 316, Scandicci, Italy
[c] University of Florence, Department of Physics, Via G. Sansone 1, Sesto F.no, Italy
[d] Venetian Institute of Molecular Medicine, via Orus 2, Padova, Italy

Abstract. Multiphoton microscopy has become essential for dynamic imaging in thick living tissues. High-rate, full-field image acquisition in multiphoton microscopy is achievable by parallelization of the excitation and detection pathways. We developed our approach via a Diffractive Optical Element (DOE) which splits a pulsed laser into 16 beamlets and exploits a descanned detection system constituted by an array of beamlet-associated photomultiplier tubes (PMTs). The optical performance of the multiphoton multispot system (MCube) has been characterized in cardiac tissue sections, and subsequently used for the first time for fluorescence imaging of cardiomyocyte Ca^{2+} dynamics in viable acute cardiac slices. Multispot multiphoton microscopy (MMM) has never been used before to monitor Ca^{2+} dynamics in thick, viable tissue samples. Acute heart slices are a powerful close-to-*in vivo* model of Ca^{2+} imaging allowing the observation of several cells simultaneously in their own tissue environment exploiting the multiphoton excitation ability to penetrate scattering tissues. Moreover we show that the concurrent high spatial and temporal resolution afforded by the parallel scanning in MMM can be exploited to assess subcellular Ca^{2+} dynamics simultaneously in different cells in the tissue. We recorded local Ca^{2+} release events including macrosparks, travelling waves and rotors.

Keywords: multiphoton microscopy, multispot microscopy, calcium imaging, heart slices.

1. INTRODUCTION

The advent of two-photon excitation microscopy (TPEM) has revolutionized biological imaging by enabling the detection of dynamic cellular processes in intact tissues deep into the organs of living organisms. When combined with the use of fluorescent Ca^{2+} indicators, TPEM can be used to follow the variation of intracellular [Ca^{2+}] within the cells in their physiologic environment (i.e. the tissue).

In the heart, intracellular Ca^{2+} is a key determinant of cardiomyocyte function, that is regulated by a complex of signals shaped in time (from ms to sec) and space (from subcellular to cell-wide) within the single cell. In addition, fast and chaotic Ca^{2+} signals occurring during arrhythmias involving by definition multiple cells in the tissue, adds another layer of complexity as cell-cell interactions take part to the arrhythmia pathophysiology. The ideal method to visualize intracellular Ca^{2+} fluctuations in the intact myocardium would thus be endowed with high temporal and spatial resolution and, preferentially, be able to record cellular fluorescence from a wide field of view.

Up to now, one of the limitations of conventional TPEM is the difficulty in acquiring full frame (512x512 pixels) images at a frame rate significantly higher than 1 Hz, thus hampering the simultaneous detection of transient dynamic events lasting fractions of a second in a wide sample region [81, 82]. Different solutions have been used [83] to achieve high speed and resolution while retaining the advantages of two-photon excitation (TPE), such as penetration depth and reduced out of focus phototoxicity, with respect to the traditional confocal or fluorescent microscopy [84]. Reduced scanned area and/or pixel resolution are the straightforward ideas developed by microscopy companies and normally used by several research groups to increase image acquisition rate [85-87]. However, all these strategies allow faster acquisition at the expense of the spatial details, up to the most extreme case of single line scan, that uses the deflector to sweep the laser beam along a single line, thus generating 2-D (x,t) images. One alternative strategy to achieve full-field imaging at high rate would exploit faster beam scanners, and compensate for the inherent reduction in pixel dwell time by intensifying the incident laser power. However, given that the photo-damage of biological specimens excited at two photons increases non-linearly with the laser power [88], this last approach has very little use in living samples. To reduce photodamage and photobleaching, Konnerth and collaborators demonstrated the possibility to shorten dwell time without compromising the signal using low-power temporal oversampling (LOTOS) [89, 90]. In this technique a

mirror-less scanning two-photon microscope is used and has been applied to image Ca^{2+} signals in vivo. Other techniques exploiting acousto-optic deflectors instead of galvanometric mirrors have been applied to Ca^{2+} imaging [78] but do not solve the problem of high resolution in a large field of view. An alternative and promising approach to image thick samples maintaining large field of view consists in the combination of two-photon excitation and selective plane illumination microscopy. This technique has been used for developmental studies [91] and fully characterized for highly scattering samples [92].

To increase the acquisition rate of TPEM, we used a parallel scanning system, based on the insertion of a diffractive optic element (DOE [93]) along the incident laser path, splitting the beam into a matrix of identical beamlets with well-defined spatial distribution. By using such arrangement, the sample area was divided into a number of contiguous sub-regions, each of which was simultaneously raster scanned by a single beamlet. Parallel acquisition by an array of detectors, with a geometry corresponding to that of the DOE, allowed to spatially resolve the detection path and reconstruct the full-filed sample image. The multiphoton multispot microscopy system described in this work (Mcube, developed by light4tech, www.light4tech.com) was installed at the Dept. of Biomedical Sciences and was used to test and compare image quality and point spread function (PSF) with those of a conventional TPEM system [94]. Subsequently, the Mcube was used for Ca^{2+} imaging experiments in acute heart slices, allowing the simultaneous detection of subcellular Ca^{2+} dynamics in several different cells in the tissue. The cardiac slices model was selected as a thick-tissue testing platform for multiphoton microscopy as it combines the preservation of the multicellular myocardial structure with the quasi-bidimensional morphology of the slice [95].

2. MATERIALS AND METHODS

Conventional TPE microscope. A multi-photon system (Radiance 2100 MP; Bio-Rad Laboratories, UK), was used for comparison of MCube image quality with respect to an existing TPE microscopy system. The Radiance system is equipped with a Tsunami mode-locked, tunable, femto-second–pulsed Ti/sapphire laser (Ti:Sa). The laser output is capable of generating 100 fs pulse trains at a rate of 82 MHz. The microscope (Eclipse E600FN; Nikon) was equipped with a Nikon objective (40×/0.8 W CORR); a Direct Detection System (Bio-Rad), fitted with a 500LP DC dichroic mirror and HQ535/50 emission filter (Chroma Technology Corp.), was used for the detection of fluorescence emission signals. The LaserSharp2000 software package (Bio-Rad) was used for data acquisition.

Acute heart slices cutting and loading. Acute ventricular heart slices were cut following the protocol described in Ref. [96]. Young mice (postnatal day 7 to 10) were sacrificed and the heart was quickly excised and washed in ice-cold Ca^{2+}-free Tyrode solution (composition in mM: NaCl 136, KCl 5.4, NaH_2PO_4 0.33, $MgCl_2$ 1, glucose 10, hepes 5; pH 7.40 with NaOH). Atria were excised by a cut on the transversal plane, creating also a basis surface for fixing the ventricular portion of the heart to the slicer support with commercial cyanoacrylate glue. Hearts from young mice were embedded in 4% Low-Melting Agarose (SIGMA-Aldrich) in Tyrode. Transversal slices (450 μm thickness) were cut in ice-cold Ca^{2+}-free Tyrode solution with a vibratome (Leica GmBH). After cutting slices were transferred in room temperature 1 mM $CaCl_2$ Tyrode for some minutes and then they were maintained into Recovery Medium (DMEM/F12 supplemented with 20% Knock-out Replacement Serum, Invitrogen) in humidified atmosphere containing 95% O_2 and 5% CO_2 at 37°C for at least 1h before loading [97].
After recovery, slices were loaded with the Ca^{2+} -sensitive indicator Fluo-4, AM (5 μM, Invitrogen) for 40 minutes at 37 °C in 1 mM Ca^{2+} Tyrode solution plus 20% Pluronic F-127 (Invitrogen) and 1 μM sulfinpyrazone (SIGMA-Aldrich).

Imaging and stimulation. Viable heart slices, loaded with Fluo-4AM, were transferred on a homemade perfusion chamber on the stage of the two-photon microscope and perfused with a 1 mM Ca^{2+}, oxygenated Tyrode solution.

To prevent curling and movement, slices were held down through a homemade platinum holder.

Slices were field stimulated by applying directly under the microscope a voltage difference at the slice sides (5V/cm); slices were thus electrically paced, applying brief voltage square waveforms (5 ms) with the fixed frequency of 1, 2 or 5 Hz. Changes in Ca^{2+} concentration were observed as variations in the green emission of the sample upon excitation.

3. RESULTS

3.1 Instrument design.

MMM allows increase the image acquisition speed several fold when compared to standard laser scanning microscopes. Analogous systems based on a microlens array have already been used to monitor Ca^{2+} dynamics in isolated cardiac cells [87] but, to the best of our knowledge, multispot multiphoton microscopy has never been employed to image cellular Ca^{2+} in whole hearts or *ex-vivo* myocardial preparations.

To obtain a MMM system suitable for high speed imaging at the cellular level in intact organs, we sought to obtain homogeneous light distribution over the sample, while at the same time, maximize light detection from the whole field of view of the objective. The system design is thus based on a DOE in the excitation light path, a descanned configuration in the emission path, and an array of PMTs (fig. 1A). A Ti:Sa pulsed IR laser (<150 fs, 80 MHz pulses, Chameleon Ultra II, Coherent, UK) providing up to 3.6W of optical power at 785 nm excitation wavelength was used as excitation light source.

The Diffractive Optical Element (DOE) was inserted along the incident light path to obtain patterned illumination of the sample, obtained by splitting laser beam in 16 parallel beamlets generating a matrix of 4 by 4 spots regularly spaced in a squared array. Such configuration, in the preliminary tests, offered the best compromise between imaging rate and signal to noise ratio. Laser power was evenly distributed throughout the spots (within a few percent due to the DOE construction, fig. 1B) thus providing uniform illumination of the entire scanned area [93]. With the laser power at the source of 3.6 W, the power per beamlet measured after the 4x4 DOE resulted of about 45 mW.

The 16 parallel beamlet pattern was deflected along the x and y axes by galvanometric mirrors, while movement of the excitation plane along the z axis was achieved by shifting the objective with a piezoelectric motor.

Detection of the emitted light is performed with a multianode photomultiplier tube (PMT), (H7546A-20SEL from Hamamatsu), with each detecting element corresponding to a single descanned beamlet. Each PMT has its own electronic board, performing signal amplification, A/D conversion, local storage on a 2MB onboard memory and parallel communication with a custom-developed control software for data acquisition and storage on the PC hard drive. This configuration minimizes optical cross-talk between different PMT elements [98], that may introduce undesired degradation of the image quality, particularly when acquiring fluorescence from highly scattering samples such as muscular tissue. The essential components of the MMM are shown in fig. 1A.

To allow experiments with living tissue samples, the MMM was adapted to an upright fluorescence microscope (DM LFSA, Leica Microsystems GmBH, Germany), equipped with a water immersion objective (Nikon, 40×/0.8 W CORR).

3.2 Optical Performance.

To evaluate the optical performance of the MMM system, we determined the PSF by collecting the 3-dimensional image profile of a sub-resolution fluorescent bead, as shown in fig. 1C. From the radial intensity profile in fig. 1C, we obtained a radial resolution of 464 ± 10 nm, a value in line with the expected theoretical resolution of 455 nm calculated for a 2-photon system at the excitation wavelength of 785 nm.

Imaging of fluorescent beads embedded in agarose has previously been used to measure the PSF of microscopy systems as shown in [87] and [98]. Although such configuration is adequate to evaluate the pure optical performance of the systems, the sample is almost transparent and isotropic, and thus is not representative of the typical experimental condition. The myocardium is densely occupied by sarcomeres, formed by alternating segments of thin and thick protein filaments arranged in a highly scattering grid, inevitably reducing the performance of an optical system. To test the optical performance of the MMM system in deep tissue imaging in the heart, we evaluated the experimental PSF using a custom generated heart phantom-sample. The phantom was made by injecting 1 μm fluorescent beads (Invitrogen) at different positions and depths in a 500 μm fixed heart slice. We measured the fluorescence profile of a 1 μm bead at 150 μm of depth in the tissue and estimated the system PSF in deep tissue imaging. The PSF obtained are shown in fig. 2A and the characteristics of fluorescence profiles reported in Table 1.

Table 1 Full width at half of maximum (FWHM) of the measured PSFs for the single beam BIORAD MP-2100 and multispot MCube systems; data refers to a fluorescent bead located 150 μm in depth in the phantom sample.

	FWHM radial (μm)	FWHM z-axial (μm)
MP-2100	2.24 ± 0.14	21 ± 1.2
MCUBE (with DOE)	1.30 ± 0.05	17.7 ± 0.7

The results obtained with the MMM were compared to that of a commercial standard, the BIORAD MP2100 multi-photon microscope powered by a Ti:Sa Spectra Physics Millennia pulsed IR laser. We obtained in both cases a PSF for TPE microscopy comparable to that reported in other papers [87], with a better resolution for the MMM, in both axial and radial direction. The improvement in the optical resolution of the MMM can be dependent, at least in part, to the spatial filtering of the DOE apparatus. To determine the effect of the DOE insertion, we next compared the quality of the images acquired in either single line mode or multispot mode, of the same field of view with comparable laser power. In single line mode the laser power was thus attenuated down to 45 mW on the sample plane. As shown in fig. 2B, the image resolution and S/N are comparable, demonstrating that the DOE insertion does not cause image deterioration. Notably, the acquisition with the DOE inserted is 16 times faster than in single line modality. In the inset, a magnification is shown.

3.3 MMM imaging of calcium dynamics in thick myocardial slices.

The system was tested on viable acute cardiac slices from mouse heart, by performing Ca^{2+} imaging using the loaded with the fluorescent calcium indicator Fluo-4AM. Acute myocardial slices are an experimental system well representing the intact myocardium, allowing to use state-of-the art imaging methods to explore Ca^{2+} signals from the subcellular to the multicellular range.

We used the MMM system to perform two different sets of experiments. In the first, Ca^{2+} imaging was performed at 16 Hz rate during field stimulation in 137x137 μm wide area of the myocardial slice, including typically 6-8 cardiomyocytes. Electrical pacing by field stimulation resulted in synchronous increases in intracellular Ca^{2+} in the cardiomyocytes in the imaging field, as reported in a typical experiment shown in fig. 3A. At the acquisition rate used in the experiments, it was possible to fit the Ca^{2+} transients decay with a single exponential function obtaining typical decay time in the range of 100 to 150 ms (n= 14 cells), in line with data in the literature [99]. In the subsequent set of experiments, MMM was used to investigate Ca^{2+} dynamics with subcellular resolution in a networked group of cells in the myocardial slices.

The spatial resolution of MMM at 16 Hz frame rate, was assessed by imaging subcellular Ca^{2+} dynamics in a wide region of the slice. The elementary Ca^{2+} signals regulating the excitation-contraction coupling in heart cells are represented by Ca^{2+} 'sparks' [14], i.e.

transient and localized releases of Ca^{2+} from the sarcoplasmic reticulum through the Ryanodine Receptor Ca^{2+} channels.

A pace-stop protocol was used to increase the frequency of Ca^{2+} release events. Intracellular, local Ca^{2+} release events, both in the form of secondary 'macrosparks' (fig. 3B) of approximately ranging 4 to 6 μm in diameter, and self sustained Ca^{2+} waves traveling through the cell (fig. 3C), could be imaged simultaneously in numerous cardiomyocytes in the slice. Such cell wide Ca^{2+} waves originated frequently from the same Ca^{2+} release hotspot and, in some cases were underlined by organized intracellular Ca^{2+} rotors (see Supplementary Movie). Moreover, it was possible to appreciate that neighboring cells displayed Ca^{2+} waves in a pattern of interdependency (figure 4).

4. DISCUSSION

The simultaneous analysis of intracellular Ca^{2+} dynamics in several neighboring cells in their physiologic environment, using fluorescence based methods, poses a number of technical challenges:

i) a suitable experimental model, with preserved cell viability and intact cell-to-cell interactions in the three dimensions, expressing a fluorescence Ca^{2+} reporter.

ii) an optical imaging method allowing high efficiency in the light collection and high resolution (µm), in an area as wide as needed to include a significant number of cells to detect cellular and subcellular Ca^{2+} variations in multiple cardiomyocytes.

iii) a system capable of temporal resolution compatible with the dynamics to be investigated.

In standard laser scanning confocal microscopes (LSCM) and TPE microscopy, a single collimated laser beam is scanned on the sample in a raster pattern. The maximal frame rate that can be achieved in such systems is determined essentially by two parameters: i) the speed of beam deflectors, typically galvanometric mirrors. ii) the pixel dwell time, determined by the shortest time necessary to achieve sufficient excitation of the sample.

The strategy chosen to increase acquisition speed was to split the laser beam into a grid of beamlets, focused in parallel portions of the sample via a DOE positioned along the laser pathway. If compared to other multispot microscopes, in which for example the beam is split using a microlens array [87], the DOE insertion guarantees an homogeneous distribution of the light intensity over the sample thus reducing the need of off-line processing of the images [93].

This detection scheme has the advantage with respect to a CCD, that optical cross-talk between the different fluorescence channels is strongly reduced [100]. This is essential when deep imaging is performed and cross-talk artifacts may completely destroy the image quality [98]. For this reason, to reconstruct a single output image with a sixteen PMTs microscope, it is crucial that the PMTs are equalized to the output intensity for identical input brightness. PMTs of the detection system have been optimized for measurements of calcium dynamics in thick tissue samples and then used for the first time for Ca^{2+} imaging of acute cardiac slices. The choice of a detection scheme exploiting parallel detection performed by an array of PMTs was essential to allow deep imaging avoiding cross-talk artifacts. However, each PMT is an independent component having different gain efficacy. To compensate for the intrinsic differences of individual PMTs,

all the tubes can be equalized by independently adjusting gain and offset. The signal level can be equalized within 1%, thus compensating any source of non-uniformity in the excitation/detection path. Notwithstanding these adjustments, perfect equalization of the PMTs could not be obtained by us and others, likely due to the inherent differences in the noise level characteristic of each PMT.

Here we showed that the multispot scanning system applied to a multiphoton microscope greatly improves its temporal resolution without worsening spatial resolution.

First, we characterized microscope resolution by calculating radial and axial resolution in a thick tissue phantom. This allowed us to verify that the laser could penetrate deep enough inside the cardiac tissue, without losing the contrast; this is important for our study because we need to enter inside the sample for at least 50 μm (around 2-3 cells) to overcome the surface directly damaged by the cutting procedure. It has to be considered that all the Ca^{2+}-imaging experiments were performed 150 μm below the slice surface, where we also measured the PSF, in order to overcome the cell layers suffering of secondary dysfunctions.

Once assessed the microscope resolution, the experimental model of acute ventricular slices of murine heart has been implemented and optimized for Ca^{2+} imaging measurements in wide myocardial areas.

The feasibility of ventricular heart slices has already been reported [96, 97], nonetheless, this model has been previously used to monitor electrophysiological parameters and as a useful model for pharmacological drug testing [101], but much less for Ca^{2+} imaging. Acute myocardial slices are a good model for fluorescence Ca^{2+} imaging because they associate the ease of a bidimensional exposition of cells under the objective, with the intrinsic complex network of a 3D tissue. A limitation in the use of murine heart slices for prolonged physiological measurements may relate to oxygen diffusion in the tissue. To reduce the impact of such problem, we have perfused the tissue slice on both sides, and used short stimulation protocols at room temperature, as suggested by Barclay with respect to a similar cardiac tissue preparation [102].

In this work we showed that a MMM can be exploited not only for morphological studies in thick tissues as previously reported [100], but also to study second messengers in tissue preparations or whole organs.

As we showed, the possibility to acquire full images at 16 Hz, without worsening the spatial resolution, opens new possibilities for studies of Ca^{2+} dynamics in intact tissues including the heart. Specifically, in cardiomyocytes physiology, releases of Ca^{2+} from the

sarcoplasmic reticulum (SR), Ca^{2+} sparks, are fundamental in the excitation-contraction coupling [14]. Moreover, abnormal Ca^{2+} releases from the SR have been associated to different channelopathies [37, 41] and the possibility to study subcellular Ca^{2+} events in the intact tissue, is now possible with a full frame approach allowing the detection of macro-sparks, Ca^{2+} waves and rotors.

The use of TPE in cardiovascular research is increasing and the need of methodological improvement is arising [59, 99]. The properties of MMM will enable the investigation of fast occurring Ca^{2+} dependent signals in the living cells within intact tissues, thus expanding the methodological toolkit for fluorescence imaging which, in the last 20 years, has become an experimental technique increasingly used in biomedical research [103].

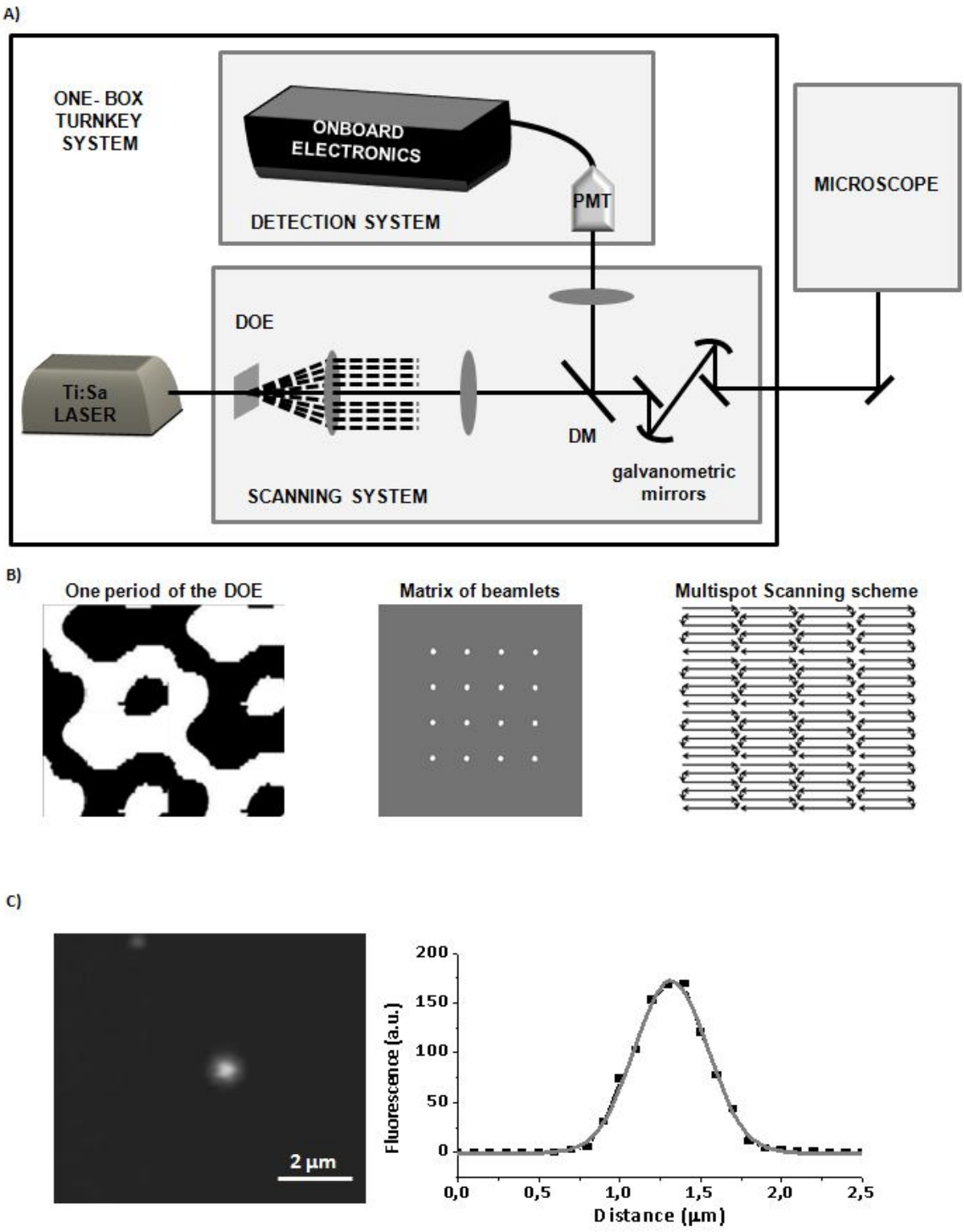

Fig. 1: A) Scheme of the multispot multiphoton microscope. B) Essential components of the MMM. C) Image and intensity profile of a subresolution bead along the radial axis.

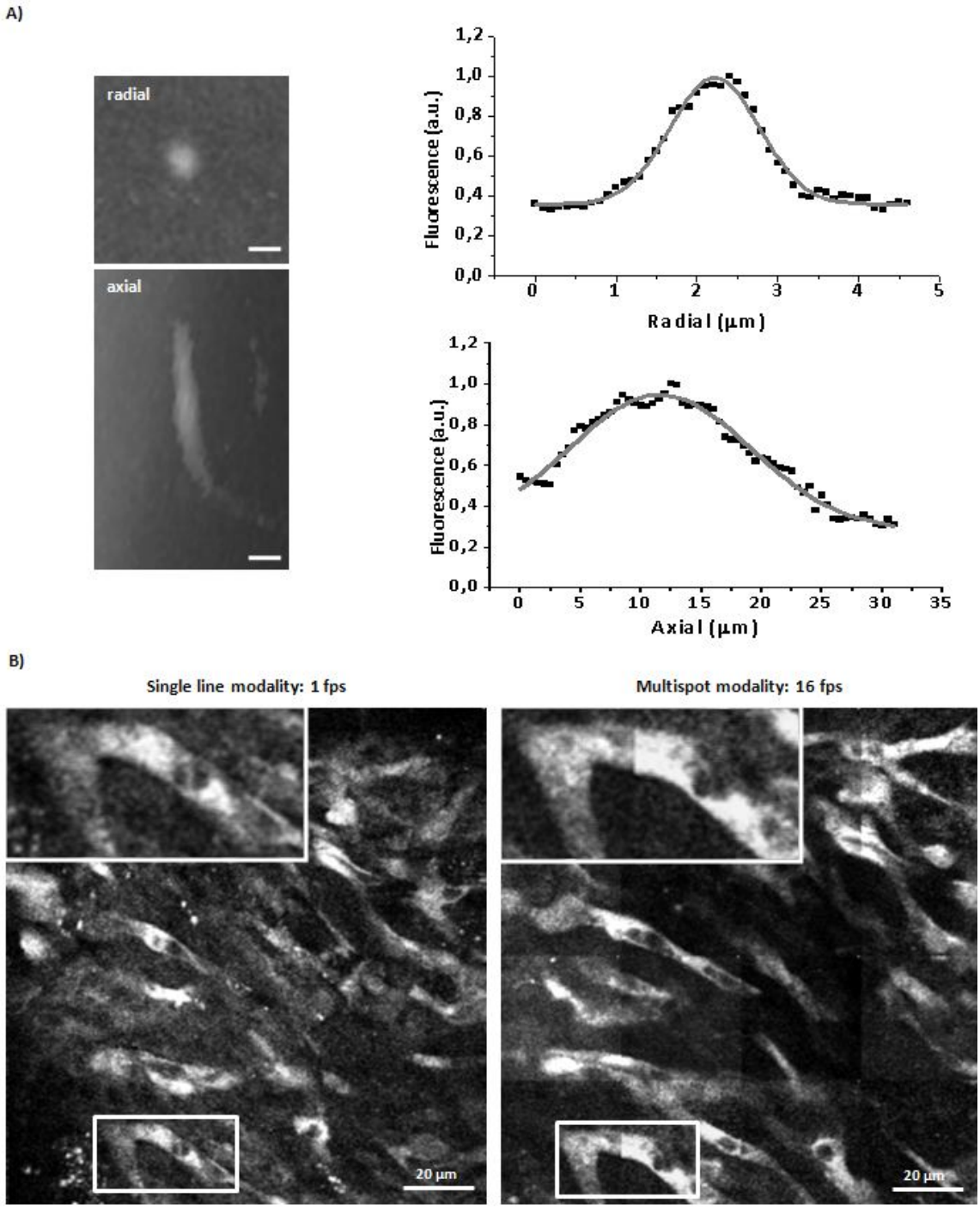

Fig. 2: A) Intensity profile of a 1 µm fluorescent bead at 150 µm depth in myocardial tissue Scale bars : 2 µm. Radial and axial views are reported as well as relative intensity profiles. B) The same image acquired in single line modality and multispot modality.

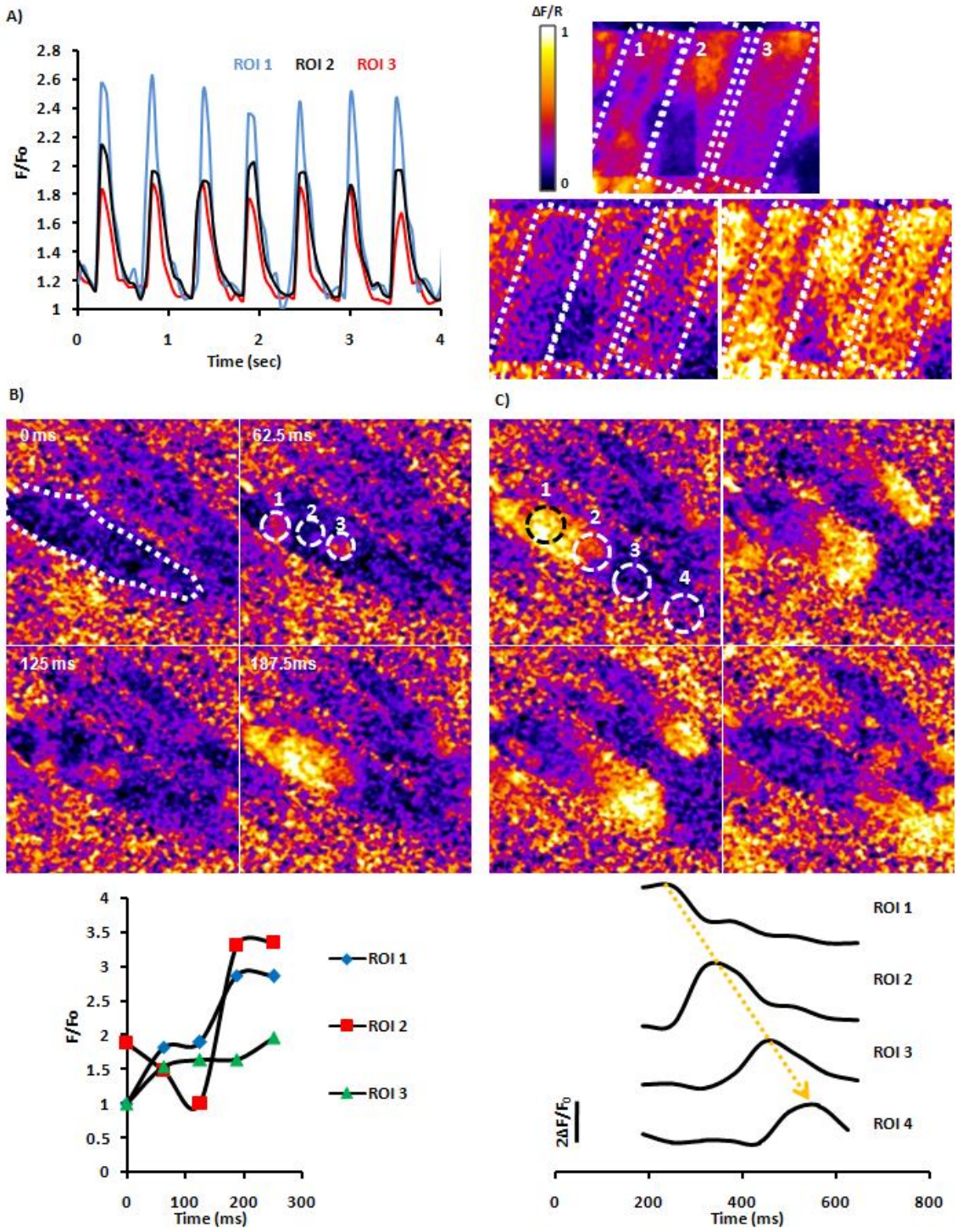

Fig. 3: A) Intensity profiles of 3 neighboring cells in the heart slice. Cell borders are highlighted by dotted squares and fluorescence profiles are reported. It can be seen that cell 2 crosses 2 sub-frames without affecting temporal fluorescence profiles. B) Simultaneous onset or macro-sparks in 2 of the 3 ROIs considered with the respective intensity profiles. C) A travelling Ca^{2+} wave recorded in the same cell and intensity profiles of the ROIs considered.

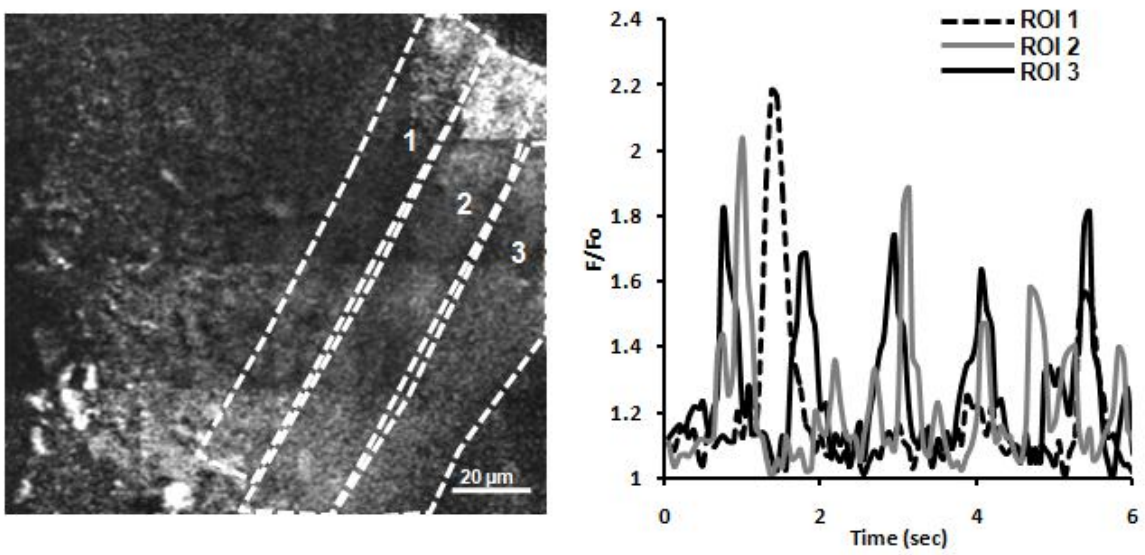

Fig. 4: Three neighboring cells in a large field of view display spontaneous Ca^{2+} releases closely related in time.

(manuscript in submission)

Multiphoton Ca^{2+} imaging in acute myocardial slices of CPVT hearts

Giulia Borile[1,2], Jonathan W Lederer[4], Marco Mongillo[1,2,3].

[1] Department of Biomedical Science, University of Padova, Viale Colombo 3, 35121 Padova, Italy; [2]Venetian Institute of Molecular Medicine, Via Orus 2, 35129 Padova, Italy. [3]Institute of Neuroscience, Italian National Research Council (CNR), Viale G. Colombo 3, 35121 Padova, Italy. [4]UMBI, University of Maryland, Baltimore, USA.

Abstract. *Rationale:* Alterations in cardiomyocyte (CM) Ca^{2+} handling play a role in initiating and sustaining inherited arrhythmias (e.g. Catecholaminergic Polymorphic Ventricular Tachycardia, CPVT). Most of the current data on Ca^{2+} dynamics in CPVT have been obtained in isolated cells. *Aim:* We aimed to establish an intact cardiac tissue model to investigate Ca^{2+} dynamics in WT and CPVT cardiomyocytes. *Results:* Acute thick (450 μm) ventricular slices were obtained from WT and $RyR2^{R2474S}$ mice. Slices were loaded with the Ca^{2+}-sensitive indicator Fluo4-AM and imaged with a multiphoton microscope (BioRad-Radiance2100) to optically monitor intracellular Ca^{2+} fluctuations during electrical pacing with or without the addition of drugs including β-adrenergic agonists. As previously reported in isolated cells, upon β-adrenergic stimulation CMs within the $RyR2^{R2474S}$ heart slice had increased propensity to develop diastolic Ca^{2+} releases (DCRs), than cells in the WT slice. When the pacing frequency was increased from 1 to 5 Hz, DCRs were substituted by Ca^{2+} alternans, that are a pathophysiologic mechanism associated to arrhythmia triggering. Moreover, after cessation of rapid pacing, CM in the $RyR2^{R2474S}$ myocardium developed whole-cell traveling Ca^{2+} waves with a significantly shorter latency compared to WT cells, which resulted in synchronization of DCR throughout the cells in the slice. *Conclusions and Perspectives:* We developed a powerful model for myocardial Ca^{2+} imaging in acute heart slices that allows simultaneous detection of Ca^{2+} dynamics in several connected cells in their physiologic tissue environment. This experimental setting expands the notions on arrhythmogenesis accrued in single cell, and enables the study of the mechanisms underlying DCRs synchronization throughout several cardiomyocytes in the myocardial network, a well-accepted requirement for arrhythmic beat triggering.

KEYWORDS: Catecholaminergic Polymorphic Ventricular Tachycardia, inherited arrhythmias, ryanodine receptor, Ca^{2+} imaging

1. INTRODUCTION

Alterations in Ca^{2+} signaling have been associated to a wide variety of cardiovascular pathologies, ranging from hypertrophy to heart failure and arrhythmias [37]. In these conditions, deregulated Ca^{2+} signals lead to transcriptional effects (as in hypertrophy), reduced strength of cardiac contraction (as in heart failure) or to altered generation and propagation of electrical signals (as in arrhythmias) [104].

Catecholaminergic polymorphic ventricular tachycardia (CPVT) is one of the most severe inherited arrhythmogenic disorders leading to exercise-induced ventricular arrhythmias and sudden cardiac death (SCD) in children and young adults [38]. In the dominant form, CPVT is caused by mutations in the *RyR2* gene, encoding the cardiac intracellular Ca^{2+} release channel (ryanodine receptor 2), the main Ca^{2+} releasing channel of the sarcoplasmic reticulum (SR) [40].

Cardiomyocyte contraction is initiated by membrane depolarization that opens the sarcolemmal L-type Ca^{2+} channel and allows Ca^{2+} to flow into the space between plasma membrane and SR cisternae, triggering RyR2 opening. Activation of a RyR2 cluster gives rise to a quantal Ca^{2+} release event, detectable as a transient and localized increase in fluorescence of a Ca^{2+} indicator in confocal imaging experiments. The resulting spatial and temporal summation of Ca^{2+} sparks generates the cell-wide Ca^{2+} transient associated to cardiomyocyte contraction [12]. Such local control of RyR2 opening allows cardiac excitation-contraction coupling (E-C coupling) to be flexibly modulated by changing both the *input* (Ca^{2+} influx) and the *gain* (RyR2 open probability) factors, both responsive to β-adrenergic dependent PKA activation [105].

Mutant RyR2 channels harbouring the CPVT linked single point mutation RyR^{R2474S} show increased open probability when PKA-phosphorylated [16, 105]. This results in altered local control of Ca^{2+} signals at the RyR2 clusters, causing increased diastolic Ca^{2+} leak from the sarcoplasmic reticulum in the CPVT cardiomyocytes challenged with β-adrenergic agonists [41, 106]. The resulting Ca^{2+}-driven depolarizing current from the NCX (I_{ti}) leads to delayed afterdepolarizations (DADs), a well accepted cellular mechanism linked to cardiac arrhythmia triggering [107]. It has to be taken into account,

however, that DADs must occur simultaneously in a sufficient number of cardiomyocytes to overcome the current *sink* of the electrotonically coupled surrounding myocardium [51]. Therefore, if DADs in the CPVT myocardium result from altered local control of Ca^{2+} signals and intracellular Ca^{2+} waves, it follows that these events must be spatially (i.e. in a group of neighbouring cardiomyocytes) and temporally synchronized throughout several cells in the tissue to act as effective arrhythmia trigger mechanism. While the electrophysiological features of arrhythmias in CPVT have thoroughly been characterized [41, 106], the role of Ca^{2+} in the molecular pathogenesis of the disease has mainly been investigated in single cardiomyocytes.

The study of dynamic Ca^{2+} signals using fluorescent indicators in the arrhythmic myocardium requires concurrent measurements at multiple sites with high temporal resolution [59]. Here, we combined acute myocardial slices [96, 101], an experimental model maintaining intact tissue topology [95] and well suited for fluorescence imaging, with two photon microscopy, allowing high resolution imaging in thick three dimensional samples [83, 99]. This approach allowed us to investigate Ca^{2+} dynamics *ex vivo* in a multicellular preparation from WT and CPVT hearts during electric pacing and in conditions mimicking adrenergic stress.

We tested the hypothesis that synchronization of DCR in several neighboring cells might be at the basis of cardiac arrhythmogenesis, suggesting that the interplay between Ca^{2+}, membrane depolarization and electrical cell-cell coupling can lead to “synchronized” intracellular Ca^{2+} releases, causing an arrhythmic ectopic beat [108, 109].

2. MATERIALS AND METHODS

TPE microscope. A multi-photon system (Radiance 2100 MP; Bio-Rad Laboratories, UK), equipped with a Tsunami mode-locked, tunable, femto-second–pulsed Ti/sapphire laser (Ti:Sa), optically pumped by a Millennia VsS 5W green laser (Spectra Physics), was used for two-photon microscopy. The laser output is capable of generating 100 fs pulse trains at a rate of 82 MHz. The excitation wavelength at 785 nm was controlled with a spectrometer (Ocean Optics USB2000; getSpec). The microscope (Eclipse E600FN; Nikon) was equipped with a Nikon objective (40×/0.8 W CORR); a Direct Detection System (Bio-Rad), fitted with a 500LP DC dichroic mirror and HQ535/50 emission filter (Chroma Technology Corp.), was used for the detection of fluorescence emission signals. The LaserSharp2000 software package (Bio-Rad) was used for data acquisition.

Mice. Knock-in mice carrying a human CPVT mutation ($RyR2^{R2474S}$, [41]), kindly provided by Andrew R. Marks, were used. Wild type littermates were used as controls.
All experimental procedures were performed according to the European Commission guidelines and have been approved by the local ethical committee and the Italian authority (Ministero della Salute), in compliance of Italian Animal Welfare Law (Law n. 116/1992 and subsequent modifications).

Acute heart slices cutting and loading. Acute ventricular heart slices were cut following the protocol described in [96]. Young mice were sacrificed and the heart was quickly excised and washed in ice-cold Ca^{2+}-free Tyrode solution (composition in mM: NaCl 136, KCl 5.4, NaH_2PO_4 0.33, $MgCl_2$ 1, glucose 10, Hepes 5; pH 7.40 with NaOH). Atria were excised by a cut on the transversal plane, while ventricles were embedded in 4% Low-Melting Agarose (SIGMA-Aldrich) in Tyrode. Transversal slices (450 μm thickness) were cut in ice-cold Ca^{2+}-free Tyrode solution with a vibratome (Leica GmBH). After cutting slices were transferred in room temperature 1 mM $CaCl_2$ Tyrode for some minutes and then they were maintained into Recovery Medium (DMEM/F12 supplemented with 20% Knock-out Replacement Serum, Invitrogen) [97, 110] in humidified atmosphere with 5% CO_2 at 37 °C for at least 1h before loading. Slices were perfused on both sides in order to reduce the risk of hypoxia.
After recovery, slices were loaded with the Ca^{2+}-sensitive indicator Fluo-4AM (5 μM, Invitrogen) for 40 minutes at 37 °C in 2 mM Ca^{2+} Tyrode solution plus 20% Pluronic F-

127 (Invitrogen) and 10 μM sulfinpyrazone (SP, SIGMA-Aldrich) in a 12-well plate positioned on a shaker.

Two-photon Ca^{2+} imaging. Viable heart slices, loaded with Fluo-4AM, were transferred on a homemade perfusion chamber on the stage of the two-photon microscope and perfused with a 2 mM Ca^{2+}, oxygenated Tyrode solution supplemented with 10 μM SP to avoid dye extrusion.

To prevent curling and movement, slices were held down through a homemade platinum holder.

Slices were field-stimulated by applying brief voltage square waveforms (5 ms) directly under the microscope with a voltage difference at the slice sides of 5V/cm. To reduce the risk of hypoxia during the experiments we used short stimulation protocols at room temperature, as suggested by Barclay with respect to a similar cardiac tissue preparation [102].

Images were thus collected upon excitation of the sample with 785 nm excitation wavelength and collection occurred through a bandpass filter selecting the green emission (535 ± 50nm). Images were recorded by the microscope software and stored. Changes in Ca^{2+} concentration were observed as variations in the green emission of the sample upon excitation. All experiments were performed at room temperature.

Image analysis. ImageJ (Wayne Rasband, NIH, Bethesda, USA) and Clampfit 10.0 (pClamp suite, Molecular Devices) were used as the main software package for image analysis.

The fluorescence emitted was expressed as F/F_0, where F represents the fluorescence at a time t and F_0 the minimum fluorescence value of the same cell. All fitting procedures were made by Clampfit 10.0.

Calcium release events included in the analysis were at least the 10% in intensity the triggered Ca^{2+} transients, whereas cells included in the analysis of Ca^{2+} alternans had large transients above 10% of small transients and this alternating behavior was maintained for at least 5 couples of transients.

Histology and viability. Acute ventricular slices not used for imaging experiments, were fixed in 1% paraformaldeyde (PFA) for 15 minutes at room temperature, after the recovery. Slices were included in freezing medium (OCT) and 10 μm-thick cryosections

were cut with a cryostat (Leica Microsystems) as described before [6]. Cryosections were stained for haematoxylin/eosin (Bio-Optica kit); immunofluorescence was performed using anti Troponin I antibody [111]; DAPI (1/5000) staining was used for nuclear staining in the heart slices. To test viability, slices were loaded with Propidium Iodide (PI, Sigma-Aldrich) 0,5 µM in Tyrode solution for 30 minutes at 4°C, then fixed with 1% PFA for 2 hours at room temperature. Transversal cryosections allowed to evaluate the viability within the slice thickness.

WB analysis. Hearts from P2, P4, P10 and P21 WT mice were frozen in liquid nitrogen immediately after removal from the animals (2 per age). Frozen tissue pieces of approximately the same size were immerged in 400 µl of RIPA BUFFER (65 mM Tris-Base, 150 mM NaCl, 0.25% sodium deoxycholate, 1% NP-40, 1 mM EDTA) supplemented with anti-phosphatases (5X, Roche) and anti-proteases (50X, Roche) and homogenized using Tissue Lyser (QIAGEN). Equivalent protein content was loaded after measurement with Bradford method and validation with Blue Coomassie staining (Bio-Rad). For the electrophoresis 40 µg of protein extracts were prepared in Loading Buffer (SB 4X, DTT 50mM in SDS 1%) and denaturated at 70°C and 1250 rpm for 10 min. Gels used were precast 4-12% gradient (Life Technologies) in MOPS (Life Technologies) as running buffer while SeeBlue Plus2 (Life Technologies) was used as protein weight standard. Proteins were then transferred on a PVDF membrane (GE Healthcare) by using Transfer Buffer (Life Technologies) at 4°C, 400 mA for 90 minutes. Serca2 antibody was purchase from Santa Cruz Biotechnology.

Model. The random behavior of the cells within the slice were obtained generating two different arrays of random numbers that represent random Ca^{2+} elevation in 2 neighboring cells. In order to compare this model with experimental data, the two arrays were requested to have "high Ca^{2+}" for the 36% of the time as measured from experiments. The probability for the two arrays to have high Ca^{2+} at the same time was in a range from 12% to 17% changing the starting arrays, and these values are always compatible with the probability for two neighboring cells with P= 0.4 to have random superimposed releases is P^2 that means 0.16.

3. RESULTS

Changes in intracellular Ca^{2+} handling have been implicated in the trigger mechanisms of arrhythmias in conditions as diverse as inherited Ca^{2+} channelopathies (e.g. CPVT) or acquired heart failure [17, 37, 41, 105]. The role of Ca^{2+} dys-regulation in cardiac pathology has extensively been investigated in single cardiomyocytes that differ substantially from the intact myocardium in which cell-cell coupling and tissue geometry contribute to shaping Ca^{2+} signals. This aspect is particularly important in arrhythmias, which are multicellular phenomena in which Ca^{2+} dysregulation occurs in a highly interdependent fashion in several cells in the tissue.

We aimed to set up a method allowing the study of intracellular Ca^{2+} dynamics in arrhythmogenic conditions in the intact myocardial tissue. To this aim, we sought to use an experimental model in which living cardiomyocytes can be investigated in their intact tissue environment using high resolution Ca^{2+} imaging. Acute myocardial slices (fig. 1A) are a system well represents the intact myocardium, allowing using state-of-the art imaging methods to explore Ca^{2+} signals from the subcellular to the multicellular range.

Acute myocardial slices were obtained from mice carrying the RyR2-R2474S point mutation, a dominant CPVT model previously shown to develop Ca^{2+}-dependent ventricular arrhythmias [41]. Ventricular transverse slices were obtained by cutting 450 µm thick sections from freshly harvested, agarose cast $RyR2^{R2474S+/-}$ and littermate control ($RyR2^{R2474S-/-}$) hearts, a procedure typically yielding 4-5 slices per heart.
Histological staining with haematoxylin/eosin and immunofluorescence were performed to assess the extent of tissue damage caused by the slicing procedure. HE and anti-TN-I immunofluorescence showed that myocardial slices retained regular cell organization and intact and morphologically normal cardiac sarcomeres, with the only exception of the external surface (fig. 1B, C). To assess cell viability, slices were stained with DAPI and PI. As shown in fig. 1D, PI positive nuclei were found close to the cutting surface, while significantly less PI-positive nuclei were found at > 50 µm depth. In line with these results, most cardiomyocytes in the slice accumulated the mitochondrial dye tetramethylrhodamine (TMRM, SIGMA-Aldrich), indicating that the cells maintained the mitochondrial membrane potential gradient (data not shown). Both the markers of cell viability and of energy production were not different from WT and CPVT hearts.

To image cardiomyocyte Ca^{2+} dynamics, acute heart slices were loaded with Fluo4-AM Ca^{2+} indicator (fig. 1E-F) and subsequently transferred in a field stimulation chamber on the microscope stage and bathed in 2 mM Ca^{2+} Tyrode solution.

Multiphoton microscopy was used to record fluorescence changes at a focal depth of at least 100 µm below the slice surface, which corresponded to about the cell layers damaged by the cutting procedure. Electrical pacing resulted in synchronous increases in intracellular Ca^{2+} in the cardiomyocytes in the imaging field, as reported in a typical experiment shown in fig. 2A-C. Ca^{2+} dynamics were compared in myocardial slices obtained from hearts of different age, ranging from P2 to P21. While no significant changes were observed in the transient amplitude (not shown), the time constant of decay progressively decreased along with the postnatal cardiac development, and was paralleled by increased protein level of SERCA-2 in myocardial tissue homogenate (figure 2C) [112]. Due to the efficient Fluo-4 loading and the ease of manipulation, and given that the time constant of decay of Ca^{2+} transients was similar to that observed in adult cardiomyocytes, the majority of the subsequent experiments were performed using p10-12 mice. We thus compared Ca^{2+} transient dynamics in normal (WT) vs CPVT ($RyR2^{R2474S+/-}$) cardiomyocytes in the slice. Transient amplitude in the individual cells was unchanged in the CPVT myocardium, at both 1 Hz and 2 Hz stimulation rate (see fig 2D), and in line with previous reports, we observed a modest prolongation of the decay time in CPVT which might be dependent on the impaired recovery of SR Ca^{2+} load secondary to diastolic Ca^{2+} leak as reported by Fernandez Velasco et al. [106].

To mimic the adrenergic stress that associates to arrhythmias in CPVT patients, Ca^{2+} fluctuations were assessed during superfusion of the slices with norepinephrine (1 µM), a β-adrenergic receptor agonist, during electrical pacing. Heart slices were incubated for 3 minutes with NE to allow diffusion of the drug into the deeper cell layers in the tissue. Ca^{2+} transient amplitude increased in both WT and CPVT hearts at 1 Hz stimulation rate (fig. 3A), while at 2 Hz the average transient amplitude decreased in CPVT slices (fig. 3B). In line with the action of PKA on SERCA stimulation, NE increased the speed of cytosolic Ca^{2+} reuptake resulting in faster decay of the Fluo-4 fluorescence (fig. 2D) to a similar degree in WT and CPVT hearts, and triggered the appearance of recurrent spontaneous Ca^{2+} releases between two consecutive paced transients. Such 'diastolic' Ca^{2+} release events (DCR, see figure 2E) occurred about four-fold more frequently than in WT cells in the same experimental conditions (figure 2F), indicating that in the $RyR2^{R2474S+/-}$ myocardium, cardiomyocytes have increased propensity to generate DCRs upon beta-

adrenergic stimulation. This is consistent with the increased open probability of CPVT mutant RyR2 channels when PKA-phosphorylated, a mechanism leading to increased diastolic Ca^{2+} release from the SR.

In a subset of experiments, NE administration caused the amplitude of Ca^{2+} transients to alternate on a beat-to-beat basis in a significant number of cells in the imaging field. Such Ca^{2+} alternans were more frequent in $RyR2^{R2474S+/-}$ heart slices (cells: 11/25, 42%, from 6 different preparations) than in WT controls (cells: 3/24, 11%, from 6 different preparations), as shown in fig. 3C, probably associated to the refractoriness of mutated RyR2 or increased leakage [113, 114]. The Ca^{2+} alternans observed during pacing at 2 Hz were synchronous in phase but not in amplitude, as shown by the time profiles of 3 neighboring cells in fig. 3D. This cell-to-cell heterogeneity has already been reported [115, 116] and has been associated to the different threshold for alternans between neighboring myocytes.

This observation may explain the apparently unusual finding of decreased amplitude of Ca^{2+} transients when paced at 2Hz and stimulated with NE.

Ca^{2+} alternans are a phenotypic trigger of intracellular calcium waves, which in turn may activate transient depolarizing current and cause delayed and early after-depolarizations, common arrhythmia initiating events. Therefore, these events are linked to arrhythmia generation in CPVT hearts and such phenomenon has been observed also in a different animal model of CPVT [117]. We used the single-line scanning acquisition mode to obtain accurate assessment of the Ca^{2+} transient kinetic at millisecond resolution (fig. 3E). In cells showing alternating amplitude of paced Ca^{2+} transients, this behaviour was stable and in agreement with previous reports [118] the decay time of large Ca^{2+} transients had the tendency to be longer than that of small transients although statistical significance was not reached (p-value: 0.06) [119]. Given the mechanistic link between altered single-channel properties of CPVT mutant RyR2, we focused on the investigation of aberrant diastolic Ca^{2+} release from the intracellular stores. To this aim, we used a pace-stop protocol in which after a brief period (5-10 s) of electrical pacing at 5 Hz causing fusion of consecutive Ca^{2+} transients and SR Ca^{2+} overload, pacing was interrupted, resulting in store overload intracellular Ca^{2+} release (SOICRs) in the form of Ca^{2+} macro-sparks and waves [120]. In slices from $RyR2^{R2474S+/-}$ hearts, the latency to development of Ca^{2+} waves was significantly shorter than in controls (CPVT: 3.0±0.3 s vs WT: 4.7±0.6 s, $p<0.05$), and the number of cells within the slice showing aberrant activity was markedly increased (CPVT: 39%, WT: 15 % of about 40 cells per genotype) fig. 4 D-E.

Norepinephrine (1 μM) administration decreased the latent period to the generation of SCR in both CPVT and WT hearts (CPVT: 1.9±0.3s vs. WT: 2.3±0.3s, $p<0.05$). The initial Ca^{2+} release generated traveling waves that diffused throughout the whole cell at higher speed in CPVT cardiomyocytes (CPVT: 44±1 μm/s vs WT: 57±1 μm/s, n=7 cells each, $p<0.01$), possibly reflecting the increased open probability of $RyR2^{R2474S+/-}$ channels upon phosphorylation.

When SCR were analyzed in all cells in the field of view, it emerged that Ca^{2+} release events tended to occur almost synchronously in neighboring cells. For a given cardiomyocyte in the slice, the experimentally determined probability of developing a SCR within the duration of a spontaneous Ca^{2+} elevation experienced by a neighboring cell (CPVT: 915±70 ms; WT: 855 ±43 ms, n=40 cells per genotype in six biological replicates; p=ns), resulted higher than the probability for two random events with the frequency of 0.4/s (average SCR/s/cell for any given cell in the slice) to occur (see figure 5). These data suggest that reciprocal influence between neighboring cardiomyocytes might participate to the synchronization of diastolic Ca^{2+} release events within a cluster of cells in the tissue, and result in their coordinated depolarization, a prerequisite for the generation of ectopic arrhythmic triggers.

4. DISCUSSION

It is well accepted that alterations in Ca^{2+} handling due to functional abnormalities of mutant RyR2 channels have a role in triggering arrhythmia-associated behavior in cardiomyocytes. Aberrant diastolic releases of Ca^{2+} have been recently associated by several groups to atrial fibrillation (AF) and CPVT [43, 108]. Despite the fact that the mechanisms of triggered arrhythmias have been well established on the cellular level, the relationship between abnormal CM Ca^{2+} cycling and focal excitation at the tissue level remains poorly understood. A key unresolved question is how spontaneous Ca^{2+} release in individual CMs can cause a sufficiently large membrane depolarization to elicit an ectopic event across the whole of myocardium, particularly because a local depolarizing current is expected to be absorbed by the electrically connected neighboring CMs serving as current sinks [51].

In the last few years, attention is rising on the clarification of this aspect and several groups have addressed this point with different experimental approaches. From mathematical models to whole perfused hearts, passing though isolated cardiomyocytes and trabeculae preparations, several approaches have been used but a clear identification of the mechanism is still lacking [43, 107-109].
Given the young age of the patients and the incomplete effectiveness of the current therapies, it is important to further expand our understanding of the pathophysiology of CPVT in order to identify novel therapeutic strategies.

Here, we used two photon microscopy in a tissue model of acute cardiac slice to investigate Ca^{2+} dynamics in the myocardium of knock-in mice harbouring the CPVT mutation $RyR2^{R2474S}$.
Murine ventricular slices have previously been used to monitor electrophysiological parameters and as a promising model for pharmacological drug testing, but much less for Ca^{2+} imaging [96, 101] and usually without high spatial detail [121]. In myocardial slices, cardiomyocytes maintain their physiologic cell-to-cell connectivity while offering the practical advantages of a bidimensional preparation and are therefore well suited for fluorescence Ca^{2+} imaging. The use of multiphoton microscopy allowed to image cells in the layers underneath the slice surface, in correspondence of which cardiomyocytes are inevitable damaged by the cutting procedure.

Cardiomyocytes in the slice responded to electrical stimulation with a synchronized, transient increase in cytoplasmic Ca^{2+} that was qualitatively comparable to that observed in isolated cells. Moreover, the kinetics of electrically stimulated Ca^{2+} changes were similar between WT and CPVT cardiomyocytes in the slice, with the only difference observed being a moderate increase in the transient decay time, that might reflect the increased diastolic Ca^{2+} leak, as previously reported for single isolated CPVT cardiomyocytes [106]. Exercise and adrenergic stress are well known arrhythmia triggers in CPVT, and NE stimulation, in experiments on isolated cells, caused increased spontaneous Ca^{2+} release and intracellular travelling Ca^{2+} waves during diastole.
As shown the β-adrenergic stimulation of our slices caused a gain-of-function in the excitation contraction coupling, in particular, we report that NE administration increases the amplitude and decreases the decay time of Ca^{2+} transients in both CPVT and WT heart slices.
As expected from data obtained in isolated cardiomyocytes, diastolic Ca^{2+} releases, during 1 Hz pacing, were observed with higher frequency in CPVT myocardium upon β-AR stimulation while practically absent in the other conditions. However, these releases never degenerated in self-sustained Ca^{2+} waves, meaning that PKA-phosphorylation of the defective channel is not able, *per se*, to sustain arrhythmic episodes.

Moreover, heart slices obtained from CPVT hearts exhibited a pro-arrhythmogenic substrate related to the development of Ca^{2+} alternans during β-adrenergic stimulation.
As reported in the review by Weiss et al. [122], Ca^{2+} alternans are a phenomenon that goes from a single cell to the entire tissue : 1) Ca^{2+} alternans at the cellular level play a key role in enhancing vulnerability at the tissue level and 2) lead to triggers at the tissue level. Taking advantage of the multicellular substrate, we could also monitor Ca^{2+} alternans that were both concordant or discordant in amplitude among neighbouring cells, as reported also by other groups [115]. It has been shown that Ca^{2+} alternans are a pathophysiologic mechanism of arrhythmia triggering [123] and their development may depend on an abnormal control of Ca^{2+} release from the SR, and it has been proposed that Ca^{2+} alternans directly depend on RyR2 refractoriness [113].
Taken together, this first part of the results says that Ca^{2+} instabilities occur also at low pacing frequency and are strictly dependent on the myocardial substrate, whereas no triggered activity could be recorded.

To further study the spontaneous releases of Ca^{2+} from the SR we challenged the slices with higher pacing frequency, overcoming the coupling breakpoint [116]. Indeed, in both myocardial preparations, 100% coupling between electrical pacing and evoked transients was maintained up to 2 Hz while at 3 Hz the mean coupling was around 85% and decreased at 67% at 4 Hz.

Our results show that the summation of β-adrenergic stimulation and rapid pacing caused a marked increase in the spontaneous activity that was similar in WT and CPVT myocardium, and in both substrates SCRs occurred in clusters in neighboring cells suggesting a common mechanism for synchronization of Ca^{2+} waves, and confirming the observation of other groups [120] that multicellular SCRs are quite common even in the absence of a disease substrate.

In isolated cardiomyocytes, SCRs can propagate as intracellular Ca^{2+} waves as a defensive way to promote SR unloading and avoid intracellular Ca^{2+} overload. In our experiments, SCRs clustered in time and space may suggest similar mechanisms in response to Ca^{2+} overload. Similar observations have been previously reported in a whole perfused heart model, by simultaneous monitoring of SCRs and voltage optical mapping. While this is a very powerful technique, it does not allow high spatial resolution, preventing Laurita and colleagues [120] to determine Ca^{2+} dynamics at the single cell level.

Our finding adds to the existing literature the concept that a SCR in a single cardiomyocyte is perceived directly by the surrounding cells. In the heart slices, we observed that in a large number of cases, Ca^{2+} waves in a cardiomyocyte were followed within a short time by Ca^{2+} waves in neighboring cells. The temporal distance between these events usually fell under a “coupling” interval equal to the mean duration of a traveling wave (around 900 ms). Ca^{2+} waves can readily propagate through the whole cell but, in multicellular preparations, they generally do not easily propagate through gap junctions from one cell to the next one [120, 124] excluding intercellular calcium diffusion as the main cause of SCRs synchronization. Another study on papillary muscles from a CPVT-associated CASQ2 mutated mouse model, suggested the decreased RyR2 refractoriness as a determinant of CMs synchronization [43].

Although apparently in contrast with the “source-sink” model for electrotonically coupled cardiomyocytes, our observation can be explained by considering that, when “source” cardiomyocytes develop [Ca^{2+}]-activated DADs, the depolarizing current would spread

through the whole myocardium if not sunk by the surrounding cardiomyocytes. Current sink is paid with the slight, below-threshold depolarization, which increases SR Ca^{2+} release and facilitate cell wide slow Ca^{2+} waves propagation [109]. The combined effect of these events may increase therefore the probability that the sink regenerates a source, thus determining a mechanism that leads to the recruitment and synchronization of DADs in groups of cardiomyocytes.

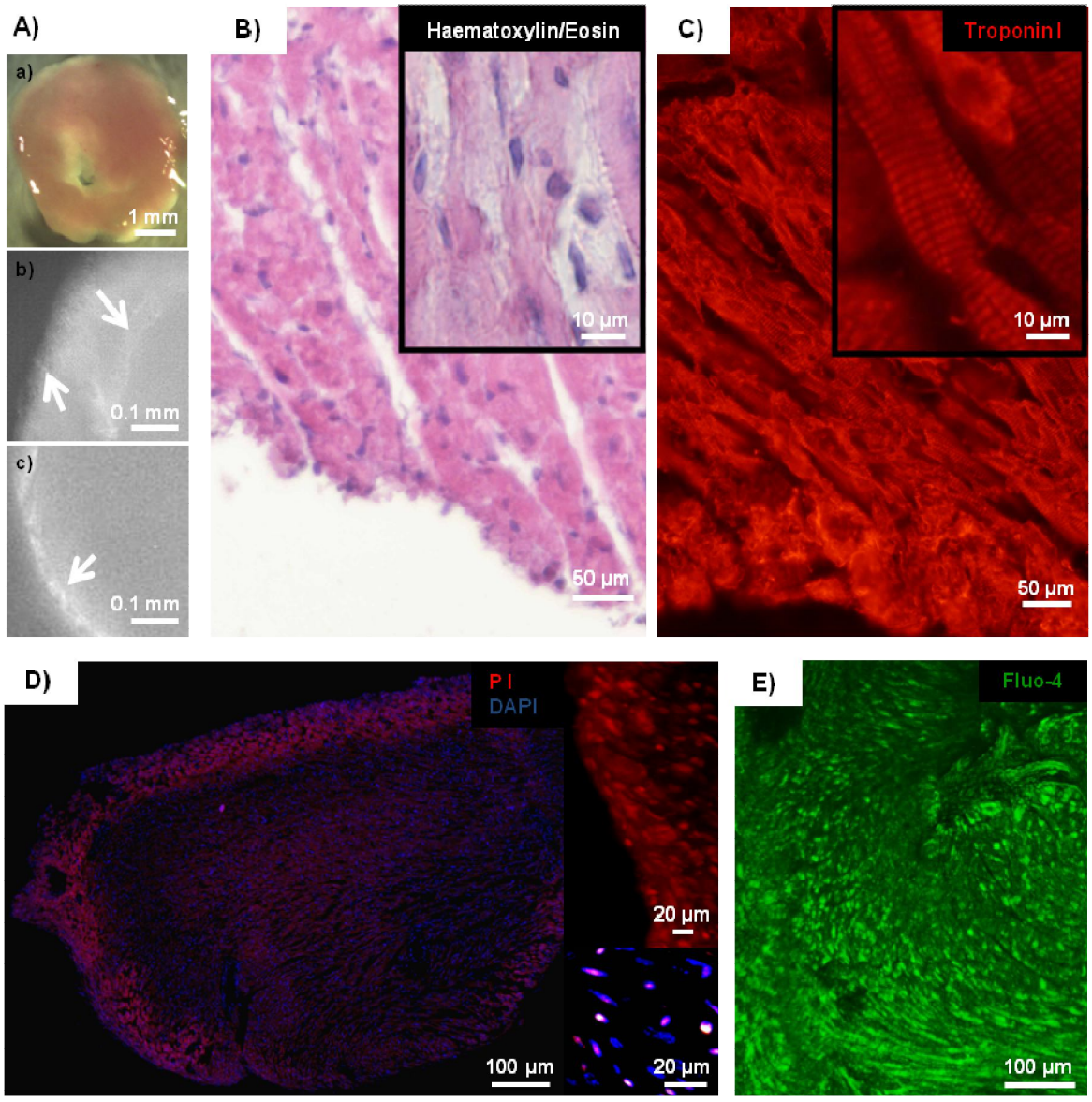

Fig. 1: Heart Slices Model Assessment and Viability. A) a stereomicroscope image of an acute heart slice (up left) and three areas in wide field 10X objective from right ventricle (up right), left ventricle chamber (down left) and left ventricle wall (down right). B) Haematoxylin/Eosin cryosection. C) anti-Troponin-I staining in a transversal cryosection. D) Entire transversal cryosection loaded with PI and stained for DAPI (merge), particular from the border loaded with PI and zoom of the colocalization of PI and DAPI (right). E) Field from the right ventricle of an acute heart slice loaded with Fluo-4AM and F) from the left ventricle- septum.

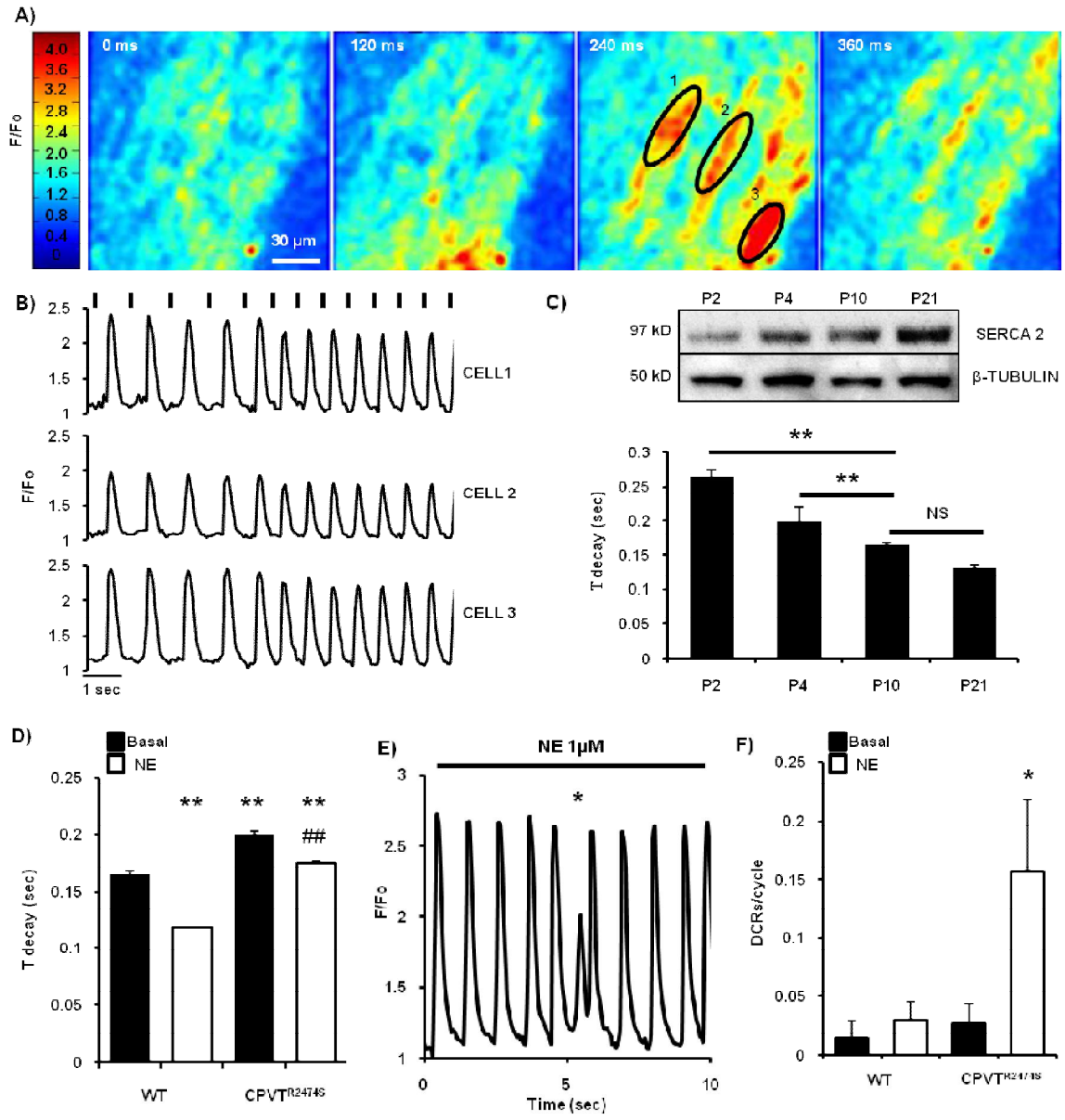

Fig. 2: Two Photon Ca^{2+} imaging of cells from WT and CPVT heart slices. A) Some cells within a heart slice showing rises in fluorescence intensity upon electrical stimulation (shown in false colors to highlight intensity variations). B) The fluorescence profile of a cell following changes in the electrical stimulation. Different cells are synchronized by the field stimulation. C) Decay time of Ca^{2+} transients in WT heart slices obtained at different ages. SERCA2 protein level increases as the decay time decreases. D) Decay time of Ca^{2+} transients for both WT and CPVT mice at 2 Hz electrical stimulation. E) Representative trace of a DCR in a CPVT cardiomyocyte during pacing upon NE administration. F) Quantification of the frequency of DCRs per cell cycle. Data are shown with SD. * P<0.05; ** P>0.01 compared to WT. # P<0.05; ## P<0.01 compared to CPVT in basal condition.

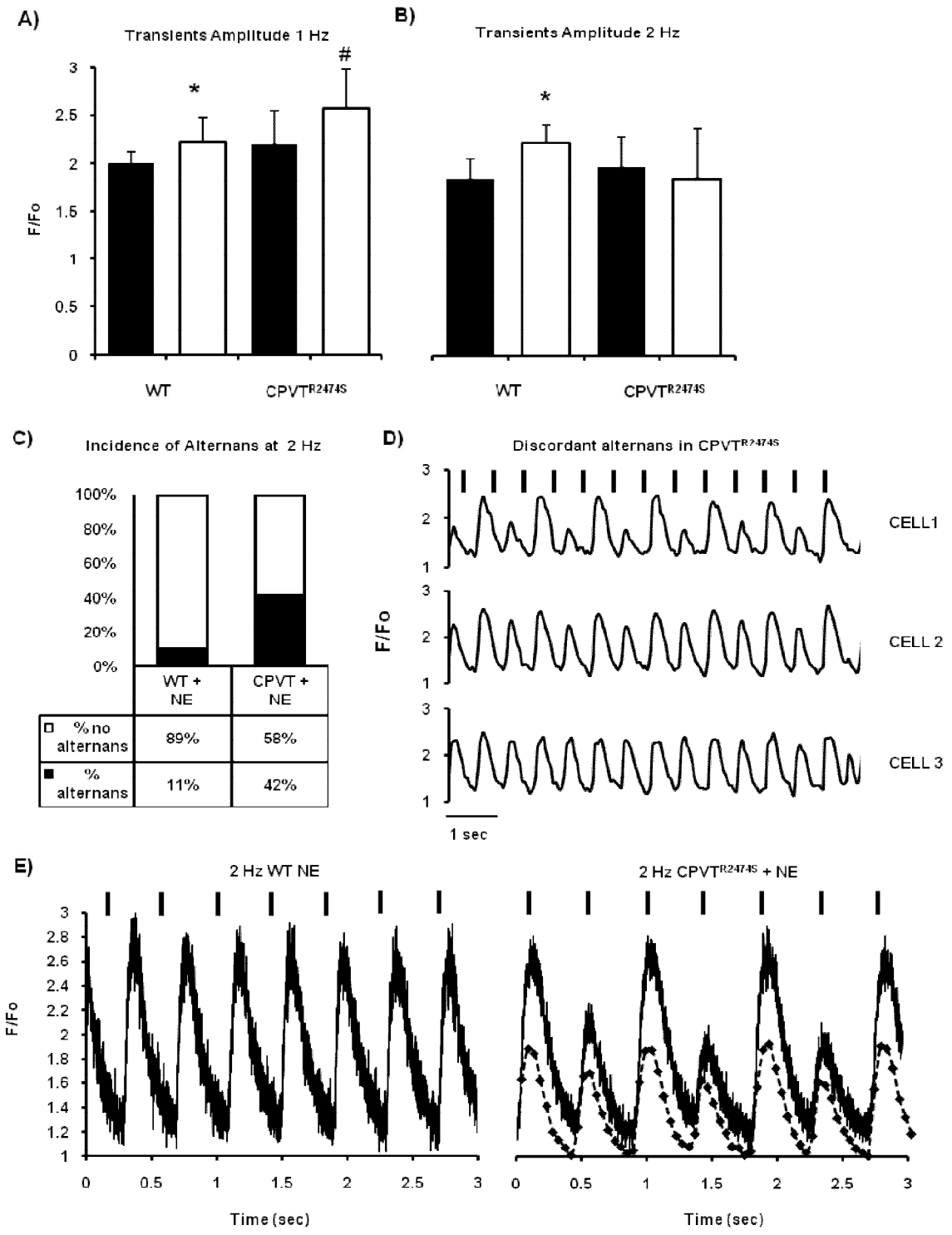

Fig. 3: Ca^{2+} alternans under NE administration. A) and B) transients amplitude at both 1 Hz and 2 Hz, in both control (black) and under norepinephrine administration (white). C) Ca^{2+} alternans observation in WT and CPVT mice. D) Three fluorescence profiles from adjacent cells from a CPVT heart show alternans that are synchronous in phase but not in amplitude (black bars indicate electrical pacing). E) Line Scan profiles from WT and CPVT cardiomyocytes during 2 Hz stimulation.

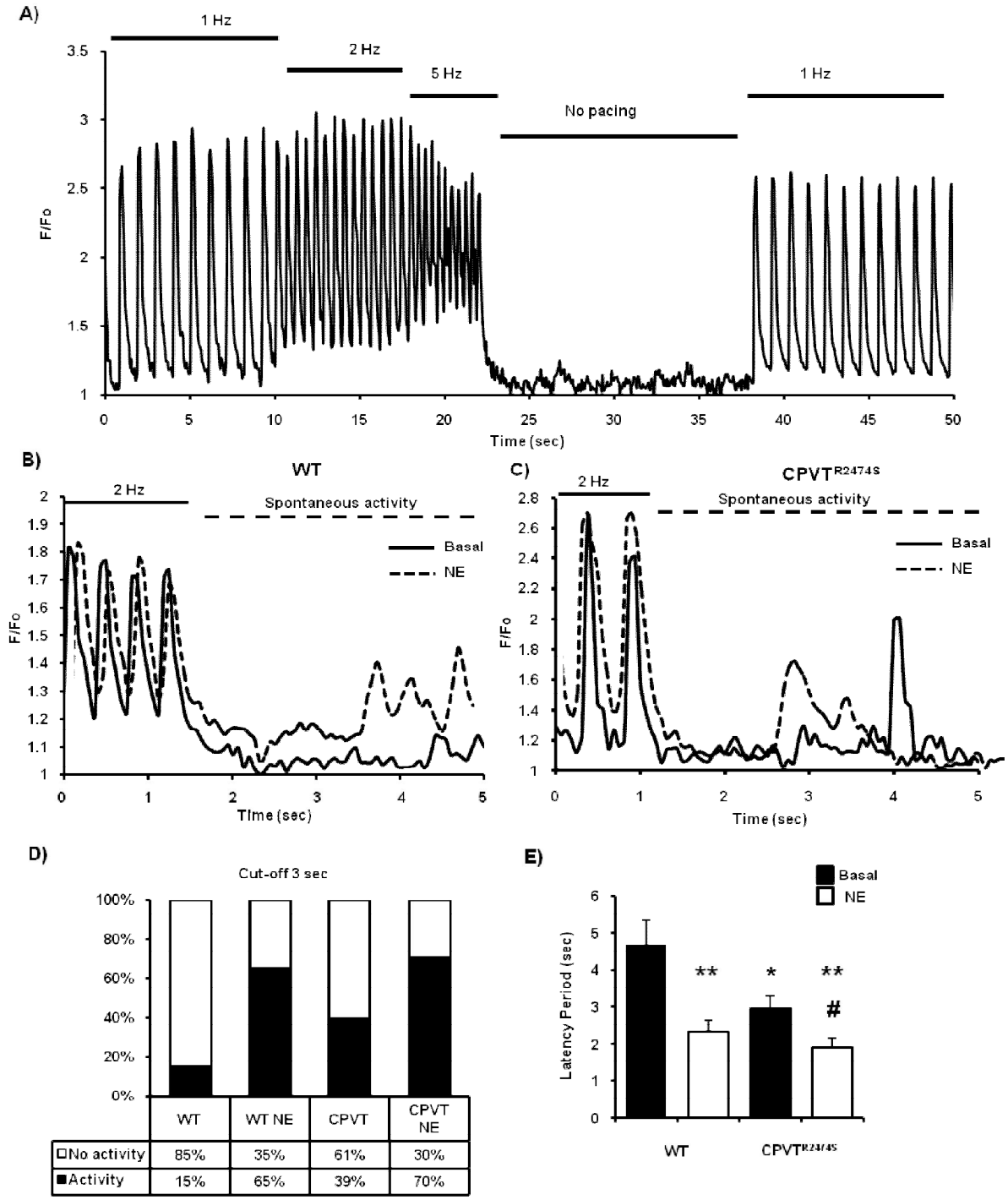

Fig. 4: A stop in the pacing procedure unmasks spontaneous non triggered releases. A) Typical fluorescence profile during a pacing stop experiment. B) and C) show representative fluorescence profiles during in WT and CPVT heart slices. D) Spontaneous releases were observed in a subset of experiments. E) WT and CPVT mice showed significantly different latency time before the first spontaneous release and release duration. (* P<0.01 if compared to WT; ** P<0.001 if compared to WT; # P<0.05 CPVT in control condition versus NE administration).

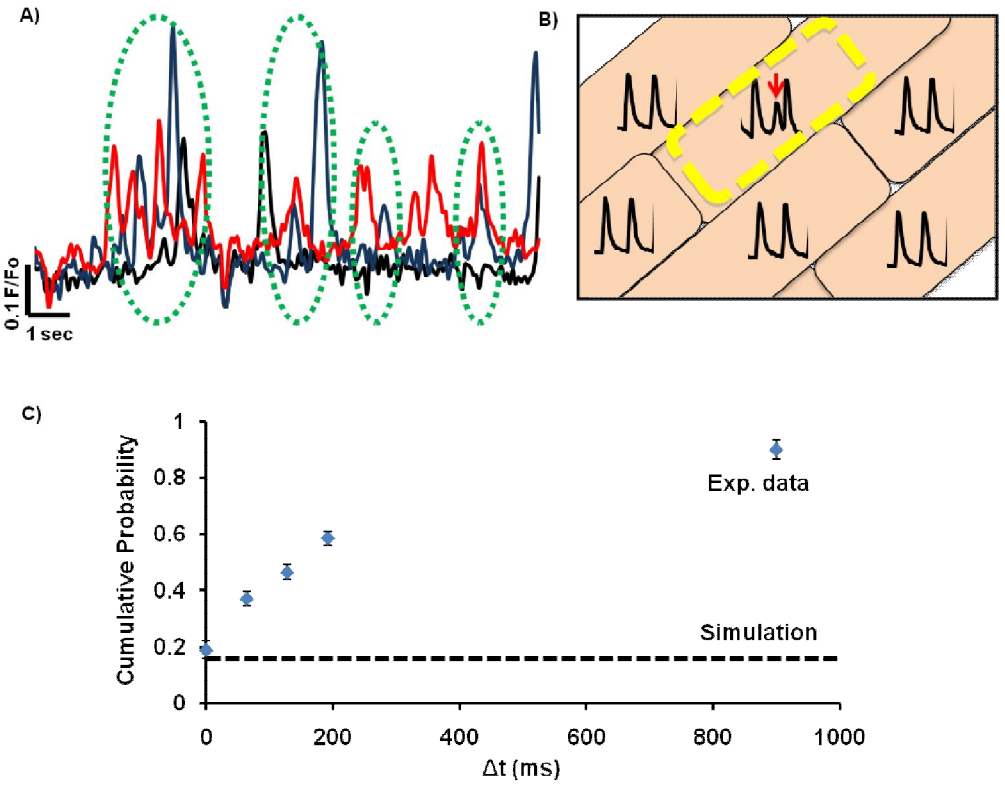

Fig. 5: Proposed model of interdependency between neighboring CMs. A) Experimental evidence of clustered DCRs. B) A DCR in a cell is sunk by the surrounding CMs that must spend partially their membrane potential. C) During the temporal window of a DCR (900 ms) a neighboring cell has >80% of probability of showing a DCR.

(manuscript in preparation)

Mitochondrial Ca^{2+} uptake machinery in cardiac physiology

Collaborators: *Tania Zaglia, Nicola Pianca, Antonio Campo, Andrea Carpi, Tullio Pozzan, Fabio Di Lisa and Rosario Rizzuto.*

1. INTRODUCTION

Arrhythmogenic events in CPVT have been widely associated to Ca^{2+} leak from the SR to the cytosol [16, 41, 46, 125]. However, it has to be considered that mitochondria are in close contact with the SR in cardiomyocytes, sensing all Ca^{2+} events in the microdomains called *dyads* [126]. While the SR contribution to Ca^{2+} dishomeostasis has been extensively studied, much less is known about whether and how mitochondrial Ca^{2+} fluxes contribute to arrhythmic events. It has been reported that SCD often involves arrhythmias triggered by metabolic stress, and regional mitochondrial depolarization has been shown to increase the propensity for re-entry of electrical current [49] between different cells in the myocardium.

Different approaches have been used in this direction, mostly using pharmacologic inhibitors of mitochondrial Ca^{2+} uptake (Ruthenium Red and Ru360) or computer simulations. The first approach allowed to consider mitochondria as players in arrhythmogenic events, i.e. Ca^{2+} alternans [127, 128] and conversion of VF to VT in isolated rat hearts [129]. With computer simulations it was possible to induce re-entrant arrhythmias acting on mitochondria membrane potential ($\Delta\Psi_m$) instability [49], and as a proof of principle this approach was translated to cultured NCMs. Even though the differences between neonatal and adult CMs are not a recent evidence [130], much is still unknown, in particular about mitochondrial calcium influx [131]. The observation that cardiac mitochondria are able to accumulate Ca^{2+} was performed decades ago, however the identification of the molecular actors of the uptake machinery started only 4 years ago [22, 23]. New molecular tools will thus allow to increase our understanding of Ca^{2+} influx in cardiac mitochondria and eventually their contribution to arrhythmia triggers.

The aim of this work is to investigate, with light emitting tools [55], Ca^{2+} uptake in NCMs in basal condition and manipulating MCU expression. Moreover, in order to translate the experimental set up to adult cardiomyocytes, the expression level of MCU complex will be analyzed across ages and the evaluation of the number of MCU channels per mitochondrion will be proposed, considering data reported in the literature [9].

2. MATERIALS and METHODS

Neonatal cardiomyocytes culture. Neonatal cardiomyocytes were prepared as previously described [132]. Briefly, hearts from 1-2 days old Sprague Dawley rats were minced in ADS (5 mM glucose, 106 mM NaCl, 5.3 mM KCl, 20 mM Hepes, 0.8 mM Na_2HPO_4, and 0.4 mM $MgSO_4$, pH 7.4) and enzymatically dissociated with collagenase A (0.4 mg/ml) (Roche) and pancreatine (1.2 mg/ml) (SIGMA-Aldrich). Cells were cultured for 24 hours in medium containing 88.8% MEM, 10% FBS, NEAA, antibiotics and 100 nM BrDU to hamper fibroblasts proliferation (all from Life Technologies, BrDU from SIGMA-Aldrich), plated on laminin-coated coverslips (1,8 μg/100 mm^2; BD) at a density of 470 cells/mm^2, and maintained in a humidified atmosphere (5% CO_2) at 37°C. On the second day, cardiomyocytes (CMs) were cultured in a medium where serum was replaces by ITS (purchased by Life Technologies).

Ca^{2+} imaging of cultured cardiomyocytes. Before seeding, NCMs were transfected with the appropriate sensor (D3CPV, 4mt-D3CPV, GCaMP6 and 2mt-GCaMP6) using Lipofectamine (Life Technologies) as recommended by the manufacturer. Twenty-four hours after plating, the medium was changed and approximately NCMs were infected with either Ad-Empty or Ad-MCU-flag (Vector BioLabs) at a multiplicity of infection (MOI) equal to 5. Forty-eight hours after infection, cells were transferred to the imaging chamber in Hepes-buffered saline (in mmol/L, 125 NaCl, 5 KCl, 1 Na_3PO_4, 1 $MgSO_4$, 5.5 glucose, 1.8 $CaCl_2$, 20 Hepes, pH 7.4) and kept at room temperature. FRET experiments were performed with an inverted Olympus IX50 microscope coupled to a CCD camera (Sensicam QE, PCO) and a custom built beam-splitter optical device (F. Mammano, Venetian Institute of Molecular Medicine). Single wavelength experiments were performed using a spinning disk confocal microscope (UltraView, Perkin Elmer). Images were analyzed and processed using ImageJ (National Institutes of Health).

Immunofluorescence analysis. Cultured NCMs were fixed with 3.7% formaldehyde for 30 min at 4°C, permeabilized with 1X PBS supplemented with 1% BSA and 0.1% Triton X-100 (all from Sigma) and stained with the antibodies indicated in the results section, diluted in 1X PBS supplemented with 1% BSA for 2 hours at 37°C. Cy3 or Alexa488-conjugated secondary antibodies from the Jackson ImmunoResearch Laboratories were

used and nuclei were counterstained with DAPI (Sigma). Cells were analyzed using a Leica TCS SP5 confocal microscope.

Western blot analysis. Cells or tissues were lysed in RIPA buffer containing complete proteases and phosphates inhibitor cocktail (all from Roche). About 40 µg of extracted proteins were loaded on 4-12% acrylamide gels (Life Technologies) and WB analysis was performed using the following antibodies: MCU, MICU1, ACTIN (from SIGMA-Aldrich), MICU2 (Abcam), MCUb (Abgent) and TOM20 (SCBT). HRP-secondary antibodies were from Bio-Rad. ECL (Thermo Fisher Scientific) was used for protein detection using a Chemidoc MP Imaging System (BioRad) and densitometry analysis was performed using ImageJ (NIH).

3. PRELIMINARY RESULTS AND DISCUSSION

3.1 Comparison between FRET-based and single wavelength calcium sensor to investigate mitochondrial Ca^{2+} dynamics

Each Ca^{2+} sensor has at least one property that makes it preferable if compared to the others. In this work we compared a FRET-based indicator from the cameleon family, with a single wavelength GCaMP sensor. The former sensor has the advantage of ratiometric measurement of Ca^{2+} levels enabling, if calibrated, to measure [Ca^{2+}] in the different cell compartments that express the sensor. However, to reach an adequate signal to noise ratio in both CPF and YFP emission channels, the minimal exposure adopted was 150-200 ms and this causes a partial loss of fast and compartmentalized Ca^{2+} events. In contrast, single wavelength sensors are more brilliant and allow to reduce the exposure time to 50 ms but their readout is only the relative change of Ca^{2+} from basal levels, thus hampering to measure the absolute Ca^{2+} concentration. Furthermore, the two families of sensors have different affinities for Ca^{2+} binding. Even though the dissociation constants (K_d) were not directly measured in our lab, it is well reported that the cameleon variant D3CPV has a K_d = 760 nM [Ca^{2+}] [67] while GCaMP6 has much higher affinity with a K_d = 167 nM [30]. The combination of high affinity and low exposure time allowed to acquire subcellular cytosolic Ca^{2+} events with GCaMP6 that were not visible with D3CPV, as shown in fig. 1.

The low K_d of GCaMP6 is of particular relevance in the mitochondria-targeted variant because it is in the range of resting mitochondrial Ca^{2+} concentration. This implies that under large cytosolic Ca^{2+} elevations, the mitochondrial sensor may saturate eventually compromising the quantitative analysis of $[Ca^{2+}]_{mt}$.

A standard protocol of NCMs stimulation consists in electrical pacing at variable frequencies. When resting NCMs were forced to contract at a given frequency (usually 0.5 or 1 Hz) they showed Ca^{2+} transients in response to the stimulation, but also an increase in the basal Ca^{2+} level up to a plateau state.

Concerning mitochondrial Ca^{2+} uptake, it has to be considered that, whether mitochondria respond to cytosolic fluctuations in a beat-to-beat fashion or acting as low-pass filters is still matter of debate [131]. Pieces of evidence in both directions, or to support a combination of the two models, can be found in the literature [130, 133]. In our experiments on NCMs, shown in fig.2, we observed that mitochondria are, actually, able to take up Ca^{2+} responding to acute cytosolic elevations, both in the case of spontaneous

activity, electrical pacing or agonist stimulation (caffeine for example). In the meantime, mitochondria are also able to accumulate Ca^{2+} up to a plateau level, corresponding to elevated frequency and fusion of subsequent transients. Not only mitochondria reach a plateau level, also the cytosol increases its basal Ca^{2+} content with increasing pacing frequency, as shown in fig. 2 and in the experiments on heart slices with Fluo-4AM [*Borile et al., submitted*].

The different kinetics was further confirmed by the experimental evidence that the time from the first electrically triggered contraction to the plateau was much larger for mitochondrial Ca^{2+} level with respect to the cytosol ($T_{plateau}^{mito}$ 17.1 ± 1.5 vs $T_{plateau}^{cyto}$ 3.9 ± 0.6; in seconds, n = 7 and 12 cardiomyocytes respectively, p-value: 10^{-7}). The data reported were obtained with D3CPV but the same measurements performed with GCaMP6 confirmed the significant difference between mitochondrial and cytosolic kinetics.

This observation is not completely striking, nor unexpected, because mitochondrial Ca^{2+} fluxes have a slower kinetics if compared to cytosolic transients, both concerning Ca^{2+} influx and efflux. This difference is probably due to the slower removal of Ca^{2+} from the mitochondrial matrix actuated by NCLX if compared to Ca^{2+} removal from the cytosol operated by SERCA2, NCX, PMCA and mitochondria too.

3.2 Mitochondrial Ca^{2+} manipulation via uniporter overexpression in neonatal cardiomyocytes

To further investigate the dynamics of mitochondrial Ca^{2+} in cardiomyocyte physiology, we genetically manipulated the expression level of the mitochondrial Ca^{2+} uniporter (MCU) taking advantage of both plasmid transfection and adenoviral (AV) infection of NCMs. The protocol of viral infection was set up in the laboratory, testing different concentrations. The best compromise between percentage of infected cells and low viral particles was set to a MOI = 5. To exclude bystander effects of the viral infection, we always use as controls NCMs infected with the same MOI of AV without the coding sequence (from now called EMPTY). The MCU-FLAG protein was efficiently overexpressed in NCMs (fig. 3A) and co-localized with the mitochondrial protein TOM20 (fig. 3B).

The amount of overexpressed protein was evaluated by WB analysis (fig. 3C). Then, the protein level of MCU partners were analyzed and while no variations could be observed in MICU1 and MICU2, MCUb level was markedly increased, probably to hamper a

dramatic entry of Ca^{2+} upon MCU overexpression (fig. 3C). This result on MCU partners protein level was surprising if we consider the existing data in the literature [31] obtained in cell lines such as HeLa and HEK-293, showing that an increase in MCU protein level causes an increase in MICUs proteins and a decrease in MCUb protein expression. To test whether our results highlighted a peculiarity of cardiac mitochondria, we repeated the same overexpression protocol with MCU-FLAG and MCU-GFP on HEK-293 cells; the use of MCU-GFP plasmid allowed to verify that the percentage of overexpressing cells is over 80% (not shown). As expected, MICU1 protein level increased slightly upon MCU-GFP overexpression, while MCUb decreased in HEK-293 cells, while the endogenous MCU is not affected (fig. 4), confirming that cardiac mitochondria may respond differently from others [2].

Once established MCU overexpression in NCMs at the protein level, we started to test whether the exogenous protein was functional in our cells, correctly folded and integrated in the Ca^{2+} entry machinery. To this aim Ca^{2+} imaging at both mitochondrial and cytosolic level was performed. D3-CPV, GCaMP6 sensors and Fluo-4AM dye, were used to perform cytosolic Ca^{2+} imaging. No significant variations were detected in MCU overexpressing (MCU^{+}) NCMs compared to controls, as shown in fig.5 a-b (data reported were obtained with D3CPV, no significant differences in cytosolic Ca^{2+} could be recorded with GCaMP6 nor with Fluo4, data not shown), only a slight increase in spontaneous firing of MCU^{+} CMs was recorded even though statistical significance was not reached.

Comparing mitochondrial Ca^{2+} dynamics in control cells and MCU^{+} cells, it is evident that, increasing the level of MCU, the entry of Ca^{2+} inside the matrix was faster (EMPTY: 15.6 ± 0.7 vs MCU^{+}: 9.7 ± 0.4, in seconds; n = 48 and 55 NCMs respectively; p-value < 10^{-3}) and the accumulation capacity was larger (EMPTY: 7.1 ± 0.5 vs MCU^{+}: 10.9 ± 0.8, in %Ratio; n = 48 and 55 NCMs respectively; p-value < 0.05), indicating that exogenous MCU could be functionally integrated in the mitochondrial influx machinery enhancing Ca^{2+} influx dynamics, as shown in fig. 5c-d.

3.3 Mitochondrial Ca^{2+} influx in neonatal and adult hearts

The observed beat-to-beat uptake of Ca^{2+} by mitochondria is not surprising in NCMs and has already been reported [130, 134], while grater debate is ongoing around the Ca^{2+} uptake in adult cardiomyocytes [130, 131, 133, 135]. In the more mature cardiomyocytes, mitochondria are in close contact with the SR cisternae, leading to the hypothesis that

these mitochondria would feel larger $[Ca^{2+}]$ in the microdomains. However, no consensus on the exact model of Ca^{2+} uptake in adult cardiomyocytes has been reached so far, and no direct extrapolation of data obtained in NCMs to adult cardiomyocytes is possible.

To complicate even more this scenario, it has been reported by several groups that isolated mitoplasts from neonatal and adult hearts display different I_{mcu} currents [2], indeed, 5 fold larger currents were recorded for neonatal mitochondria.

A review by Lederer and colleagues [9] grouped all the data available in the literature concerning mitochondrial calcium uptake, with a particular attention to the heart. Even though data were obtained by different approaches, they plotted the results in function of cytosolic calcium $[Ca^{2+}]_i$ proposing a model of cardiac Ca^{2+} flux that fits all the data, as follows:

$$J_{mcu} = N_{mito} \cdot N_{mcu} \cdot P_{open} \frac{i_{mcu}}{zFV_{myo}} \qquad (1)$$

where N_{mito} is the number of mitochondria per cell, N_{mcu} is the number of channels per mitochondrion, P_o the open probability and i_{mcu} is the single channel current.

Considering that Ca^{2+} flux, as modeled in (1), is dependent on the number of mitochondria (N_{mito}), on the number of channels (N_{mcu}) and on the open probability of the channels (P_o), we wondered whether these parameters were different in neonatal compared to adult hearts. Concerning N_{mito} it is reported that the percentage of cell volume occupied by mitochondria increases from 22% at birth to 33% in the adult [8], however, data concerning MCU current were obtained in isolated mitoplasts, regardless of the total mitochondria number. For this reason we focused our attention on N_{mcu} and P_o. Williams et al. [9] estimated for adult cardiomyocytes the number of MCUs per mitochondrion around **200**, thus repeating their calculations for mitoplasts with a 5-fold larger current, it comes that neonatal mitochondria are required to have around **1000** MCUs. Nevertheless, these calculations do not consider the possibility that the uniporter P_o varies with partners' protein expression or with $[Ca^{2+}]_i$, while the exact mechanism is yet understood.

One possibility is that the partners of MCU, MICU1 and MICU2, contribute somehow to the regulation of the uniporter P_o, while MCUb, acting as a dominant-negative, may dramatically reduce the single channel current i_{mcu} [29]. To test these entire hypotheses we adopted a strategy alternative to electrophysiology, i.e. biochemistry, with the aim to obtain pieces of evidence complementary to data present in the literature. Moreover, as shown for hearts slices experiments, Ca^{2+} handling proteins, like SERCA2 [112], are

modulated with age, so we wondered whether this may happen also for mitochondrial proteins. To this aim, we evaluated the mRNA and the protein levels of MCU complex in the growing heart as well as in other cell types.

3.4 mRNA: the MCU complex is expressed in parallel

The first step of our investigation consisted in the evaluation of mRNA expression level of MCU protein and the other identified components of the uniporter complex, MICU1, MICU2 and the dominant negative form MCUb. RT-qPCR analysis on MCU, MICU1, MICU2 and MCUb showed a parallel expression of the different components, as reported in fig. 6, with a slight different shape in MCUb only. The mRNA levels were compared with different housekeeping genes, from β-actin to GAPDH to TOM20 that was finally selected as reference because it was the most stable gene across postnatal cardiac development (data not shown).

A possible explanation for these similar expression profiles is that all the components of the uniporter complex are under the control of the same promoter or, as proposed by Mootha and coworkers [23], one of the components acts itself as a transcription control on the others, nonetheless, the responsible for the transcription levels is unknown, so far. Strikingly, in contrast with the calculations of the number of MCU complexes in neonatal hearts reported in the previous chapter, mRNA data suggest that adult hearts have a larger number of uniporters if compared to neonatal hearts. To further elucidate this unexpected result, we performed WB analysis on the components of the complex.

3.5 Protein level analysis of the MCU complex in heart postnatal development

WB analysis was performed on the same hearts used to extract mRNA and perform the RT-qPCR experiments. MICU-1 showed a protein regulation parallel to the mRNA transcription profile that was not surprising, while MCU protein level decreased with age (fig. 7). A decrease in MCU protein level is in line with the calculations described above. Furthermore, the varying ratio between MICU1 and MCU protein level can be associated, at least in part, to a modulation in the P_o of the uniporter, even though a further analysis on the other components, MICU2 and MCUb, is needed.

Considering the relevance of this observation to elucidate Ca^{2+} uptake modality in cardiac mitochondria, we wondered whether this observation is a peculiarity of mice hearts, or it is a more general feature. To this aim, we repeated the same WB analysis on rat samples,

obtaining a similar result, thus suggesting a conserved regulation across species, at least in rodents.

Then, to understand whether this post-natal MCU regulation is a peculiarity of the heart we analyzed other tissues, in particular the liver which is widely used in mitoplasts experiments and no variation in MCU current have been reported [2]. Indeed, in our WB analysis no significant variations on MCU protein expression were detected across ages, further suggesting that cardiac mitochondria undergo a specific protein modulation to answer to contractility needs, as well as dramatic metabolic changes, to sustain the huge ATP requests [112, 136-138].

On one hand, the result obtained from WB analysis about MCU protein expression fits well with the electrophysiology data available in the literature about the larger MCU current observed in neonatal hearts. Even more important, it adds another component to the intricate dispute about the ability of mitochondria to take up Ca^{2+} on a beat-to-beat basis [135]. While beat-to-beat Ca^{2+} uptake has been reported in NCMs [130, 134] and also measured by us, the hypothesis that if it is observed in immature cardiomyocytes it must be more evident in mature cardiomyocytes where mitochondria and SR are much closer. However, the larger MCU current and the larger MCU protein level in neonatal hearts [2] can, at least in part, explain why the beat-to-beat fashion is easily recorded in NCMs while it is not so evident, if present, in adult cardiomyocytes.

Last but not least, from our results it comes that MCU is post-transcriptionally regulated. This observation is not completely novel because MCU contains a sequence at the N-terminus that is cleaved in order to target the protein uniquely to mitochondria [29]. Moreover, Pinton's group [139] reported that miR-25, a cancer-related miR, can modulate MCU levels opening the route to the identification of other miRNAs regulating MCU. However, this observation allows us to speculate that protein degradation or miRNA silencing may take part to the postnatal regulation of MCU.

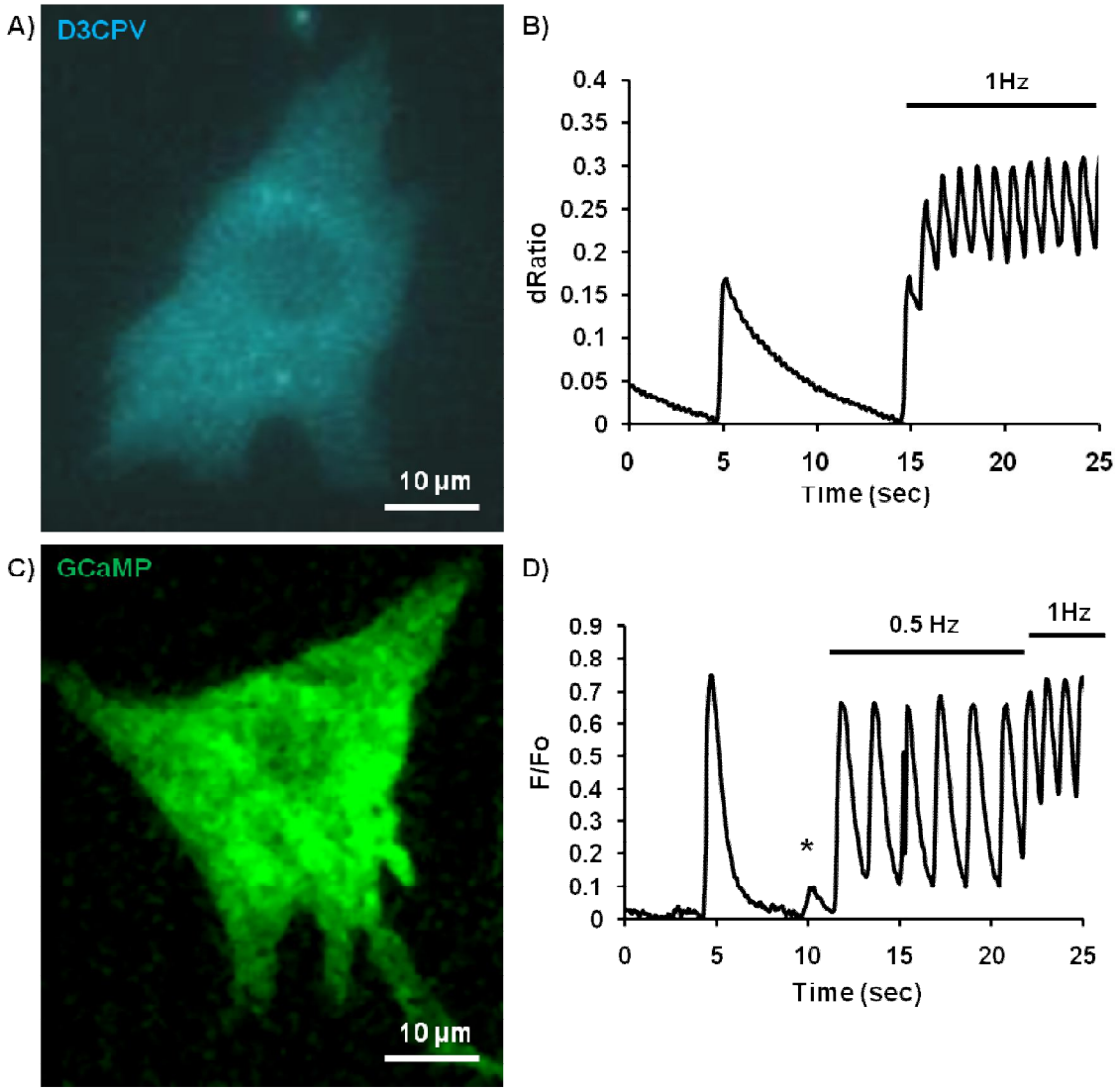

Fig. 1: Cytosolic Ca^{2+} imaging with D3CPV (A and B) and GCaMP6 (C and D). The faster kinetics of GCaMP6 allowed to visualize small subcellular events (*) that were not visible with D3CPV.

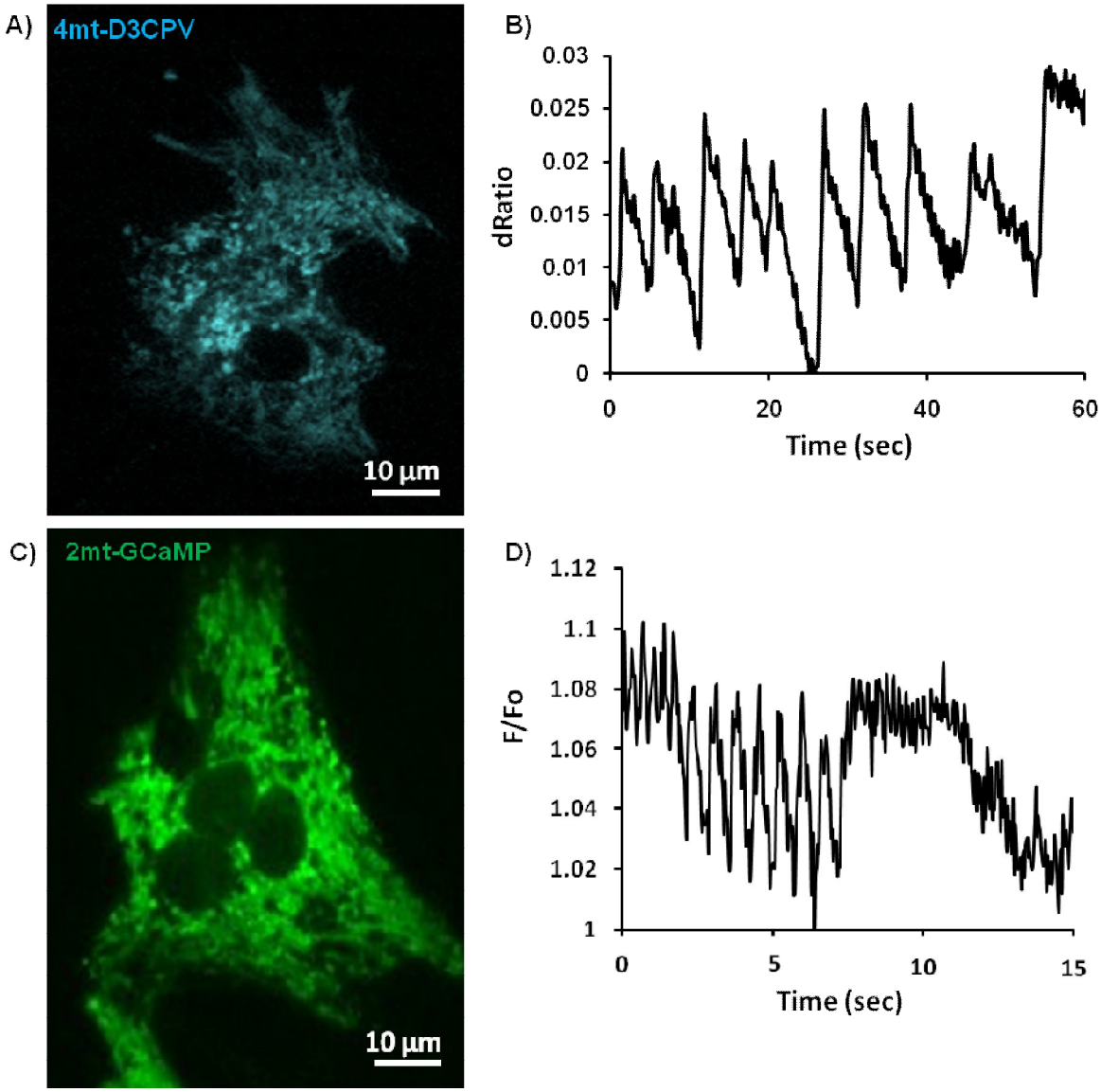

Fig. 2: Mitochondrial Ca^{2+} imaging with 4mt-D3CPV (upper panels) and 2mt-GCaMP6 (lower panels). With both sensors it was possible to record beat-to-beat variations of Ca^{2+} in NCMs.

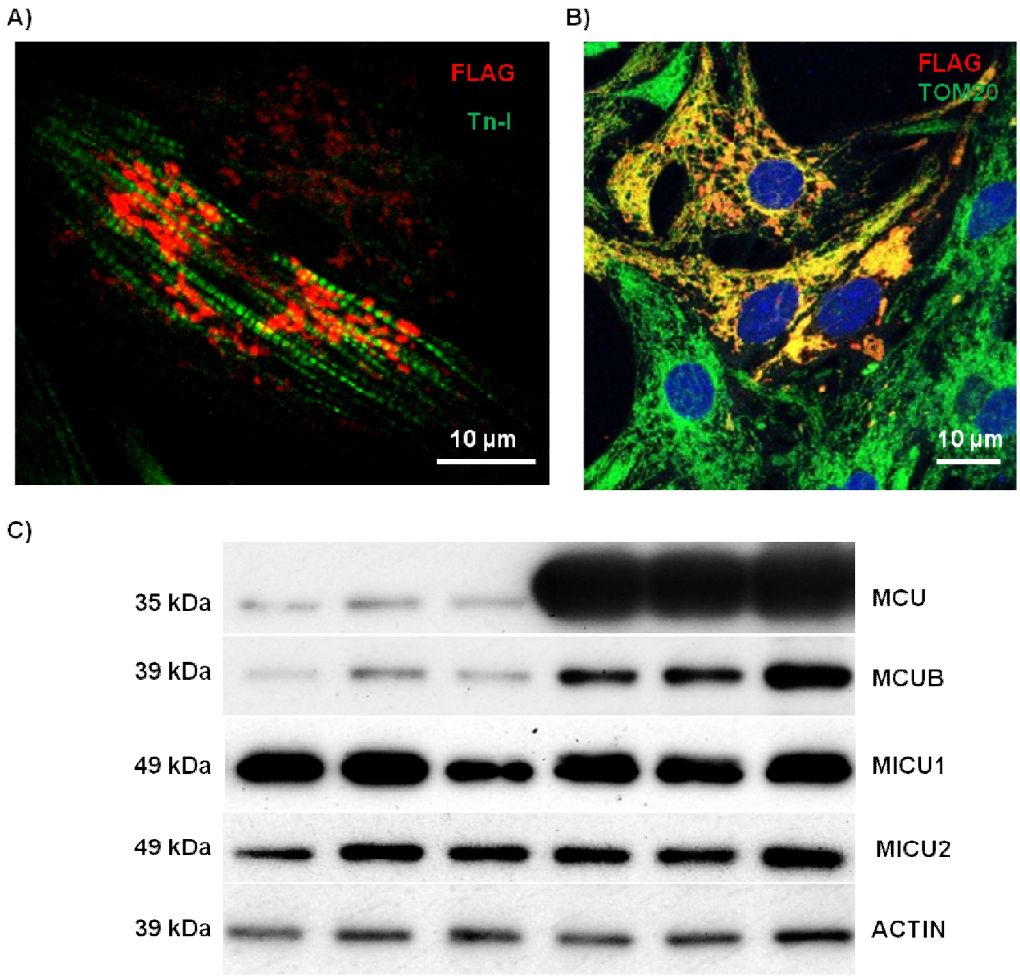

Fig. 3: MCU overexpression in NCMs. A) and B) MCU is overexpressed in NCMs without altering sarcomere morphology and co-localizes with the mitochondrial protein TOM20. C) MCU overexpression is quantified with WB analysis on NCMs protein extracts. MICUs do not show variations in the expression level while MCUb increases.

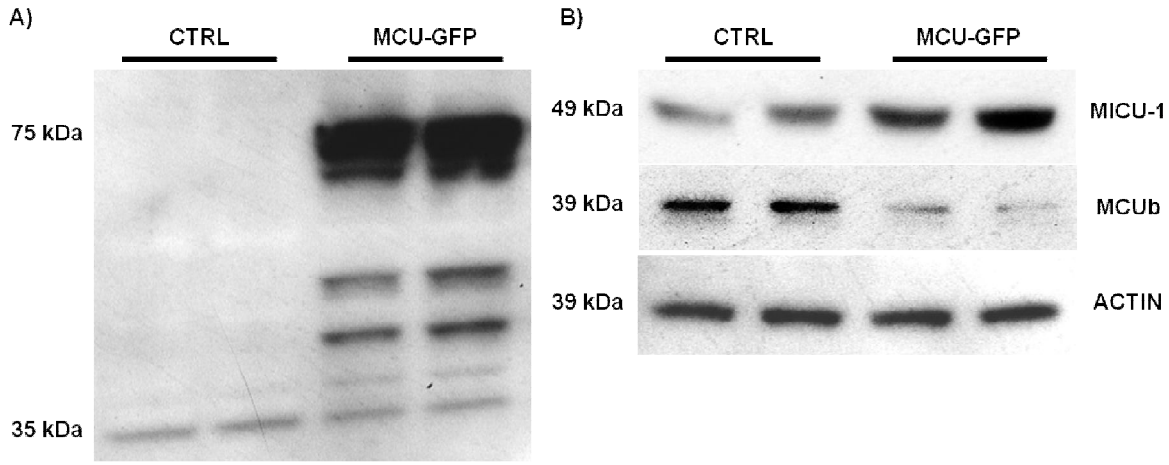

Fig. 4: MCU was overexpressed in HEK-293T cells. In this cell line, MCU partners show a different regulation than in NCMs: MICU-1 increases while MCUb decreases.

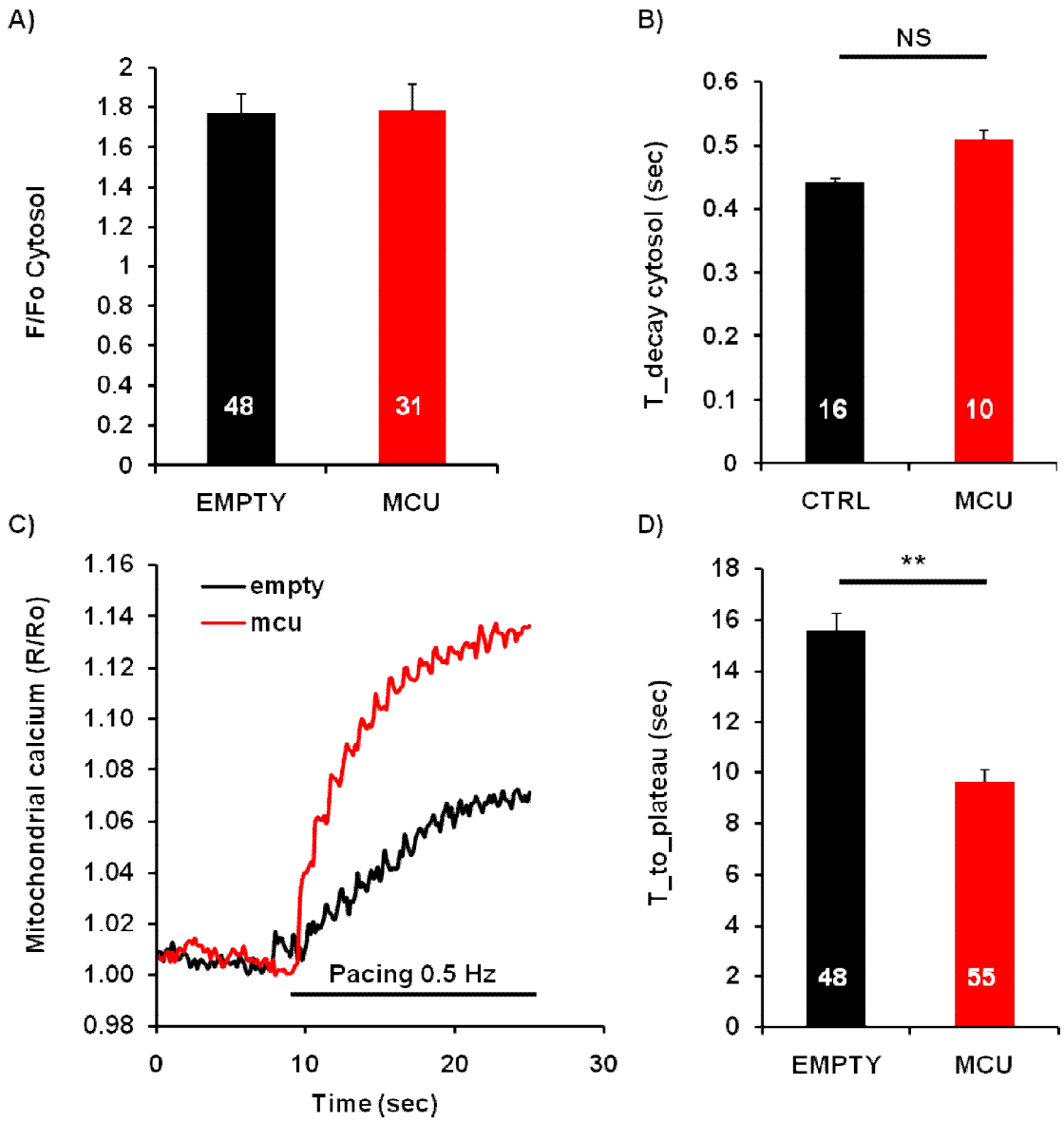

Fig. 5: MCU overexpression in NCMs does not affect cytosolic Ca^{2+} transients' amplitude A) or duration B). Mitochondrial Ca^{2+} uptake in MCU^{+} NCMs shows larger accumulation during pacing C) and a faster uptake D). ** means p-value < 0.01. Data represent 3 different experimental replicates and the total number of CMs is indicated over the graph bars.

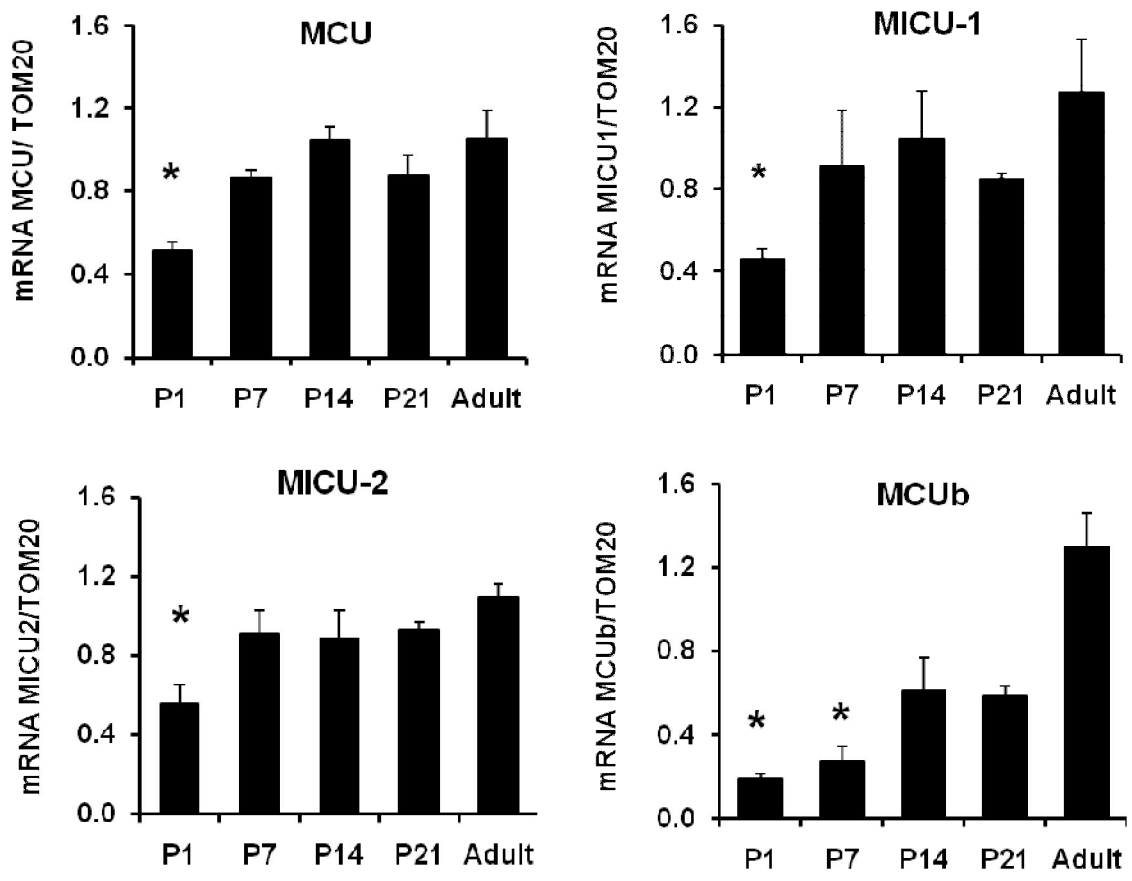

Fig. 6: RT-qPCR analysis shows that MCU complex is regulated in parallel during postnatal heart development in mice. * means p-value < 0.05. Data represent 3 different samples in 2 experimental replicates (3 replicates for MCU).

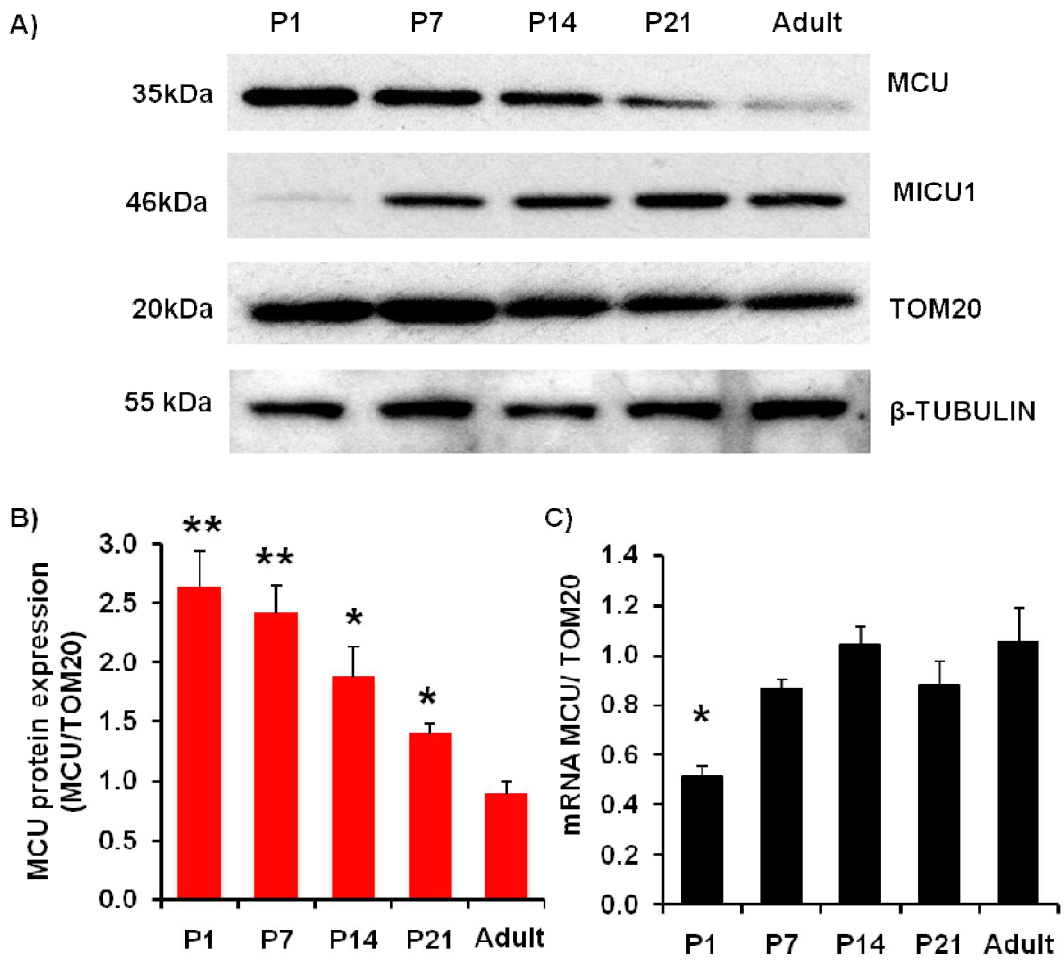

Fig. 7: WB analysis shows that MCU protein level decreases with age while MICU-1 follows mRNA expression profile. Densitometric analysis of WB and quantification of mRNA expression show that MCU is post-transcriptionally modulated. * means p-value < 0.05; ** means p-value < 0.01. Data represent the average of 3 different samples in 3 experimental replicates.

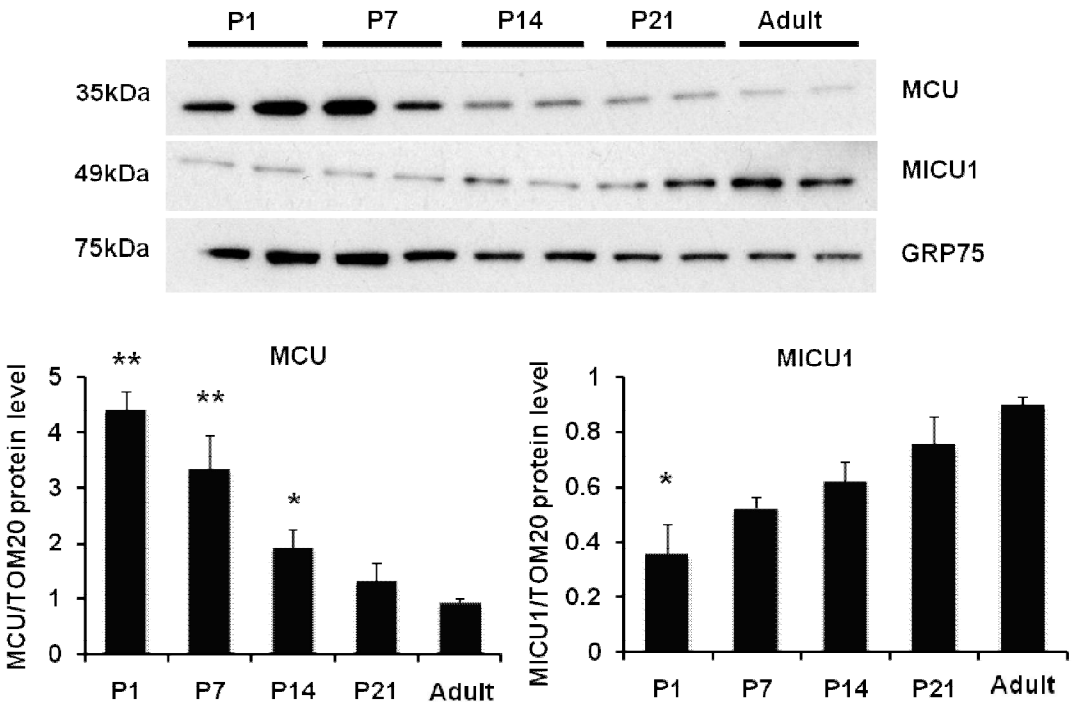

Fig. 8: WB analysis on rat hearts shows that MCU decreases with age while MICU1 does not follow MCU expression profile. * means p-value < 0.05; ** means p-value < 0.01. Data represent the average of 3 different samples in 2 experimental replicates.

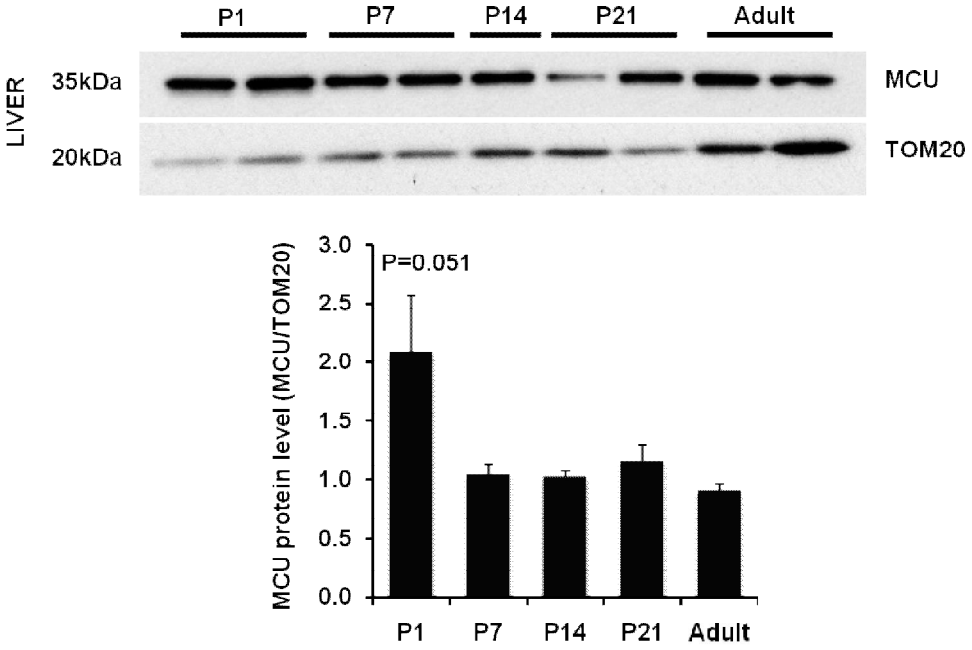

Fig. 9: WB analysis on mice liver samples shows that MCU expression profile is tissue specific. Data represent the average of 3 different samples in 2 experimental replicates. P-value is indicated.

(manuscript in preparation)

Modeling blue light transmission for cardiac optogenetics

Collaborators: *Tania Zaglia, Nicola Pianca.*

1. INTRODUCTION

Optogenetics is a technique that combines physics with genetics and electrophysiology [140]. Named "Method of the Year" in 2010 by Nature Methods, its core idea is to control cellular activity modulating membrane light sensitivity. This is possible through the transgenic expression of *opsin* proteins, like Channelrhodopsin that derives from unicellular green algae forming a light-gated ion channels [54, 141].

This technique allows a millisecond control of action potentials in excitable cells and is widely used in neuroscience research where it is becoming a gold-standard technique. In parallel, several studies on light-gray matter interaction are helping to elucidate the effects of light intensity, wavelength and, most important, the extent of light propagation in the tissue [69, 73, 140, 142, 143].

A part from neuroscience, the control of cardiac activity has been proposed in terms of direct stimulation of transgenic myocardium in zebrafish [75] and mouse [53] or isolated cardiomyocytes [74], however studies on light-myocardium interaction as those performed for the brain are much less. Some studies on scattering properties have been performed in different animals and with aims far from optogenetics [144-146]. Thus, a direct approach to evaluate light penetration depth in the myocardium with the standard light sources used in optogenetics, such as LEDs and optical fibers is lacking.

In this work we built myocardium phantoms to measure light transmission in the heart, in order to evaluate the extent of myocardium illuminated in our conditions. Moreover, experimental values will be used to fit different models of light-matter interaction, Beer-Lambert law [73, 140, 143, 144] and Kubelka-Munk model [69, 147, 148]. In the discussion we will compare and discuss data present in the literature obtained from different animals and different preparations [144].

2. MATERIALS AND METHODS

Blue light exiting from an optic fiber tip. A blue LED (AM470L2 powered at 1000 mA, Thorlabs, 470 nm) is controlled by an ECG-coupled recording system (Powerlab 8/30, Bioamp and LabChart 7.1 software; AD Instruments) through a LED driver (LEDD1B, Thorlabs). Varying the voltage tension in entrance we obtain a proportional light power emerging from the LED (see Fig 1A).
A LED-fiber coupler (SM1FC, Thorlabs) allows coupling the LED to the optic fibers: AFS105/125Y, FT200EMT, FT400EMT, and FT800EMT. The optic fiber more relevant for the final calculations is the FT200EMT with a diameter of 200 μm and a numerical aperture NA = 0.39.
Then the fiber tip was positioned against an agarose cube to further evaluate the light shape and the numerical aperture given by the manufacturer (see fig. 1B).

Experimental measure of light attenuation in cardiac phantom. To estimate light attenuation in our experimental model, we built optic phantoms and measured light transmitted for different phantoms thickness. The total transmitted fraction of light was measured as the power measured with the phantoms present divided by the power with no sample. We cut both fresh and frozen cardiac slices in the longitudinal direction and used both the preparations to measure the transmitted light. Fresh slices were cut from freshly harvested hearts with a vibratome (Leica) upon including the hearts in agarose. The procedure was carried in ice-cold Tyrode solution. Frozen samples were obtained fixing the tissue with PFA 1% and then dehydrating the hearts with sucrose 30% before freezing in liquid nitrogen. Then slices of different thickness were cut with a cryostat (Leica) and collected on a glass coverslip.
Tissue phantoms were thus placed over the light sensor of an optical power meter (PM100D, Thorlabs) and the distance of the fiber tip was maintained at fixed distance with a glass coverslip in order to exclude compression of the fresh tissue. The same optical fibers used in the in vivo experiments were used to illuminate the tissue phantoms and measure the emerging light with the radiometer (see fig 1C).

In vivo control of cardiac function. As described in detail in [Zaglia *T., Pianca N., Borile G. et al., Appendix 1*] mice expressing ChR2 under the transcriptional control of α-MHC promoter were generated using CRE-Lox recombination and fully characterized. The

epicardial stimulation protocol consists in an open-chest anesthetized mouse model in order to deliver light directly from as LED to the heart through the differently sized optical fibers described above. The outcome of the experiments is the superficial ECG recorded with a dedicated apparatus (Powerlab 8/30, Bioamp and LabChart 7.1 software; AD Instruments) that controls also LED triggering.

3. RESULTS

3.1 Light attenuation exponential decay: Beer-Lambert law and corresponding calculation of N

A commonly used approximation to evaluate light penetration in thick tissue is the Beer-Lambert law:

$$I(h) = I_0 e^{-h(\mu_s + \mu_a)} \qquad (1)$$

where I(h) is the irradiance, μ_s and μ_a are the scattering and absorption coefficients, respectively [140]. This law assumes an exponential decay of light with tissue thickness (h) and, in its simpler formulation (1), it excludes light reflection at the surface. Moreover, it considers the tissue as a homogeneous scattering medium.

For our evaluation we will consider $\varepsilon_\lambda = \mu_a + \mu_s$:

$$I(h) = I_0 e^{-h(\varepsilon_\lambda)} = I_0 e^{-\frac{h}{\delta}} \qquad (2)$$

where δ is the scattering length.

Experimental measurements on both fresh and frozen samples were fitted with the Beer-Lambert Law to obtain the scattering length δ (called penetration depth).

As expected light absorption profiles followed the exponential decay with a good coefficient of determination ($R^2 \sim 0.9$) meaning that the experimental data obtained fit the model well. Then we could calculate δ, the decay coefficient that is wavelength dependent. In our conditions we obtained $\delta \sim 250$ µm.

To evaluate the number of cardiomyocytes that are depolarized upon illumination, we built a geometrical model that relates the light density exiting from the optic fiber to the number of cell in a portion of myocardium.

The minimum light density necessary to depolarize a single cell (from now called *J*) has been widely reported in the literature ranging from a minimum of 0.2 mW/mm^2 up to a 10-fold higher power [73, 75].

We consider that this minimal intensity is reached, upon illumination, at a certain depth called h^* :

$$J = I_0 e^{-\frac{h^*}{\delta}} \qquad (3)$$

Resolving eq. (2) for h^*we obtain the depth reached by a sufficient light density J proportional to our experimental set up:

$$h^* = \delta \ln \frac{I_0}{J} \qquad (4)$$

Defining the shape of light propagated inside the myocardium and knowing the depth reached by light h^* it is now possible to evaluate the number of cells depolarized.

In the approximation of a cylindrical shape (probably not too far from the experiments considering the reduced numerical aperture of the optic fibers) with a diameter dependent on the optic fiber used in the experiments, we can estimate:

$$N(h) = \frac{Volume\ (h)}{Volume\ cell} = \frac{\pi R^2 h}{V_1} \qquad (5)$$

$$N^* = \frac{\pi R^2 h^*}{V_1} = \frac{\pi R^2}{V_1} \delta \ln\left(\frac{I_0}{J}\right) \qquad (6)$$

From (6) it can be appreciated that the number of cells N* irradiated with a sufficient light power varies in function of the fiber radium (R), on the light density at the epicardial surface (I_0) and on the minimal light density J.

The minimal combination of starting irradiance and radius that was sufficient in our in vivo experiments to induce an ectopic beat was I_0 = 5.4 mW/mm^2 and r = 100 μm. With this elements it was possible to calculate a number of cells N* ~ 1450 - 1950.

3.2 Beer-Lambert Law with conical volume

Whether the cylindrical approximation is not far from reality, we also considered conical spread of light calculating the emerging half angle from the optic fiber numerical aperture (NA=0.39) and the refractive index (n≥1.4) of myocardium [143] as

$$\Theta = \sin^{-1}\left(\frac{NA}{n}\right) \qquad (7)$$

that resulted to be Θ = 16°.

The truncated cone thus increases its major radius R with distance h as

$$R(h) = h \tan(\Theta) + r \qquad (8)$$

where r is the radius of the fiber tip, meaning that the total irradiated area duplicates at 150 μm, triplicates at 250 μm, quadruplicates at 350 μm and so on. In our conditions, we

could calculate a number of cells N* ~ 1500 – 2450, in line with the cylindrical approximation.

3.3 Light attenuation: Kubelka-Munk model and corresponding calculation of N

To further evaluate the scattering properties of cardiac muscles, we evaluated our experimental data with an alternative model for light-tissue interaction. In this model, the tissue is considered a uniform diffusive media where isotropic scattering occurs and the approximation of no absorption is present.

The transmitted light experimentally measured was fit the following model:

$$T = \frac{1}{(Sh+1)} \qquad (9)$$

where S is the scatter coefficient of the tissue.

As reported by Aravanis et al. [69] for the optogenetic control of brain function, we fitted our datasets of fresh and frozen murine myocardium with the Kubelka-Munk model and the data corresponded quite well with the model (see fig. 3). It was then possible to obtain an estimation of the scattering coefficient for the heart as the best fit value $S_{frozen} = 20 \pm 2$ mm^{-1} for frozen tissue and $S_{fresh} = 14 \pm 2$ mm^{-1}, which are consistent with the value of 12 mm^{-1} reported for the less scattering gray matter [69].

Then it was possible to apply the complete expression for light loss:

$$I(h) = I_0 \frac{\rho^2}{(Sh+1)(h+\rho)^2} \qquad (10)$$

The equation in (8) accounts for the intensity losses caused by the geometrical component and the scattering, where S is the scattering coefficient. In particular, the ρ parameter is proportional to the numerical aperture (*NA*) of the optic fibers, to the refractive index of the scattering medium (*n*) and to the radius of the fiber as it follows:

$$\rho = r\sqrt{\left(\frac{n}{NA}\right)^2 - 1} \qquad (11)$$

With the measured coefficient S and the calculated value for ρ = 345 μm it was possible to calculate the complete light intensity ratio, as shown in fig. 4.

In this way it was possible to evaluate the number of irradiated cells with a sufficient light density, within the illumination truncated cone obtaining a number of cells ranging from 850 to 1225, the same order of magnitude of the values calculated previously.

4. DISCUSSION

Optogenetics has the potential to considerably increase our knowledge on cardiac electrophysiology and arrhythmias, but at the current stage, such technique has only been used scarcely in molecular cardiology studies. Here, we have set the protocols and validated the methodology to answer questions related to basic mechanisms of heart regulation and specifically:

1. What is the minimal number of cells required to conduct an ectopic beat and function as arrhythmia trigger?
2. What is the contribution of Purkinje fibers to normal and arrhythmogenic events of the heart?
3. Is it possible to elicit an arrhythmogenic behavior with photopacing of the heart?

To validate the optogenetics approach in the study of cardiac physiology, we first set out to accurately determine the myocardial tissue volume illuminated with the light activation hardware, and based our experiments on the comparison between experimentally measured values and modeling using Monte Carlo simulations [143]. The direct measurement of penetration depth and scattering coefficient for murine myocardium and our values are compared with data existing in the literature.

A recent paper [142] proposed an analysis of the differences in optical properties between fresh and frozen tissues. They compared tissues from heart, kidney liver and brain gray matter, providing new data on absorption and scattering values especially in the visible light spectrum. By adapting the algorithms developed in such work to the heart tissue, it was possible to obtain the scattering and absorption coefficients of rat heart tissue at 470 nm, the same wavelength that we used:

$$\mu_s = 1.95\ mm^{-1}$$

$$\mu_a = 1.2\ mm^{-1}$$

$$\varepsilon_{470\ nm} = \mu_s + \mu_a = \frac{1}{\delta}$$

Thus, the calculated penetration depth is δ = 317 μm for rat heart. We identified a number of factors that may be responsible for such discrepancy, and specifically:

(1) species differences may impact on light penetration depth, as shown by a number of reports; penetration depth coefficients range from 800 μm for sheep, through 570 μm for rabbit myocardium to 290 μm for guinea-pig, however all these measures have been performed with different methodological approaches and aims, thus making the

comparison between values less informative. Indeed, all these values were calculated to estimate the depth-dependent optical signal present in optical mapping experiments on isolated perfused hearts.

(2) the intrinsic variability of tissue preparation. In all the experiments, regardless on the strategy to fix and preserve the tissue (snap freezing or fixation), the slices were cut with a vibratome that does not allow a micrometric precision; moreover, the hemoglobin content is variable and its light absorption is elevated at the wavelength used.

Another paper [143] proposes a detailed method for the evaluation of scattering coefficient with experimental measurements and Monte Carlo simulations. Starting from the Beer-Lambert law, with this double approach they validated the wavelength dependency of scattering coefficient for highly anisotropic tissues like murine muscles. Even though muscles are less scattering then the heart, they obtained μ_s = 1.16 mm^{-1}, leading to $\delta \sim 860$ μm, however, the contribution of absorption by hemoglobin is not considered.

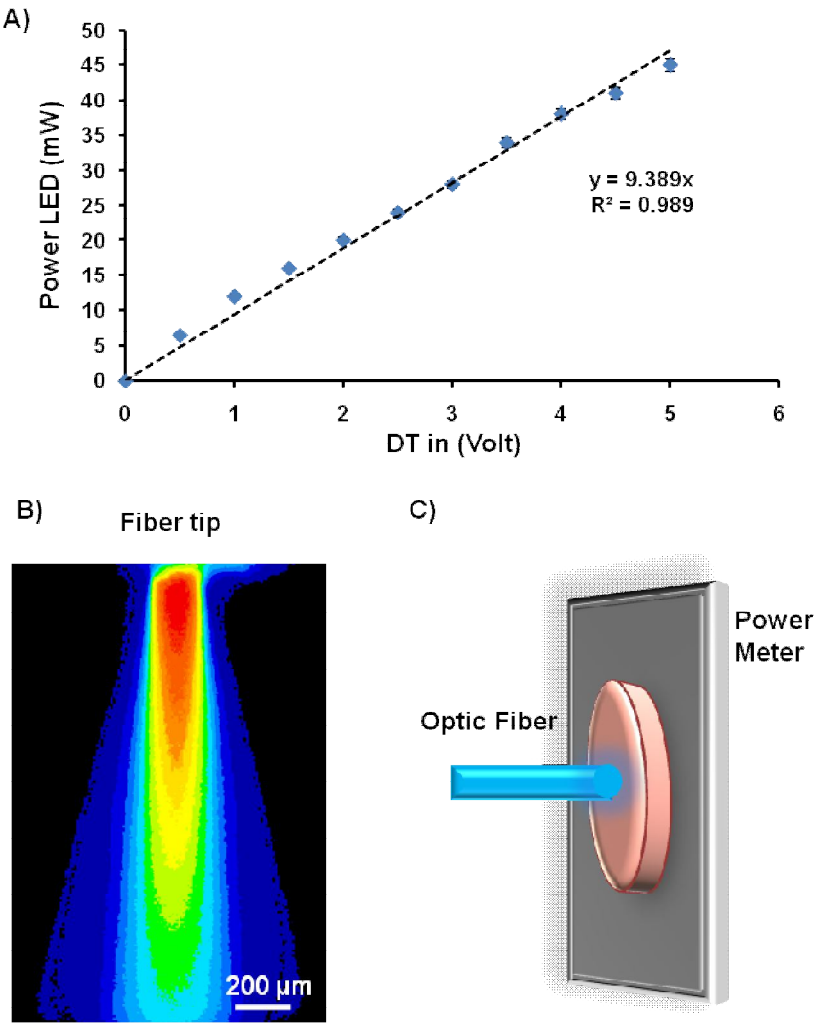

Fig. 1: A) Experimentally measured linearity between driving voltage and emitted light power by the LEDs. B) Shape of blue light exiting from the fiber tip in agarose, shown in false colors. C) Cartoon showing the setup for light scattering measurement.

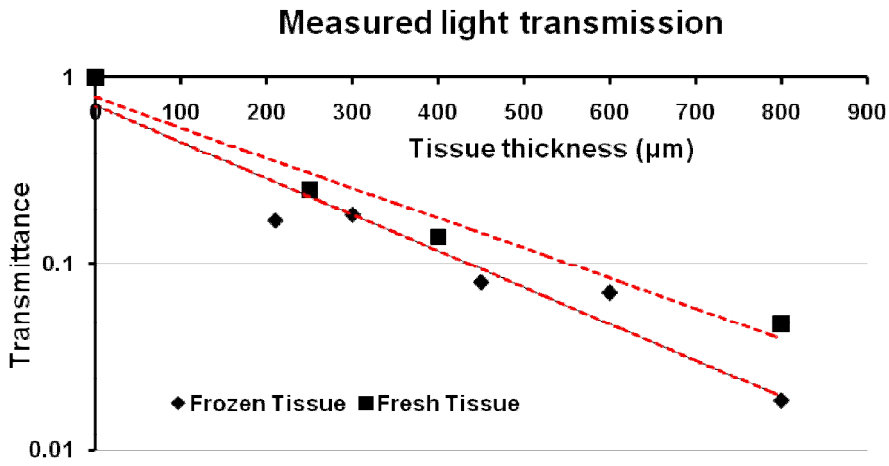

Fig. 2: Experimental data obtained from fresh and frozen tissue samples fitted with Beer-Lambert law.

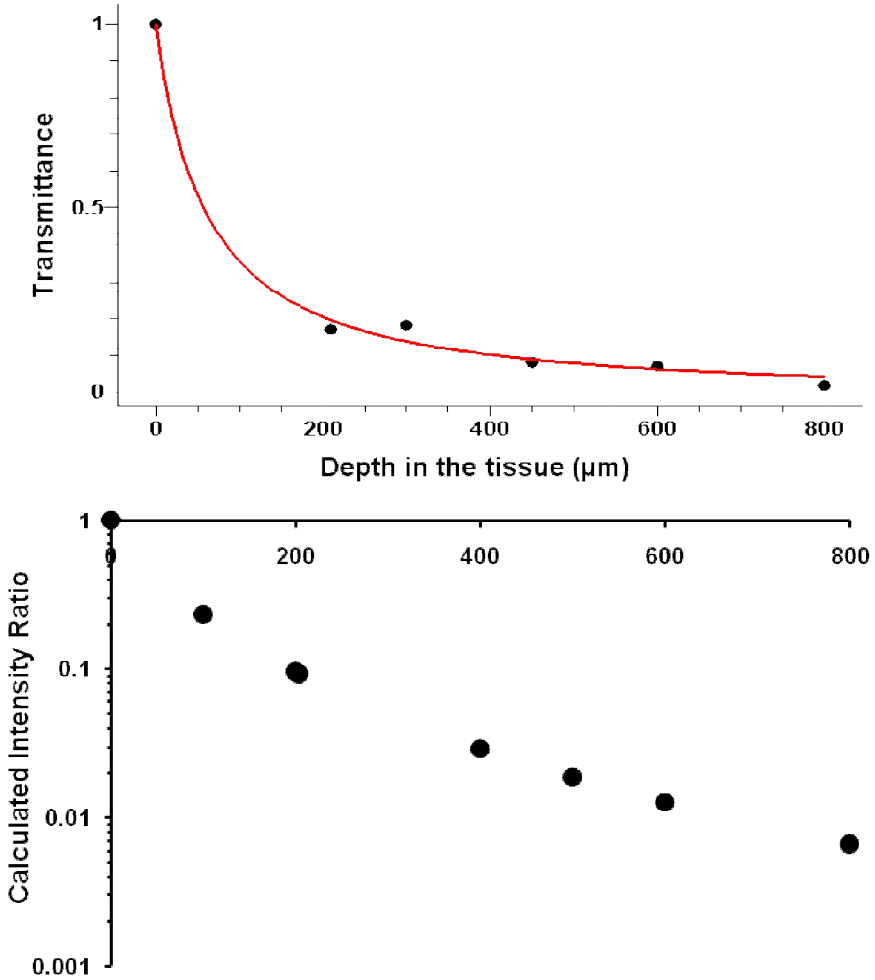

Fig. 3: Experimental data obtained from frozen tissue samples fitted with Kubelka-Munk model (upper graph). Calculated transmission intensity (lower graph).

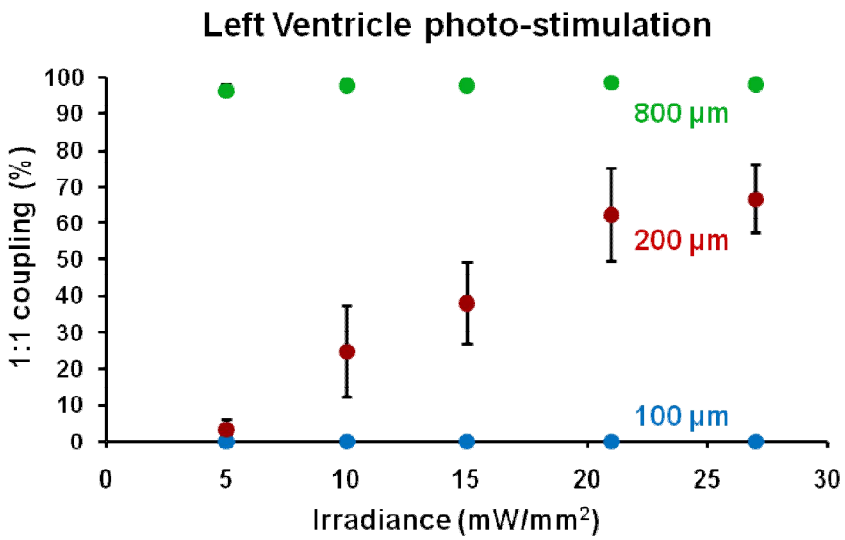

Fig. 4: Summation of in vivo epicardial stimulation data used to evaluate the minimal number of cells required to conduct an ectopic beat.

(manuscript in preparation)

Optogenetic investigation of arrhythmia triggers in CPVT

Collaborators: *Tania Zaglia, Nicola Pianca.*

1. INTRODUCTION

Optogenetics is a powerful tool that has largely been used in neuroscience and shown to allow light control of cardiac muscle [53]. We previously applied optogenetics to investigate arrhythmogenesis in a model of acute myocardial infarction and used the same model to stimulate a single group of cells in order to evaluate the critical cell mass for focal cardiac pacing [*Zaglia T., Pianca N., Borile G. et al., Appendix 1*]. This technique is expected to provide a powerful tool to investigate unresolved aspects of CPVT trigger mechanism.

Bidirectional ventricular tachycardia (BVT) is the most common arrhythmic manifestation observed in CPVT patients [42, 149]. This phenomenon has a peculiar morphology consisting in ectopic activity originated alternatively in the RV and LV. Based on experimental observation that Purkinje fibers (PFs) are more sensitive to Ca^{2+} overload if compared to working cardiomyocytes, Priori and coworkers proposed that alternative firing of right and left branches of cardiac conduction system could be responsible for BVTs [150]. In their model, BVT is the result of “ping-pong” dynamics of PF branches activation [50]. To validate this hypothesis they ablated the right portion of cardiac conduction system with intracavity Lugol injection, and the bidirectional tachycardia was converted to monomorphic VT, even though sinus rhythm could not be restored [150].

Even assuming that the initial triggers of CPVT are localized in the PFs, it is currently unclear whether the complete disease mechanism is fully explained by altered activity in the conduction system. Moreover, at the time of writing, the experiments performed to investigate the role of PFs or spontaneously firing groups of cardiomyocytes adopted indirect strategies.

To this aim we set up a protocol of BVT stimulation with optogenetics that was applied in identical conditions in WT and CPVT mice in order to understand what is the role of altered function in CPVT cardiomyocytes in sustaining and propagating arrhythmias.

2. MATERIALS AND METHODS

Histology and immunofluorescence analysis. WT and CPVT mice were humanely sacrificed, hearts were excised, emptied from blood and weighted. Hearts were then fixed with 1% PFA in 1X PBS for 15 minutes at room temperature and washed carefully after fixation, as previously described [151]. After overnight dehydration in 30% sucrose (SIGMA-Aldrich) hearts were embedded in OCT (Kaltec) and frozen in liquid nitrogen vapors. Ten microns cryosections were cut from frozen hearts using a cryostat (LEICA Mycrosystems) on the transversal direction. HE staining was performed with HE kit (Bio-Optica) following manufacturer's instructions. Immunofluorescence staining was performed as previously described [151] incubating the slices with the antibody against Dystrophin (1:200, Abcam) in 1X PBS supplemented with 5% BSA and 0.1% Tx-100. Cy3-conjugated secondary antibody (Jackson Lab.) was then used.

Telemetric recording of ECG. The ECG recording in freely moving mice required the intraperitoneal implantation of transmitters (DSI). Mice with telemeters were then positioned over the receivers (DSI).

In vivo control of cardiac function. As described in [*Zaglia T., Pianca N., Borile G. et al., Appendix 1*], mice expressing ChR2 under the transcriptional control of α-MHC promoter were generated using CRE-Lox recombination and fully characterized. The epicardial stimulation protocol consists in an open-chest anesthetized mouse model in order to deliver light directly from as LED to the heart through the differently sized optic fibers described above. The outcome of the experiments is the superficial ECG recorded with a dedicated apparatus (Powerlab 8/30, Bioamp and LabChart 7.1 software; AD Instruments) that controls also LED triggering.

3. PRELIMINARY RESULTS AND DISCUSSION

3.1 Characterization of CPVT^{R2472S} mouse model with ECG

Results obtained in heart slices experiments suggest that synchronization of Ca^{2+} dependent depolarization among neighboring cardiomyocytes can occur [1], and evidence obtained in the optogenetic experiments performed in WT mice shows that a limited number of depolarizing cells are required to trigger an ectopic beat. With these results in mind, we aimed to mimic bidirectional ventricular tachycardia using optical stimulation in CPVT hearts.

To this purpose, we generated a transgenic mouse line expressing ChR2 in hearts bearing the CPVT associated point mutation RyR2-R2474S. Mouse hearts were characterized using histology and telemetric recording of electrocardiogram (ECG). CPVT^{R2474S} mice were kept in heterozygous background because homozygous genotype is lethal (only 1 born over 200 mice, dead before weaning). Heterozygous RyR2-R2474S mice and WT littermates, HE staining, as well as immunofluorescence against dystrophin, did not show differences between the two genotypes, nor variations were observed in the heart weight to body weight ratio (fig. 1a-c).

To evaluate electrocardiographic parameters in freely moving animals, telemeters were implanted in 3 months aged male mice. During the analysis, the presence of circadian rhythms was considered, and for these reason the values reported in fig. 1 refer to the mean value of 8 nocturne hours of 2 mice per genotype from 2 different days. CPVT^{R2474S} mice had slightly reduced HR if compared to WT littermates, in agreement with previous reports in humans and mouse models [39]. Even though the origin of this difference is not clearly understood, it has been proposed to depend on SAN dysfunction. The phenotypical manifestation of BVT is initiated by adrenergic stimulation, and for this reason we adopted a well accepted protocol of NE and caffeine (2 mg/kg and 120 mg/kg, respectively) administration, that caused BVT in all CPVT^{R2474S} mice, see fig. 2, while in WT mice caused only the expected chronotropic response (increase in heart rate) without ectopic activity (not shown). In CPVT^{R2474S} mice, BVT was sustained for minutes without degenerating in ventricular fibrillation and this phenomenon was maintained for a couple of days before the syncopal event.

3.2 Optogenetic stimulation of bidirectional ventricular tachycardia

To test whether the CPVT substrate is sufficient *per se* in sustaining a bidirectional tachycardia, we set up a protocol to externally trigger BVT.

Mice expressing ChR2 at the heart level were backcrossed in the CPVT background. Via epicardial photostimulation it was possible to alternatively stimulate left and right ventricles obtaining an ECG trace very similar to that recorded with telemeters, see fig. 3, for BVT. In resting conditions, BVTs ceased with optical stimulation in both WT and $CPVT^{R2474S}$ mice.

Then, anesthetized mice were treated with NE and caffeine administration. Upon β-AR stimulation, $CPVT^{R2474S}$ mice exhibited spontaneous BVTs not triggered by epicardial photo-stimulation that were not sustained nor present in WT mice. In the same condition, in both phenotypes we recorded episodes of PVCs, bigeminy or non sustained VTs after ceasing stimulation. In WT these VTs were monomorphic while in $CPVT^{R2474S}$ hearts were bidirectional. However these phenomena, were not sustained, nor degenerated in ventricular fibrillation VF, as shown in fig. 4.

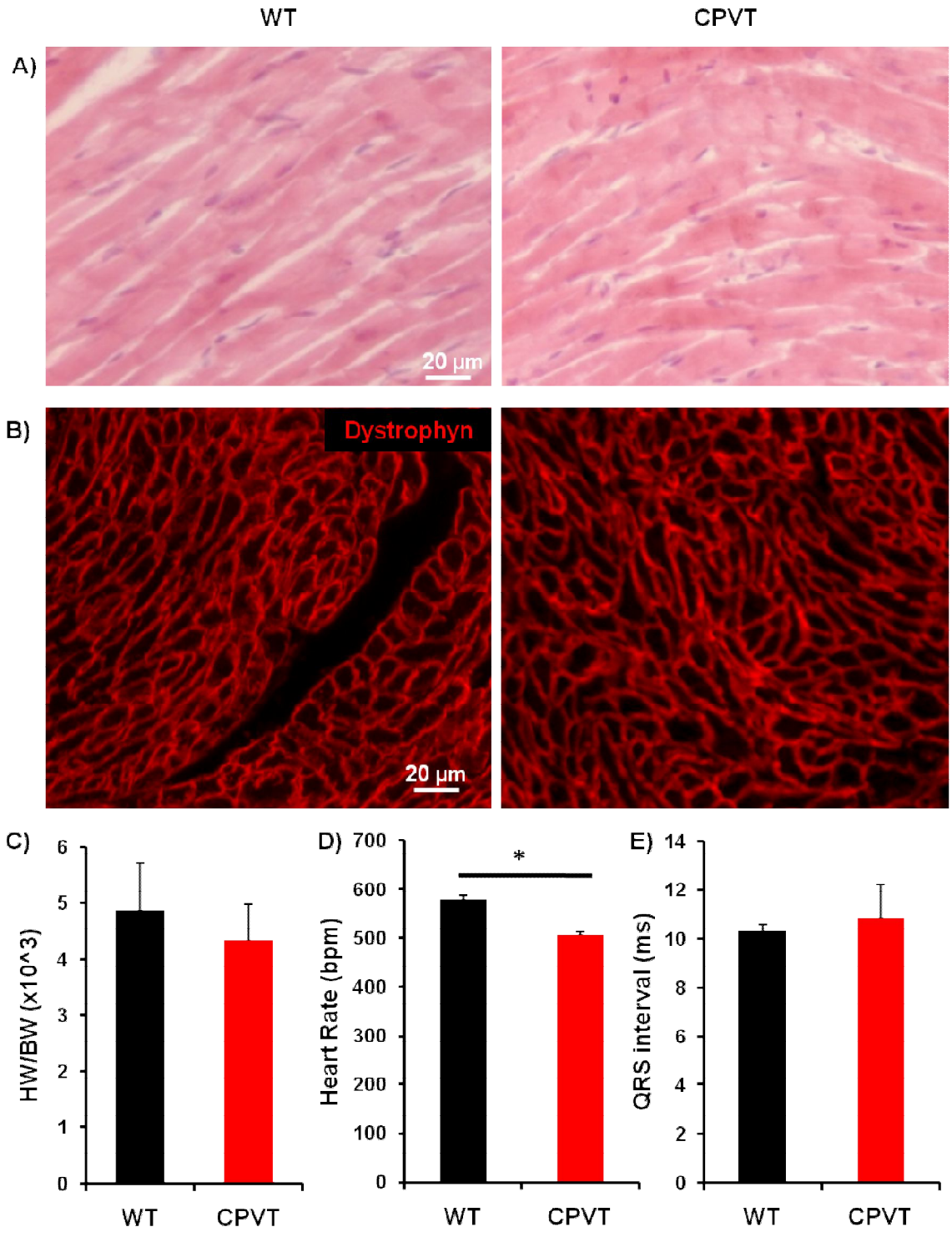

Fig. 1: A) Hematoxylin/eosin staining in CPVT^{R2474S} heart cryosections did not show morphological abnormalities if compared to WT. B) Immunofluorescence staining on WT and CPVT^{R2474S} cryosections did not show differences. C) Heart weight/body weight ratio is unaffected in CPVT mice. D-E) Telemetric recording of ECG in freely moving animals showed a slight decrease in heart frequency in CPVT^{R2474S} but no variation in QRS morphology. * means p-value < 0.05.

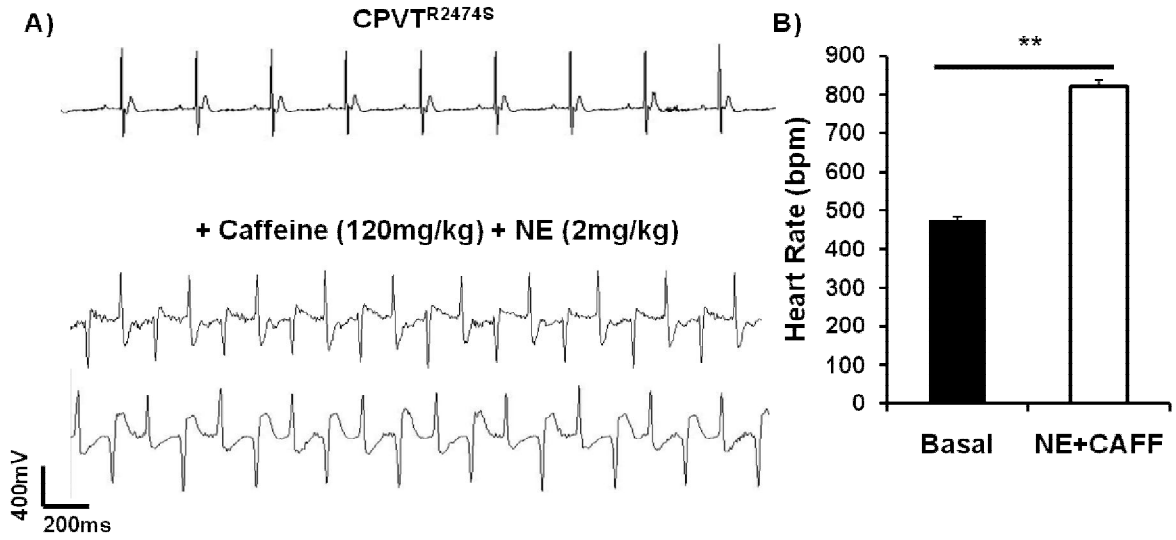

Fig. 2: Telemetric recording of ECG in freely moving mice. A) NE and caffeine administration caused a BVT in CPVT^{R2474S} mice but not in WT (not shown). B) HR almost doubled during BVT in CPVT^{R2474S} mice. ** means p-value < 0.01.

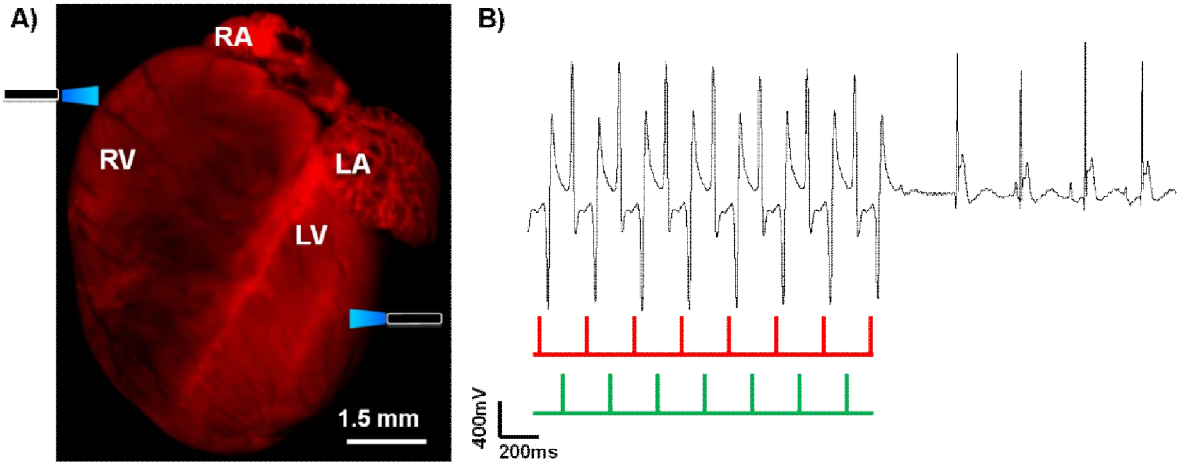

Fig. 3: Setup of a protocol to optically stimulate a BVT in ChR2 expressing mice. A) Two equally-sized optic fibers are placed on RV and LV walls, respectively and alternatively activated. B) Light pulses are indicated below the ECG trace. The ECG trace is indistinguishable from a spontaneous BVT in shape. Red is LV stimulation; green is RV stimulation.

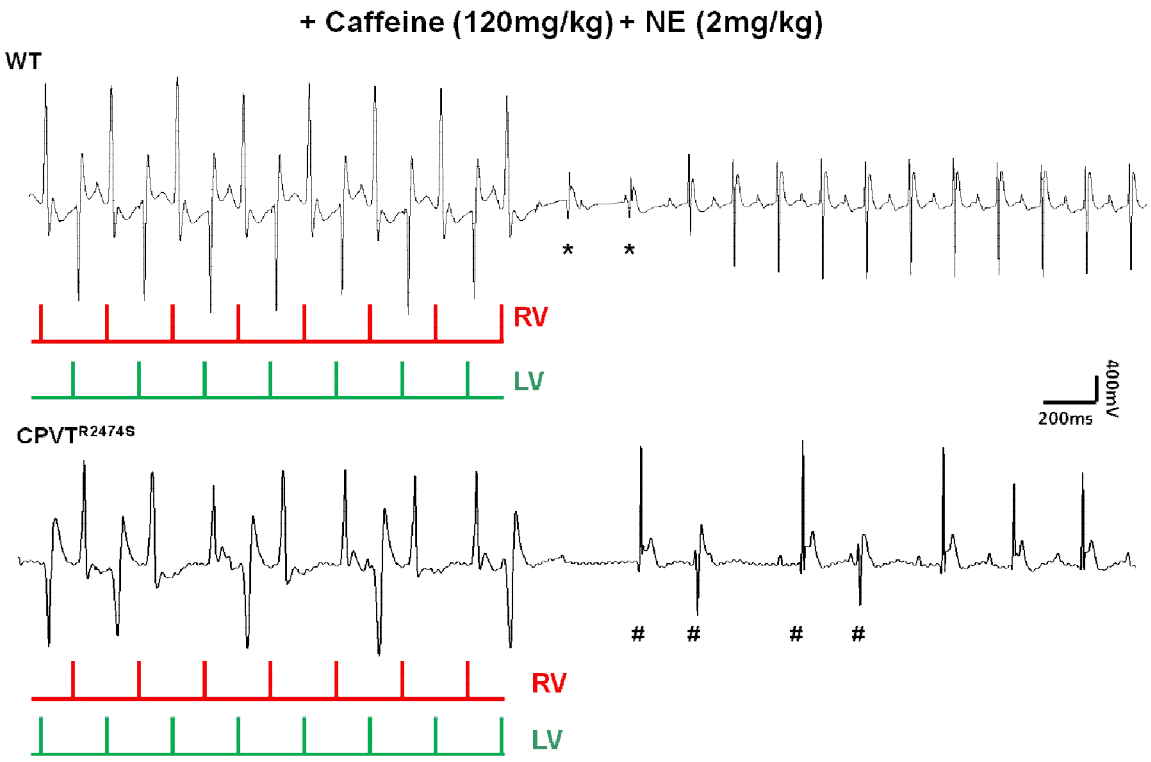

Fig. 4: Upon NE and caffeine administration the tachycardia was sustained for few beats after ceasing the optical stimulation. While WT mice presented monomorphic tachycardia (*),CPVT^{R2474S} mice showed the characteristic BVT (#). Red and green bars indicate the

3. CONCLUSIONS

The *fil rouge* of this PhD project is the study of the disease mechanisms in CPVT, a severe inherited disease causing lethal arrhythmias in young subjects, with structurally normal hearts, under stress conditions. Although the genetic defects causing CPVT have been identified, current therapies are partially ineffective in preventing life threatening arrhythmias in patients.

The need for improvement of existing technologies permeates all scientific fields and often exploits the increasing interdisciplinary methodological 'cross-contamination': examples of this include the use of techniques developed in engineering for the study of physiology, or bio-physical methods in molecular biology and medicine. The investigation performed in this PhD project experimented several different biophysical approaches to investigate CPVT mechanisms. On one hand novel experimental methods were developed or implemented, on the other mathematical models were used to fit experimental data, increasing their physiological relevance.

The characterization and optimization of a MMM was a starting point that led to the application of such microscopy setup to cardiovascular research. Moreover, even though cardiac slices are not an entirely novel experimental model, we here used this method for the first time in a transgenic mouse model of human disease. The exploitation of this multicellular model, alternative to isolated cardiomyocytes, allowed to visualize tissue wide phenomena, such as non-synchronous Ca^{2+} alternans in adjacent cells and reciprocal influence of neighboring cardiomyocytes experiencing DCRs. Furthermore, the use of cardiac slices as a testing platform for pharmaceutical trials would reduce the number of animals if compared to the same procedure in isolated hearts.

Concerning the second aim, a role for mitochondrial Ca^{2+} uptake and release in triggering and sustaining arrhythmias has been proposed, but still poorly explored. To this aim, we exploited two widely used GECIs in mitochondrial Ca^{2+} imaging experiments. This study was accompanied by the analysis of expression and constitution of the protein complexes governing mitochondrial Ca^{2+} fluxes, and other Ca^{2+} handling proteins, like SERCA2 [112], in the heart at different post-natal developmental stages. Functional and biochemical data were interpreted using modeling of mitochondrial Ca^{2+} uptake in the heart, as proposed by Lederer and coworkers [9], and the reduced I_{mcu} current in adult hearts parallels with the reduced protein content. As a parallel observation, we showed

that MCU is post-transcriptionally processed because mRNA and protein expression profiles are different in the developing heart.

In the third aim of the thesis, we combined biophysics with animal and experimental genetics, and implemented cardiac optogenetics to understand the basic tissue requirements for the generation of arrhythmogenic beats. To set the ground for these studies, we investigated light-tissue interactions to understand and characterize the photoactivating light path throughout the myocardium. While a number of studies have been performed in brain samples, much less has been done for cardiac optogenetics that is still a novel application. To this aim, we measured light transmission in fresh and frozen cardiac samples and fitted the data with two different models of light-tissue interaction that have been widely applied in neuroscience. With the evaluation of light path inside the myocardium, a geometrical model of illuminated tissue was built that was, in turn, used to determine the minimal number of cells needed to generate extrasystoles in the murine heart.

Altogether these approaches are guiding us to address unresolved questions about the tissue requirements for triggering and sustaining arrhythmias. Indeed, a cardiomyocyte experiencing a DCR influences membrane potential of adjacent CMs that in turn approach to their activation threshold. While the potent electrotonic coupling of the myocardium hampers the propagation of a depolarizing wave from a single cell to the entire heart, the number of cardiomyocytes required to trigger an arrhythmia is likely much lower than previously hypothesized. Finally, the molecular identification of the mitochondrial Ca^{2+} influx machinery would help to clarify the role of mitochondria in shaping intracellular Ca^{2+} instability, possibly acting as buffers.

4. FUTURE PERSPECTIVES

The future perspectives that arise from data obtained during this PhD project follows three main directions. First, the role of mitochondria facing increased Ca^{2+} leak in CPVT CMs has never been evaluated. Second, the contrasting mRNA and protein expression profiles of MCU in the developing heart, suggest that it undergoes post-translational modifications or degradation. Last, the investigation of tissue determinants for CPVT arrhythmogenic trigger requires the calculation of the cardiac critical mass in this background, but also the investigation of the role of Purkinje fibers separately from the working cardiomyocytes.

4.1 The role of mitochondria in CPVT

The role of mitochondrial Ca^{2+} fluxes in modulating arrhythmogenesis is not completely understood. The large majority of the studies present in the literature focus on the role of mitochondria in ischemia-reperfusion injury where $\Delta\Psi_m$ is disrupted compromising ATP production and balanced ROS generation. Excessive ROS production affects a variety of cell signaling pathways and can impair cardiac excitability by affecting the function of various channels and transporters (i.e. nitrosation or ROS-sensitive kinases).

However, much less is known about the action of mitochondria as dynamic buffers for sarcolemmal Ca^{2+} [152] and how mitochondria react to increased Ca^{2+} leak from the SR, for example in a disease model like CPVT. To elucidate this phenomenon we are going to investigate cytosolic and mitochondrial Ca^{2+} fluxes in cardiomyocytes from these mice with altered control of Ca^{2+} homeostasis.

The data reported in the last chapter of results section showed that MCU has a larger protein level in neonatal than adult hearts, hampering the extrapolation of data from NCMs to adult CMs, thus, we are currently working in order to express D3CPV and 4mt-D3CPV in adult CMs. To do so, an adeno-associated virus (AAV) coding for the sensor was injected in mice and exogenous protein expression was evaluated at least 4-6 weeks after injection, following a protocol optimized in the laboratory. A preliminary experiment of infection is shown in fig. 2 where we used AAV9-D3CPV.

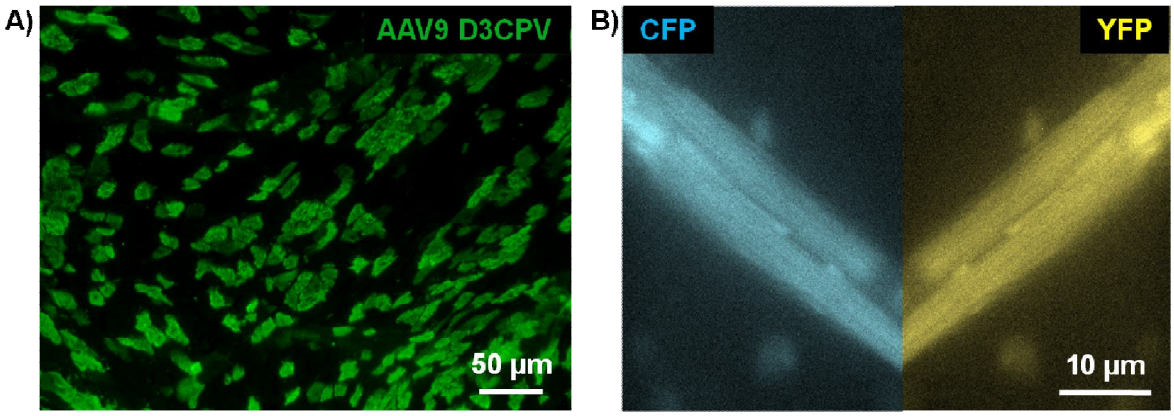

Figure 1. AAV9-D3CPV infection efficiency in mouse myocardium (A) and in an adult CM isolated from infected heart (B).

Another indication that MCU may have an active role in CPVT is the increasing evidence that uniporter activity plays a role in the heart responses to β-adrenergic stimulation [153-155].

4.2 MCU post-transcriptional regulation in heart development

In parallel, we are evaluating the different responsible for MCU post-translational modification in cardiac post-natal development. There are two main processes that can explain the discrepancy between mRNA and protein level.

On one hand MCU protein may be degraded and a possible contributor is the ubiquitin/proteasome system (UPS). Proteins to be degraded by the protesome, are labeled with at least 4 ubiquitin monomers and then translocated to the cytosolic proteasome. Whereas UPS-dependent mitochondrial protein degradation has been reported, this was observed with proteins located in the OMM, like TOM20, and only UCPs were shown to be degraded by the proteasome [156]. To test this hypothesis for MCU, we used a well established protocol [151] to test whether MCU accumulates upon proteasome inhibition with MG-132 (Merck-Millipore) in NCMs. Our experiment showed that MG-132 caused an accumulation of ubiquitinated proteins but no accumulation for MCU while TOM20, considered as positive control, significantly accumulated 24h after inhibition, as shown in figure 3.

On the other hand an unidentified miRNA can prevent MCU mRNA from being translated [157]. To explore this route, we performed bioinformatics analysis to identify the miRNAs that are predicted to target MCU mRNA. A list of more than 200 miRNAs was found using miRANDA, miRDB [158], microRNA.org [159] algorithms, among

which some are expressed also in the heart making them good candidates for MCU inhibition of translation.

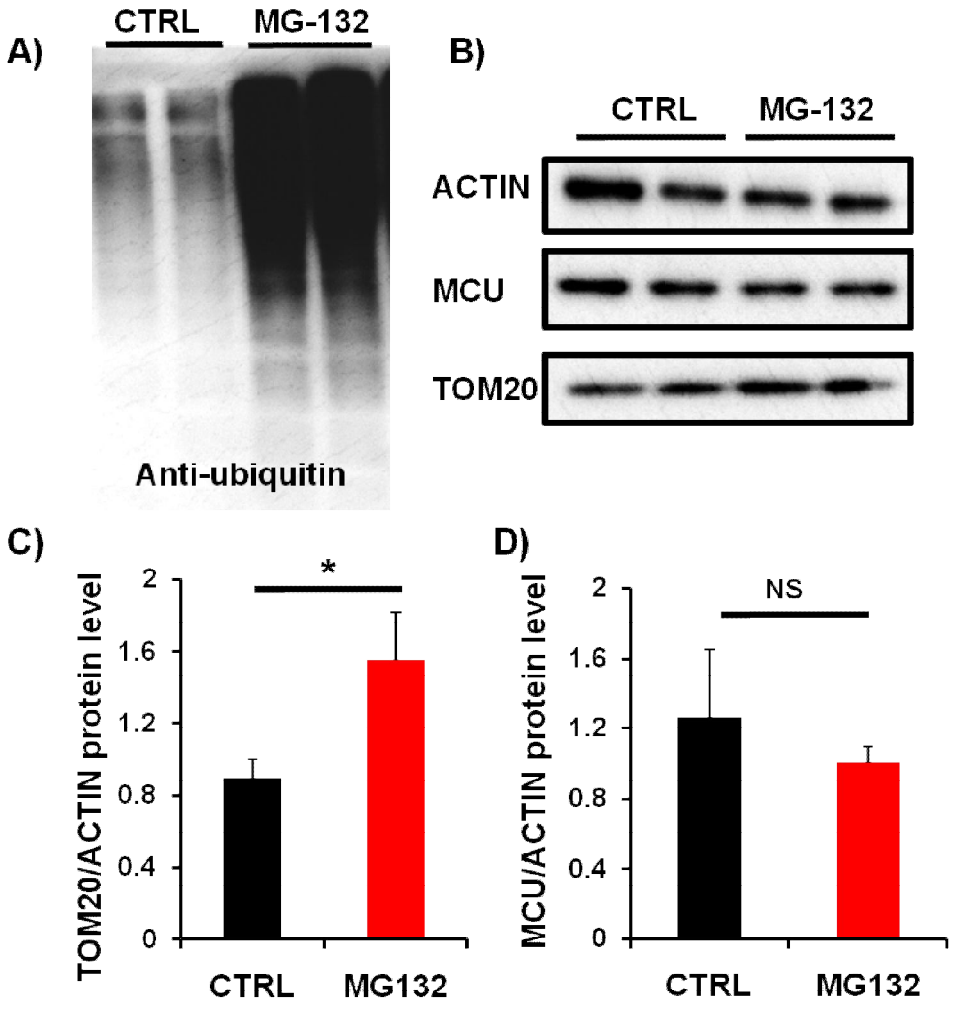

Figure 2. UPS-dependent degradation of MCU protein. A) MG-132 treatment of NCMs was effective in blocking UPS causing a massive accumulation of ubiquitinated proteins

4.3 The role of Purkinje fibers in CPVT arrhythmogenesis

The investigation of the role of PFs in CPVT has been addressed so far with indirect methods ablating cardiac conduction system with Lugol injection [150]. In this paper, the authors were able to convert BVT into monomorphic VT that was clearly monofocal. This led to hypothesis that BVT can be caused by two foci in the His-Purkinje system, one in the RV, the other in the LV, alternatively activating the ventricles. However, they could not address the mechanism by which triggered activity spontaneously generated the

peculiar pattern of BVT. Later on, a kind of ping-pong between the two branches of His-Purkinje system was modeled to investigate the mechanism of BVT [50].

Up-to-date the understanding of PFs role in BVT triggering is partial and obtained with indirect methods. To this aim we generated in the lab transgenic mice expressing ChR2 under the transcriptional control of Connexin 40 (Cx40), using CRE-lox recombination. Cx40-CRE mice were kindly provided by Prof. Miquerol, that demonstrated the specific expression of Cx40 in atria and cardiac conduction system [160, 161]. Cx40-ChR2 mice were generated in the laboratory and right branch of Purkinje fibers could be optically stimulated positioning the optic fibers on the RV epicardial surface. This epicardial optical stimulation was able to trigger ectopic beats from the RV, but not from the LV that is probably too thick to ensure light penetration. With the application of the previously described model of light-tissue interaction and considering the ramification of PFs in the RV, we could estimated that the minimum number of PFs sufficient to conduct an ectopic beat is around 100, in agreement with the model proposed by Weiss and co-workers for a mono-dimensional cable of CMs [52].

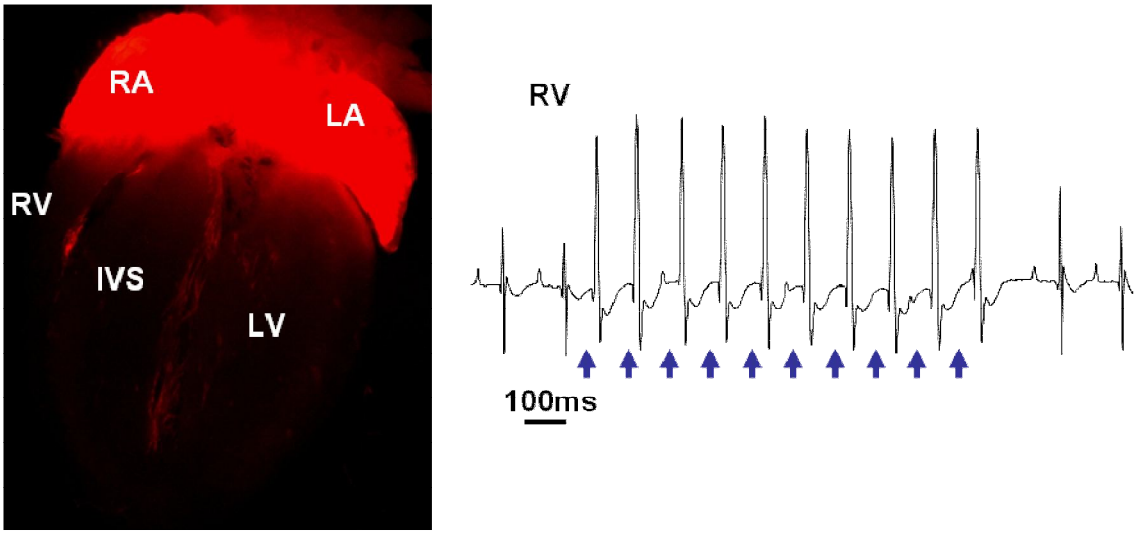

Figure 3. Cx40-ChR2 expressing mouse heart (left) and efficient photostimulation (blue arrows) from RV epicardium (right). From [*Zaglia T., Pianca N., Borile G. et al, Appendix 1*].

In parallel, triple transgenic mice Cx40-ChR2^{R2474S} have been generated and will be used to understand whether PFs stimulation is sufficient *per se* in triggering BVT in the CPVT myocardium.

5. SUPPLEMENTARY METHODS

This section collects an expanded version of the methods used during this PhD thesis, from transgenic animals used, to GECIs to live imaging techniques.

In vivo procedures

Several strains of transgenic mice were used in this work:

1. $CPVT^{R2474S}$ [41];
2. αMHC-CRE;
3. LoxP-ChR2.

Moreover, double and triple transgenic mice (αMHC-ChR2 and αMHC-ChR2-$CPVT^{R2474S}$, respectively) were obtained by cross-breeding. All experimental procedures were performed according to the European Commission guidelines and have been approved by the local ethical committee and the Italian authority (Ministero della Salute), in compliance of Italian Animal Welfare Law (Law n. 116/1992 and subsequent modifications).

The genetic identification of transgenic mice was assessed by the analysis of genomic DNA extracted from mouse tissue samples. Performing a polymerase chain reaction (PCR) it is possible to identify and amplify a sequence inserted in the murine genome that is not present in wild type mice. The adopted protocol employs a heat-stable DNA polymerase (Taq Platinum Polymerase, Life Technologies) that assembles a new DNA strand from single nucleotides using single-stranded DNA as a template and specific primers to initiate the synthesis.

DNA extraction from mouse tissue

DNA extraction and purification were performed following the instructions of the Genomic prep kit purchased by Sigma-Aldrich. A small sample of mouse tail or tissue was digested in 180 µL of Lysis Solution T supplemented with 20 µl of Proteinase K (20 mg/ml) for 4 hours at 56°C. Lysis Solution C in ratio 1:1 was added and tissue was incubated at 70°C for 10 minutes at 1000 rpm.

In the meanwhile, 500 µL of Column Preparation Solution were added to each pre-assembled GenElute Miniprep Binding Column and centrifuged at 12000 × *g* for 1 minute.

To ensure the binding of the DNA to the column, 200 µL of ethanol 100% (EtOH, Sigma-Aldrich) were added to the lysate and mixed thoroughly to obtain a homogeneous solution. The obtained lysate was transferred into the treated binding column. Binding of the DNA to the column was ensured by a centrifugation at 10000 × *g* for 1 minute.

Three steps of washing allowed to purify the extracted DNA. In the first step, 500 µL of Wash Solution were added to the binding column and centrifuged for 1 minute 10000 × *g*. Then, another 500 µL of Wash Solution were added and centrifuged for 3 minutes at maximum speed (12000 × *g*) to dry the binding column. The column was then spun for 1 additional minute at maximum speed to completely remove residual ethanol. To elute the DNA, 40 µL of the Elution Solution were pipetted directly into the centre of the binding column; after an incubation for 5 minutes at room temperature, the column was centrifuged for 1 minute at 10000 × *g* to elute the DNA.

DNA quantification was performed using a spectrophotometer (NanoDrop, Thermo Scientific) that calculates the concentration of nucleic acids measuring the amount of UV absorbed light, i.e. the optical density (OD) of the samples. The typical concentration obtained with this method is around 150 ng/µl with a high level of purity evaluated by the ratio OD_{260}/OD_{280} around 1.8.

CPVT^{R2474S}

The used primers are the following:

5′-GCTGTCCTGGAACTGACTTGTA-3′

5′-ACCCTGTGAGGCAGATAGTGC-3′.

CPVT^{R2474S}

Component	Quantity
H_2O sterile	37.4 µl
Buffer 10X	5 µl
$MgCl_2$	3 µl
RyR Fw (10 µM)	2.5 µl
RyR ReV (10 µM)	0.5 µl
dNTPs (10 mM)	0.4 µl
Platinum Taq	0.2 µl
DNA	1 µl

Table 1. Mix for R2474S genotyping.

The PCR was performed in a Thermal cycler (GenePro, BIOER).

PCR Program:

94 °C	4 min
94 °C	30 sec
65 °C	30 sec
72 °C	1 min
Repeat 38 cycles	
72 °C	3 min
4 °C	on hold

The PCR product of 819 bp was purified using the GenElute Gel Extraction kit provided by SIGMA-Aldrich, following a protocol similar to that described for genomic DNA purification. Finally, the PCR product was eluted in 30 µL of DNase-free H_2O.
Approximately 1 µg of purified PCR product was digested with BstZ17I (NewEngland Biolabs) for 2 hours at 37°C, with the mix reported in table 2.

CPVT^{R2474S} Digestion mix

Component	Quantity
H_2O sterile	14 µl
NEB 4 10X	5 µl
BSA 10X	5 µl
Bstz17I	1 µl
PCR product	25 µl

Table 2. R2472S digestion mix.

The digestion results in 2 specific bands at 506 bp and 313 bp from the mutant allele while the WT allele is not cut.

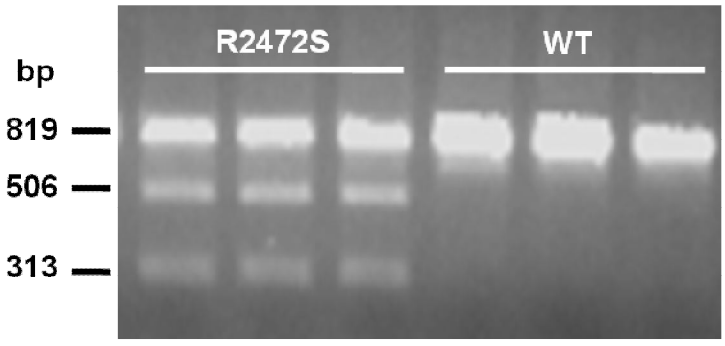

Figure 1. Digestion products of R2474S and WT mice.

αMHC-CRE

The used primers are the following:

5′- GAACCTGATGGACATGTTCAGG - 3′

5′- AGTGCGTTCGAACGCTAGAGCCTGT - 3′.

αMHC-CRE

Component	Quantity
H_2O sterile	19.2 µl
Buffer 10X	2.5 µl
$MgCl_2$	1.5 µl
CRE Fw (10 µM)	0.25 µl
CRE ReV (10 µM)	0.25 µl
dNTPs (10 mM)	0.2 µl
Platinum Taq	0.1 µl
DNA	1 µl

Table 3. Mix for CRE genotyping.

PCR Program:

94 °C	4 min
94 °C	30 sec
62 °C	30 sec
72 °C	1 min

Repeat 35 cycles

72 °C	10 min
4 °C	on hold

A band at 300 bp will be present in animals carrying the CRE gene.

LoXP-ChR2

The primers used were the following:

5’ - AAG GGA GCT GCA GTG GAG TA – 3’	Wild type Forward
5’ - CCG AAA ATC TGT GGG AAG TC – 3’	Wild type Reverse
5’ - GGC ATT AAA GCA GCG TAT CC – 3’	Mutant Reverse
5’ - CTG TTC CTG TAC GGC ATG G – 3’	Mutant Forward

LoXP-ChR2

Component	Quantity
H_2O sterile	19.2 µl
Buffer 10X	2.5 µl
$MgCl_2$	1.5 µl
Fwd (10 µM)	0.25 µl
ReV (10 µM)	0.25 µl
dNTPs (10 mM)	0.2 µl
Platinum Taq	0.1 µl
DNA	1 µl

Table 4. LoXP-ChR2 genotyping mix.

PCR Program:

94° C	4 min
94°C	30 sec
61°C	30 sec
72°C	45 sec

Repeat 35 cycles

72°C	5 min
4°C	on hold

Two separate PCRs were performed, one for each primers pair, while the mix and the program used are the same. The expected result is a band at 300 bp for positive DNA, that means a band in each reaction for heterozygous mice, a band only with the WT primers for WT mice and a band only with mutant primers for homozygous mice.

Electrocardiography in mice

Electrocardiography (ECG) is the recording of cardiac electrical activity. It records the electrical pulses of polarization and depolarization of the heart and translate them into a waveform. The typical ECG trace consists of a P wave that reflects atria depolarization and a QRS complex that reflects the depolarization of right and left ventricles. Many important parameters can be evaluated with this technique, in particular the heart rate (in beats per minute) and the QRS duration. The amplitude and the shape of this latter parameter is indicative of the origin of the depolarizing wave, that means it is possible to discriminate from a QRS originating from RV or LV.

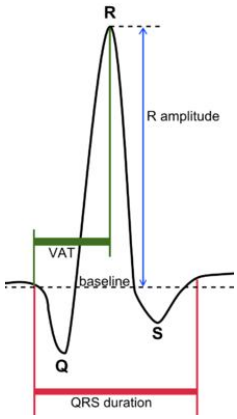

Figure 2. QRS complex

This experimental procedure can be performed in both anesthetized and freely moving mice. In the first condition, animals were anesthetized with Avertin 2.5% (intra-peritoneal injection, 400 mg/kg) and a standard lead I ECG was recorded (Powerlab 8/30, Bioamp; AD Instruments). The ECG recording in freely moving mice required the intraperitoneal implantation of transmitters (DSI). To record ECG activity, mice with telemeters were positioned over the receivers (DSI). In both cases, offline data analysis was performed with LabChart Software 7 (AD Instruments).

Morphological analysis on fixed samples

Mice were sacrificed by cervical dislocation and hearts were quickly harvested and cut in two portions in the transverse direction. Blood clots were carefully removed as well as excess of vessels, then hearts were weighted with a precision balance. If necessary the lower portion of the heart was immediately frozen in liquid nitrogen to perform biochemical analysis, while for histological analysis the upper portion of the heart was

fixed to maintain structural integrity with 1% paraformaldehyde in phosphate buffered saline (PBS 1X: 137 NaCl, 2.7 KCl, 10 Na_2HPO_4, 1.8 KH_2PO_4, in mM) at room temperature for 15 minutes. After 3 washes of 5 minutes with PBS 1X, hearts were allowed to dehydrate in sucrose 30% (w/v in distilled water) at 4°C overnight. The following day, hearts were embedded in OCT freezing medium (Optimal Cutting Temperature, Kaltec) and carefully frozen in liquid nitrogen vapor. Frozen samples were maintained at -80°C.

Immunofluorescence staining on tissue samples

Frozen hearts were cut in 10 µm slices using a cryostat (LEICA CM1850) and placed on superfrost glass slides (Vetrotecnica) maintained at -80°C until use.

The day of immunofluorescence staining, slides with cryosections were allowed to equilibrate at room temperature for 10 minutes. Then slices were encircled with DAKO Pen (DAKO) and rehydrated for 10 minutes in PBS 1X. After rehydration, sections were incubated with the primary antibody diluted in PBS 1X supplemented with 1% BSA and 0.5% Triton-X. The incubation was performed overnight at 4°C in a humidified chamber to prevent samples drying.

The following day, slices were washed 3 times with PBS 1X before incubation with the secondary antibody that was performed at 37°C for 30 minutes, diluting the antibody in PBS 1X supplemented with 1% BSA. Three additional washes were performed at the end of the staining, before mounting the slides with the mounting medium (elvanol).

Haematoxylin and eosin staining

Haematoxylin-eosin (HE) staining on cryosections is a standard histological protocol to evaluate tissue morphology. Heart cryosections, after a re-equilibration period at room temperature, were stained with the HE kit (Bio-Optica) following manufacturer's instructions. Briefly, after a 30 seconds treatment with hematoxylin, cryosections were washed to remove the excess of reagent, then 10 seconds in the toning solution allowed hematoxylin to reach its blue-violet coloration. Three additional washes were performed before incubation with eosin that was maintained for 1 minute. Washout of the excess reagent was carefully performed, then slices were dehydrated in 2 steps: 95% EtOH for 5 seconds, 100% EtOH for 2 minutes and 100% xylene for 5 minutes. Final mounting was perfomed with Eukitt (SIGMA-Aldrich), a mounting medium based on xylene.

Confocal Microscopy

To acquire immunofluorescence staining with high contrast and resolution a confocal microscope (Leica TCS SP5) was used. In this set up a laser is deflected on the specimen with a raster pattern. In order to collect only the fluorescence coming from the focal point a pinhole is positioned just before the detection system. The pinhole can physically block light coming from outside the focal plane. The microscope is equipped with four different lines of lasers (405 nm, 488 nm, 561 nm and 633 nm) combined with a set of emission filters.

Cell Culture

Neonatal Cardiomyocytes Culture

Neonatal cardiomyocyte (NCM) culture is a well establish cellular method to investigate signaling pathways and ion homeostasis in cardiac cells.

Neonatal cardiomyocytes were prepared from newborn (P1-P3) rat hearts. Rats were sacrificed by cervical dislocation and hearts quickly removed. Atria were carefully excised, then ventricles were collected in a 50 mL tube half-filled with ice-cold ADS buffer (see table 5).

Under a sterile hood, ventricles were washed to remove excess of blood then minced in a 10 cm petri dish, placed on ice, in 5 mL of ADS in order to obtain heart fragments around 1 mm^3. Ventricles mechanically minced were then transferred to a 50 mL sterile tube with a 5 mm magnetic stir bar. ADS Buffer was completely removed and replaced with 6 mL of Digestion Buffer (see table 6) and positioned on a magnetic stirrer inside a water-bath at 37°C. The first cycle of 10 minutes allows to remove damaged cells so the supernatant was discarded at the end of this time. Another 6 mL of Digestion Buffer were added to the heart pieces for 20 minutes always at 37°C on a stirrer. The supernatant of this cycle was then transferred to a 15 mL tube containing 1 mL of Horse Serum in order to block the enzymatic activity then centrifuged at 1500g for 5 minutes. The supernatant was removed and cells were resuspended in 2.5 mL of First Day Medium (see table 7) and maintained in the incubator until the digestion cycles were completed.

Non digested heart pieces repeated the digestion step previously described; usually a total of 5-6 cycles are required to complete the enzymatic digestion of 10 hearts. At the end of the digestion cycles, isolated cells from the different cycles were mixed and seeded in a 10 cm tissue culture dish (BD Falcon) and maintained in the incubator at 37°C for 1 hour.

This step is named “pre-plating” and allows to separate cardiomyocytes from cardiac fibroblasts that are characterized by faster adhesion to the dish. After the pre-plating step, cells in suspension were collected in a new 50 mL tube. The total number of cells obtained was determined diluting cells in 0.2% Trypan Blue and counting viable cells in a Bürker chamber. Cardiomyocytes were then plated on laminin coated glass coverslips (1.8 µg/100 mm^2) at a density of 470 cells/mm^2 for live imaging and immunofluorescence analysis while for protein and RNA extraction the density was raised to 550 cells/mm^2. Twenty-four hours after plating, the medium was removed, cells washed twice with ADS Buffer, to remove dead cells, and incubated with Second Day Medium (see table 7).

ADS Buffer

Component	Concentration
NaCl	106 mM
Hepes	20 mM
Na_2HPO_4	0.8 mM
KCl	5.3 mM
$MgSO_4 \cdot 7H_2O$	0.4 mM
Glucose	5 mM
	pH 7.4

Table 5. ADS buffer for NCMs. Sterilized by 0.22 µm filtration.

Digestion Buffer

Component	Concentration
Collagenase A (Roche)	0.45 mg/mL
Pancreatin (SIGMA-Aldrich)	1.2 mg/mL
	in ADS Buffer

Table 6. Digestion buffer. Sterilized by 0.22 µm filtration.

First Day Medium

Component	Concentration
MEM	88.8%
Fetal Bovine Serum (FBS, Gibco)	10%
Non-essential Amino Acids (NEAA, Gibco)	0.1%
Penicillin/Streptomycin (P/S, Gibco)	1%
BrDU (100 µM in DMSO, SIGMA-Aldrich)	0.1%

Second Day Medium

Component	Concentration
MEM	98.8%
Insulin-Transferrin-Selenite (ITS, Gibco)	0.1%
Non-essential Amino Acids (NEAA, Gibco)	0.1%
Penicillin/Streptomycin (P/S, Gibco)	1%

Table 7. NCMs culture media. Sterilized by 0.22 µm filtration.

HEK-293T cell line

HEK-293T cell line is commonly used because these cells grow rapidly and do not suffer genetic manipulation, such as transfection and viral infection. For this reason these cells were used to test plasmids and viral vectors. HEK-293T cells were maintained in Standard Medium in T25 or T75 flasks (Corning) and split around 80% confluence. Before cells splitting, culture medium was removed and cells were washed twice with PBS 1X to eliminate dead cells and serum. Then 1 mL of 0.25% Trypsin with EDTA was added and incubated for 3 minutes at 37°C. Trypsinization was blocked adding 3 mL of Standard Medium (table 8). Cells in suspension were spun at 1250 rpm for 5 minutes and resuspended in fresh medium. For cell line expansion, a dilution 1:10 was plated in a T75 flask, whereas for experiments cells were seeded at a density around 125 cells/mm^2.

Standard Medium

Component	Concentration
DMEM	89%
FBS	10%
Pen/Strep (100X)	1%

Table 8. HEK-293T culture medium.

Immunofluorescence analysis on cultured cells

Cells seeded on coverslips were fixed with formaldehyde 3.7% in PBS (v/v, SIGMA-Aldrich) for 30 minutes at 4°C and washed 3 times for 10 minutes in PBS 1X. As first step, cells were permeabilized with PBS 1X supplemented with BSA 1% and Triton-X 0.1% for 5 minutes at room temperature, then washed 3 times with PBS 1X for 5 minutes. Cells were then incubated with the primary antibody (or antibodies if multiple staining is required) in PBS 1X-BSA 1% for 2 hours at 37°C in a humidified chamber. At the end of the incubation with the primary antibody, cells were washed 3 times for 5 minutes, then incubated with the secondary antibody in PBS 1X-BSA 1% for 30 minutes at 37°C. If 2 secondary antibodies were required, this last step was repeated using the other secondary antibody. The sequence was decided in order to reduce the risk of cross-reactivity between the secondary antibodies. When secondary antibodies incubation was concluded, cells were washed 3 times with PBS 1X for 5 minutes. Then nuclei were stained with DAPI (1:5000, v/v in PBS 1X) for 5 minutes at room temperature. Finally, the coverslips were mounted with elvanol over a glass slide (Vetrotecnica).

Molecular Biology

For this PhD thesis, several plasmids encoding Ca^{2+} sensors were used (tables 9 and 10).

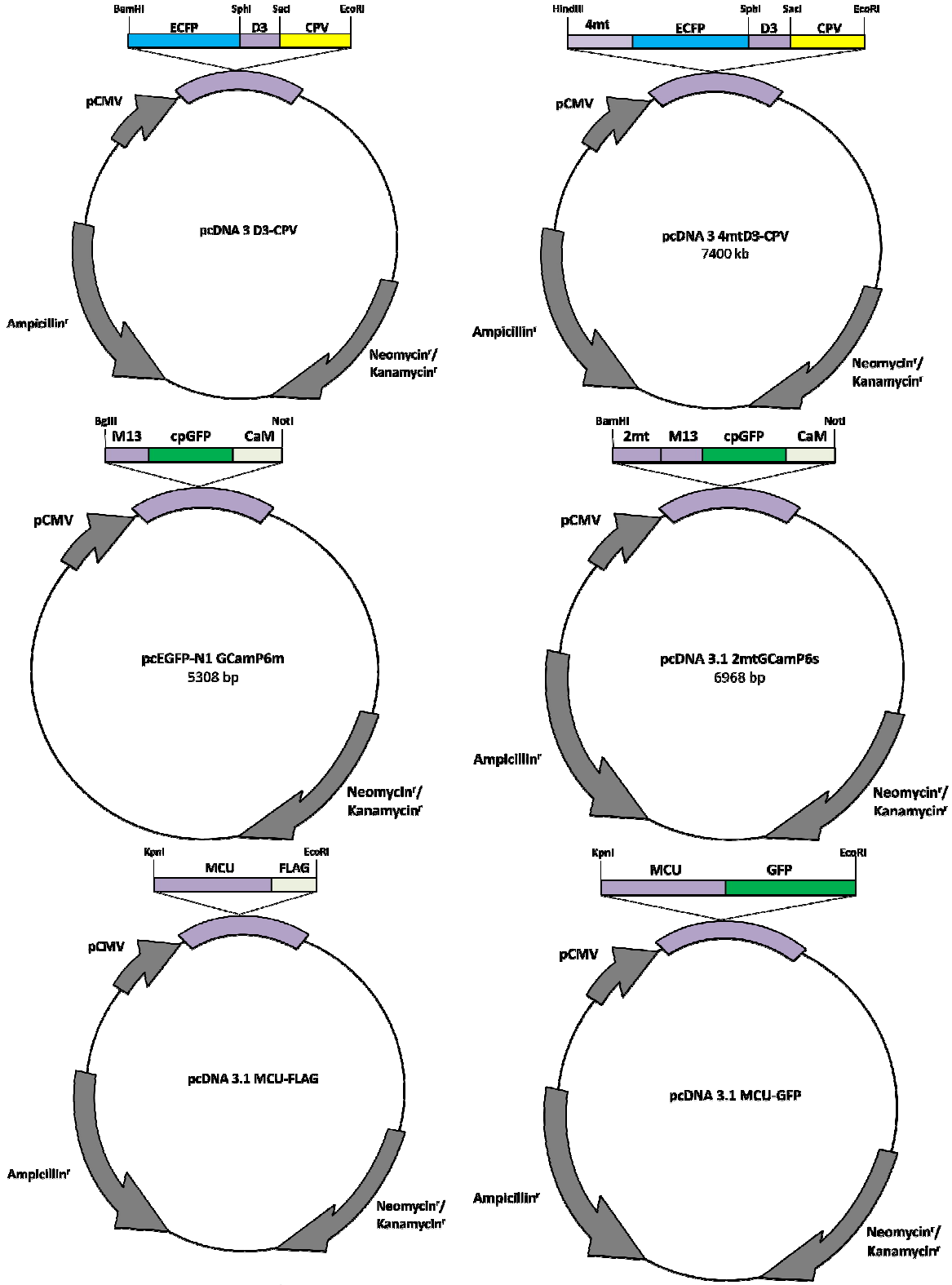

Table 9. Schematic representation of used plasmids.

Plasmids used in this thesis

Plasmid name	Function and employment
D3-CPV[1]	Ratiometric cytosolic Ca^{2+} measurement
4mt D3-CPV[1]	Ratiometric mitochondrial Ca^{2+} measurement
GCaMP6m[2]	cytosolic Ca^{2+} measurement
2mt GCaMP6s[2]	mitochondrial Ca^{2+} measurement
MCU-FLAG[2]	Overexpression of MCU protein
MCU-GFP[2]	Expression of MCU protein

Table 10. Table of used plasmids and their application.

Ca^{2+} sensors of the Cameoleon family were kindly provided by Prof. Tullio Pozzan. GCaMP sensors, as well as MCU plasmids were kindly provided by Prof. Rosario Rizzuto.

Transformation of competent TOP10 E. coli

Transformation is the process by which foreign DNA is introduced into the bacteria in order to store and replicate the desired plasmids. All the plasmids carry both the bacterial origin of replication, in order to expand the plasmid, and an antibiotic resistance sequence in order to select the bacteria carrying the plasmid.

To expand the plasmids used in the PhD thesis I used chemically competent TOP 10 E.coli purchased by Life Technologies and stored in aliquots at -80°C until use. The transformation protocol is the standard heat-shock transformation protocol for this kind of bacteria. 50 µL of bacteria were transformed with 50 ng of DNA and maintained in ice for 30 min. The heat shock was performed putting the bacteria at 42°C for 30 seconds and the left in ice for 2 minutes.

LB without antibiotic was added to the bacteria up to a volume of 500 µL and incubated at 37°C for 1 hour. Half of the bacteria were then plated on LB agar plates with the proper antibiotic and let grow overnight at 37°C.

[1] Kind gift of Prof. Pozzan, Department of Biomedical Sciences, CNR Neuroscience Institute, University of Padova and Venetian Institute of Molecular Medicine, Padova, Italy.

[2] Kind gift of Prof. Rizzuto, Department of Biomedical Sciences, CNR Neuroscience Institute, University of Padova, Italy.

DNA extraction using Maxi prep kit

Bacteria transformed with the desired plasmids were grown on the LB agar plate, then, DNA amplification, extraction and purification were performed following the instructions of the Maxi prep kit purchased by Sigma-Aldrich. A single bacterial colony selected from the LB agar plate was pick up and let grow in 3mL of LB supplemented with the antibiotic for 8 hours at 37°C in agitation (Gallenkamp at 180 rpm). The obtained bacteria suspension was diluted in a ratio 1:1000 in 150 mL LB medium and incubated overnight at 37°C in agitation (180 rpm). The next day bacteria were chilled in ice and pelleted in 3 different 50 mL tubes at 4000g at 4°C.

The bacteria pellets were then resuspended in 12 mL of Resuspension solution. An equal volume of Lysis solution was added to the suspension inverting the tube 8 times to obtain an homogeneous mixture and allowed to clear for few minutes.

Then 12 mL of Neutralization solution were added to the suspension, inverting 8 times. In order to optimize the binding of the DNA to the column, the suspension was supplemented with 9 mL of binding solution and added to the barrel of the filter syringe, then let sit for 5 minutes. In the meanwhile, the binding column was activated with 12 mL of Column Preparation solution and centrifuged for 2 minutes at 3000g in order to discard the flow-through.

The cleared lysate was then filtered through the syringe to the binding column. After a centrifugation at 3000g for 2 minutes the DNA is linked to the column membrane. Two subsequent steps of wash solution allow to clean the DNA, then an additional centrifugation at 300g for 5 minutes allow to completely remove the residual ethanol present in the column after the washing steps.

Finally the column was transferred to a new collection tube and the DNA was eluted in 3 mL of Elution Solution and centrifuges at 3000g for 5 minutes. The eluted DNA was quantified with the spectrophotometer. The typical concentration range is 250-400 ng/µl. The DNA was then divided in aliquots stored at -20°C until use.

Plasmid transfection in cell lines and cardiomyocytes

Transfection is a process that allows to introduce an exogenous sequence of DNA into the cell. The method used for cell lines and cardiomyocytes takes advantage of liposomes which fuse with the external membrane and let the DNA enter inside the cell. This leads to a transient perturbation of the plasma membrane, so the adequate transfection protocol must be adapted to the specific target cell type.

HEK-293T cells and NCMs underwent different transfection protocol.

HEK-293T cells were seeded with a density of 100 cells/mm^2 in a 6-well plate (BD Falcon) the day before transfection. The day of transfection, two mix were prepared in separated polystyrene tubes following manufacturer's instructions: 5 µL of Lipofectamine (Life Technologies) were diluted in 245 µL of M199 (Life Technologies) and 3 µg of DNA were diluted in a total volume of 250 µL (quantities reported refer to a single well). Dilutions were left for 5 minutes at room temperature and then mixed together for additional 20 minutes always at room temperature. In the meanwhile, HEK were washed twice with PBS 1X and maintained in 500 µL of M199. Finally, 500 µL of the previously prepared mixture of transfection were added to the cells and left in the incubator for 5 hours. At the end of this incubation period, transfection solution was replaced with standard culture medium. With this protocol usually HEK cells expressing the exogenous plasmid were more than the 80%.

NCMs are more sensitive to liposomal transfection so both the quantities and the timing were modified and set up in the lab.

Transfection was performed the day of culture preparation. Before seeding the cells, two solutions were prepared in polystyrene tubes. One solution contains Lipofectamine (2µL + 73µl of OptiMEM), the other contains the DNA (2 µg in 75 µL of OptiMEM). As for cell lines, the 2 solutions were left for 5 minutes at room temperature, then put together for additional 20 minutes. After this period, 150 µL of the mixture were laid on coated 24 mm coverslips and left for additional 20 minutes. Finally cells were seeded over this mixture in their medium and left overnight to allow adhesion. The day after cells were washed twice and 1st day medium was replaced with 2nd day medium.

Usually with this protocol the percentage of transfected cells is not as elevated as for HEK cells, however for single cell imaging, which is the main application of transient transfection in this work, the result was adequate.

Adenoviral infection in cell lines and cardiomyocytes

Transient transfection with Lipofectamine reaches a percentage of transfected cells that is extremely variable among different cell types. An alternative method to achieve DNA manipulation consists in viral infection. Cultured cells were infected with adenoviral vectors (serotype 5) coding for the protein of interest 24 hours after plating. We used a multiplicity of infection (MOI) set to 5 based on preliminary experiments performed in the laboratory. Viral vectors were diluted in culture medium and removed after 24 hours.

The viral vectors used were Ad-MCU-FLAG (obtained starting from the plasmid) and Ad-Empty, consisting in the viral vector without coding DNA, used as control. Both viruses were provided by Vector Biolabs.

RT-qPCR

To evaluate the mRNA expression levels of different genes, RT-qPCR analysis was performed.

RNA isolation from both frozen tissue and cultured cells was performed using the SV total RNA isolation kit (Promega, Z3100) accordingly to the manufacturer's instructions.

Frozen tissue pieces of approximately the same size were immerged in 175 µl of RNA Lysis Buffer, previously supplemented with β-mercaptoethanol, and homogenized using Tissue Lyser (Qiagen) at 30 Hz for 1 minute. 350 µL of RNA dilution Buffer were then added and mixed by inverting the tube few times. The tubes were centrifuged for 10 minutes, to remove undesired material, and the cleared lysate was transferred into a new tube. To optimize the binding of the RNA to the column, 200 µL of 95% Ethanol were added, mixed thoroughly and transferred to the Spin Basket Assembly. A centrifugation of 1 minute allowed the binding to the column, then a passage with 600 µL of RNA Wash Solution was performed. To obtain a pure extraction of RNA, 50 µL of DNase incubation mix were added to the membrane and incubated for 15 minutes at room temperature. To stop the enzyme, 200 µL of DNase Stop Solution were addend and the column centrifuged for 1 minute in order to discard the flow-through. An additional wash was then performed. To elute the RNA, 70 µL of RNase-Free Water were added to the membrane. After 1 minute of centrifugation the RNA is collected in the tube.

The RNA extracted was quantified using the NanoDrop (ThermoScientific), as described for DNA. RNA purification, quantification and retro-transcription were performed on the same day in order to minimize the RNA degradation.

Single-strand cDNA was synthesized following manufacturer's instruction for SuperScript III (Life Technologies). The retro-transcription "preparation mix" was prepared for each sample and put in autoclaved 0.2 µL tubes, as follows:

Retro-transcription "preparation mix"

Component	Concentration
RNA	400 ng in 11.5 µL H_2O
dNTPs (10mM)	1 µL
Random Primers mix (3µg/µL)	1 µL

Table 9. Retro-transcription preparation mix.

After an incubation at 65°C for 5 minutes the samples were left in ice of 2 minutes then spin down.

Another mix containing the enzyme used to perform the retro-transcription was prepared than added to the "preparation mix" as follows:

Retro-transcription "final mix"

Component	Concentration
"preparation mix"	13.5 µL
Buffer (5X)	4 µL
DTT (1M)	1 µL
RNase out	1 µL
Reverse Transcriptase	0.5 µL
RNase-free H_2O	30 µL

Table 10. Retro-transcription final mix.

The program set in the Thermocycler to perform the retro-transcription consisted in 2 steps:

25 °C	5 min
50 °C	60 min
70 °C	15 min

RT-qPCR analysis was performed using a C1000 Thermal Cycler BioRad coupled with a GeneAmp 7500 Sequence Detection System by Nicola Pianca (PhD Student).

To evaluate differences in gene expression, the relative quantification using the ΔΔct method was adopted, normalizing to the internal reference of TOM20. The reference gene adopted was selected among those used in the literature selecting the more stable in our experimental conditions. Gene specific primer pairs were designed by Nicola Pianca using Prime3 software and are listed below.

RT-qPCR primers	
Primer name	**Sequence**
TOM20 mouse FWD	5'-AGCTGGGCTTTCCAAGTTACC-3'
TOM20 mouse REV	5'-GGTCCACACCCTTCTCGTAG-3'
MCU mouse FWD	5'-TTGTGCCCTCTGATGACGTG-3'
MCU mouse REV	5'-CAAAGTCCCAGGCAGTTTCT-3'
MICU1 mouse FWD	5'-GTCGAACTCTCGGACCATGT-3'
MICU1 mouse REV	5'-CAAAGTCCCAGGCAGTTTCT-3'
MICU2 mouse FWD	5'-GGTGTCGGCGCAGAAAAAT-3'
MICU2 mouse REV	5'-AAGAGGAAGTCTCGGGGTGT-3'
MCUb mouse FWD	5'-AGTTACCTTCTTCCTGTCGTTTGCG-3'
MCUb mouse REV	5'-CAGGGATTCTGTAGCCTCAGCAAGG-3'

Table 11. Primers used for RT-qPCR analysis.

WB analysis

Western Blotting is a technique for protein analysis. The specific interaction of the antibody with the antigen sequence allows to identify the target protein in a complex protein ensemble.

WB analysis were performed on tissues extracts from mice and rats as well as from NCMs.

Protein extraction

Tissues from mice and rats were frozen in liquid nitrogen immediately after removal from the animals. Frozen tissue pieces of approximately the same size were immerged in 400 µl of RIPA BUFFER (see table 12) and homogenized using Tissue Lyser (Qiagen) at 30 Hz for 1 minute. Tissue lysates were incubated for 1h at 4°C then centrifuged at 12000 rpm (10000g) for 15 min at 4°C. Pellet was discarded and the supernatants were collected in new 1.5 mL tubes, then denaturated in a thermo mixer (10 min. at 70°C and 1250 rpm). Protein quantification were performed using the Bradford assay subsequently validated with a blue coomassie staining. Protein extracts were then aliquoted and stored at -80°C.

To obtain protein extracts from cells, NCMs were washed with cold PBS 1X then incubated with 150 µL of RIPA BUFFER for 1 minute. Cells were scraped from the plate and lysates were collected in 1.5 mL tubes. To complete protein extraction the subsequent steps were the same as for tissue lysates.

RIPA BUFFER

Component	Concentration
Tris Base	65 mM
NaCl	150 mM
Sodium Deoxycholate	0.025%
NP-40	1%
EDTA	1 mM
Anti-phosphatases (Roche)	5X
Anti-proteases (Roche)	50X

Table 12. RIPA buffer used for protein extraction from cells and tissue samples.

SDS-PAGE

The electrophoresis is used to separate molecules of different molecular weights. To this purpose, 20 µg to 60 µg of protein extracts were prepared in Loading Buffer (table 13) and denaturated at 70°C and 1250 rpm for 10 min. Electrophoresis was performed with gels purchased by Life Technologies (4-12% gradient) and MOPS was used as running buffer at 130 mV. SeeBlue Plus2 was the protein weight standard adopted. All the chemicals are from Life Technologies. Running time was adjusted depending on the molecular weight of the protein of interest.

Loading Buffer

Component	Concentration
DTT	50 mM
Sample Buffer (4X)	1X
SDS 1%	to volume

Table 13. Loading buffer for protein electrophoresis.

Coomassie Brilliant Blue

SimplyBlue^{TM} SafeStain purchased from Life Technologies was used to stain protein samples after electrophoresis. This staining allows to evaluate the quality of the extracted protein (single bands reflect good protein extract without signs of protein degradation) and control the calibration of different samples.

Briefly, gels were incubated for 30 minutes, with Simply Blue dye, at room temperature over a shaker. Gels were then incubated with Fixing Solution (table 14) for 30 minutes at room temperature to fix the dye; then gels were incubated for 1 hour up to few days with Destaining Solution (table 15) at room temperature to remove the excess of dye from the gel (to clearly visualize the protein bands).

Fixing Solution

Component	Concentration
H_2O	45%
Methanol	45%
Acetic Acid	10%

Table 14. Fixing solution composition.

Destaining Solution

Component	Concentration
H_2O	88%
Methanol	5%
Acetic Acid	7%

Table 15. Destaining solution.

Protein Transfer

Proteins were then transferred on a methanol-activated PVDF membrane (GE Healthcare, 0.2 µm porosity) by using Transfer Buffer at 4°C, 400 mA for 90 minutes. After the transfer, membranes were usually stained with red ponceau dye (SIGMA-Aldrich) to check the transfer efficiency and quality.

Membranes were saturated in 0.1% TTBS supplemented with 5% milk for at least 1 hour at room temperature, to reduce the non-specific binding of the primary antibody to the membrane. The antibodies used in this PhD thesis are reported in the table at the end of this chapter, and were incubated on a shaker.

TTBS 0.1%

Component	Concentration
Tris Base – HCl (pH 7.6)	50 mM
NaCl	150 mM
Tween20	0.1%

Transfer Buffer

Component	Concentration
Transfer Buffer (20X)	1X
Methanol	20%
Antioxidant	0.05%

Table 16. TTBS and Transfer buffer composition.

After incubation with the primary antibody, membranes were washed with 0.1% TTBS 3 times for 10 minutes. The adequate HRP conjugated secondary antibody was incubated for 90 minutes at room temperature; other 3 washes were then performed. Finally, for the detection we used a chemiluminescent substrate (ECL Plus, Pierce) that produces light when combined with the enzyme. The output was detected using Kodak films (SIGMA-Aldrich).

Live Imaging

a. Multi-photon microscopy and Ca^{2+} imaging
b. GECIs: FRET-based microscope
c. GECIs: single wavelength. Ultraview, spinning disk confocal microscope

Two photon microscopy

Two photon excitation (TPE) fluorescence technique is an important example of non linear optical microscopy. It allows the excitation of a fluorescent molecule by the simultaneous absorption of two photons that have approximately a double wavelength if compared to that used in standard fluorescence excitation.

In two-photon microscopy the laser is focused by the objective on the focal plane as it happens for single photon microscopy, but in TPEM molecules excitation is possible only in a limited volume around the focal plane: only in this volume the probability for two photons to reach, in the same temporal window, a particular molecule is sufficiently high to induce fluorescence excitation.

A multi-photon system (Radiance 2100 MP; Bio-Rad Laboratories, UK, showed in fig. 3), equipped with a Tsunami mode-locked, tunable, femto-second–pulsed Ti/sapphire laser (Ti:Sa), optically pumped by a Millennia VsS 5W green laser (Spectra Physics), was used for two-photon microscopy. The laser output is capable of generating 100 fs pulse trains at a rate of 82 MHz. The excitation wavelength at 785 nm was controlled with a spectrometer (Ocean Optics USB2000; getSpec). The microscope (Eclipse E600FN; Nikon) was equipped with a Nikon objective (40×/0.8 W CORR); a Direct Detection System (Bio-Rad), fitted with a 500LP DC dichroic mirror and HQ535/50 emission filter (Chroma Technology Corp.), was used for the detection of fluorescence emission signals. The LaserSharp2000 software package (Bio-Rad) was used for data acquisition.

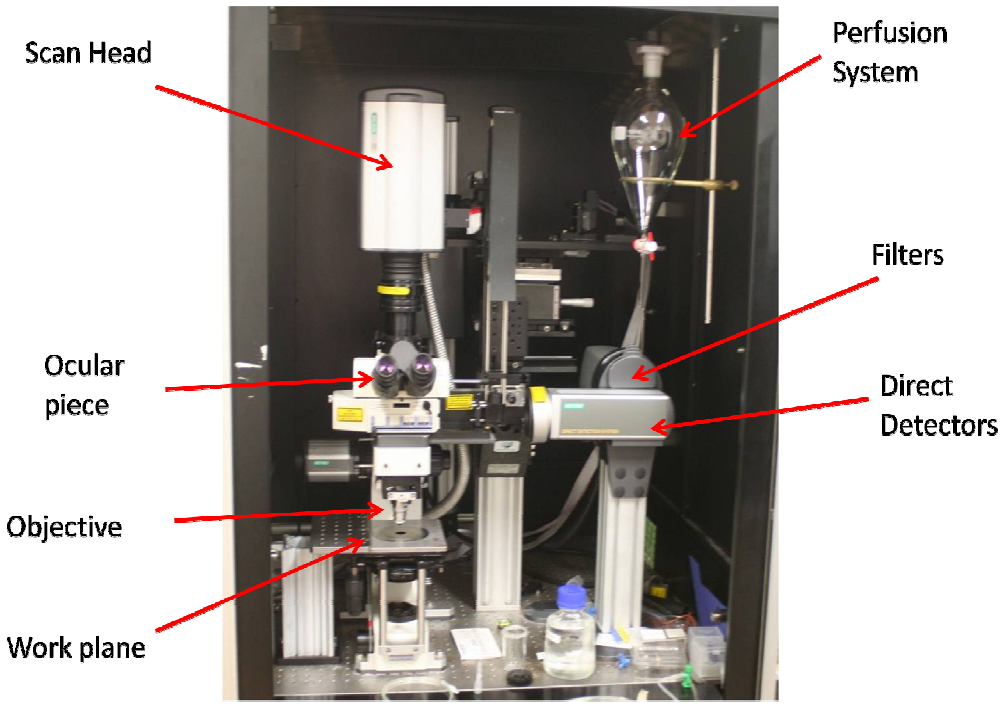

Figure 3. BIORAD2100 multiphoton microscope setup available at VIMM.

In order to perform Ca^{2+} imaging on acute heart slices, these were loaded with Fluo4AM (Life Technologies). Fluo-4AM, is a visible light, single wavelength fluorescent dye. It is a derivate of EGTA, common divalent ion chelator. It is available in the form of acetomethoxyl ester (AM ester), which can diffuse across the cell membrane. Once inside, it is cleaved by endogenous esterases becoming cell impermeant and trapped inside the cell. Fluo-4 diffuses throughout the whole cytoplasm, allowing measurement of cytosolic Ca^{2+}.

After the cutting procedure described above in the dedicated chapter, slices had a recovery time. After this period, slices were loaded with the Ca^{2+}-sensitive indicator Fluo-4AM (10 µM) for 40 minutes in 2 mM Ca^{2+} Tyrode solution (see table 17) plus 20% Pluronic F-127 (Life Techonologies) and 10 µM sulfinpyrazone (SP, SIGMA-Aldrich) in a 12-well plate positioned on a shaker in a cell incubator (37°C, 5% CO_2, controlled humidity), as shown in fig. 4.

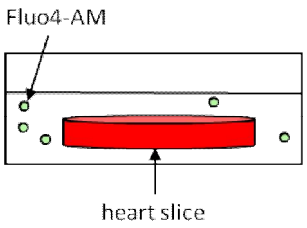

Figure 4. Schematic representation of heart slices loading protocol.

Slices were then washed twice with Tyrode Solution supplemented with 10 μM SP to limit dye extrusion from the cell. An additional 10 minutes long washout in this last solution allowed complete de-esterification of the dye.
The slices were then transferred on the imaging chamber under the microscope objective, always in Tyrode solution with 10 μM SP for the entire imaging period.

Tyrode Solution

Component	Concentration
NaCl	136 mM
KCl	5.4 mM
NaH_2PO_4	0.33 mM
$MgCl_2$	1 mM
Glucose	10 mM
Hepes	5 mM
$CaCl_2$	2 mM

Table 17. Tyrode solution composition. The solution was brought to pH 7.4 and filter-sterilized.

Genetically Encoded Calcium Indicators (GECIs) Imaging

FRET-based sensors

FRET experiments on neonatal cardiomyocytes were all performed on an inverted fluorescence microscope Olympus IX50 equipped with a Nikon 40X oil immersion objective. The light source used was either a Xenon Arc Lamp or a LED (Thorlabs, 410 nm), depending on speed and light power needed for the experiments. FRET sensors were excited with a bandpass filter 430/25 nm, then emitted fluorescence was split with a dichroic mirror and acquired simultaneously at 530 nm (YFP) and 480 nm (CFP) in two portions of the camera (Hamamatsu), shown in fig. 5.
The acquisition system of the microscope is synchronized with shutter movement or LED activation by the software Roboscope (kindly provided by Prof. Fabio Mammano). The exposure time was set at 150-200 ms to obtain a good signal to noise ratio.

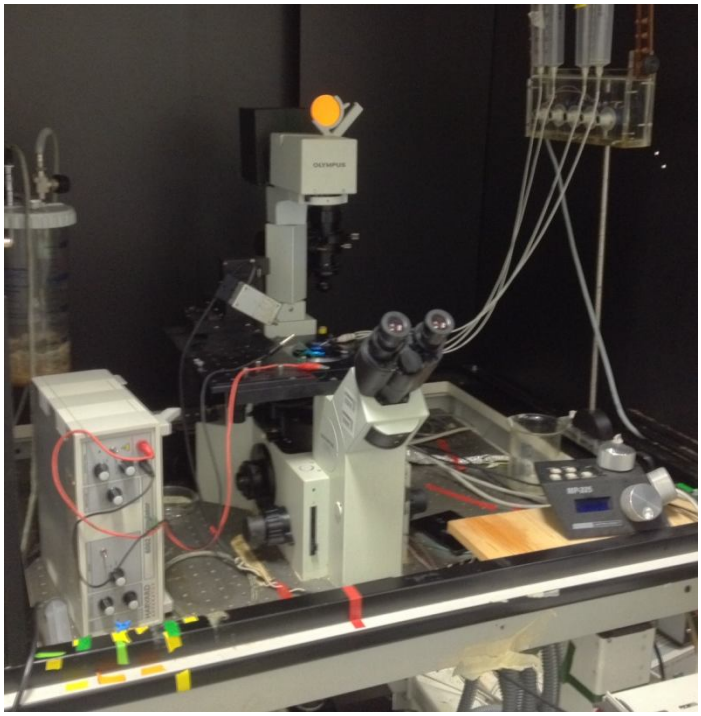

Figure 5. FRET-imaging setup at VIMM.

Neonatal rat cardiomyocytes seeded on round coverslips (VWR) and transfected at least 48 hours prior to experiments were washed twice with NCMs imaging solution (see table 18) and mounted on the imaging chamber.

To stimulate electrically the cardiomyocytes, the 6002 Stimulator (Harvard Apparatus) was connected to the chamber conceived for pacing. Electrical squared pulses, 5 ms long, were given at different frequency controlled in remote.

Neonatal Cardiomyocytes Imaging Solution

Component	Concentration
NaCl	125 mM
KCl	5 mM
Na_3PO_4	1 mM
$MgSO_4$	1 mM
Glucose	5.5 mM
Hepes	20 mM
$CaCl_2$	1.8 mM

Table 18. NCMs imaging solution composition. The solution was brought to pH 7.4 and filter-sterilized.

FRET-based Ca^{2+} measurements analysis

Offline image analysis was performed using ImageJ software. A ROI was manually drawn around transfected cells (excluding the nucleus) and the fluorescence intensity of CFP and Venus channels was reported in an Excel worksheet. Then each channel was background subtracted and the ratio between the two was used to evaluate FRET signals.

Single wavelength Ca^{2+} imaging: Ultraview

The microscope adopted for single wavelength measurements is an inverted Nikon Eclipse TE200, Ultraview. This is a confocal spinning disk microscope that offers several advantages for live cell imaging applications, compared to conventional confocal microscopes, as depicted in fig.6.

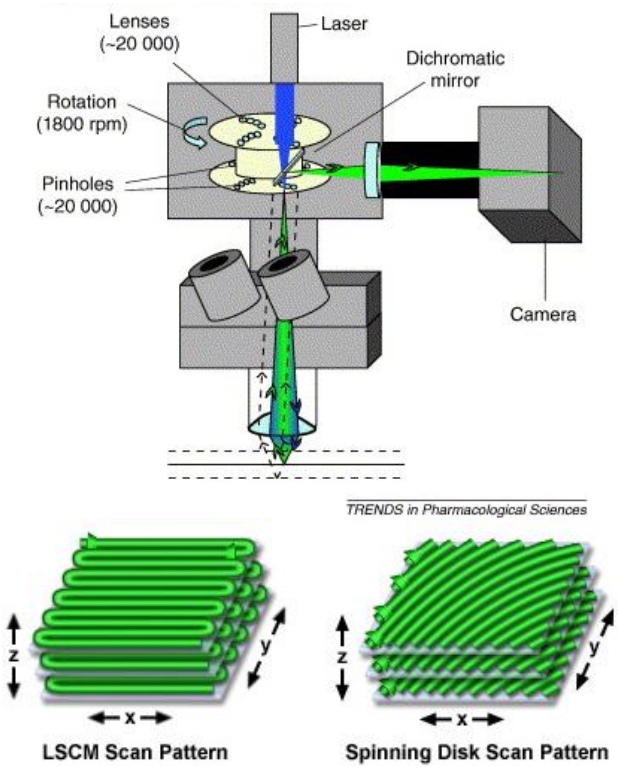

Figure 6. Spinning disk microscope set up and Scan pattern. Modified from [162].

The light source consists of lasers as for confocal microscopy, but the spinning disk confocal microscope collects multiple points in parallel rather than scanning a single point at a time, lowering light power on the sample and increasing acquisition speed.

The set up installed at VIMM is equipped with two lasers (488 nm and 570 nm) and with a Nikon oil immersion 60X objective.

This imaging setup has been used for GCaMP experiments on neonatal cardiomyocytes adopting the transfection and electrical pacing protocols described for cameleons. These sensors were excited 488 nm wavelength and emission acquired through a 525/30 filter. Exposure time was set at 50-100 ms to reach an adequate signal to noise ratio.

Fluo 4AM Ca^{2+} sensitive dye

The Ultraview microscope was used also for experiments on neonatal cardiomyocytes loaded with Fluo4AM. Cardiomyocytes were loaded with a protocol similar to that of cardiac slices, Fluo-4AM 2.5 μM, for 40 minutes in neonatal cardiomyocytes imaging solution plus 20% Pluronic F-127 and 10 μM SP in the cell culture incubator (37°C, 5% CO_2 and controlled humidity).

Image analysis

Off-line image analysis was performed with the dedicate software ImageJ.

For live imaging experiments, ROIs (Regions of Interest) were manually drawn to select the cytosol or the mitochondrial area. In both cases nuclei were excluded from the ROI.

In FRET experiments, CFP and YFP channels were evaluated separately and each channel was background subtracted selecting as background an ROI without transfected cells. Ca^{2+} levels were evaluated as ratio R= YFP/CFP. In the case of single wavelength sensors, a ROI was selected and fluorescence (F) was monitored over time, with respects to the basal level of fluorescence of the ROI (F_0) and analyzed as a relative intensity signal F/F_0.

For WB analysis, a semi-quantitative evaluation of the relative protein content was performed using the ImageJ plug-in "*Gels*" for densitometry that allows to evaluate the optical density of protein bands in the photographic films. In every experiment, values were normalized to the housekeeping protein.

Statistical analysis

For data analysis Excel® was used. Data fitting was performed with Clampfit® (version 10.2). Least squares was used as minimization method and the coefficient of determination, R^2, was considered to evaluate the goodness of fit. For comparison between sets of experiments the t-test was used. P-values lower than 0.05 were considered statistically significant.

Table of the antibodies

Protein	Company	Dilution	Host Species	Application
Actin	SIGMA A5060	1:2000	Rabbit	WB
α-Actinin	SIGMA A7732	1:200	Mouse	IF
MCU	SIGMA HPA016480	1:100 ; 1:1000	Rabbit	IF; WB
MCUb	Abgent AP12355b	1:1000	Rabbit	WB
MICU-1	SIGMA HPA037480	1:1000	Rabbit	WB
MICU-2	Abcam AB101465	1:1000	Rabbit	WB
Tom20	Santa Cruz sc-11415	1:400 ; 1:10000	Rabbit	IF; WB
Serca2	Santa Cruz sc-8095	1:2000	Goat	WB
Grp75	Santa Cruz h-155	1:1000	Rabbit	WB
Flag	SIGMA F7425	1:200	Rabbit	IF
Troponin I	[111]	1:100	Mouse	IF
Dystrophin	Abcam AB15277	1:200	Rabbit	IF

6. REFERENCES

1. Borile, G., et al., *Multispot multiphoton Ca2+ imaging in acute myocardial slices.* J Biomed Opt, 2015. **20**(5): p. 51016.
2. Fieni, F., et al., *Activity of the mitochondrial calcium uniporter varies greatly between tissues.* Nat Commun, 2012. **3**: p. 1317.
3. Boyden, P.A., M. Hirose, and W. Dun, *Cardiac Purkinje cells.* Heart Rhythm, 2010. **7**(1): p. 127-35.
4. Bailey, J.C., D.A. Lathrop, and D.L. Pippenger, *Differences between proximal left and right bundle branch block action potential durations and refractoriness in the dog heart.* Circ Res, 1977. **40**(5): p. 464-8.
5. Goldberger, A.L., D.R. Rigney, and B.J. West, *Chaos and fractals in human physiology.* Sci Am, 1990. **262**(2): p. 42-9.
6. Zaglia, T., et al., *Cardiac sympathetic neurons provide trophic signal to the heart via beta2-adrenoceptor-dependent regulation of proteolysis.* Cardiovasc Res, 2013. **97**(2): p. 240-50.
7. Dobrzynski, H., et al., *Structure, function and clinical relevance of the cardiac conduction system, including the atrioventricular ring and outflow tract tissues.* Pharmacol Ther, 2013. **139**(2): p. 260-88.
8. Page, E., *Quantitative ultrastructural analysis in cardiac membrane physiology.* Am J Physiol, 1978. **235**(5): p. C147-58.
9. Williams, G.S., et al., *Mitochondrial calcium uptake.* Proc Natl Acad Sci U S A, 2013. **110**(26): p. 10479-86.
10. Morita, H., J. Seidman, and C.E. Seidman, *Genetic causes of human heart failure.* J Clin Invest, 2005. **115**(3): p. 518-26.
11. Bers, D.M., *Cardiac sarcoplasmic reticulum calcium leak: basis and roles in cardiac dysfunction.* Annu Rev Physiol, 2014. **76**: p. 107-27.
12. Bers, D.M., *Cardiac excitation-contraction coupling.* Nature, 2002. **415**(6868): p. 198-205.
13. Fabiato, A., *Calcium-induced release of calcium from the cardiac sarcoplasmic reticulum.* Am J Physiol, 1983. **245**(1): p. C1-14.
14. Cheng, H., W.J. Lederer, and M.B. Cannell, *Calcium sparks: elementary events underlying excitation-contraction coupling in heart muscle.* Science, 1993. **262**(5134): p. 740-4.
15. Lehnart, S.E., et al., *Stabilization of cardiac ryanodine receptor prevents intracellular calcium leak and arrhythmias.* Proc Natl Acad Sci U S A, 2006. **103**(20): p. 7906-10.
16. Wehrens, X.H., et al., *FKBP12.6 deficiency and defective calcium release channel (ryanodine receptor) function linked to exercise-induced sudden cardiac death.* Cell, 2003. **113**(7): p. 829-40.
17. Lehnart, S.E., et al., *Sudden death in familial polymorphic ventricular tachycardia associated with calcium release channel (ryanodine receptor) leak.* Circulation, 2004. **109**(25): p. 3208-14.
18. Zalk, R., et al., *Structure of a mammalian ryanodine receptor.* Nature, 2015. **517**(7532): p. 44-9.
19. Molkentin, J.D., *Locating heart failure.* Nat Med, 2005. **11**(12): p. 1284-5.
20. Huxley, H.E., *The mechanism of muscular contraction.* Science, 1969. **164**(3886): p. 1356-65.

21. Egger, M. and E. Niggli, *Regulatory function of Na-Ca exchange in the heart: milestones and outlook.* J Membr Biol, 1999. **168**(2): p. 107-30.
22. De Stefani, D., et al., *A forty-kilodalton protein of the inner membrane is the mitochondrial calcium uniporter.* Nature, 2011. **476**(7360): p. 336-40.
23. Baughman, J.M., et al., *Integrative genomics identifies MCU as an essential component of the mitochondrial calcium uniporter.* Nature, 2011. **476**(7360): p. 341-5.
24. Ferrari, R., C. Ceconi, and G. Guardigli, *Pathophysiological role of heart rate: from ischaemia to left ventricular dysfunction.* Vol. 10. 2008. F7-F10.
25. Akar, F.G. and B. O'Rourke, *Mitochondria are sources of metabolic sink and arrhythmias.* Pharmacol Ther, 2011. **131**(3): p. 287-94.
26. Brown, D.A. and B. O'Rourke, *Cardiac mitochondria and arrhythmias.* Cardiovasc Res, 2010. **88**(2): p. 241-9.
27. Deluca, H.F. and G.W. Engstrom, *Calcium uptake by rat kidney mitochondria.* Proc Natl Acad Sci U S A, 1961. **47**: p. 1744-50.
28. Marchi, S. and P. Pinton, *The mitochondrial calcium uniporter complex: molecular components, structure and physiopathological implications.* J Physiol, 2014. **592**(Pt 5): p. 829-39.
29. Raffaello, A., et al., *The mitochondrial calcium uniporter is a multimer that can include a dominant-negative pore-forming subunit.* EMBO J, 2013. **32**(17): p. 2362-76.
30. Patron, M., et al., *MICU1 and MICU2 finely tune the mitochondrial Ca2+ uniporter by exerting opposite effects on MCU activity.* Mol Cell, 2014. **53**(5): p. 726-37.
31. Sancak, Y., et al., *EMRE is an essential component of the mitochondrial calcium uniporter complex.* Science, 2013. **342**(6164): p. 1379-82.
32. Kovacs-Bogdan, E., et al., *Reconstitution of the mitochondrial calcium uniporter in yeast.* Proc Natl Acad Sci U S A, 2014. **111**(24): p. 8985-90.
33. Pan, X., et al., *The physiological role of mitochondrial calcium revealed by mice lacking the mitochondrial calcium uniporter.* Nat Cell Biol, 2013. **15**(12): p. 1464-72.
34. Murphy, E., et al., *Unresolved questions from the analysis of mice lacking MCU expression.* Biochem Biophys Res Commun, 2014. **449**(4): p. 384-5.
35. Carafoli, E., E. Garcia-Martin, and D. Guerini, *The plasma membrane calcium pump: recent developments and future perspectives.* Experientia, 1996. **52**(12): p. 1091-100.
36. Carafoli, E., *Calcium pump of the plasma membrane.* Physiol Rev, 1991. **71**(1): p. 129-53.
37. Houser, S.R., *Ca(2+) signaling domains responsible for cardiac hypertrophy and arrhythmias.* Circ Res, 2009. **104**(4): p. 413-5.
38. Liu, N., Y. Ruan, and S.G. Priori, *Catecholaminergic polymorphic ventricular tachycardia.* Prog Cardiovasc Dis, 2008. **51**(1): p. 23-30.
39. Postma, A.V., et al., *Catecholaminergic polymorphic ventricular tachycardia: RYR2 mutations, bradycardia, and follow up of the patients.* J Med Genet, 2005. **42**(11): p. 863-70.
40. Marks, A.R., et al., *Involvement of the cardiac ryanodine receptor/calcium release channel in catecholaminergic polymorphic ventricular tachycardia.* J Cell Physiol, 2002. **190**(1): p. 1-6.

41. Lehnart, S.E., et al., *Leaky Ca2+ release channel/ryanodine receptor 2 causes seizures and sudden cardiac death in mice.* J Clin Invest, 2008. **118**(6): p. 2230-45.
42. Priori, S.G., et al., *Mutations in the cardiac ryanodine receptor gene (hRyR2) underlie catecholaminergic polymorphic ventricular tachycardia.* Circulation, 2001. **103**(2): p. 196-200.
43. Brunello, L., et al., *Decreased RyR2 refractoriness determines myocardial synchronization of aberrant Ca2+ release in a genetic model of arrhythmia.* Proc Natl Acad Sci U S A, 2013. **110**(25): p. 10312-7.
44. Jiang, D., et al., *Enhanced store overload-induced Ca2+ release and channel sensitivity to luminal Ca2+ activation are common defects of RyR2 mutations linked to ventricular tachycardia and sudden death.* Circ Res, 2005. **97**(11): p. 1173-81.
45. Jiang, D., et al., *RyR2 mutations linked to ventricular tachycardia and sudden death reduce the threshold for store-overload-induced Ca2+ release (SOICR).* Proc Natl Acad Sci U S A, 2004. **101**(35): p. 13062-7.
46. George, C.H., *Sarcoplasmic reticulum Ca2+ leak in heart failure: mere observation or functional relevance?* Cardiovasc Res, 2008. **77**(2): p. 302-14.
47. George, C.H., et al., *Arrhythmogenic mutation-linked defects in ryanodine receptor autoregulation reveal a novel mechanism of Ca2+ release channel dysfunction.* Circ Res, 2006. **98**(1): p. 88-97.
48. Herron, T.J., et al., *Purkinje cell calcium dysregulation is the cellular mechanism that underlies catecholaminergic polymorphic ventricular tachycardia.* Heart Rhythm, 2010. **7**(8): p. 1122-8.
49. Zhou, L., et al., *Effects of regional mitochondrial depolarization on electrical propagation: implications for arrhythmogenesis.* Circ Arrhythm Electrophysiol, 2014. **7**(1): p. 143-51.
50. Baher, A.A., et al., *Bidirectional ventricular tachycardia: ping pong in the His-Purkinje system.* Heart Rhythm, 2011. **8**(4): p. 599-605.
51. Myles, R.C., et al., *Local beta-adrenergic stimulation overcomes source-sink mismatch to generate focal arrhythmia.* Circ Res, 2012. **110**(11): p. 1454-64.
52. Xie, Y., et al., *So little source, so much sink: requirements for afterdepolarizations to propagate in tissue.* Biophys J, 2010. **99**(5): p. 1408-15.
53. Bruegmann, T., et al., *Optogenetic control of heart muscle in vitro and in vivo.* Nat Methods, 2010. **7**(11): p. 897-900.
54. Miller, G., *Optogenetics. Shining new light on neural circuits.* Science, 2006. **314**(5806): p. 1674-6.
55. Miesenbock, G., *The optogenetic catechism.* Science, 2009. **326**(5951): p. 395-9.
56. Boyle, P.M., E. Entcheva, and N.A. Trayanova, *See the light: can optogenetics restore healthy heartbeats? And, if it can, is it really worth the effort?* Expert Rev Cardiovasc Ther, 2014. **12**(1): p. 17-20.
57. Abilez, O.J., *Cardiac optogenetics.* Conf Proc IEEE Eng Med Biol Soc, 2012. **2012**: p. 1386-9.
58. Kohl, T., et al., *Superresolution microscopy in heart - cardiac nanoscopy.* J Mol Cell Cardiol, 2013. **58**: p. 13-21.
59. Scherschel, J.A. and M. Rubart, *Cardiovascular imaging using two-photon microscopy.* Microsc Microanal, 2008. **14**(6): p. 492-506.
60. Heim, R. and R.Y. Tsien, *Engineering green fluorescent protein for improved brightness, longer wavelengths and fluorescence resonance energy transfer.* Curr Biol, 1996. **6**(2): p. 178-82.

61. Miyawaki, A., et al., *Dynamic and quantitative Ca2+ measurements using improved cameleons.* Proc Natl Acad Sci U S A, 1999. **96**(5): p. 2135-40.
62. McCombs, J.E. and A.E. Palmer, *Measuring calcium dynamics in living cells with genetically encodable calcium indicators.* Methods, 2008. **46**(3): p. 152-9.
63. Rose, T., et al., *Putting a finishing touch on GECIs.* Front Mol Neurosci, 2014. **7**: p. 88.
64. Akerboom, J., et al., *Genetically encoded calcium indicators for multi-color neural activity imaging and combination with optogenetics.* Front Mol Neurosci, 2013. **6**: p. 2.
65. Kotlikoff, M.I., *Genetically encoded Ca2+ indicators: using genetics and molecular design to understand complex physiology.* J Physiol, 2007. **578**(Pt 1): p. 55-67.
66. Akerboom, J., et al., *Optimization of a GCaMP calcium indicator for neural activity imaging.* J Neurosci, 2012. **32**(40): p. 13819-40.
67. Palmer, A.E., et al., *Ca2+ indicators based on computationally redesigned calmodulin-peptide pairs.* Chem Biol, 2006. **13**(5): p. 521-30.
68. Boyden, E.S., et al., *Millisecond-timescale, genetically targeted optical control of neural activity.* Nat Neurosci, 2005. **8**(9): p. 1263-8.
69. Aravanis, A.M., et al., *An optical neural interface: in vivo control of rodent motor cortex with integrated fiberoptic and optogenetic technology.* J Neural Eng, 2007. **4**(3): p. S143-56.
70. Zhang, F., et al., *Multimodal fast optical interrogation of neural circuitry.* Nature, 2007. **446**(7136): p. 633-9.
71. Zhang, F., et al., *Circuit-breakers: optical technologies for probing neural signals and systems.* Nat Rev Neurosci, 2007. **8**(8): p. 577-81.
72. Nussinovitch, U., R. Shinnawi, and L. Gepstein, *Modulation of cardiac tissue electrophysiological properties with light-sensitive proteins.* Cardiovasc Res, 2014. **102**(1): p. 176-87.
73. Boyle, P.M., et al., *A comprehensive multiscale framework for simulating optogenetics in the heart.* Nat Commun, 2013. **4**: p. 2370.
74. Jia, Z., et al., *Stimulating cardiac muscle by light: cardiac optogenetics by cell delivery.* Circ Arrhythm Electrophysiol, 2011. **4**(5): p. 753-60.
75. Arrenberg, A.B., et al., *Optogenetic control of cardiac function.* Science, 2010. **330**(6006): p. 971-4.
76. Wagner, E., et al., *Stimulated emission depletion live-cell super-resolution imaging shows proliferative remodeling of T-tubule membrane structures after myocardial infarction.* Circ Res, 2012. **111**(4): p. 402-14.
77. Crocini, C., et al., *Functional cardiac imaging by random access microscopy.* Front Physiol, 2014. **5**: p. 403.
78. Crocini, C., et al., *Defects in T-tubular electrical activity underlie local alterations of calcium release in heart failure.* Proc Natl Acad Sci U S A, 2014. **111**(42): p. 15196-201.
79. Tsubota, T., et al., *Optogenetic manipulation of cerebellar Purkinje cell activity in vivo.* PLoS One, 2011. **6**(8): p. e22400.
80. Cheng, M.Y., et al., *Optogenetic neuronal stimulation promotes functional recovery after stroke.* Proc Natl Acad Sci U S A, 2014. **111**(35): p. 12913-8.
81. Denk, W., J.H. Strickler, and W.W. Webb, *Two-photon laser scanning fluorescence microscopy.* Science, 1990. **248**(4951): p. 73-6.
82. Zipfel, W.R., R.M. Williams, and W.W. Webb, *Nonlinear magic: multiphoton microscopy in the biosciences.* Nat Biotechnol, 2003. **21**(11): p. 1369-77.

83. Helmchen, F. and W. Denk, *Deep tissue two-photon microscopy.* Nat Methods, 2005. **2**(12): p. 932-40.
84. Hoover, E.E. and J.A. Squier, *Advances in multiphoton microscopy technology.* Nat Photonics, 2013. **7**(2): p. 93-101.
85. Nielsen, T., et al., *High efficiency beam splitter for multifocal multiphoton microscopy.* J Microsc, 2001. **201**(Pt 3): p. 368-76.
86. Svoboda, K., D.W. Tank, and W. Denk, *Direct measurement of coupling between dendritic spines and shafts.* Science, 1996. **272**(5262): p. 716-9.
87. Bahlmann, K., et al., *Multifocal multiphoton microscopy (MMM) at a frame rate beyond 600 Hz.* Opt Express, 2007. **15**(17): p. 10991-8.
88. Hopt, A. and E. Neher, *Highly nonlinear photodamage in two-photon fluorescence microscopy.* Biophys J, 2001. **80**(4): p. 2029-36.
89. Chen, X., et al., *LOTOS-based two-photon calcium imaging of dendritic spines in vivo.* Nat Protoc, 2012. **7**(10): p. 1818-29.
90. Chen, X., et al., *Functional mapping of single spines in cortical neurons in vivo.* Nature, 2011. **475**(7357): p. 501-5.
91. Truong, T.V., et al., *Deep and fast live imaging with two-photon scanned light-sheet microscopy.* Nat Methods, 2011. **8**(9): p. 757-60.
92. Lavagnino, Z., et al., *Two-photon excitation selective plane illumination microscopy (2PE-SPIM) of highly scattering samples: characterization and application.* Opt Express, 2013. **21**(5): p. 5998-6008.
93. Sacconi, L., et al., *Multiphoton multifocal microscopy exploiting a diffractive optical element.* Opt Lett, 2003. **28**(20): p. 1918-20.
94. Diaspro, A., et al., *Three-dimensional optical behaviour of a confocal microscope with single illumination and detection pinhole through imaging of subresolution beads.* Microsc Res Tech, 1999. **45**(2): p. 130-1.
95. de Boer, T.P., et al., *Myocardial tissue slices: organotypic pseudo-2D models for cardiac research & development.* Future Cardiol, 2009. **5**(5): p. 425-30.
96. Halbach, M., et al., *Ventricular slices of adult mouse hearts--a new multicellular in vitro model for electrophysiological studies.* Cell Physiol Biochem, 2006. **18**(1-3): p. 1-8.
97. Habeler, W., et al., *An in vitro beating heart model for long-term assessment of experimental therapeutics.* Cardiovasc Res, 2009. **81**(2): p. 253-9.
98. Niesner, R., et al., *The power of single and multibeam two-photon microscopy for high-resolution and high-speed deep tissue and intravital imaging.* Biophys J, 2007. **93**(7): p. 2519-29.
99. Rubart, M., et al., *Two-photon molecular excitation imaging of Ca2+ transients in Langendorff-perfused mouse hearts.* Am J Physiol Cell Physiol, 2003. **284**(6): p. C1654-68.
100. Kim, K.H., et al., *Multifocal multiphoton microscopy based on multianode photomultiplier tubes.* Opt Express, 2007. **15**(18): p. 11658-78.
101. Bussek, A., et al., *Tissue slices from adult mammalian hearts as a model for pharmacological drug testing.* Cell Physiol Biochem, 2009. **24**(5-6): p. 527-36.
102. Barclay, C.J., *Modelling diffusive O(2) supply to isolated preparations of mammalian skeletal and cardiac muscle.* J Muscle Res Cell Motil, 2005. **26**(4-5): p. 225-35.
103. Rudolf, R., et al., *Looking forward to seeing calcium.* Nat Rev Mol Cell Biol, 2003. **4**(7): p. 579-86.
104. Rubart, M. and D.P. Zipes, *Mechanisms of sudden cardiac death.* J Clin Invest, 2005. **115**(9): p. 2305-15.

105. Lehnart, S. and A.R. Marks, *Regulation of ryanodine receptors in the heart.* Circ Res, 2007. **101**(8): p. 746-9.
106. Fernandez-Velasco, M., et al., *Increased Ca2+ sensitivity of the ryanodine receptor mutant RyR2R4496C underlies catecholaminergic polymorphic ventricular tachycardia.* Circ Res, 2009. **104**(2): p. 201-9, 12p following 209.
107. Fujiwara, K., et al., *Burst emergence of intracellular Ca2+ waves evokes arrhythmogenic oscillatory depolarization via the Na+-Ca2+ exchanger: simultaneous confocal recording of membrane potential and intracellular Ca2+ in the heart.* Circ Res, 2008. **103**(5): p. 509-18.
108. Lou, Q., et al., *Alternating Vm/Ca interplay underlies repetitive focal activity in a genetic model of calcium-dependent atrial arrhythmias*
109. Sato, D., et al., *Depolarization of cardiac membrane potential synchronizes calcium sparks and waves in tissue.* Biophys J, 2014. **107**(6): p. 1313-7.
110. Habeler, W., M. Peschanski, and C. Monville, *Organotypic heart slices for cell transplantation and physiological studies.* Organogenesis, 2009. **5**(2): p. 62-6.
111. Saggin, L., et al., *Troponin I switching in the developing heart.* J Biol Chem, 1989. **264**(27): p. 16299-302.
112. Gombosova, I., et al., *Postnatal changes in contractile time parameters, calcium regulatory proteins, and phosphatases.* Am J Physiol, 1998. **274**(6 Pt 2): p. H2123-32.
113. Alvarez-Lacalle, E., et al., *Dependency of calcium alternans on ryanodine receptor refractoriness.* PLoS One, 2013. **8**(2): p. e55042.
114. Nivala, M. and Z. Qu, *Calcium alternans in a couplon network model of ventricular myocytes: role of sarcoplasmic reticulum load.* Am J Physiol Heart Circ Physiol, 2012. **303**(3): p. H341-52.
115. Aistrup, G.L., et al., *Pacing-induced heterogeneities in intracellular Ca2+ signaling, cardiac alternans, and ventricular arrhythmias in intact rat heart.* Circ Res, 2006. **99**(7): p. e65-73.
116. Jia, Z., et al., *Cardiac cellular coupling and the spread of early instabilities in intracellular Ca2+.* Biophys J, 2012. **102**(6): p. 1294-302.
117. Kornyeyev, D., et al., *Calsequestrin 2 deletion shortens the refractoriness of Ca(2)(+) release and reduces rate-dependent Ca(2)(+)-alternans in intact mouse hearts.* J Mol Cell Cardiol, 2012. **52**(1): p. 21-31.
118. Cordeiro, J.M., et al., *Cellular and subcellular alternans in the canine left ventricle.* Am J Physiol Heart Circ Physiol, 2007. **293**(6): p. H3506-16.
119. Xie, W., et al., *Imaging atrial arrhythmic intracellular calcium in intact heart.* J Mol Cell Cardiol, 2013. **64**: p. 120-3.
120. Plummer, B.N., et al., *Spontaneous calcium oscillations during diastole in the whole heart: the influence of ryanodine reception function and gap junction coupling.* Am J Physiol Heart Circ Physiol, 2011. **300**(5): p. H1822-8.
121. Wang, K., et al., *Cardiac Tissue Slices: Preparation, Handling, and Successful Optical Mapping.* Am J Physiol Heart Circ Physiol, 2015: p. ajpheart 00556 2014.
122. Weiss, J.N., et al., *Alternans and arrhythmias: from cell to heart.* Circ Res, 2011. **108**(1): p. 98-112.
123. Laurita, K.R. and D.S. Rosenbaum, *Cellular mechanisms of arrhythmogenic cardiac alternans.* Prog Biophys Mol Biol, 2008. **97**(2-3): p. 332-47.
124. Li, Y., D.A. Eisner, and S.C. O'Neill, *Do calcium waves propagate between cells and synchronize alternating calcium release in rat ventricular myocytes?* J Physiol, 2012. **590**(Pt 24): p. 6353-61.

125. Zhang, Y., et al., *Abnormal Ca(2+) homeostasis, atrial arrhythmogenesis, and sinus node dysfunction in murine hearts modeling RyR2 modification.* Front Physiol, 2013. **4**: p. 150.
126. Yaniv, Y., et al., *Crosstalk between mitochondrial and sarcoplasmic reticulum Ca2+ cycling modulates cardiac pacemaker cell automaticity.* PLoS One, 2012. **7**(5): p. e37582.
127. Smith, R.M., et al., *Uncoupling the mitochondria facilitates alternans formation in the isolated rabbit heart.* Am J Physiol Heart Circ Physiol, 2013. **305**(1): p. H9-18.
128. Florea, S.M. and L.A. Blatter, *The role of mitochondria for the regulation of cardiac alternans.* Front Physiol, 2010. **1**: p. 141.
129. Kawahara, K., M. Takase, and Y. Yamauchi, *Ruthenium red-induced transition from ventricular fibrillation to tachycardia in isolated rat hearts: possible involvement of changes in mitochondrial calcium uptake.* Cardiovasc Pathol, 2003. **12**(6): p. 311-21.
130. Robert, V., et al., *Beat-to-beat oscillations of mitochondrial [Ca2+] in cardiac cells.* EMBO J, 2001. **20**(17): p. 4998-5007.
131. Griffiths, E.J., D. Balaska, and W.H. Cheng, *The ups and downs of mitochondrial calcium signalling in the heart.* Biochim Biophys Acta, 2010. **1797**(6-7): p. 856-64.
132. Castaldi, A., et al., *MicroRNA-133 modulates the beta1-adrenergic receptor transduction cascade.* Circ Res, 2014. **115**(2): p. 273-83.
133. O'Rourke, B. and L.A. Blatter, *Mitochondrial Ca2+ uptake: tortoise or hare?* J Mol Cell Cardiol, 2009. **46**(6): p. 767-74.
134. Drago, I., et al., *Mitochondrial Ca2+ uptake contributes to buffering cytoplasmic Ca2+ peaks in cardiomyocytes.* Proc Natl Acad Sci U S A, 2012. **109**(32): p. 12986-91.
135. Huser, J., L.A. Blatter, and S.S. Sheu, *Mitochondrial calcium in heart cells: beat-to-beat oscillations or slow integration of cytosolic transients?* J Bioenerg Biomembr, 2000. **32**(1): p. 27-33.
136. Brillantes, A.M., S. Bezprozvannaya, and A.R. Marks, *Developmental and tissue-specific regulation of rabbit skeletal and cardiac muscle calcium channels involved in excitation-contraction coupling.* Circ Res, 1994. **75**(3): p. 503-10.
137. Piquereau, J., et al., *Postnatal development of mouse heart: formation of energetic microdomains.* J Physiol, 2010. **588**(Pt 13): p. 2443-54.
138. Chen, H.W., et al., *Dynamic changes of gene expression profiles during postnatal development of the heart in mice.* Heart, 2004. **90**(8): p. 927-34.
139. Marchi, S., et al., *Downregulation of the mitochondrial calcium uniporter by cancer-related miR-25.* Curr Biol, 2013. **23**(1): p. 58-63.
140. Deng, W., et al., *Optogenetics, the intersection between physics and neuroscience: light stimulation of neurons in physiological conditions.* Am J Physiol Regul Integr Comp Physiol, 2014. **307**(11): p. R1292-R1302.
141. Fenno, L., O. Yizhar, and K. Deisseroth, *The development and application of optogenetics.* Annu Rev Neurosci, 2011. **34**: p. 389-412.
142. Mesradi, M., et al., *Experimental and analytical comparative study of optical coefficient of fresh and frozen rat tissues.* J Biomed Opt, 2013. **18**(11): p. 117010.
143. Hall, G., et al., *Goniometric measurements of thick tissue using Monte Carlo simulations to obtain the single scattering anisotropy coefficient.* Biomed Opt Express, 2012. **3**(11): p. 2707-19.

144. Bishop, M.J., et al., *Synthesis of voltage-sensitive optical signals: application to panoramic optical mapping.* Biophys J, 2006. **90**(8): p. 2938-45.
145. Baxter, W.T., et al., *Visualizing excitation waves inside cardiac muscle using transillumination.* Biophys J, 2001. **80**(1): p. 516-30.
146. Girouard, S.D., K.R. Laurita, and D.S. Rosenbaum, *Unique properties of cardiac action potentials recorded with voltage-sensitive dyes.* J Cardiovasc Electrophysiol, 1996. **7**(11): p. 1024-38.
147. Gaonkar, H.A., et al., *Decoupling scattering and absorption of turbid samples using a simple empirical relation between coefficients of the Kubelka-Munk and radiative transfer theories.* Appl Opt, 2014. **53**(13): p. 2892-8.
148. Roy, A., R. Ramasubramaniam, and H.A. Gaonkar, *Empirical relationship between Kubelka-Munk and radiative transfer coefficients for extracting optical parameters of tissues in diffusive and nondiffusive regimes.* J Biomed Opt, 2012. **17**(11): p. 115006.
149. Faggioni, M., C. van der Werf, and B.C. Knollmann, *Sinus node dysfunction in catecholaminergic polymorphic ventricular tachycardia: risk factor and potential therapeutic target?* Trends Cardiovasc Med, 2014. **24**(7): p. 273-8.
150. Cerrone, M., et al., *Arrhythmogenic mechanisms in a mouse model of catecholaminergic polymorphic ventricular tachycardia.* Circ Res, 2007. **101**(10): p. 1039-48.
151. Zaglia, T., et al., *Atrogin-1 deficiency promotes cardiomyopathy and premature death via impaired autophagy.* J Clin Invest, 2014. **124**(6): p. 2410-24.
152. Maack, C., et al., *Elevated cytosolic Na+ decreases mitochondrial Ca2+ uptake during excitation-contraction coupling and impairs energetic adaptation in cardiac myocytes.* Circ Res, 2006. **99**(2): p. 172-82.
153. Gutierrez, T., et al., *Alteration in mitochondrial Ca 2+ uptake disrupts insulin signaling in hypertrophic cardiomyocytes.* Cell Commun Signal, 2014. **12**(1): p. 68.
154. Fernandez-Sada, E., et al., *Cardiac responses to beta-adrenoceptor stimulation is partly dependent on mitochondrial calcium uniporter activity.* Br J Pharmacol, 2014. **171**(18): p. 4207-21.
155. Wu, Y., et al., *The mitochondrial uniporter controls fight or flight heart rate increases.* Nat Commun, 2015. **6**: p. 6081.
156. Heo, J.M. and J. Rutter, *Ubiquitin-dependent mitochondrial protein degradation.* Int J Biochem Cell Biol, 2011. **43**(10): p. 1422-6.
157. Lim, L.P., et al., *Microarray analysis shows that some microRNAs downregulate large numbers of target mRNAs.* Nature, 2005. **433**(7027): p. 769-73.
158. Wong, N. and X. Wang, *miRDB: an online resource for microRNA target prediction and functional annotations.* Nucleic Acids Res, 2014.
159. Betel, D., et al., *The microRNA.org resource: targets and expression.* Nucleic Acids Res, 2008. **36**(Database issue): p. D149-53.
160. Miquerol, L., et al., *Resolving cell lineage contributions to the ventricular conduction system with a Cx40-GFP allele: a dual contribution of the first and second heart fields.* Dev Dyn, 2013. **242**(6): p. 665-77.
161. Beyer, S., R.G. Kelly, and L. Miquerol, *Inducible Cx40-Cre expression in the cardiac conduction system and arterial endothelial cells.* Genesis, 2011. **49**(2): p. 83-91.
162. Norman, K., *Techniques: Intravital microscopy--a method for investigating disseminated intravascular coagulation?* Trends Pharmacol Sci, 2005. **26**(6): p. 327-32.

163. Sedmera, D. and R.G. Gourdie, *Why do we have Purkinje fibers deep in our heart?* Physiol Res, 2014. **63 Suppl 1**: p. S9-18.
164. Hoyt, R.H., M.L. Cohen, and J.E. Saffitz, *Distribution and three-dimensional structure of intercellular junctions in canine myocardium.* Circ Res, 1989. **64**(3): p. 563-74.
165. Rohr, S., et al., *Paradoxical improvement of impulse conduction in cardiac tissue by partial cellular uncoupling.* Science, 1997. **275**(5301): p. 841-4.
166. Wilders, R., et al., *Effects of anisotropy on the development of cardiac arrhythmias associated with focal activity.* Pflugers Arch, 2000. **441**(2-3): p. 301-12.
167. Peters, N.S. and A.L. Wit, *Myocardial architecture and ventricular arrhythmogenesis.* Circulation, 1998. **97**(17): p. 1746-54.
168. Goldberger, J.J., et al., *American Heart Association/American College of Cardiology Foundation/Heart Rhythm Society scientific statement on noninvasive risk stratification techniques for identifying patients at risk for sudden cardiac death: a scientific statement from the American Heart Association Council on Clinical Cardiology Committee on Electrocardiography and Arrhythmias and Council on Epidemiology and Prevention.* Circulation, 2008. **118**(14): p. 1497-1518.
169. Campbell, R.W., A. Murray, and D.G. Julian, *Ventricular arrhythmias in first 12 hours of acute myocardial infarction. Natural history study.* Br Heart J, 1981. **46**(4): p. 351-7.
170. Zheng, Z.J., et al., *Sudden cardiac death in the United States, 1989 to 1998.* Circulation, 2001. **104**(18): p. 2158-63.
171. Bogun, F., et al., *Role of Purkinje fibers in post-infarction ventricular tachycardia.* J Am Coll Cardiol, 2006. **48**(12): p. 2500-7.
172. Hayashi, M., et al., *Novel mechanism of postinfarction ventricular tachycardia originating in surviving left posterior Purkinje fibers.* Heart Rhythm, 2006. **3**(8): p. 908-18.
173. Kang, G., et al., *Purkinje cells from RyR2 mutant mice are highly arrhythmogenic but responsive to targeted therapy.* Circ Res, 2010. **107**(4): p. 512-9.
174. Scheinman, M.M., *Role of the His-Purkinje system in the genesis of cardiac arrhythmia.* Heart Rhythm, 2009. **6**(7): p. 1050-8.
175. Li, P. and Y. Rudy, *A model of canine purkinje cell electrophysiology and Ca(2+) cycling: rate dependence, triggered activity, and comparison to ventricular myocytes.* Circ Res, 2011. **109**(1): p. 71-9.
176. Syed, F.F., et al., *The infrahisian conduction system and endocavitary cardiac structures: relevance for the invasive electrophysiologist.* J Interv Card Electrophysiol, 2014. **39**(1): p. 45-56.
177. Davidenko, J.M. and C. Antzelevitch, *Electrophysiological mechanisms underlying rate-dependent changes of refractoriness in normal and segmentally depressed canine Purkinje fibers. The characteristics of post-repolarization refractoriness.* Circ Res, 1986. **58**(2): p. 257-68.
178. Wellens, H.J., *Forty years of invasive clinical electrophysiology: 1967-2007.* Circ Arrhythm Electrophysiol, 2008. **1**(1): p. 49-53.
179. Saba, S., P.J. Wang, and N.A. Estes, 3rd, *Invasive cardiac electrophysiology in the mouse: techniques and applications.* Trends Cardiovasc Med, 2000. **10**(3): p. 122-32.
180. Entcheva, E., *Cardiac optogenetics.* Am J Physiol Heart Circ Physiol, 2013. **304**(9): p. H1179-91.

181. Merrill, D.R., M. Bikson, and J.G. Jefferys, *Electrical stimulation of excitable tissue: design of efficacious and safe protocols.* J Neurosci Methods, 2005. **141**(2): p. 171-98.
182. Wikswo, J.P., Jr., S.F. Lin, and R.A. Abbas, *Virtual electrodes in cardiac tissue: a common mechanism for anodal and cathodal stimulation.* Biophys J, 1995. **69**(6): p. 2195-210.
183. Ward, D.E. and A.J. Camm, *Methodologic problems in the use of atrial pacing studies for the assessment of A-V conduction.* Clin Cardiol, 1980. **3**(3): p. 155-62.
184. Peters, R.W., et al., *Determination of His-Purkinje refractoriness in man with His bundle pacing.* Circulation, 1979. **60**(4): p. 956-9.
185. Pang, B.J., et al., *Capturing the His-Purkinje system is not possible from conventional right ventricular apical and nonapical pacing sites.* Pacing Clin Electrophysiol, 2014. **37**(6): p. 724-30.
186. Plazzo, A.P., et al., *Bioinformatic and mutational analysis of channelrhodopsin-2 protein cation-conducting pathway.* J Biol Chem, 2012. **287**(7): p. 4818-25.
187. Chow, B.Y., X. Han, and E.S. Boyden, *Genetically encoded molecular tools for light-driven silencing of targeted neurons.* Prog Brain Res, 2012. **196**: p. 49-61.
188. Sasse, P., *Optical pacing of the heart: the long way to enlightenment.* Circ Arrhythm Electrophysiol, 2011. **4**(5): p. 598-600.
189. Beiert, T., T. Bruegmann, and P. Sasse, *Optogenetic activation of Gq signalling modulates pacemaker activity of cardiomyocytes.* Cardiovasc Res, 2014. **102**(3): p. 507-16.
190. Cha, Y.M., et al., *Effects of chemical subendocardial ablation on activation rate gradient during ventricular fibrillation.* Am J Physiol, 1995. **269**(6 Pt 2): p. H1998-2009.
191. Chen, P.S., et al., *Effects of subendocardial ablation on anodal supernormal excitation and ventricular vulnerability in open-chest dogs.* Circulation, 1993. **87**(1): p. 216-29.
192. Damiano, R.J., Jr., et al., *The effect of chemical ablation of the endocardium on ventricular fibrillation threshold.* Circulation, 1986. **74**(3): p. 645-52.
193. Uhley, H.N. and L.M. Rivkin, *Visualization of the left branch of the human atrioventricular bundle.* Circulation, 1959. **20**: p. 419-21.
194. Taufic, M., F.A. Bashour, and F.J. Lewis, *Production of heart block in dogs, under direct vision.* Surg Forum, 1955. **5**: p. 96-101.
195. Robinson, R.B., et al., *Electrical restitution process in dispersed canine cardiac Purkinje and ventricular cells.* Am J Physiol, 1987. **253**(5 Pt 2): p. H1018-25.
196. Carmeliet, E., *Electrophysiological effects of encainide on isolated cardiac muscle and Purkinje fibers and on the Langendorff-perfused guinea-pig heart.* Eur J Pharmacol, 1980. **61**(3): p. 247-62.
197. Persson, F., et al., *Functional effects of the late sodium current inhibition by AZD7009 and lidocaine in rabbit isolated atrial and ventricular tissue and Purkinje fibre.* Eur J Pharmacol, 2007. **558**(1-3): p. 133-43.
198. Denker, S., et al., *Effects of alternating cycle lengths on refractoriness of the His-Purkinje system.* J Clin Invest, 1984. **74**(2): p. 559-70.
199. Denker, S., et al., *Effects of abrupt changes in cycle length on refractoriness of the His-Purkinje system in man.* Circulation, 1983. **67**(1): p. 60-8.
200. Clements-Jewery, H., D.J. Hearse, and M.J. Curtis, *Phase 2 ventricular arrhythmias in acute myocardial infarction: a neglected target for therapeutic antiarrhythmic drug development and for safety pharmacology evaluation.* Br J Pharmacol, 2005. **145**(5): p. 551-64.

201. Curtis, M.J., *Characterisation, utilisation and clinical relevance of isolated perfused heart models of ischaemia-induced ventricular fibrillation.* Cardiovasc Res, 1998. **39**(1): p. 194-215.
202. Johnston, K.M., B.A. MacLeod, and M.J. Walker, *Responses to ligation of a coronary artery in conscious rats and the actions of antiarrhythmics.* Can J Physiol Pharmacol, 1983. **61**(11): p. 1340-53.
203. Peters, N.S., *New insights into myocardial arrhythmogenesis: distribution of gap-junctional coupling in normal, ischaemic and hypertrophied human hearts.* Clin Sci (Lond), 1996. **90**(6): p. 447-52.
204. Takahashi, Y., A. Takahashi, and M. Isobe, *Ventricular fibrillation initiated by premature beats from the ventricular myocardium not associated with the Purkinje system after myocardial infarction.* Heart Rhythm, 2008. **5**(10): p. 1458-60.
205. Atkinson, A., et al., *Anatomical and molecular mapping of the left and right ventricular His-Purkinje conduction networks.* J Mol Cell Cardiol, 2011. **51**(5): p. 689-701.
206. Tusscher, K.H. and A.V. Panfilov, *Modelling of the ventricular conduction system.* Prog Biophys Mol Biol, 2008. **96**(1-3): p. 152-70.
207. Miquerol, L., et al., *Architectural and functional asymmetry of the His-Purkinje system of the murine heart.* Cardiovasc Res, 2004. **63**(1): p. 77-86.
208. Han, J. and G.K. Moe, *NONUNIFORM RECOVERY OF EXCITABILITY IN VENTRICULAR MUSCLE.* Circ Res, 1964. **14**: p. 44-60.
209. Burton, F.L. and S.M. Cobbe, *Dispersion of ventricular repolarization and refractory period.* Cardiovasc Res, 2001. **50**(1): p. 10-23.
210. Miquerol, L., et al., *Biphasic development of the mammalian ventricular conduction system.* Circ Res, 2010. **107**(1): p. 153-61.
211. Ahn, D., et al., *Induction of myocardial infarcts of a predictable size and location by branch pattern probability-assisted coronary ligation in C57BL/6 mice.* Am J Physiol Heart Circ Physiol, 2004. **286**(3): p. H1201-7.
212. Rudnicki, M.A., et al., *Actin and myosin expression during development of cardiac muscle from cultured embryonal carcinoma cells.* Dev Biol, 1990. **138**(2): p. 348-58.

APPENDIX 1

Under revision, PNAS

Optogenetic interrogation of arrhythmia mechanisms by cell-type specific targeting of Channelrhodopsin-2 in the heart.

Tania Zaglia *[1,2], Nicola Pianca *[1,2], Giulia Borile [1,2], Francesca Da Broi [2], Marina Campione [1,3], Stefan Luther [4,5,6,7], Domenico Corrado [8], Lucile Miquerol [9] and Marco Mongillo [1,2,3]

[1]Department of Biomedical Sciences, University of Padova, Via Ugo Bassi 58, 35122 Padova, Italy. [2]Venetian Institute of Molecular Medicine (VIMM), Via Orus 2, 35129 Padova, Italy. [3] Neuuroscience Institute, CNR, Viale G. Colombo 3, 35121 Padova, Italy. [4] Heart Research Center Göttingen, Göttingen, Germany, [5] Biomedical Physics, Max Planck Institute for Dynamics and Self-Organization, Göttingen, Germany, [6] Institute for Nonlinear Dynamics, Georg-August-Universität Göttingen, Göttingen, Germany, [7]German Centre for Cardiovascular Research (DZHK), partner site Göttingen (DZHK-GOE), Göttingen, Germany; [8] Department of Cardiologic, Thoracic and Vascular Sciences, University of Padova, Via Giustiniani 2, 35128, Padova, Italy; [9] Developmental Biology Institute of Marseille, CNRS UMR 7288, Aix Marseille University, , Marseille, France

* : equal contributors

Keywords: optogenetics, arrhythmia, Purkinje fibers, myocardial ischemia, channelrhodopsin-2, cardiac ectopy, premature ventricular contraction

ABSTRACT

Extrasystolic heartbeats associate to a wide range of consequences, ranging from uneventful palpitations to the triggering of lethal ventricular arrhythmias in the presence of pathologies, such as myocardial ischemia. The role of working *vs* conducting cardiomyocytes, as well as the tissue requirements for the generation of extrasystoles (minimal cardiomyocyte number and location) have not been determined directly *in vivo*. In addition, the properties characterizing effective arrhythmia triggers during myocardial ischemia are unexplored, mainly due to inherent limits of conventional cardiac electrophysiology. Here, we used optogenetics in transgenic mice expressing ChannelRhodopsin-2, either in the whole heart or selectively in the conduction system, to achieve cell-type specific, non-invasive control of cardiomyocyte activity *in vivo* with high spatial and temporal resolution. We demonstrated that focal ectopies originate in the normal myocardium from the aberrant depolarization of foci enclosing 1450-1800 working cardiomyocytes or 70-160 Purkinje fibers. To interrogate the relationship between the distribution of the ventricular conduction system and its arrhythmogenic potential, in the normal and ischemic heart, we combined optogenetics with data from the three-dimensional imaging reconstruction of the Purkinje fibers network arborization. Focal ectopies arising from the origin of the right ventricular outflow tract and including both Purkinje fibers and the surrounding working cardiomyocytes, had the highest propensity to trigger sustained arrhythmias during acute myocardial ischemia.

In conclusion, we explored cardiac physiology using cardiac optogenetics to determine the requirement of extrasystolic beats, and the factors causing ectopies to be arrhythmia triggers.

SIGNIFICANCE

Arrhythmias are potentially life threatening electrical heart diseases difficult to predict and mostly treated by empirical interventions. The mechanisms of arrhythmia initiation (trigger) are still poorly understood, mostly due to the technical limits of conventional experimental methods in cardiac electrophysiology. Here, we use optogenetics, a technique based on the expression of photoactivated proteins such as ChannelRhodopsin-2 (ChR2), allowing non-invasive control of cell membrane potential through illumination with blue light. By developing mice with cardiac expression of ChR2, we investigated the role of the different cardiomyocyte types present in the heart, and determined the factors triggering arrhythmic beats in the normal heart and during myocardial ischemia, a condition frequently associated to lethal arrhythmias causing sudden cardiac death.

INTRODUCTION

Aberrant heartbeats caused by the ectopic depolarization of a group of cardiomyocytes are associated to a wide range of consequences, from the commonly experienced feeling of 'palpitation' to the triggering of potentially lethal ventricular arrhythmias in diseased hearts. Physiologic conduction of normal heartbeats is orchestrated by the interaction of at least two functionally and anatomically distinct population of cardiomyocytes: the working cardiomyocytes and the conduction system (i.e. Purkinje fibers at the ventricular level) [163]. Electrotonic coupling of the myocardium allows the effect of spontaneous activity in sparse cardiomyocytes to be 'sunk' by the surrounding cells. A critical mass of cardiomyocytes needs to simultaneously depolarize to prevail over such protective mechanism and generate arrhythmic beats [51, 52, 164, 165]. When the source-sink mismatch is focally overcome, it results in a premature ventricular contraction (PVC) that, in the presence of arrhythmogenic substrates may evolve into chaotic and self sustained ventricular arrhythmias [166, 167]. In fact, ventricular tachycardia (VT) and fibrillation (VF) frequently occur in coronary artery disease during both the acute ischemic phase and the infarct evolution phase, and are responsible for most cases of sudden cardiac death (SCD) occurring yearly in the United States of America (USA) [168-170].

The tissue determinants of a focal arrhythmic source (i.e. critical cell number, topology) has so far only been estimated using biophysical modeling, suggesting that almost one million cells are required to generate ventricular ectopies in the rabbit heart [52]. Moreover, while pharmacologic approaches and single cell electrophysiology studies suggest that abnormal activation of the Purkinje fiber network is a likely arrhythmia trigger mechanism both in acquired (e.g. myocardial ischemia) and inherited (LQTS, CPVT) arrhythmias [3, 48, 150, 171-173], the role of the cardiac conduction system has not been addressed directly in the intact animal so far, mainly due to methodological constraint [174-177]. The most commonly used experimental technique to investigate cardiac electrophysiology *in vivo* is based on the delivery of electrical pulses to the epicardial surface during ECG recording [178, 179]. However, electrical stimulation is inevitably associated to tissue damage, no uniform dispersion of depolarization, and faradaic effects, all of which interfere with the control of shape and size of the activated myocardial volume [180-182]. In addition, electrical stimulation does not allow to obtain information on the individual role of the conduction system cells, as they are embedded in

the myocardium and not easily accessible to electrophysiological investigation [177, 183-185].

Optogenetics exploits the targeting of photoactivatable ion channels in specific cell types to achieve non invasive control of membrane potential [141].
Channelrhodopsin-2 (ChR2) is a microbial derived cation channel, that alike visual rhodopsin and bacteriorhodopsin, undergoes a conformational change upon illumination resulting in the immediate increase in ionic permeability, with high conductance to Na^+ [68, 186]. ChR2 exhibits fast and reversible activation kinetics (in the order of ms), instrumental to drive reliable trains of high frequency action potentials *in vivo*. ChR2 is widely used in neuroscience to modulate neuronal circuits in *in vivo* models [70, 71, 187] and has been proposed as an attractive tool to control cardiomyocyte membrane potential [53, 56, 57, 75, 180]. However, the use of optogenetics in cardiac research is still in very early stages and has mainly been applied to *in vitro* and regenerative medicine studies [72-74, 188, 189].

We have applied optogenetics in transgenic mice with cardiac specific ChR2 expression to determine the critical cell mass necessary to generate focal ectopic beats *in vivo*, and to address the vulnerability of the ischemic heart to ventricular arrhythmias, in relation to the characteristics of the focal trigger. Furthermore, we exploited genetic targeting of ChR2 to Purkinje cells to interrogate the role of this cellular network in cardiac electrophysiology and arrhythmogenesis.

RESULTS

1. Non-invasive generation of cardiac ectopies *in vivo* using cardiomyocyte specific expression of ChannelRhodopsin-2.

To achieve ChR2 expression in cardiomyocytes, we crossed B6.Cg-Gt (ROSA) 26Sortm27.1 $^{(CAG-COP4*H134R/tdTomato)\ Hze}$/J expressing mice with a transgenic strain encoding Cre-recombinase under the control of cardiac-specific α-Myosin Heavy Chain (αMyHC) promoter. The resulting offspring had the STOP cassette deleted in cardiomyocytes, driving the expression of ChR2 (hChR2 (H134R)-*tdTomato* fusion protein). Expression of ChR2 was detected in >95% of the cardiomyocytes, with indistinguishable level throughout the myocardium (**Fig.1a,b** and **Fig.S1b**). ChR2-expressing mice had normal heart size, morphology, and gross electrophysiology (Heart Rate, α-MyHC-ChR2: 340±39 *vs* control: 322±9, in bpm; n=10 mice for each group) (QRS interval, α-MyHC-ChR2: 12.43±0.63 *vs* control: 13.05±0.87, in ms; n=10 mice for each group).

To obtain timely and spatially controlled photostimulation of ChR2 hearts *in vivo*, we used fiber optics delivering 470nm light pulses generated by a time-controlled Light Emitting Diode (LED), in an open-chest anesthetized mice during continuous ECG monitoring (**Fig.1c**). The effect of local cardiac photostimulation was mapped by delivering brief (1-5 ms) light pulses with the fiber tip placed close to the epicardium of different heart regions (**Fig.1d-e**). Atrial stimulation evoked supraventricular paced beats with normal QRS and wider P waves (left atrium P waves, baseline: 14.28±0.26 *vs.* photostimulation: 27.90±0.63, in ms; n=15 mice). Ventricular stimulation triggered beats with enlarged QRS complexes from the heart base to the apex in both the right and left sections (basal QRS: 12.43±0.63 vs photostimulated QRS: 21.82±0.90, in ms; n=10 mice for each group) (**Fig1d**). Repetitive stimulation at the same site evoked VT that, consistent with the fixed ventricular origin had enlarged and identical QRS morphology (monomorphic VT) (**Fig.1e**). Photo-pacing did not cause histochemical or functional signs of tissue damage, even when stimulation of the same focus was prolonged for several minutes (data not shown). In addition, placement on the epicardial surface of the fiber optics tip disconnected from the light source, as well as photostimulation of WT littermates did not cause any alteration in the sinus rhythm.

We thus demonstrated that experimentally induced ectopies can be experimentally evoked, by using optogenetics, with high spatial and temporal resolution and

implemented such methodology for the non-invasive investigation of cardiac electrophysiology.

2. Direct optogenetic assessment of Purkinje fiber function *in vivo* using cx40 driven expression of ChannelRhodopsin-2.

The Purkinje fibers network constitutes the distal ventricular conduction system, branching throughout the subendocardial cell layers of both ventricles, with a high density in the right ventricular wall. *In vitro* studies and mathematical modelling indicate that Pukinje fiber cells have unique structural and electrophysiological properties, but the direct assessment of their function *in vivo*, with conventional approaches (i.e. electrical stimulation), is limited by their subendocardial location and proximity to the surrounding cardiomyocytes. To interrogate the specific role of the Purkinje fibers in heart physiology, we exploited the spatial accuracy of optogenetic photoactivation by genetically targeting ChR2 to ventricular conduction system cells. To this aim, we crossed double-floxed ChR2 with cx40-cre mice, previously shown to drive transgene expression throughout the conduction system cells, including Purkinje myocytes, and the atria [161] (**Fig.2a**). ChR2 expression was assessed by confocal imaging of the red fluorescence of *tdTomato*, and by immunofluorescence using anti-cx40 antibodies, and was detected in the majority of atrial cardiomyocytes and Purkinje fibers, as expected by the cx40 distribution (**Fig.2b-d**). Hearts of cx40-ChR2 mice had normal morphology and function (Heart Rate, cx40-ChR2: 351±20 *vs* control: 322±9, in bpm; n=10 mice for each group) (QRS interval, cx40-ChR2: 12.82±0.25 *vs* control: 13.05±0.87, in ms; n=10 mice for each group), indistinguishable from control littermates (**Fig.S3**).

We therefore used the photoactivation hardware and protocols described above (**Fig.1c**) to selectively stimulate, by illuminating the epicardial surface, discrete foci of Purkinje fibers in the intact heart *in vivo*, and analyze the effects on cardiac electrical activation. Consistent with the ubiquitous expression of ChR2 in atrial cells, photoactivation of the right and left atria resulted in supraventricular pacing, with ECG morphology superimposable to that obtained in the α-MyHC-ChR2 transgenic hearts at corresponding pacing sites (**Fig.2e**). By scanning the heart surface with the fiber optics tip the ventricular conduction system was activated at different sites from the proximal (septal) to the distal Purkinje fiber network. Consistent with the functional role of the conduction system, ectopies triggered by photoactivation of the proximal conduction system had

QRS duration identical to the spontaneous complex (cx40-ChR2 basal QRS: 12.82±0.25 *vs* photostimulated QRS: 13.04±0.33, in ms; n=10 mice for each group) (**Fig.2f**).

At difference with the uniform response to photoactivation of the α-MyHC-ChR2 ventricles, Purkinje fiber stimulation yielded highly variable effects depending on the illumination site. Albeit ectopies were in general evoked with the stimulation of all RV regions, successfully coupled light pulses were almost 100% in a small (about 2 mm^2 wide) region of the lateral RV free wall (**Fig 2e,f** and **Fig 3a**), in correspondence to the origin of the right ventricular outflow tract (RVOT). We used confocal immunofluorescence of Purkinje fibers and Optical Projection Tomography in intact cx40-GFP to gain insight on the relationship between the geometry of Purkinje fibers arborization and the response to photostimulation. The small RV hyperactivable region identified functionally with optogenetics was characterized by the presence of Purkinje fibers arranged in multiple cell layers (**Fig 3a,b**). Moreover the 3-D reconstruction of the conduction system network showed that in such region, Purkinje fibers connect to the right septal branch (**Fig.3c-f**), suggesting that the increased responsiveness to local activation might be explained by high degree of interconnection with other sectors of the conduction system. Regardless on the photoactivation site or intensity, responses to photoactivation of cx40-ChR2 hearts were abolished by intracavital injection of iodine/potassium iodine solution (Lugol's solution), a common strategy used to ablate Purkinje fibers [150, 190-194], further proving the specificity of the cx40-ChR2 mouse model (**Fig.3g**). Intracavital injection of physiologic solution did not alter heart responsiveness to photostimulation (n=5 mice for each group).

Our results show that the cx40-ChR2 model represents a unique tool to investigate the role of the cardiac conduction system *in vivo*, using a simple experimental setup that allows accuracy and flexibility without requiring invasive approaches, i.e. endocardiac electrophysiology.

3. Requirement for afterdepolarizations to trigger ectopies in the working *vs* conducting myocardium.

Propagation of focal arrhythmic beats in the heart occurs when the current density generated by the abnormally depolarizing cardiomyocytes (current source) is sufficient to overcome the electrotonic sink of the surrounding polarized tissue. The critical cell number needed to bring the sink to its activation threshold has never been determined directly in the intact heart, and neither has been elucidated the individual contribution of

the two distinct myocyte populations (i.e. working *vs.* Purkinje myocytes). Here, we exploited the ability of optogenetics to specifically control a distinct myocardial cell population, in a well-defined volume, to determine the tissue requirements for the generation of a globally spreading wavefront causing arrhythmic beats *in vivo*.

To quantify the relationship between the number of activated cells and the vulnerability to generate ectopies, we implemented an optogenetic assay based on gradually increasing the photoactivation light intensity and fiber optics diameter (light density: 0.36 to 27 mW/mm^2; fiber tip diameter: 100 to 1500, in µm). Mathematical modelling of tissue light absorption was used to estimate the fraction of illuminated tissue irradiated by light at a density sufficient to trigger action potentials in cardiomyocytes, based on threshold values obtained by us and others in isolated cells (0.8-0.5 mW/mm^2) [53, 73] (**Fig.4**). By independently modulating light intensity and fiber diameter it was possible to control the light penetration depth (h) and width (d), respectively, thus shaping the cylinder of illuminated myocardium as shown in **Figure 4**. When all cardiomyocytes were photoactivated (α-MyHC-ChR2, n=10 mice), ventricular beats were triggered upon illumination of a tissue cylinder of (d:200; h: 458-572,µm) in the LV, and of (d:100; h:607-720, in µm) in the RV, corresponding to a range of 1450-1800 and 480-570 cardiomyocytes, respectively (**Fig. 4c-d**). It is likely that the differences observed in the critical tissue mass in the two ventricles may reflect the contribution of Purkinje fibers in the photoactivation of the thinner RV, although a role played by the different electrophysiological properties of RV and LV cardiomyocytes cannot be excluded. To more specifically establish the critical tissue requirements to generate premature ventricular contractions (PVC) upon right ventricular stimulation, we chemically ablated Purkinje fibers using intracardiac injection of Lugol's solution. In these conditions, the liminal photoactivated volume increased to values comparable to those measured in the LV (RV+Lugol's solution: 1950-2300 working myocytes, n=5 mice) (**Fig.4d**).

It is well-accepted that Purkinje fibers are prone to develop early- or delayed afterdepolarizations that, in turn, represent common trigger mechanisms of ventricular arrhythmias. How many Purkinje fiber cells are needed to simultaneously fire for successful propagation of their AP into the myocardium, has not been determined so far. Thus, we calculated the minimal volume to be irradiated to evoke Purkinje fibers driven PVCs in the most responsive regions of the RV, which resulted of about d: 200; h: 625-740, in µm (d,h), corresponding, based on our immunohistochemical quantification to about 70-160 cells (n=8; cx40-ChR2 mice). Collectively, our results demonstrate that

ectopies can be triggered *in vivo* by the afterdepolarization of either a substantial number of working cardiomyocytes, or a much lower quantity of Purkinje fibers. Although with disparities in the cell number presumably due to species differences, our findings support the concept suggested by computational modelling of the rabbit heart, whereby afterdepolarizations arising in Purkinje fibers are more likely to overcome the source-sink mismatch and trigger ectopic beats [52].

4. Selective electrophysiological study of Purkinje fibers in vivo.

To assess the maximal ventricular pacing rate, we photostimulated hearts with trains of light pulses delivered at incrementally shorter cycle repetition rate, from 10 to 25 Hz, and determined the threshold for 1:1 capture by analyzing the ECG trace. The α-MyHC-ChR2 hearts were responsive up to 18 Hz (1080 bpm) (n=5 mice), while the cx40-ChR2 mice responded with 1:1 capture up to about 15Hz (900 bpm) (n=5 mice), and above this threshold, stimulation was effective in variable percentage of activation flashes (**Fig.5a**). These results are compatible with the increased refractoriness reported for the conduction system cells with respect to the working cardiomyocytes. However, the Effective Refractory Period (ERP) of Purkinje fibers, has only been determined in *ex vivo* preparations [3, 4, 192, 195-197], or inferred using intracavital microelectrodes to deliver electrical pulses to an area that includes, but is not limited to, the conduction system [183-185, 198, 199]. We thus performed non-invasive epicardial optical programmed stimulation to determine selectively the ERP of Purkinje fibers and that of the working cardiomyocytes *in vivo*. The standard electrophysiological protocol of 'extrastimulus' (see **methods** and **Fig.5b**), was used for optical stimulation and demonstrated that, in accord with the data acquired on *ex vivo* preparation, the ERP of Purkinje fibers measured directly *in vivo* was significantly longer than that of the working myocardium (ERP, RV cx40-ChR2: 59.7±1.2 *vs* α̃MyHC-ChR2: 38.4±2.6, in ms; n=5 cx40-ChR2 mice and n=10 α̃-MyHC-ChR2 mice) (**Fig.5c**).

5. Optogenetic investigation of arrhythmia mechanisms.

Sudden cardiac death (SCD) caused by ventricular arrhythmias in the early phase of acute myocardial ischemia accounts for a large number of fatalities yearly [168]. Ischemia induces heterogeneities in excitability, refractoriness and/or conduction that generate a permissive myocardial environment (substrate) upon which abnormal depolarizations, although uneventful in the healthy heart, may act as trigger for self-sustained arrhythmias.

What are the factors, i.e. location relative to the ischemic area, size and cell type (working *vs.* Purkinje myocytes), that characterize an efficient focal trigger for sustained ventricular arrhythmias during ischemia has not been addressed directly. To explore this, optogenetics was used during the acute phase of experimental ischemia in the α-MyHC-ChR2 and the cx40-ChR2 mice. Myocardial ischemia was obtained by ligating the left anterior descending (LAD) coronary artery during continuous ECG monitoring. The tributary myocardium became immediately pale and within the first fifteen minutes, ischemia caused the expected alterations in the QRS complex (**Fig.6a,b**). In both the α-MyHC-ChR2 (n=10 mice) and the cx40-ChR2 (n=8 mice) hearts in the initial ischemic phase (0-15 min), responses to focal photostimulation were similar to the non-ischemic controls, with the exception of the non-perfused area that became progressively unresponsive. Repetitive pacing at various epicardial foci outside the ischemic region of the left and right ventricles, at frequencies ranging from 10 to 25 Hz, caused monomorphic VT terminating promptly after pacing cessation (**Fig.6c,d**). Such behaviour differed in the α-MyHC-ChR2 ischemic hearts at 15-30 min. after LAD coronary ligation, as epicardial photo-pacing evoked frequent episodes of ventricular flutter continuing for a few (2-5) beats after pacing, that were never observed in the shams stimulated with identical protocols (n=6 mice) (**Fig.6e,f**).

During the transitional phase to the irreversible ischemic damage [200-202], at 45-60 min after LAD ligation, the effect of cardiac photostimulation of the working myocardium (α-MyHC-ChR2) and the Purkinje fibers (cx40-ChR2) was different. In fact, optical pacing with brief (1s) bursts of light flashes, in the RV area enclosing the junctional region between the septal and RV conduction system, triggered sustained polymorphic VT and VT/VF lasting up to 50s, in 80% of the α-MyHC-ChR2 mice analyzed (**Fig.3** and **Fig.7a,b**). These arrhythmias were evoked by pacing at repetition cycle times close to the ERP for the same animal (**Fig.7b**). Remarkably, the same photostimulation protocols applied to the Purkinje fibers of ischemic cx40-ChR2 hearts resulted in monomorphic VT that only lasted the pacing period, and failed to induce sustain arrhythmias, regardless of the burst stimulation frequency and location (**Fig.7c**). These results indicate that, in the presence of myocardial ischemia, focal ectopic beats originating in the RV, and in particular in the region corresponding to the RVOT origin, from the simultaneous depolarization of Purkinje fibers and surrounding cardiomyocytes, are potential triggers for sustained arrhythmias.

DISCUSSION.

Most ventricular arrhythmias are caused by the combined effect of factors creating a *substrate* in the heart tissue favouring electrical instability, with events of localized depolarization in the cardiomyocytes serving as *trigger* [51, 52]. While great progress has been made in the identification of the mechanisms determining the pro-arrhythmogenic substrate (e.g. genetic mutations altering the single cell electrophysiology or cell-cell communication, myocardial fibrosis) [166, 167, 203], the fundamental requirements of arrhythmia triggers are poorly understood yet. Here, we used cardiac optogenetics to define such requirements, by determining the minimal cell number of working *vs* conducting cardiomyocytes that characterize a triggering focus of ectopic heartbeats in the normal heart. Moreover, we investigated the arrhythmogenic potential of such ectopies in the context of acute myocardial ischemia, a condition associated to increased arrhythmia susceptibility [169, 171, 172], and correlated arrhythmias with the location in the heart and the different cell systems involved in the triggering focus (working *vs* conducting cardiomyocytes).

Critical determinants of arrhythmogenic foci

Ectopic heartbeats are common disturbances of the heart rhythm whereby the untimely depolarization of groups of cardiomyocytes, mainly due to early- or delayed-afterdepolarizations, disrupts the physiologic sequence of impulse formation resulting in premature contractions. The electrotonic coupling of the myocardium protects from the propagation of action potentials originated from a afterdepolarization, that requires a sufficient number of cardiomyocyte activated simultaneously to overcome the source-sink mismatch [51, 52]. Here we quantitatively studied the critical determinants of arrhythmogenic focal sources, including the minimal cell number, their cardiac topology and the type of cells involved. These aspects were only indirectly estimated in *ex vivo* preparations or with simulation modeling based on cellular data, thus far [51, 52]. We used optogenetics that allows the direct activation, *in vivo*, of selective cardiac cell populations expressing the photoactivable channels (i.e. ChR2 in this study) in confined regions of the heart wall, thus mimicking focal spontaneous electrical activity. As a prerequisite to our experimentation, we determined the attenuation of the blue light across the myocardial wall, by combining light penetrance data in tissue phantoms with mathematical modeling, and were thus able to accurately measure the photoactivated myocardial volume and the size of the experimentally generated ectopic foci. Our data

demonstrated that the minimal number of cardiomyocytes required to form a focal ectopic site of ventricular activation is, in the mouse heart, in the order of few thousand (from 1400 to 2000) cells. When premature depolarization was selectively induced in the Purkinje fiber subsystem, a much lower number of simultaneously depolarizing cells (about 100) was needed to trigger ventricular activation. This observation is in agreement with the prediction of simulation modelling [52] suggesting that, irrespective of their sensitivity to develop afterdepolarizations, a lower number of cells acting as current source is required in Purkinje fibers than in common cardiomyocytes to overcome the protective effect of myocardial current *sinks*, solely due to their quasi mono-dimensional arrangement. In further proof of this concept, more cells were required to trigger ectopic heartbeats in the RV free wall at the origin of the RVOT, where the Purkinje fiber network is densely arborized, with complex interconnectivity between fiber bundles. According to the results of simulation modeling, this cell arrangement, by approximating a higher-dimensional tissue structure, increases the current load necessary to overcome the source-sink mismatch [52]. Notably, when light pulses were delivered to this region at supra-threshold intensity, the success rate in the activation of ectopic heartbeats was close to 100%. Taken together, these results demonstrate that the selective optogenetic interrogation of the Purkinje fibers, combined with the topological study of their distribution, informs on the structure/function relationship of this cardiac sub-system with unprecedented detail.

Ischemia and arrhythmias

Acute myocardial ischemia is a major cause of sudden cardiac death (SCD) [169, 170]. The sudden cessation of myocardial blood flow causes heterogeneities in excitability, refractoriness and/or conduction. All of these factors contribute to creating the pro-arrhythmogenic myocardial *substrate* that, in the presence of ectopic excitation from focal sources, may *trigger* the lethal ventricular arrhythmias [171, 200, 204]. Having established the tissue determinants for the generation of focal ectopic beats, we aimed to ascertain the characteristics of focal ectopic triggers of ventricular arrhythmias potentially causing SCD, by coupling optogenetic investigation to the experimental model of acute myocardial ischemia. Central to such experimental design, the optogenetic investigation is non-invasive, and does not associate to heterogeneity in myocardial depolarization nor to tissue damage due to the production of damaging gases (Cl_2, H_2, O_2) and pH alterations, all of which are common effects of electrical stimulation of the heart [181,

182]. As such, focal ventricular pacing in the healthy heart could be performed even at elevated rate and for a prolonged period of time (up to 30 min), and never triggered arrhythmic episodes. In contrast, focal pacing during myocardial ischemia triggered several arrhythmia types, progressing from short runs of extra beats to sustained ventricular tachycardia/fibrillation, along with ischemia time. Remarkably, the longer and more complex arrhythmias were triggered by local pacing in correspondence of the right ventricular portion showing a complex organization in the terminal Purkinje fibers.

The same structure has been identified in the human heart [205, 206], and it is tempting to speculate that cardiac conduction system might contribute to generate ectopies arising from the RVOT [7].

We have used here a rather simple hardware setup for the photoactivation experiments in the mouse, but our preliminary investigations indicate that technical strategies allowing complex light patterns, e.g. multiple photopacing foci or delivery of complex spatial illumination patterns, can be used to mimic relevant arrhythmogenic phenotypes, including bidirectional ventricular tachycardias or spiral depolarization wavefronts.

In conclusion, we have extended the cardiac optogenetics toolkit with a novel murine model with ChR2 expression restricted to the conduction system, and developed experimental protocols to address physiological and pathological mechanisms relevant to the understanding of cardiac arrhythmias. In perspective development, optogenetics can be employed for the study of other arrhythmia-linked genetic (e.g. LQTS, CPVT) or acquired arrhythmogenic conditions and for pharmacological research aimed at the identification and testing of antiarrhythmic compounds.

METHODS

Mouse models. Transgenic mice expressing cre-recombinase under the control of either alpha-Myosin Heavy Chain (α-MyHC) or connexin-40 (cx40) promoter were bred with B6.Cg-Gt(ROSA)26Sor$^{tm27.1(CAG-COP4*H134R/tdTomato)Hze}$/J expressing mice (Jackson Lab. Bar Harbor, Maine, USA). The resulting offspring has the STOP cassette deleted in the heart, resulting in cardiomyocyte (α-MyHC-ChR2) or Purkinje fibers (cx40-ChR2) expression of the hChR2(H134R)-*td*Tomato fusion protein. Both α-MyHC-CRE$^{+/-}$ and cx-40-CRE$^{+/-}$ lines were used to maintain the colonies. Hearts from cx40-GFP transgenic mice were also be analyzed [207]. All experimental procedures described in this manuscript have been approved by the local ethical committee (Authorization number C54) and communicated to the relevant Italian authority (Ministero della Salute, Ufficio VI), in compliance of Italian Animal Welfare Law (Law n 116/1992 and subsequent modifications).

***In vivo* epicardial photostimulation.** Adult ChR2 expressing transgenic male mice and littermate controls were anesthetized by isofluorane administration (1,5%-3%), secured to the table in supine position and intubated with a 24G needle for ventilation (tidal volume 0.4ml; 120 strokes/min) from an artificial ventilator (SAR-830). Body temperature was monitored constantly during the experiment. The skin was dissected by a lateral sub-ascellary 1.5cm cut, subcutaneous muscles were removed and a 0.5 cm incision was performed at the level of the 4th intercostal space. Self-retaining microretractors were then used to separate the 3rd and 4th ribs enough to get adequate exposure of the operating region. The heart was exposed and different epicardial regions from the atria and the left and right ventricles were stimulated by differently-sized (from 100 to 1500 diameter, in μm) fiber optics (Thorlabs, Germany), coupled to a 470nm LED (Thorlabs, Germany), controlled by an ECG-coupled recording system (Powerlab 8/30, Bioamp and LabChart 7.1 software; AD Instruments).

ECG recording and analysis. A standard lead I ECG was recorded (Powerlab 8/30, Bioamp; AD Instruments) during the experiment. ECG parameters (QRS, PR interval and heart rate) were calculated by using LabChart 7.1 software (AD Instruments).

Measurement of The Ventricular Effective Refractory Period (VERP). The VERP of both the working cardiomyocytes and Purkinje fibers was evaluated in α-MyHC-ChR2 and cx40-ChR2, respectively, by using the extrastimulus technique [208, 209]. The epicardial surface of the right ventricle was photostimulated by a train of 10 light pulses (5 ms), at a frequency of 10Hz (cycle length=100ms) (**S1**), followed by a premature optical stimulus (**S2**) at progressively shorter coupling interval until the S2 failed to trigger an ectopy at the VERP (see **Fig. 5b**).

Evaluation of blue light penetration throughout the myocardial tissue. Hearts from both control and ChR2 expressing mice were harvested and the left and right ventricular walls dissected. Intact ventricles, as well as longitudinally cut ventricular slices of different thickness (0; 250; 400 and 800, in µm) were placed with the endocardial side in contact with the light sensor of an optical power meter (Thorlabs, PM100D). The same fiber optics used in the *in vivo* experiments were used to illuminate the tissue phantoms and measure the emerging light with the radiometer. Emerging light intensity was measured with dependency on the fiber output light intensity, fiber size diameter (from 100 to 1500 µm), and phantom thickness. Myocardial light attenuation was modelled by adapting previous studies made in the brain [69]. Briefly, values of light intensity experimentally determined using the tissue phantoms described above were fitted to a monoexponential decay curve to extrapolate light intensity as a function of the depth from the epicardial surface. Light intensity threshold for ChR2 activation were obtained from [53, 73].

Pharmacological Purkinje Fiber ablation. Lugol's solution (10 µl) or vehicle, supplemented with an equal volume of Heparin (all from SIGMA), were carefully injected into either the RV or the LV cavity by using a Hamilton syringe supporting a 34G needle. To increase permanence of Lugol's solution in the ventricles, the pulmonary artery or the aorta were transiently clamped (about 10 s).

Optical Projection Tomography. Hearts from cx40-GFP transgenic mice were analyzed as previously described in [210].

Left anterior descending (LAD) coronary artery ligation. The main trunk of the LAD coronary artery was ligated by using a 7/0 polypropylene suture [211]. Epicardial

photostimulation was performed at different time points (from 5 to 90 minutes) after coronary occlusion, during constant ECG recording.

Tissue samples and immunofluorescence analysis. The hearts were harvested from transgenic, as well as control mice, fixed in 2% paraformaldehyde (PFA) (Sigma) for 1 hour at room temperature, equilibrated in sucrose gradient at 4°C, embedded in OCT and frozen in liquid nitrogen. Ten-micron myocardial sections were obtained with a cryostat (Leica CM1850, Leica Microsystems GmbH, Wetzlar, Germany) and processed for histological and immunofluorescence analyses. Immunofluorescence analysis was performed as described in [6]. The following primary antibodies were used in this study: rabbit anti-cx40 (1:200, Invitrogen); mouse anti-α-MyHC (1:200, clone BAG5; [212]) and rabbit anti-cx43 (1:200, Chemicon). FITC-conjugated secondary antibodies, all from Jackson lab. (UK), were used to detect primary antibodies. Sections were analyzed with a Leica TCS SP5 confocal microscope.

Statistical analysis. All data are expressed as the mean±s.e.m. Comparison between the experimental groups has been performed by using the non-paired Student's *t* and Anova tests with $P<0.05$ being considered statistically significant.

ACKNOWLEDGMENTS

This work was supported by the following grants: the European Community Seventh Framework Program FP7/2007-2013 under Grant Agreement HEALTH-F2-2009-241526, EUTrigTreat to MM, SL and Telethon-Italy (GGP11224) to MM. We are grateful to: Tullio Pozzan, Nicola Elvassore, Davide Gobbo, Niccolò Roda for critical discussion; Anna Pia Plazzo and Emilio Bigon for technical assistance.

Authors contribution: MM, TZ, NP, SL designed research; TZ, NP, GB, FDB, MM, LM executed the experiments and analysed the data; MC provided reagents; TZ, NP, DC, LM, MM wrote the manuscript.

COMPETING FINANCIAL INTEREST

The authors declare no conflicting financial interests.

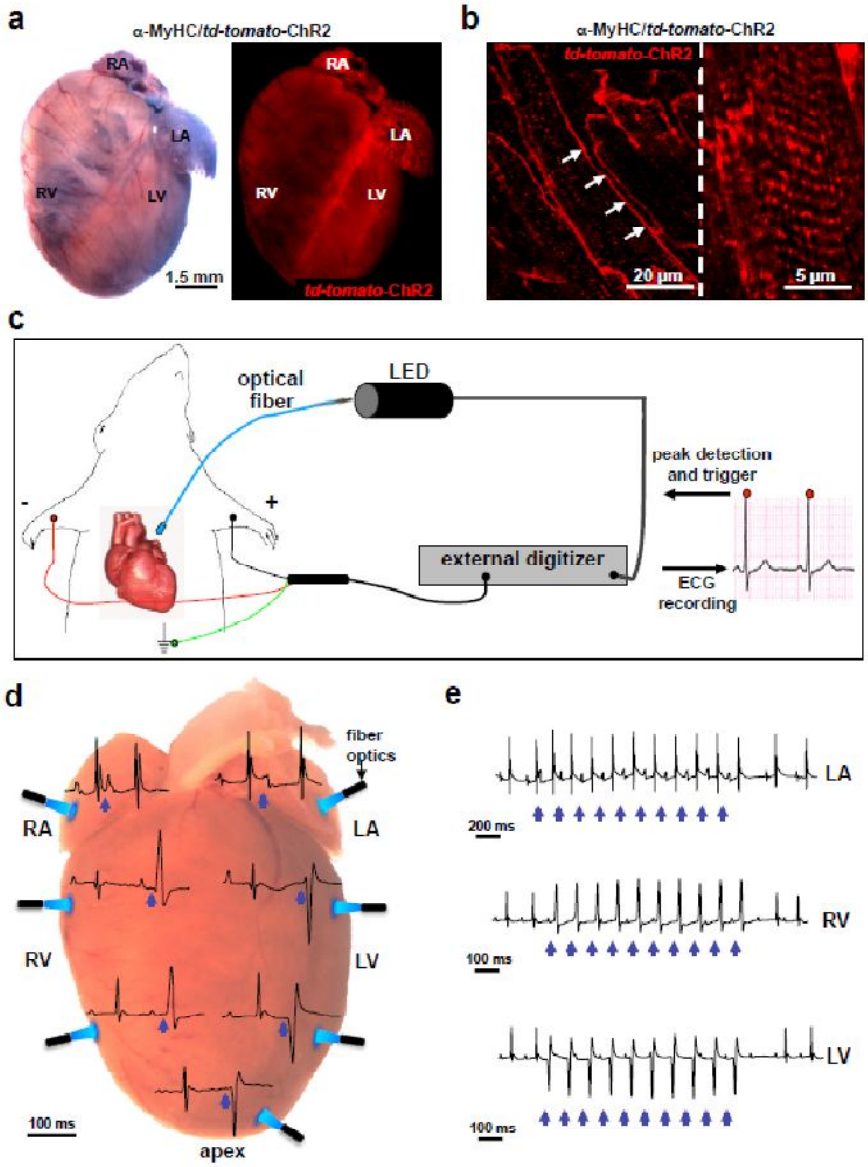

Figure 1. Cardiac optogenetics allows non-invasive investigation of heart electrophysiology *in vivo*.

(**a**) Bright field (left panel) and fluorescence (right panel) images of α-MyHC/*td-tomato*-ChR2 heart. The right image of *td-tomato* fluorescence shows expression of ChR2 in both the atria and the ventricles. RA, right atrium; LA, left atrium; RV, right ventricle; LV, left ventricle. Scale bar: 1.5mm. (**b**) Confocal image of ventricular cryosections from α-MyHC/*dt-tomato*-ChR2 transgenic hearts showing ChR2 localization at the level of cardiomyocyte sarcolemma (white arrows) and T-tubules. Scale bar: 20µm; high magnification, 5µm. (**c**) Representation of the set up used for epicardial photostimulation in open-chest anesthetized mice. LED stimulation occurred through fiber optics delivering time controlled pulses of 470nm blue light. The LED was connected to the ECG apparatus, allowing to synchronize the LED stimulation with specific time point of the ECG recording. (**d-e**) Representative ECG traces of ectopic beats originated by epicardial light-stimulation of different regions of the myocardium from α-MyHC-ChR2 mice (n=10 mice). Blue arrows in (**d**) and (**e**) indicate light pulses (5ms). LA, RV and LV photostimulation originates ectopic beats with different QRS shape.

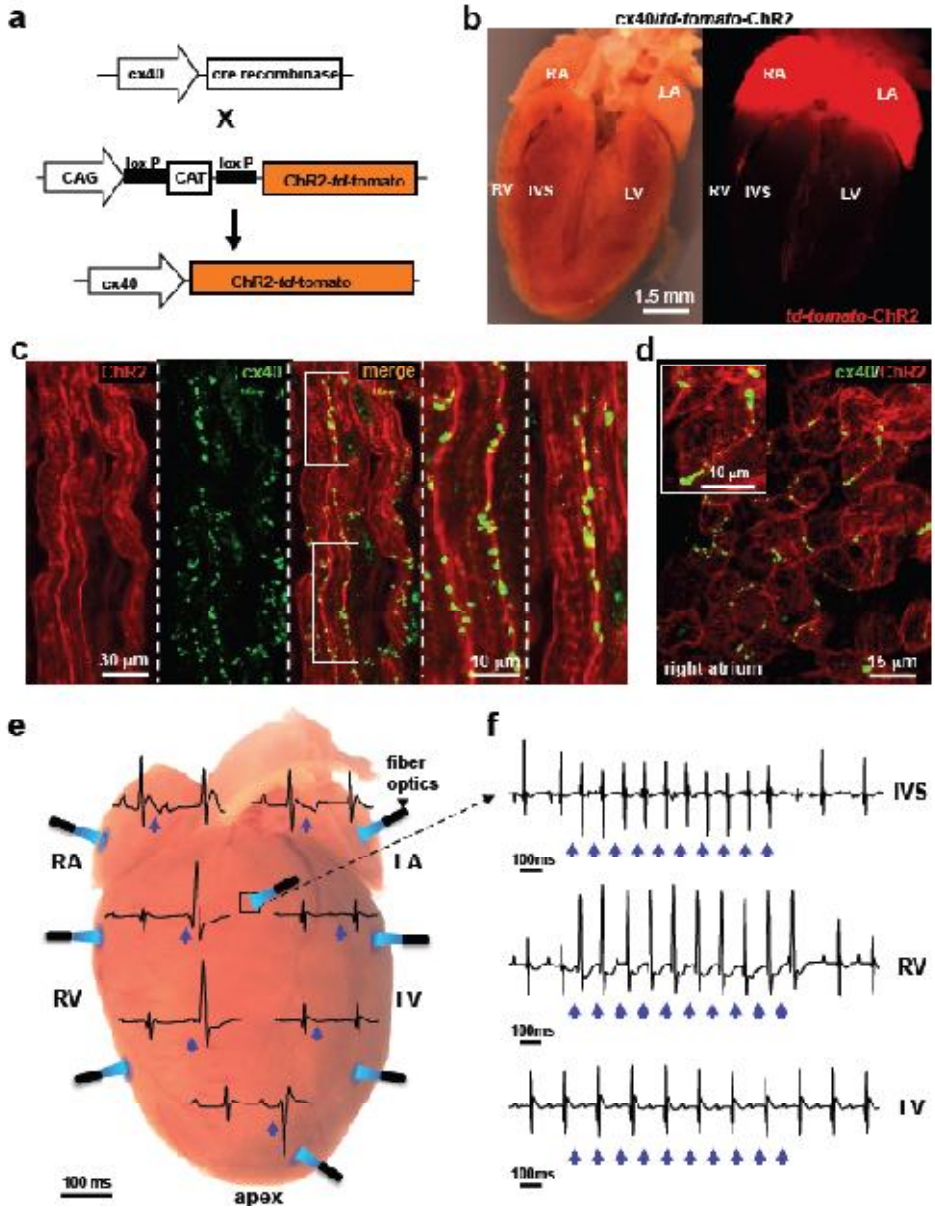

Figure 2. Direct optogenetic assessment of Purkinje fiber function *in vivo*.
(**a**) Scheme of the generation of the transgenic mouse expressing the fused protein, *td-tomato*-ChR2, under the control of connexin-40 (cx40) promoter, (cx40-ChR2). (**b**) Bright field (left panel) and fluorescence (right panel) images of a longitudinally sectioned whole cx40-ChR2 heart. The right image shows specific expression of ChR2 in the atria and the conduction system. RA, right atrium; LA, left atrium; RV, right ventricle; LV, left ventricle. Scale bar: 1.5mm. (**c-d**) Confocal immunofluorescence analysis on ventricular (**c**) and atrial (**d**) cryosections from red fluorescent cx40-ChR2 mice stained with an antibody specific for cx40 (green signal). Scale bars: (**c**) 30µm; high magnifications, 10µm; (**d**) 15µm. (**e-f**) Representative ECG traces of ectopic beats originated by epicardial photostimulation of different regions of the myocardium from cx40-ChR2 mice. Blue arrows indicate light pulses (5 ms). RV and IVS photostimulation originates ectopic beats with different QRS shape, while LV epicardial stimulation failed to induce ectopies.

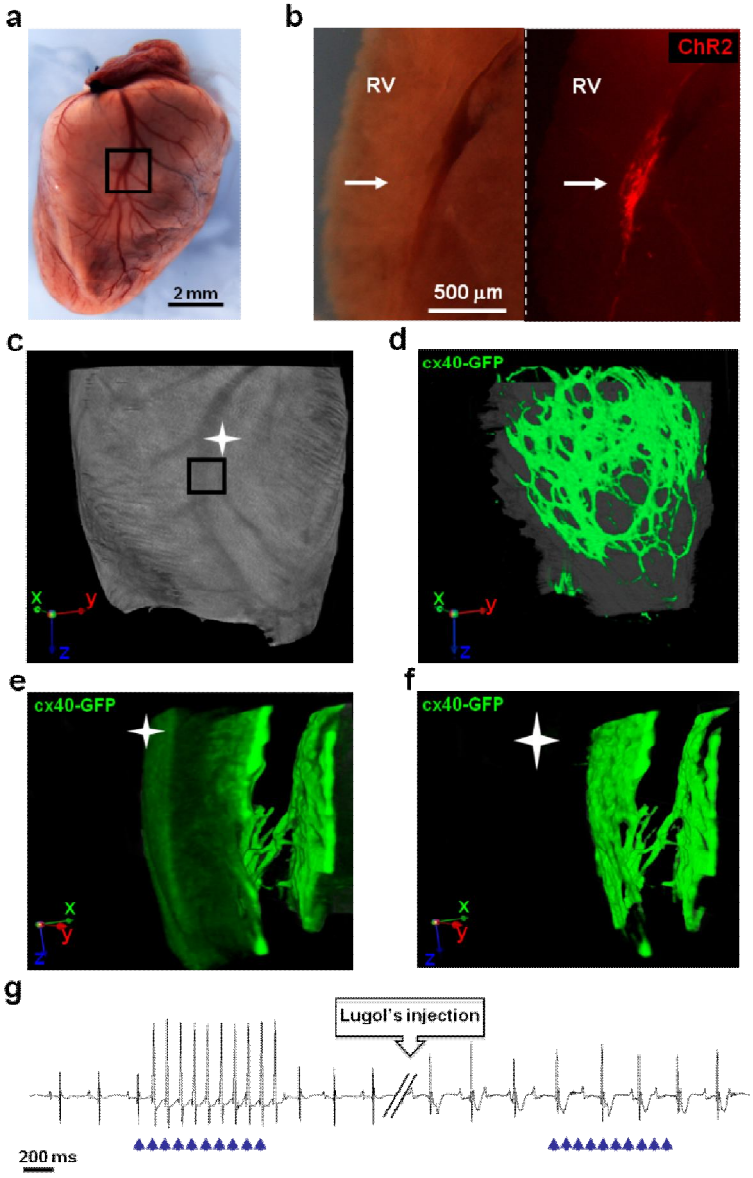

Figure 3. Correlation between distribution and function of the Purkinje fiber network in the right ventricle.

(**a**) RV epicardial surface from a whole cx40-ChR2 heart. The black box indicates the RV region with the highest responsivity to photostimulation. Scale bar: 2mm. (**b**) Bright field (left panel) and fluorescence (right panel) images of the RV section at the anatomical level enclosed in the black box in (**a**). Scale bar: 500µm.

(**c-f**) three-dimensional reconstruction of the RV Purkinje Fiber arborization obtained in cx40-GFP transgenic mice by optical projection tomography. Rotation of the 3-D reconstructed image (see coordinates in the panel corner) (**e,f**) highlights the connecting bundle between the septal and the right ventricular branches of PF. **(g)** ECG traces of ectopic beats originated by epicardial light-stimulation of the RV from cx40-ChR2 mice before and after (15 min) RV intracavital Lugol's solution injection. Blue arrows indicate the light pulses. Lugol's solution treatment caused enlargement of the QRS complex and abolished light induced ectopies.

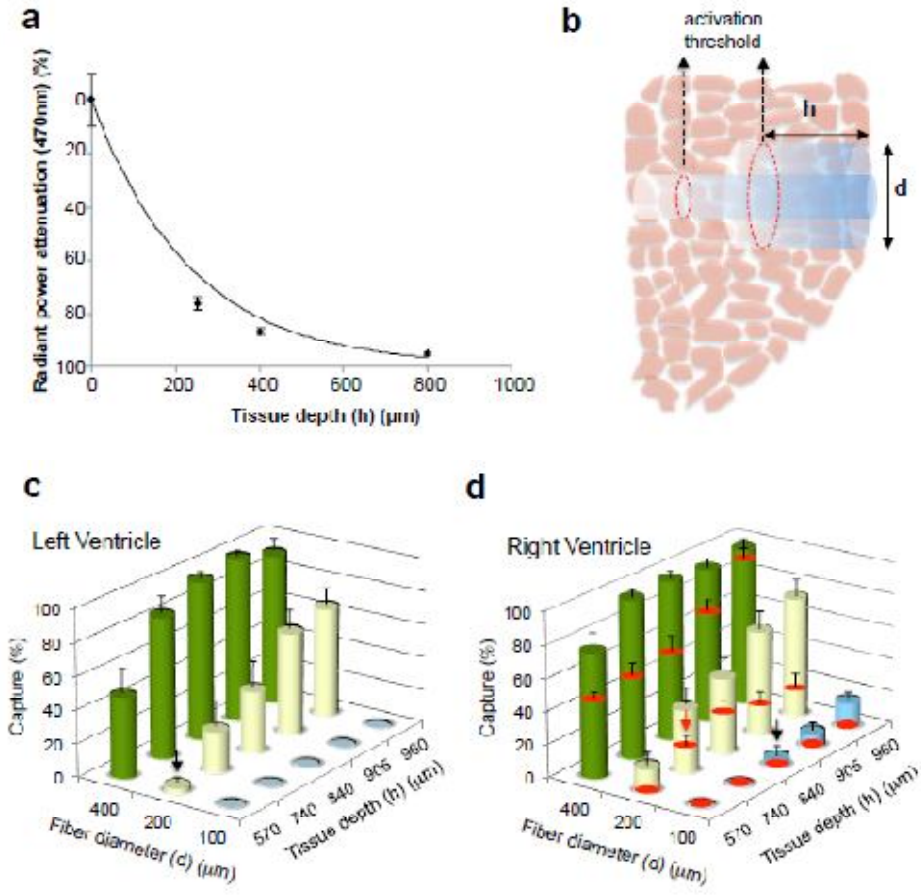

Figure 4. Assay of the minimal myocyte number required to trigger focal ectopic beats in the normal myocardium.

(**a**) Measure of 470nm light penetrance into the ventricular myocardium upon epicardial illumination. Experimental data were fitted to a monoexponential decay function (R^2>0,9) [69], shown with the dashed line. Bars represent sem. (n=10). (**b**) Modulation of light intensity and fiber diameter shapes depth (h) and width (d), respectively, of the illuminated myocardial cylinder. (**c-d**) Optogenetic assay of minimal myocyte number required for successful trigger of ectopies in the LV (**c**) and RV (**d**). The red circle in the columns in (**d**) indicates the captured beats after Purkinje fiber ablation with Lugol's solution. Arrows in (**c**) and (**d**) indicate the minimal tissue volume to be irradiated to evoke ectopic beats before (black arrow) and after (red arrow) Lugol's solution injection. Bars represent s.e.m. (measures repeated in triplicate, in n=10 independent experiments). Numbers above the columns indicate the minimal calculated number of cells required for ectopic beats stimulation.

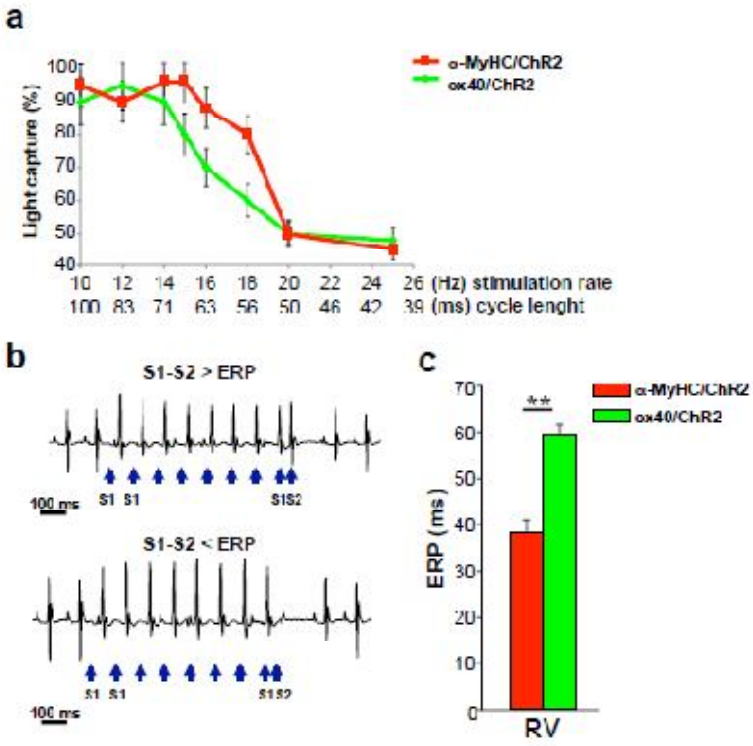

Figure 5. Optogenetics allows selective interrogation of Purkinje fiber electrophysiology *in vivo*.

(**a**) Stimulation rate/cardiac capture relationship obtained in α-MyHC-ChR2 and cx40-ChR2 mice. Bars represent s.e.m. (n=10 hearts for each group). (**b**) Optical programmed stimulation using the extrastimulus (S1-S2) protocol to measure the effective refractory period (ERP). Blue arrows indicate the light pulses (**c**) Evaluation of the ERP in the RV of both α -MyHC-ChR2 (red bar) and cx40-ChR2 (green bar) mice. Bars represent s.e.m. (**, $p<0.01$; n=10 α-MyHC-ChR mice and n=8 Cx40-ChR mice).

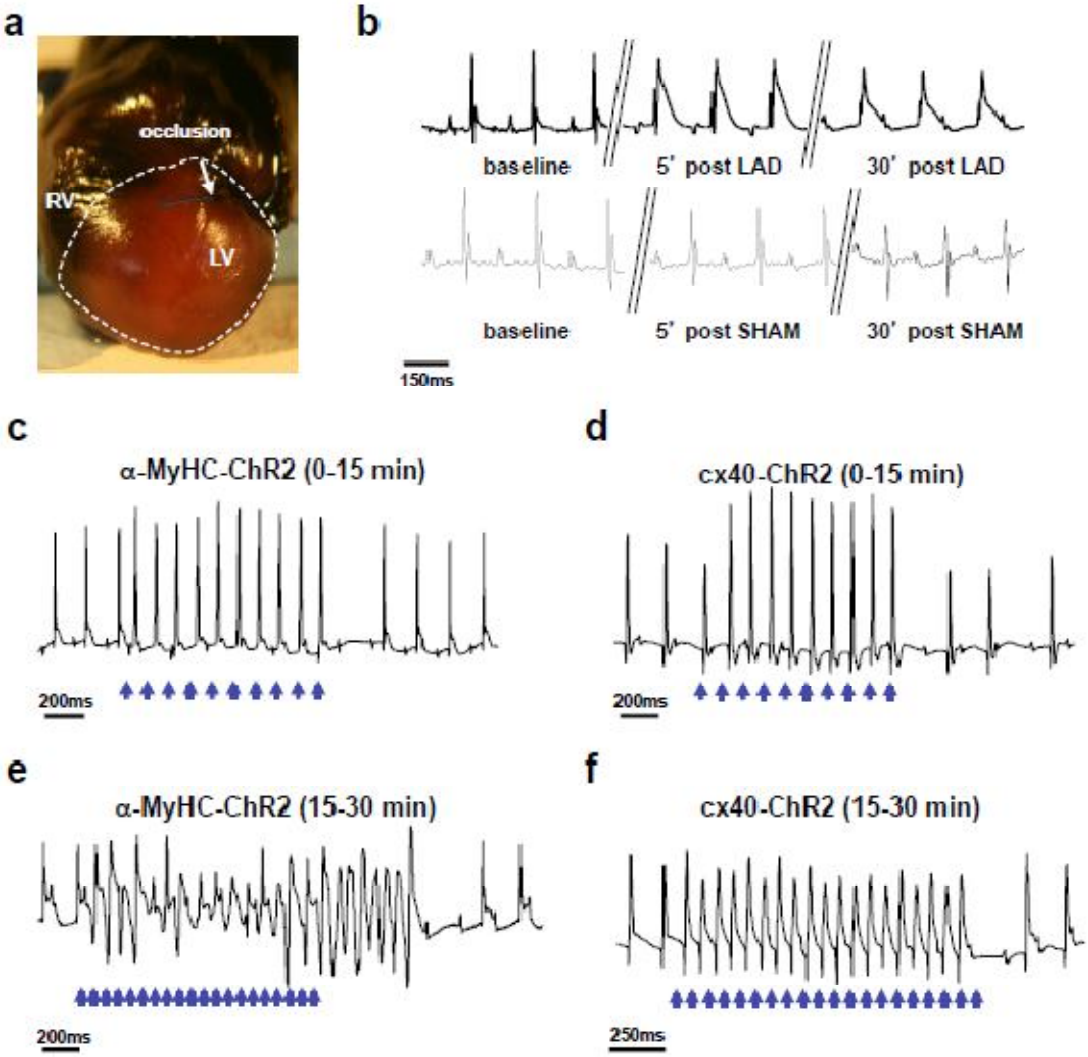

Figure 6. Optogenetic study of post-ischemic arrhythmia mechanisms.
(**a**) Image of a whole heart from a mouse undergone left anterior descending (LAD) coronary artery ligation and subsequent intravenous injection of Evans Blue, to identify the ischemic pale area. White arrow indicates the coronary ligation. (**b**) ECG traces from α-MyHC-ChR2 transgenic mouse at baseline, 5 and 30 minutes after LAD ligation. ECG recording evidences alterations of the QRS complex upon ischemia, which are absent in sham operated mice at the same time point. (**c,d**) ECG traces of RV photostimulation during the first fifteen minutes after LAD ligation in α-MyHC-ChR2 (**c**) and cx40-ChR2 (**d**) hearts. Photostimulation evoked episodes of monomorphic VT terminating with pacing cessation. (**e**) Representative ECG trace recorded between 15 and 30 minutes after LAD ligation in α-MyHC-ChR2. Photostimulation induced ventricular flutter which lasts some beats after pacing cessation. (**f**) Representative ECG trace recorded between 15 and 30 minutes after LAD ligation in cx40-ChR2 mouse. Blue arrows indicate the light pulses.

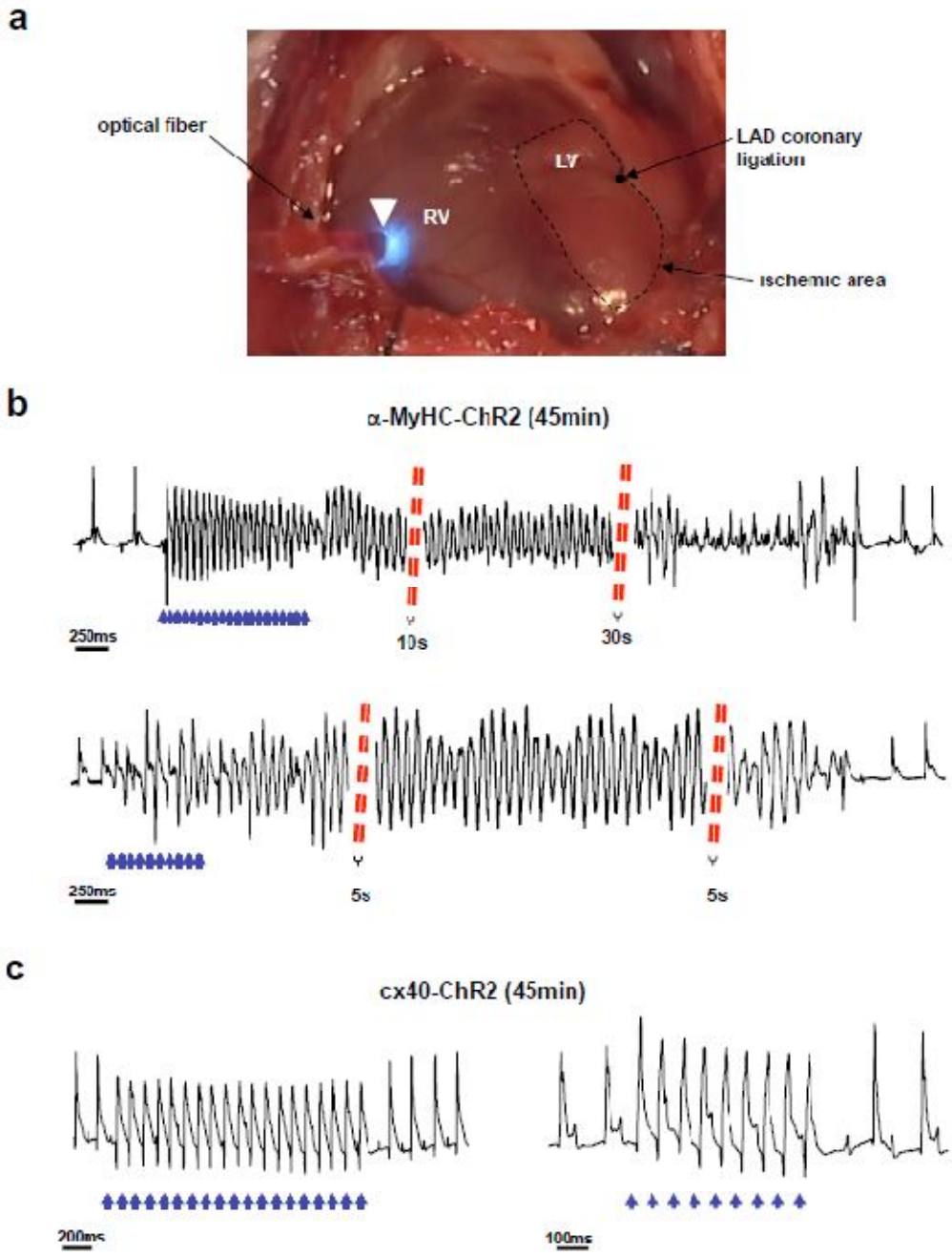

Figure 7. Optical pacing of sustained ventricular arrhythmias in the advanced post ischemic phase.

(**a**) Photograph of the optogenetic experiment, picturing the heart of the anesthetized mouse seen through the toracotomic window, during delivery of a light pulse to the RV epicardium via the fiber optics. The white star shows the heart region described in Fig 3c-f. (**b**) ECG traces of different sustained arrhythmias originated by light-stimulation of the right ventricle, at the free-wall/septal Purkinje fiber junctional site, in α-MyHC-ChR2 during post-ischemic phase 2. (**c**) The same photostimulation protocol used in (**b**) failed to trigger sustained arrhythmias in cx40-ChR2 mice. Two representative experiments are shown. Blue arrows indicate the light pulses.

ACKNOWLEDGEMENTS

This PhD thesis collects the research work that I did in the last 3 years, but also reflects the contributions of people that always believed in me.

It feels like only yesterday I was a physics student looking for a final project in biophysics. First of all, I have to thank my supervisor, Marco Mongillo, that for *inexplicable* reasons believed in me giving me the opportunity to work in his lab that seemed far from my physics lessons, but was extremely close to my personal interests. During this PhD he always encouraged me to maintain and develop my physics background, he taught me how a scientist works and how is supposed to behave when interacting with other scientists (and this, I think, was the most difficult part of my scientific maturation). He taught me that (*probably*) I'm not always right, but when we do agree on something it must be an universal law ☺. Scientific discussion of data and experiments helped and inspired my work during these years, so thank you very much.

When I met Tania in the lab I was not directly her student, but she helped me whenever I was in trouble. I had the opportunity to "study" Tania's work in the lab trying to learn as much as possible, and she gave a large contribution to this thesis. She became a scientific model for me, but also, and probably more important, a real friend. I am honest if I say that, while teaching me how to mature as a scientist, she taught me, probably unknowingly, to grow up as a woman (*girl power!*). Thank you very much!!

Working in Mongillo's lab has been a privilege for me because I met fantastic people. I have to thank Mauro for your *not-always-patient-but-extremely-helpful* answers to all my questions and Nik that contributed a lot to this work. It has been a pleasure to share the *men's office* with you for a while. I would like to thank Valentina, Antonio and Giulia that are always present when it's time to help or laugh together. Many thanks to Niccolò and Davide for the discussion on light-tissue modeling.

For all the microscopy techniques used in this thesis I would like to thank a couple of people. The CUBE group, starting from prof. Pavone that led the project with Marco. Thanks Claudio and Mimmo for the amazing moments and the hard work with the MCUBE and thanks Cimbro both for experimental help and scientific discussion of data (and amazing moments, of course). For Ca^{2+} imaging experiments I would like to thank Francesca and Marika.

I'm grateful to Prof. Pozzan for cameleon probes, Prof. Rizzuto and his group, in particular Diego, for the GCaMPs and MCU constructs and all of them for suggestions and discussion of the data obtained with their plasmids.
I'm thankful to all the expert scientists that contributed with critical discussion of data, in particular Prof. Marks, Prof. Lederer, Prof. Lehnart, Prof. Di Lisa, Prof. Bernardi, Prof. Montecucco. I would like to thank Dr. Catalucci for his suggestions about post-

translational modifications. I'm grateful also to Dr. Andrea Carpi (and it's not a mistake that you are listed with the professors, because it's where I think you belong).

I would like to conclude with people that helped me from a different point of view. I'm grateful to my mom Monica that encouraged and sustained me (especially economically) in starting a new chapter of my life, my *papi* Sandro that showed me that you can change your life when everybody think it's too late and my little brother Giacomo for being my exact opposite.
Finally, I am grateful to Enrico, that always supported me (*ma anche sopportato*) from the beginning of my University carrier. I love you.